

Chapter VII
AERODYNAMICS OF BLUNT BODIES OF REVOLUTION

Editor's Introduction

A COMPREHENSIVE REVIEW of theoretical and numerical methods for calculating inviscid flow over blunt bodies is contained in Hayes and Probstein (*Hypersonic Flow Theory*, 1966). More detailed descriptions of numerical methods of solution are given by Belotserkovskii (NASA TT F-453, June 1967), with emphasis on the direct method developed by himself and Dorodnitsyn (that discussed in the present book). Methods are described for flows of an ideal gas, flows with equilibrium and nonequilibrium dissociation and ionization, and flows of a radiating gas.

Traugott (J. Aero. Sci., May 1960) has developed general relations for the radius of curvature of the shock wave and the velocity gradient at the stagnation point in the form of similarity parameters:

$$\tilde{s}_0 [1 + (r_N/R_N)\bar{s}_0] = \Gamma(\gamma, M_\infty), \quad \frac{\bar{s}_0}{1 + (r_N/R_N)\bar{s}_0} \left(\frac{r_N}{\gamma_\infty} \right) \left(\frac{dV_x}{dx} \right)_0 = \Pi(\gamma, M_\infty).$$

The improved formulas for shock detachment distance on spherical noses given in the footnote on p. 572 of Section 20 can be used to establish the values of the similarity parameters Γ and Π . If the shock detachment parameter \bar{s}_0 is known for a given nose shape, as from Eqs. (20.43), (20.49), or (20.50), it is easy to determine the curvature of the shock ($\bar{R}_{s0} = \bar{s}_0/\tilde{s}_0$) and the velocity gradient for the given nose shape. For example, for a flat nose $R_N \rightarrow \infty$ and $(\tilde{s}_0)_f = [1 + (\bar{s}_0)_{\text{sph}}]/(\bar{s}_0)_{\text{sph}}$. Then

$$(\bar{R}_{s0})_f = \frac{1.03(1 + \sqrt{8\bar{\rho}/3})}{(1 + 0.78\bar{\rho}) \sqrt{\bar{\rho}(1 - \bar{\rho})}} \quad (20.45a)$$

$$\left(\frac{dV_x}{dx} \right)_f = \frac{(\tilde{s}_0)_{\text{sph}}}{(\bar{s}_0)_f [1 + (\bar{s}_0)_{\text{sph}}]} \left(\frac{dV_x}{dx} \right)_{\text{sph}}, \quad (20.45b)$$

where $(dV_x/dx)_{\text{sph}}$ is calculated for a sphere with radius r_N . The parametric equations cannot be used for flat noses with rounded corners as $\bar{r} \rightarrow 1$, since the radius of curvature of the body at the stagnation point changes discontinuously from infinity to r_N at $\bar{r} = 1$. Clearly, higher order terms must be retained in the solution at this singularity.

Theoretical calculations for blunt noses have recently been published by Inouye, Marvin, and Sinclair (NASA TN D-4397, February 1968) for flat-faced cylinders with rounded corners, and by South (NASA TN D-4563, May 1968) for spherical segment noses and other blunt shapes with sonic corners. The latter include very blunt cones with and without spherical tips, for which the shock is detached even with a pointed nose.

The well known curve of Chernyi (Fig. 223), which indicates that the drag of a blunt cone can be less than that of a sharp cone at hypersonic speeds, has been shown to be misleading by Chushkin (USSR Computational Math. and Math. Phys., 1962) and by Cleary (NASA TN D-2969, August 1965), on the basis of more exact calculations. Their results indicate that the pressure drag coefficients of blunt cones are always greater than those of the equivalent pointed cones and that Chernyi's result is due to the approximate nature of his theory.

Several reports are now available that present the results of detailed numerical calculations of the flow about spherically blunted cones of the type discussed briefly in Section 22. The original work is that of Chushkin and Shulishnina (USSR Computation Center Monograph, 1961, translated in AVCO Tech. Memo RAD-TM-62-63, September 1962), which has been retabulated and replotted by Ellett (Sandia Corporation SC-KR-64-1796, January 1965). Similar calculations are presented by Cleary (op. cit.) with emphasis on the flow properties in the inviscid shock layer. Roberts, Lewis, and Reed (AEDC-TR-66-121, August 1966) have independently calculated results similar to those of Chushkin and Shulishnina, but for different ranges of the variables and in more detailed graphical form.

The "universal" curve for pressure distribution on blunt cones presented in Fig. 225 appears to give a reasonable agreement with experimental data. However, the numerical solutions cited above provide a large amount of accurate data for correlation, and better parameters than Krasnov's empirical ones could be used. For example, Greenberg (J. Aero. Sci., March 1962) proposes the variables p/p_c and $[(p_c/p_0)/\sqrt{CD_N}](x/D_N)$ as basic correlation parameters, and indicates good agreement with experimental data. The numerical solutions for sphere-cones and sphere-cylinders also correlate well with the experimental data shown by Greenberg and with the equation of Van Hise (NASA TR R-78, 1960). The pressures near the junction with the blunt tip are not correlated by these parameters, but the pressure ratio at the junction (p_j/p_c) can be obtained from the numerical solutions and plotted in a manner similar to that suggested by Traugott (J. Aero. Sci., April 1962). There is no general method available for predicting the transition from the junction pressure to the correlation curve, but the curve can usually be faired through this region.

At the end of Section 24, Krasnov mentions the technique of matching a Prandtl-Meyer expansion to a Newtonian pressure distribution, as suggested originally by Lees and Kubota.⁽⁸⁾ Useful curves for this method are given by Wagner (J. Aero. Sci., December 1959). Although the results are an improvement over Newtonian theory, they still differ considerably from those given by the numerical solutions cited above.

An excellent correlation of the normal force coefficient and the pitching moment coefficient at angle of attack for blunt cones at hypersonic speeds has been published by Whitfield and Wolny (AEDC-TDR-62-166, August 1962, and AIAA J., February 1963).

§ 19. THE FLOW CHARACTERISTICS OF BLUNT-NOSED BODIES

SOME DATA CONCERNING THE AERODYNAMICS of bodies of revolution with blunt noses are presented in this chapter. These bodies are important for practical application to hypersonic flight in the atmosphere because the total heat load to the nose is less compared with pointed bodies, and less mass is lost.

A diagram of the flow around a blunt body of arbitrary shape is presented in Fig. 196. A detached shock wave is generated ahead of the body with variable intensity at various points on its surface, as indicated by the local slope of the wave. Far from the nose, where the slope is $\mu_\infty = \text{arc sin } (1/M_\infty)$, the shock wave degenerates into an ordinary Mach wave of infinitesimally small strength. The maximum strength will occur at the axis of the wave where $\theta_s = \pi/2$. Since the angle θ_s differs little from $\pi/2$ in the vicinity of the nose, the strength of the shock in this region is close to that of a normal shock.

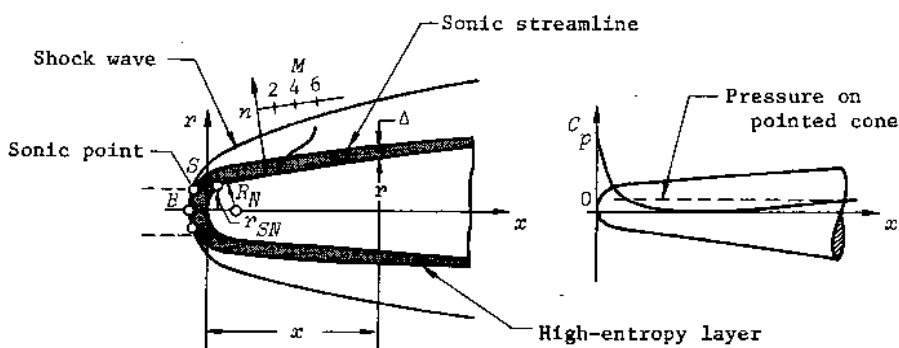


Fig. 196--Flow diagram for a blunt body

The transition of the gas particles through such a strong shock wave is accompanied by a considerable loss of total pressure and by an increase in entropy. As a result, the body surface is covered by a high-entropy layer of gas. The entropy in the various streamlines in this layer depends on the region of the shock wave through which the streamline passed. Obviously, the largest entropy is on the axial streamline, which passes through the apex of the wave (the normal shock) and coincides with the surface of the body.

The shock angle decreases with distance from the axis, and the entropy decreases in comparison with its value on the axial streamline. The velocity losses are greatest directly behind the normal part of the shock, and these losses decrease with distance along the curved surface of the shock. Thus, the farther the streamline is from the axis, the greater the local velocity. A similar picture of velocity distribution also exists at an arbitrary flow section behind the nose, due to the unequal degree of deceleration at various points on the shock wave (Fig. 196).

Thus, a region of small velocities exists near the surface, which has a pronounced effect on the development of the boundary layer. For example, the skin friction decreases due to the velocity decrease in the boundary layer. In addition, the flow regimes in the boundary layer around a blunt body differ in comparison with a pointed body. The laminar boundary layer becomes turbulent considerably farther downstream due to a decrease in the local Reynolds number, which can be calculated from the velocity at the edge of the layer. Since the extent of the laminar boundary layer increases, there is a significant reduction in friction, which results in a decrease in the thermal flux from the heated gas to the surface.

The reduction in heat flux can be interpreted as resulting from the increase in entropy of the gas on passing through the shock wave. Therefore, the effect of the use of blunting that we have discussed is called the entropy effect.

It should be noted that the physical interpretation of the entropy effect is not limited to a decrease in velocity at the external edge of the boundary layer; the density also decreases along with the decrease

in velocity. To illustrate, let us use some data for the pressure distribution on a blunt cone. It is evident from Fig. 196 that the pressure on the surface, except for the local region around the nose, is lower than that on a pointed body, and that the region of lower pressures extends for several bluntness diameters downstream. A section then follows where the pressure coefficient is almost the same as that on the pointed body. The equation for density can be written in the form $\rho = \rho'_0(p/p'_0)^{1/\gamma}$ or $\rho = \rho'_0 v^{(\gamma-1)/\gamma} (p/p'_0)^{1/\gamma}$, where $v = p_0/p'_0$ is the stagnation pressure ratio across the shock in the vicinity of the nose. Obviously, the quantity v will be considerably less for those streamlines that pass through the shock close to its normal portion than it is for a pointed cone. Therefore, if it is assumed that the ratio p/p'_0 is approximately equal to its value for a pointed cone, the density on the blunt body will be less than on the cone, and the pressure reduction due to the blunting effect on the forward part of the body will increase this difference.

It is true that cases exist in which the local pressure is greater than that on a pointed cone (e.g., for cones with flat blunting). However, the effect of the entropy increase is dominant and, as a result, the density is still decreased.

In addition, the increase in entropy in comparison with the pointed body also leads to a temperature increase at the external edge of the boundary layer. This results in an effect opposite to that of the high-entropy layer and to some increase in the thermal flux from the boundary layer to the wall. However, the total entropy effect is usually dominant and results in a decrease in the heat flow with the proper choice of the degree and the shape of the blunting.

It is possible that the pressure drag can decrease in comparison with a pointed body if the blunting is slight and the axisymmetric body is fairly slender. The drag reduction is due to the net effect of the decreased pressure on a considerable portion of the body despite the pressure increase on the blunt nose. However, the chief effect of the use of blunting does not lie in a reduction of the drag. This reduction, even if attained, is generally small. The fundamental advantage in using a blunt body is the substantial decrease in friction. Specifically, this

provides for the dissipation into the atmosphere of a significant amount of heat in the form of losses in the bow shock wave and also in the form of other losses (local shock waves, trailing shocks, vortices, etc.). As a consequence, the heat flow to the wall is significantly reduced, and for blunt bodies it can constitute only a few percent of the total kinetic energy of the flow.

However, the importance of such research is not only due to the intentional use of blunt bodies. Actually, all bodies of revolution are blunted to some degree because it is impossible, in a practical sense, to achieve a perfectly pointed nose. Blunting can result from accidental mechanical effects, or the nose can be blunted by melting in the case of motion of a body with very high velocity in a dense gaseous medium.

§ 20. INVISCID FLOW AROUND A BLUNT NOSEGENERAL SOLUTION FOR A NOSE OF ARBITRARY SHAPE

THE STUDY OF THE AERODYNAMICS of a complete blunt body is dependent on the investigation of the flow about the blunt nose itself. The results of these investigations are fundamental to the calculation of the flow parameters on the remaining part of the body. In addition, they are of value in themselves because it is then possible to determine the aerodynamic characteristics of an isolated blunt nose. The total aerodynamic characteristics can be specified by the summation of the components for the nose and the remaining parts.

Although the flow around the aft part of the body depends on the amount and type of blunting, the flow conditions around the nose itself are determined only by its shape or, more accurately, by the shape of the section of the nose up to the sonic point on its surface. Thus, it follows that the problem of flow around a blunt nose can be solved independently of the rest of the body.

We shall consider first the inviscid flow field. In addition to determining the basic pressure field, the solution to this problem is of value because it enables us to establish the basic flow conditions outside the boundary layer, which are necessary for the investigation of friction and heat transfer processes in the boundary layer.

A series of methods for solving the problem of flow around a blunt body have already been developed. A considerable number of authors have based their methods on a given shape and location of a shock found from experiment, for example. Then the inverse problem was solved: A system of nonlinear, partial differential equations was integrated approximately for known boundary conditions on the curved shock wave, and the

flow around the blunt surface was thus calculated. At the same time, the shape of the nose itself was determined.

Academician A. A. Dorodnitsyn proposed a method for the integration of a system of partial differential equations that reduces to the numerical solution of an approximate system of ordinary differential equations in a given region.⁽¹⁾ In particular, this method can be used when the boundary of the region is unknown, e.g., a curved shock wave in front of a blunt surface. Hence, the shape and location of the wave are determined in the process of solving the problem of flow around the nose.

Using this method, O. M. Belotserkovskii⁽²⁾ has calculated the flow around blunt bodies of revolution with detached shock waves on an electronic computer. More detailed information concerning Dorodnitsyn's method and its application for the solution of these problems is available in the specialized literature. We shall examine briefly the mechanics of this solution and show some results obtained on the computer.

It is convenient to use a system of equations in spherical coordinates (Fig. 197) to calculate the mixed rotational flow that exists between the curved shock wave and a blunt nose of arbitrary shape. Since symmetric flow is considered, the equations of motion, Eq. (3.9), continuity, Eq. (3.17), and isentropic flow, Eq. (3.48), are simplified.

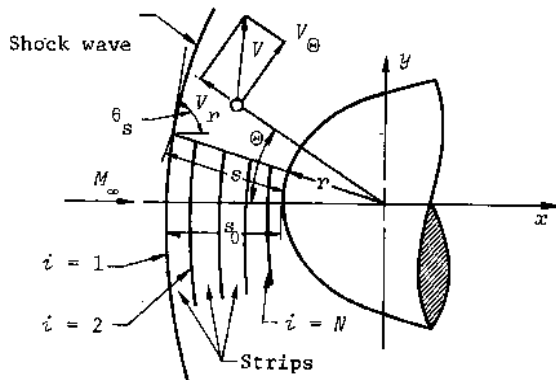


Fig. 197--Flow around a blunt nose and the region of integration

It is also convenient to transform the equation of motion with the help of the Bernoulli equation and to introduce the stream function Ψ . Then the whole system of equations has the following form:

$$\frac{\partial[\bar{r}^2(\bar{p} + \bar{\rho}\tilde{V}_r^2) \sin \Theta]}{\partial \bar{r}} + \frac{\partial[\bar{r}\bar{\rho}\tilde{V}_\Theta \tilde{V}_r \sin \Theta]}{\partial \Theta} = \bar{r}(2\bar{p} + \bar{\rho}\tilde{V}_\Theta^2) \sin \Theta,$$

$$\frac{\partial(\bar{r}^2 \tau \tilde{V}_r \sin \Theta)}{\partial \bar{r}} + \frac{\partial(\bar{r}\tau \tilde{V}_\Theta \sin \Theta)}{\partial \Theta} = 0, \quad (20.1)$$

$$\frac{\partial \Psi}{\partial \Theta} = \bar{r}\bar{\rho} \left(\tilde{V}_\Theta \frac{d\bar{r}}{d\Theta} - \bar{r}\tilde{V}_r \right) \sin \Theta,$$

$$\varphi = \varphi(\Psi),$$

where

$$\tau = \left[\frac{\gamma - 1}{2\gamma} (1 - \tilde{V}^2) \right]^{1/(\gamma-1)}, \quad \varphi = \frac{\bar{p}}{\bar{\rho}^\gamma}, \quad (20.2)$$

$$\bar{p} = \frac{\gamma - 1}{2\gamma} \bar{\rho}(1 - \tilde{V}^2), \quad \bar{\rho} = \frac{\tau}{\varphi^{1/(\gamma-1)}}.$$

The dimensionless parameters are defined as $\tilde{V} = V/V_{\max}$, $\bar{\rho} = \rho/\rho_\infty$, $\bar{p} = p/\rho_\infty V_{\max}^2$, and $\bar{r} = r/l$, where l is a characteristic linear dimension of the body. The entropy function φ varies from one streamline to another; i.e., it varies with the stream function Ψ and is determined from the relation $S = c_v \log \varphi$.

The unknown quantities \tilde{V}_r , \tilde{V}_Θ , φ , and Ψ can be calculated from the system of four equations given in Eq. (20.1). The solution must satisfy the boundary conditions on the surfaces of the nose and the shock wave. On the surface of a blunt nose whose equation is $r = r_0(\Theta)$, the boundary conditions are

$$\tilde{V}_r = \frac{\tilde{V}_\Theta}{r_0} \frac{dr_0}{d\Theta}, \quad \Psi = 0, \quad \varphi = \varphi(0) = \text{const.} \quad (20.3)$$

The entropy function can be found for the conditions behind the normal part of the shock and can be written in the form

$$\psi(0) = \frac{2}{\gamma + 1} \left(\frac{\gamma - 1}{\gamma + 1} \right)^{\gamma} \frac{1}{\tilde{V}_{\infty}^{2\gamma}} \left[\tilde{V}_{\infty}^2 - \frac{(\gamma - 1)^2}{4\gamma} (1 - \tilde{V}_{\infty}^2) \right]. \quad (20.4)$$

The boundary conditions on a shock specified by $r = r_0(\theta) + s(\theta)$ (where s is the distance along a radial line $\theta = \text{const}$ from the body to the shock) are found from the theory of a curved shock wave and have the form[†]

$$\tilde{V}_r = \tilde{V}_y \sin \theta - \tilde{V}_x \cos \theta,$$

$$\tilde{V}_{\theta} = \tilde{V}_x \sin \theta + \tilde{V}_y \cos \theta,$$

$$\tilde{V}_x = \frac{2\tilde{V}_{\infty}}{\gamma + 1} \left(\cos^2 \theta_s + \frac{\gamma - 1}{2\tilde{V}_{\infty}^2} \right),$$

$$\tilde{V}_y = (\tilde{V}_{\infty} - \tilde{V}_x) \cot \theta_s, \quad (20.5)$$

$$\bar{p} = \frac{2}{\gamma + 1} \left[\tilde{V}_{\infty}^2 \sin^2 \theta_s - \frac{(\gamma - 1)^2}{4\gamma} (1 - \tilde{V}_{\infty}^2) \right],$$

$$\bar{\rho} = \frac{\gamma + 1}{\gamma - 1} \frac{\tilde{V}_{\infty}^2 \sin^2 \theta_s}{1 - \tilde{V}_{\infty}^2 \cos^2 \theta_s},$$

$$\Psi \equiv \Psi_{\infty} = \frac{(\bar{r}_0 + \bar{s})^2}{2} \tilde{V}_{\infty} \sin^2 \theta.$$

The boundary condition for the entropy function is found from the expressions for \bar{p} and $\bar{\rho}$.

Equation (20.1) can be solved by means of the Dorodnitsyn method.

[†]Editor's note: Several of these equations have been revised from those in the original text, and a number of errors have been corrected.

According to this method, $N - 1$ lines are drawn between the body and the shock with equations

$$r = r_i(\Theta) = r_0(\Theta) + \xi_i s(\Theta),$$

where $\xi_i = (N - i + 1)/N$ and $i = 2, 3, \dots, N$. Thus, these lines partition the area for integration; i.e., the perturbed portion of the flow between the body and the shock is divided into N strips (Fig. 197). The first two equations of Eq. (20.1) can then be integrated with respect to r along an arbitrary radial line $\Theta = \text{const}$ from the body to the edge of each of the strips, i.e., between the limits r_0 and r_i .

As a result, $2N$ independent integral relations are derived. The remaining two equations in Eq. (20.1) are written for conditions along each of the $N - 1$ intermediate lines, $r = r_i(\Theta)$, thus increasing the number of equations in the system to $4N - 2$. If we add the relation on the shock,

$$\frac{ds}{d\Theta} = -(r_0 + s) \cot (\theta_s + \Theta) - \frac{dr_0}{d\Theta}, \quad (20.6)$$

which can be derived from the condition $dy/dx = \tan \theta_s$, the system will consist of $4N - 1$ equations.

It should be noted that the first $2N$ equations contain integral terms resulting from the integration of the first two equations of Eq. (20.1) between the limits r_0 and r_i . If the integrands are denoted by $f(r, \Theta)$, the integrals can be computed by approximating the functions f with polynomials of the form

$$f(r, \Theta) = \sum_{m=0}^N a_m \left(\frac{r - r_0}{s} \right)^m, \quad (20.7)$$

where the coefficients $a_m(\Theta)$ are linear functions of the values of f at the boundaries of the strips.

After integration, we obtain a system of $4N - 1$ approximate equations, which can be solved for the derivatives with respect to Θ of the unknown functions \tilde{V}_{ri} , $\tilde{V}_{\Theta i}$, ψ_i , s , θ_s , and $\tilde{V}_{\Theta 0}$, resulting in a system of ordinary differential equations. These can then be solved numerically, using the boundary conditions for $\Theta = 0$ (i.e., on the axis of

symmetry), where $\tilde{V}_{\theta 0} = \tilde{V}_{\theta z} = 0$, $\psi_i = 0$, $\theta_s = \pi/2$, and $\varphi = \varphi_1(0)$, and the boundary conditions on the so-called singular line, the points of which are located in the vicinity of the sonic line where $V_0 = a^*$. Thus, the flow around bodies with detached shocks can be calculated for bodies with different types of blunting, e.g., in the shape of a sphere, a flat surface, a curved surface with a discontinuity, etc.

The effectiveness of the method is dependent on the use of high-speed electronic computers for the numerical integration, from which final results can be obtained with any required degree of accuracy. These results enable us to make judgments concerning the shape and location of the shock wave and concerning the magnitude and character of the distribution of the flow parameters between the shock wave and the blunt nose. We shall present below some of the results obtained on the basis of this method of integral relations.

The calculation scheme presented according to the Dorodnitsyn method does not take into account the variations in the physical-chemical properties of the air behind the shock wave for very high velocities. This can lead to inaccurate results for the shape and location of the shock wave and to inaccurate values of density, but it is claimed that the pressures are comparatively accurate. Some questions associated with the solution of the problem of flow near the blunt nose taking into account the effect of variable specific heats and dissociation are discussed in the next section.

SPHERICAL NOSES

Solution in the Vicinity of the Stagnation Point

For a more complete idea of the character of the flow around blunt bodies, let us examine separately the flow with a detached shock wave, first in front of a sphere and then in front of a flat surface. The study of the flow in the vicinity of the stagnation point on a spherical nose is of interest primarily because the heat transfer is largest at that point. It is shown below that the heat flow is a function of the initial velocity gradient along the spherical surface, which can be found from the solution for the inviscid flow around a blunt nose. In

addition, the solution of the problem of flow in the vicinity of the stagnation point enables us to determine the standoff distance of the shock wave and the distribution of the gas dynamic parameters in this local region. In general, the solution can be obtained taking into account the physical-chemical changes in the gas.

The solution to this problem can be obtained⁽³⁾ by using the equations of motion, Eq. (3.11), and continuity, Eq. (3.19), in a curvilinear orthogonal system. The origin of the coordinates of this system coincides with the stagnation point, the coordinate x is measured along the surface, and the coordinate y is measured along the normal to the surface (Fig. 198).

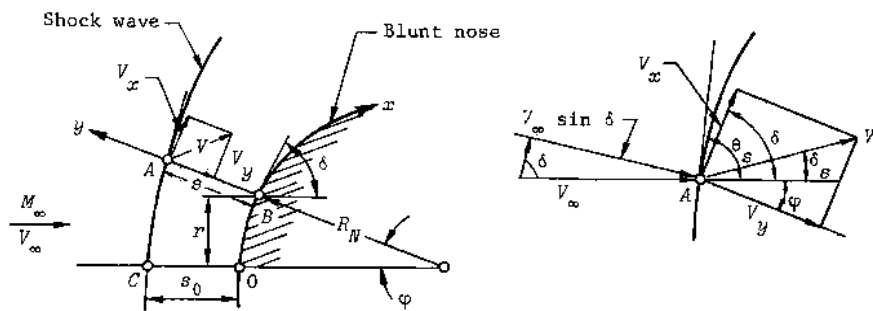


Fig. 198--Velocity components in curvilinear coordinates

If it is assumed that only the region in the vicinity of the stagnation point is being considered and that the incident flow has a very high supersonic velocity, the original complex equations can be simplified. In fact, for these conditions, the flow behind the shock wave can be assumed incompressible, since the Mach number M_2 differs little from the value $\sqrt{(\gamma - 1)/2\gamma}$, corresponding to the case of limiting flow (for $M_\infty \rightarrow \infty$), behind a normal shock. Therefore, the density in this region can be assumed constant and equal to $\rho \approx \rho_\infty/\bar{\rho}$, where $\bar{\rho} = \rho_\infty/\rho_s$, ρ_s is the density behind a normal shock wave (or at the stagnation point),

and a constant value for ρ can be used in the equations of motion and continuity.[†]

Since, in this case, large velocities are considered, the shock will lie very close to the surface of the body. The region of perturbed flow is contained in a thin layer of thickness δ , which is very small compared with the radius of curvature R_N of the body in the vicinity of the stagnation point.

Therefore, if it is assumed that $s/R_N \ll 1$, $y/R_N \ll 1$ also, since $0 \leq y \leq s$. Thus, the quantity $y/R \approx y/R_N$ can be neglected with respect to unity in the flow equations. In addition, the third terms on the left side of Eqs. (3.11) can be neglected, since they are also of a lesser order due to the fact that $y \ll R$, $x \ll R$. Finally, the continuity equation for conditions in the vicinity of the stagnation point can be simplified if it is assumed that $r \approx x$.

If all of these simplifications are taken into account, Eqs. (3.11) and (3.19) take the form

$$V_x \frac{\partial V_x}{\partial x} + V_y \frac{\partial V_x}{\partial y} = - \frac{\bar{\rho}}{\rho_\infty} \frac{\partial p}{\partial x}, \quad (20.8)$$

$$V_x \frac{\partial V_y}{\partial x} + V_y \frac{\partial V_y}{\partial y} = - \frac{\bar{\rho}}{\rho_\infty} \frac{\partial p}{\partial y}, \quad (20.9)$$

$$\frac{\partial (V_x x)}{\partial x} + \frac{\partial (V_y y)}{\partial y} = 0. \quad (20.10)$$

The solution of these equations must satisfy the conditions at an arbitrary point on the body surface, where the normal velocity component $V_y = 0$ for $y = 0$, and at the stagnation point, where $V_x = V_y = 0$ for $y = x = 0$. In addition, the solution must satisfy the flow conditions behind the shock wave. These conditions, written for the velocity components at point A, located at a distance s from the surface, have the form (see Fig. 198)

[†] Editor's note: Note that this definition of $\bar{\rho}$ is inverted from that defined in connection with Eq. (20.2). For the remainder of this section, $\bar{\rho}$ is defined as $\bar{\rho} = \rho_\infty / \rho$.

$$V_x = V \cos (\delta - \delta_s), \quad V_y = -V \sin (\delta - \delta_s). \quad (20.11)$$

The total velocity and pressure at point A are obtained from Eqs. (4.31) and (4.12), assuming that $\rho = \rho_\infty / \bar{\rho}$ directly behind the shock:

$$\frac{V}{V_\infty} = \sqrt{\bar{c}^2 \sin^2 \theta_s + \cos^2 \theta_s}, \quad (20.12)$$

$$\frac{p}{p_\infty} = 1 + \gamma M_\infty^2 (1 - \bar{\rho}) \sin^2 \theta_s. \quad (20.13)$$

The pressure and density can be eliminated from Eqs. (20.8) and (20.9) by differentiation with respect to y and x , respectively. Equating the results and including Eq. (20.10), we obtain

$$\frac{\xi V}{x} = V_x \frac{\partial \xi}{\partial x} + V_y \frac{\partial \xi}{\partial y}, \quad (20.14)$$

where the vorticity $\xi = \partial V_x / \partial y - \partial V_y / \partial x$ is known from Stokes' theorem for rotational flow. Thus, the problem lies in a search for solutions of Eqs. (20.10) and (20.14), in terms of V_x and V_y , that satisfy the boundary conditions indicated above.

Let us assume that the solution for V_x in the vicinity of the axis ($x = 0$) can be represented in the form of a series:

$$V_x = a_0(y) + a_1(y)x + a_2(y)x^2 + \dots,$$

in which x is assumed to be small. Since the velocity component V_x must be equal in absolute value but opposite in sign for plus and minus values of x , only terms with odd exponents of x remain in the expansion; i.e.,

$$V_x = a_1(y)x + a_3(y)x^3 + \dots$$

As x approaches zero, only the first term need be considered, resulting in the expression $V_x = a_1(y)x$. Further, let us introduce the function

$$F(y) = \int_0^y a_1(y) dy,$$

so that $F'(y) = a_1(y)$ and $F(0) = 0$. Then V_x can be rewritten as

$$V_x = xF'(y). \quad (20.15)$$

From the continuity equation, Eq. (20.10), the other velocity component is

$$V_y = -2F(y) + f(x).$$

But from the boundary condition at the surface $V_y(x, 0) = 0$. Then $-2F(0) + f(x) = 0$, and since $F(0) = 0$, $f(x) = 0$. Therefore,

$$V_y = -2F(y). \quad (20.16)$$

Introducing these relations into Eq. (20.14), we obtain

$$F''(y) = 0, \quad (20.17)$$

which has the general solution

$$-\frac{y}{2} = F(y) = C_0 + C_1 y + C_2 y^2. \quad (20.18)$$

Since $F(0) = 0$, $C_0 = 0$. The other two coefficients can be determined by using the conditions on the shock near the stagnation point at $x \rightarrow 0$. At point C , we get

$$V_y = -2(C_1 s_0 + C_2 s_0^2) = V_C \quad \text{and} \quad \theta_s = \frac{\pi}{2},$$

and $V_C = -\bar{\rho} V_\infty$ from Eq. (20.12). Therefore,

$$C_1 s_0 + C_2 s_0^2 = \frac{\bar{\rho} V_\infty}{2}. \quad (20.19)$$

On the other hand,

$$V_x = xF'(y) = x(C_1 + 2C_2 y). \quad (20.20)$$

The value of V_x behind the shock wave can be determined from Eqs. (20.11) and (20.12). In the limit as $x \rightarrow 0$, we obtain

$$\lim_{x \rightarrow 0} \frac{\cos(\delta - \delta_s)}{x} = \frac{C_1 + 2C_2 s_0}{\bar{\rho} V_\infty}.$$

The limit on the left side can be computed in the following way. It is evident from Fig. 198 that the angle $\delta - \delta_s = \pi/2 - (\varphi + \delta_s)$ at an arbitrary point. Therefore, $\cos(\delta - \delta_s) = \sin(\varphi + \delta_s)$, and for small values of φ and δ_s it can be assumed that $\sin(\varphi + \delta_s) \approx \varphi + \delta_s$. Then

$$\lim_{x \rightarrow 0} \frac{\cos(\delta - \delta_s)}{x} = \lim_{x \rightarrow 0} \frac{\varphi + \delta_s}{x} = \frac{1}{R_N} + \frac{1}{R_{s0}} \left(\frac{\delta_s}{\omega} \right)_{x \rightarrow 0},$$

where ω is the angle between the vector representing the radius of curvature of the shock and the axis of flow, and R_{s0} is the radius of curvature of the shock wave at the axis. The ratio

$$\left(\frac{\delta_s}{\omega} \right)_{x \rightarrow 0} = \left(\frac{d\delta_s}{d\omega} \right)_{\delta_s \rightarrow 0}$$

is equal to $1/\bar{\rho} - 1$, which can be obtained from Eq. (4.2) by substituting $\Delta V_n/V_{n1} = 1 - \bar{\rho}$ and $\delta_s = \pi/2 - \omega$, and taking the limit as $\omega \rightarrow 0$.

Assuming that R_N is approximately equal to R_{s0} , we get

$$C_1 + 2C_2 s_0 = \frac{V_\infty}{R_{s0}}. \quad (20.21)$$

Another relation must be added to Eqs. (20.19) and (20.21), since they contain three unknown constants, C_1 , C_2 , and s_0 . This relation results from the expression for vorticity behind the shock wave. Using Eq. (20.20) and the boundary conditions on the body surface, we obtain the relation $\xi = \partial V_x / \partial y = 2C_2 x$. On the other hand, from the theory for curved shock waves it is known that the vorticity is given by

$$\xi = 2C_2 x = \frac{V_\infty (1 - \bar{\rho})^2 \sin \theta_s \cos \theta_s}{\sin (\theta_s - \delta_s) \sqrt{\bar{\rho}^2 \sin^2 \theta_s + \cos^2 \theta_s}} \frac{d\theta_s}{dx}.$$

The coefficient C_2 can be obtained from this expression by determining the limit as $x \rightarrow 0$:

$$C_2 = \frac{(1 - \bar{\rho})^2}{2} \frac{V_\infty}{5R_{s0}^2}. \quad (20.22)$$

If we substitute the coefficient C_2 into Eqs. (20.19) and (20.21) and solve them jointly, we obtain the coefficient C_1 and the detachment distance s_0 as follows:

$$C_1 = \mp \sqrt{1 - \Delta^2} \frac{V_\infty}{R_{s0}}, \quad (20.23)$$

$$s_0 = \frac{1 \pm \sqrt{1 - \Delta^2}}{\Delta} \bar{\rho} R_{s0}, \quad (20.24)$$

where $\Delta = 1 - \bar{\rho}$.

The Initial Velocity Gradient and Velocity Distribution

There are two possible solutions for the gas parameters in the vicinity of a blunt surface, as indicated by the plus and minus signs in the equations above. It can be shown that the lower sign corresponds to the physically real process. In fact, it follows from Eq. (20.20) that at the surface of the body, where $y = 0$, the velocity is $V_x = C_1 x$, or from Eq. (20.23),

$$V_x = \mp \sqrt{1 - \Delta^2} \frac{V_\infty}{R_{s0}} x.$$

Since for $x > 0$ or $x < 0$ the velocity V_x must be correspondingly positive or negative, it is apparent that the lower sign must be used, and this applies also to Eqs. (20.23) and (20.24). Then the velocity components can be determined using the expressions for C_1 and C_2 :

$$\frac{V_y}{V_\infty} = -2\bar{\rho}y \left(\frac{\sqrt{1 + \Delta^2}}{\bar{\rho}R_{s0}} + \frac{\Delta^2}{2\bar{\rho}^2 R_{s0}^2} \cdot y \right), \quad (20.25)$$

$$\frac{V_x}{V_\infty} = \bar{\rho}x \left(\frac{\sqrt{1 - \Delta^2}}{\bar{\rho}R_{s0}} + \frac{\Delta^2}{\bar{\rho}^2 R_{s0}^2} \cdot y \right), \quad (20.26)$$

where $\bar{\rho}R_{s0}$ is given as a function of s_0 by Eq. (20.24).

On the surface of the nose ($y = 0$), the total velocity is equal to the component V_x and is given by

$$\frac{V}{V_\infty} = \frac{V_x}{V_\infty} = \bar{\rho}x \frac{\sqrt{1 - \Delta^2}}{\bar{\rho}R_{s0}}. \quad (20.26a)$$

Hence, it is evident that V_x varies linearly in the vicinity of the stagnation point on the body surface.

As already noted, it is necessary to know the value of the gradient of the velocity V_x on the surface for the heat transfer problem. According to Eq. (20.26a), this is

$$\left(\frac{\partial V_x}{\partial x} \right)_{y=0} = \tilde{\lambda} = \frac{V_\infty}{\bar{\rho}R_{s0}} \sqrt{1 - \Delta^2}. \quad (20.27)$$

Experimental studies have shown that this relation, obtained from an analysis of very high velocity flow, can be used for approximate calculations at relatively small velocities. This is illustrated in Fig. 199, where experimental values of the dimensionless velocity gradient $\tilde{\lambda}D_N/V_\infty$ are presented.⁽³⁾

Obviously, Eq. (20.26a) can be rewritten as $V_x = \tilde{\lambda}x$ and the angle φ can be introduced, where φ is related to x by the expression $x = \varphi R_N$. Then $V_x = \tilde{\lambda}R_N \varphi$, which implies a linear dependence of V_x on φ . Although this relation is obtained from an analysis of hypersonic flow over a small region of the nose, experimental research has shown that a linear velocity variation is valid for a relatively large part of the curved surface, and at comparatively small Mach numbers.

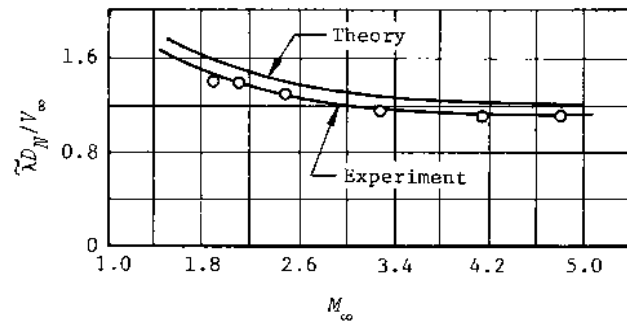


Fig. 199--Velocity gradient at the stagnation point

This is confirmed by the data in Fig. 200, where the dimensionless velocity $V_x / \tilde{\lambda} D_N$ is shown for a hemispherical nose. These values were determined by wind-tunnel measurements at four different Mach numbers. Linearity is maintained up to values of φ of 45° to 50° , and the results deviate only slightly from linear even at the largest angles.

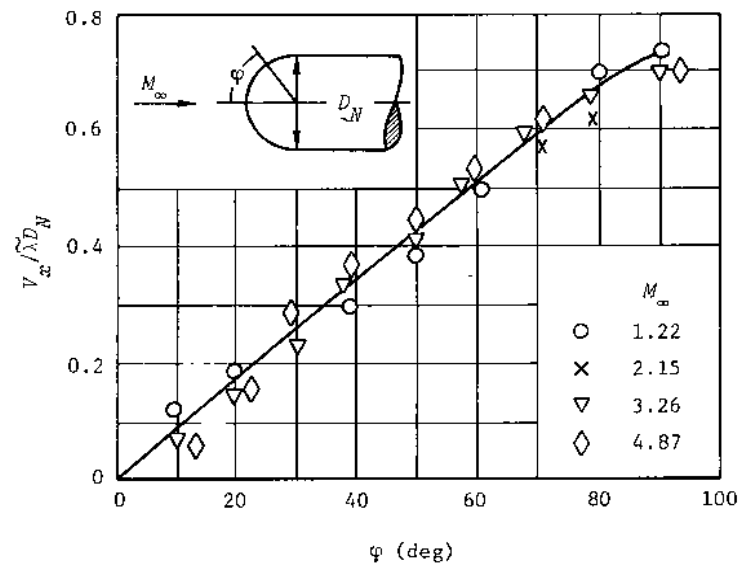


Fig. 200--Velocity distribution on a hemisphere

The equation for this linear law, $V_x = \tilde{\lambda} R_N \phi$, can be written in the form $V_x = \bar{\lambda} V_\infty \bar{x}$, where $\bar{x} = x/D_N$, and $\bar{\lambda} = D_N \tilde{\lambda}/V_\infty$. The experimental and theoretical data are compared in Fig. 201. The velocity gradient can be found from the approximate relation

$$\tilde{\lambda} = \left(\frac{\partial \gamma}{\partial x} \right)_{x=0} = \frac{1}{R_N} \sqrt{\frac{2(p'_0 - p_\infty)}{p'_0}}, \quad (20.27a)$$

which is obtained in the following way. The velocity distribution over the spherical nose is related to the local static pressure by the expression for isentropic flow behind a shock wave:

$$\frac{V_x^2}{V_\infty^2} = \left(1 + \frac{2}{\gamma_\infty - 1} \frac{1}{M_\infty^2} \right) \left[1 - \left(\frac{p}{p'_0} \right)^{(\bar{\gamma}-1)/\bar{\gamma}} \right], \quad (20.28)$$

where γ_∞ is the ratio of specific heats in the unperturbed flow, and $\bar{\gamma}$ is the average ratio of specific heats behind the shock wave, which is of the order of 1.1 to 1.2 at very high temperatures. The pressure ratio in Eq. (20.28) can be determined from the Newtonian equation:

$$\frac{p}{p'_0} = \cos^2 \phi + \frac{p_\infty}{p'_0} \sin^2 \phi, \quad (20.29)$$

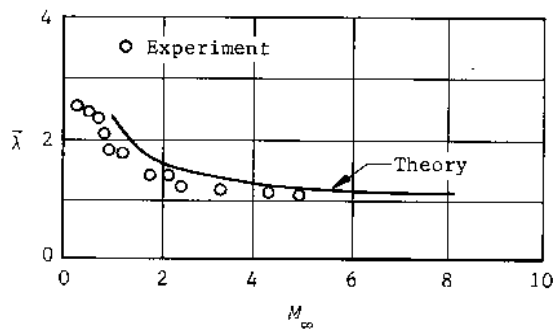


Fig. 201--Velocity gradient at the stagnation point as a function of Mach number

where it can be assumed that p_∞/p'_∞ is approximately equal to $1/\gamma_\infty M_\infty^2$ at sufficiently high Mach numbers. Equation (20.28) can be simplified for the velocity and velocity gradient in the vicinity of the stagnation point:

$$\frac{V_x}{V_\infty} = \bar{K}\varphi, \quad \left(\frac{1}{V_\infty} \frac{dV_x}{d\varphi} \right)_{\varphi=0} = \bar{K}, \quad (20.30)$$

where

$$\bar{K} = \sqrt{\frac{\bar{\gamma} - 1}{\bar{\gamma}}} \left(1 + \frac{2}{\bar{\gamma} - 1} \frac{1}{M_\infty^2} \right) \left(1 - \frac{1}{\bar{\gamma} M_\infty^2} \right). \quad (20.31)$$

For hypersonic velocities, the terms that are inversely proportional to M_∞^2 can be set equal to zero, which amounts to assuming that the flow in the vicinity of the stagnation point is incompressible, so that the stagnation pressure can be approximated by $p'_0 = p + p'_0 V_x^2/2$. The static pressure can be replaced by Eq. (20.29), in which, since φ is small, it can be assumed that $\cos \varphi \approx 1$ and $\sin \varphi \approx \varphi \approx x/R_N$. Differentiating V_x with respect to x , we obtain Eq. (20.27a) for the velocity gradient. For larger velocities, p_∞ can be neglected with respect to p'_0 under the radical in Eq. (20.27a).

It is of interest to estimate the dimensions of the region of incompressible flow and the distance to the sonic point on the sphere. Equation (20.28) for isentropic flow can be used, assuming that the flow begins from the stagnation point. The conditions at this point can be assumed to be the same as those directly behind the normal portion of the shock. For example, the region of undissociated incompressible flow for $\gamma = 1.4$, $M_\infty = 5.1$, and $\bar{p} = 0.2$ is shown schematically in Fig. 202, assuming that the region is bounded by a local Mach number of 0.3. The angle to the point on the spherical nose where the local Mach number is 0.3 is shown as a function of free-stream Mach number in Fig. 203.

These results agree well with data for the sonic points on a sphere (Fig. 204) obtained by O. M. Belotserkovskii on an electronic computer.⁽²⁾ Figure 204 also gives an idea of the shape of the sonic lines and the location of the sonic points on the shock wave for various Mach numbers.

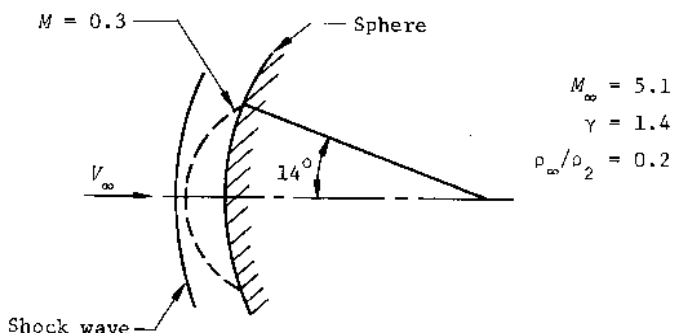


Fig. 202--Region of incompressible flow in the vicinity of a sphere

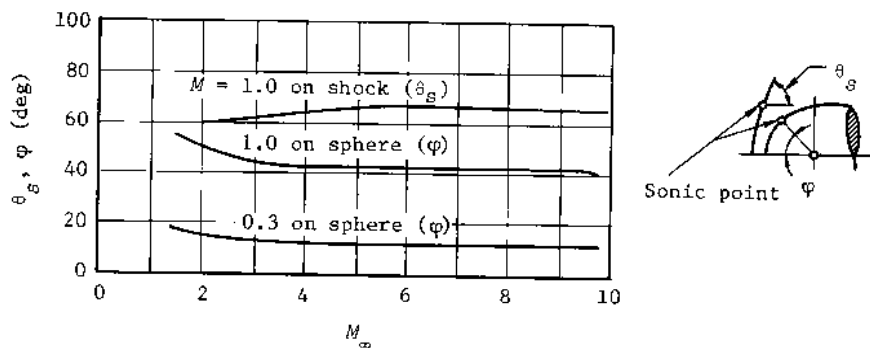


Fig. 203--Angular distance to the end of the incompressible region and to the sonic point on the surface and the shock

The shock angles corresponding to these points are shown in Fig. 203. It should be noted that, under real conditions, the regions of incompressible and subsonic compressible flows will be less than those calculated here, because either the vibrational motions of the molecules or dissociation behind the shock wave at high velocities will result in a reduction in temperature and a decrease in the velocity of sound. Consequently, the local Mach numbers increase for the same velocity on the sphere and the points for $M = 0.3$ and $M = 1$ are shifted over.

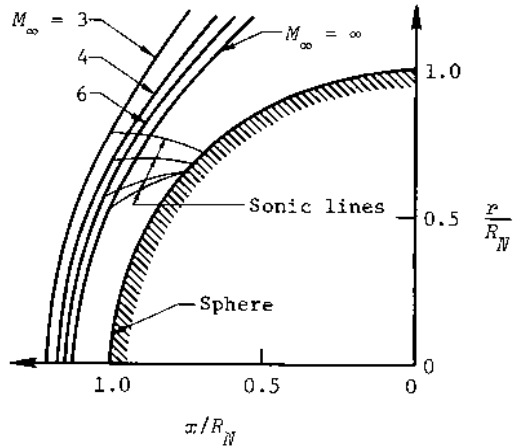


Fig. 204--Shock waves and sonic lines ahead of a sphere

The Pressure Distribution and Drag Coefficient

The results obtained for velocity allow the determination of the pressure distribution in the thin shock layer in the vicinity of the axis and also on the body surface close to the stagnation point. Using the incompressible Bernoulli equation, we obtain the pressure coefficient at an arbitrary point in the shock layer:

$$C_p = \frac{2(p - p_\infty)}{\rho_\infty V_\infty^2} = C_{pA} + \frac{1}{\delta} \left[\left(\frac{V_A}{V_\infty} \right)^2 - \left(\frac{V_y}{V_\infty} \right)^2 - \left(\frac{V_x}{V_\infty} \right)^2 \right]. \quad (20.32)$$

Since the layer is thin, the pressure coefficient C_{pA} and the velocity directly behind the shock wave at a point on its curved surface can be replaced, approximately, by the values C_{pC} and V_C , respectively, behind the normal portion at point C (Fig. 198). These values follow from Eqs. (20.13) and (20.12):

$$C_{pC} = 2(1 - \delta) = 2\Delta, \quad V_C = V_\infty \delta.$$

For conditions on the axial (or what is called the zero) streamline,

C_{pA} equals C_{pC} exactly, and $V_A = V_C$. In this case, the pressure coefficient at an arbitrary point on the zero streamline (where $V_x = 0$) is

$$C_p = 2\Delta + \bar{\rho} \left[1 - \left(\frac{V_y}{\bar{\rho} V_\infty} \right)^2 \right], \quad (20.33)$$

where $V_y/\bar{\rho} V_\infty$ is derived from Eq. (20.25). After assigning various values to y/s_0 , we can calculate the pressure coefficient at each point on the axial streamline. For example, at the stagnation point on the surface, where $V_y = 0$, the pressure coefficient is

$$C_{p0} = 2 - \bar{\rho}. \quad (20.34)$$

Thus, in going from the shock wave to the stagnation point on the body, the gas undergoes an additional compression, and the pressure coefficient changes from $C_{pC} = 2(1 - \bar{\rho})$ to the larger value $C_{p0} = 2 - \bar{\rho}$. The nature of this change is shown in Fig. 205.

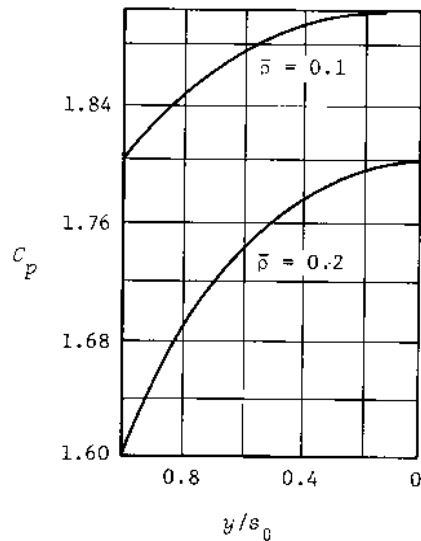


Fig. 205--Variation of the pressure coefficient along the axial streamline

It is apparent that the density ratio $\bar{\rho}$ is the only parameter that determines the value of the pressure coefficient, and the smaller $\bar{\rho}$ is, the larger the coefficient and the lesser the degree of compression. Thus, the pressure in the perturbed flow is distributed more uniformly either for very high velocity cold flow, in which the gas is strongly heated in the shock layer and $\bar{\rho}$ is rather small, or for lesser velocities of a preheated gas (which also results in a decrease in $\bar{\rho}$).

The pressure distribution on the surface of the body in the vicinity of the stagnation point can be calculated from Eq. (20.32) by setting $V_y = 0$ and $V_x = \tilde{\lambda}x$:

$$C_p = 2\Delta + \bar{\rho} \left[1 - \left(\frac{\tilde{\lambda}x}{\bar{\rho}V_\infty} \right)^2 \right].$$

Substituting the value of the gradient $\tilde{\lambda}$ from Eq. (20.27) and assuming that $R_{s0} = R_N$, we obtain

$$C_p = (2 - \bar{\rho}) \left[1 - \left(\frac{x}{R_N} \right)^2 \right] = C_{p0} \left[1 - \left(\frac{x}{R_N} \right)^2 \right]. \quad (20.35)$$

This equation is derived for small values of x . However, studies show that, after a simple transformation, it can be extended to apply to a fairly large part of the body surface. In fact, since $x/R_N \approx \varphi \approx \sin \varphi$, $C_p = (2 - \bar{\rho}) \cos^2 \varphi$. The quantity $2 - \bar{\rho}$ is the pressure coefficient C_{p0} at the stagnation point, so that $C_p = C_{p0} \cos^2 \varphi$, and we arrive at the modified Newtonian equation.

Experimental results and theoretical studies show that this equation predicts, with sufficient accuracy, the pressure distribution on practically the entire surface of the hemisphere, although the accuracy decreases somewhat at the end of the blunt nose.

Figure 206 presents for comparison experimental and theoretical data for a hemispherical nose at $M_\infty = 5.8$.⁽⁴⁾ The theoretical data were calculated by the method of integral relations discussed earlier, using an electronic computer. It is evident that the Newtonian theory gives results somewhat lower than the experimental data only on a small part of the nose near the junction of the hemisphere and the cylinder.

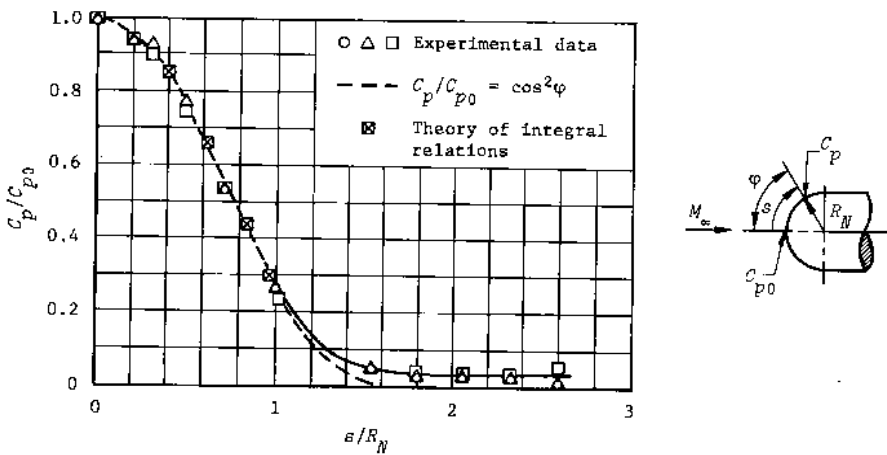


Fig. 206--Pressure distribution on a hemisphere cylinder

The good accuracy of the Newtonian equation allows it to be used for the calculation of the pressure drag coefficient of a spherical nose. According to Eq. (1.6), the drag coefficient with respect to the area πR_N^2 is

$$C_{Dp} = \int_0^{\sin^2 \varphi} C_p d(\sin^2 \varphi).$$

Introducing $C_p = C_{p0} \cos^2 \varphi$ and integrating, we find

$$C_{Dp} = C_{p0} \sin^2 \varphi \left(1 - \frac{\sin^2 \varphi}{2} \right). \quad (20.36)$$

Thus, the drag coefficient of a hemisphere is $C_{Dp} = C_{p0}/2$. The experiments (Fig. 207) agree well with Eq. (20.36), showing that its accuracy increases with an increase in velocity.

It is evident that it is necessary to find the pressure coefficient at the stagnation point to determine the drag coefficient of a hemisphere, or of a part of it. We already know how to determine its value taking

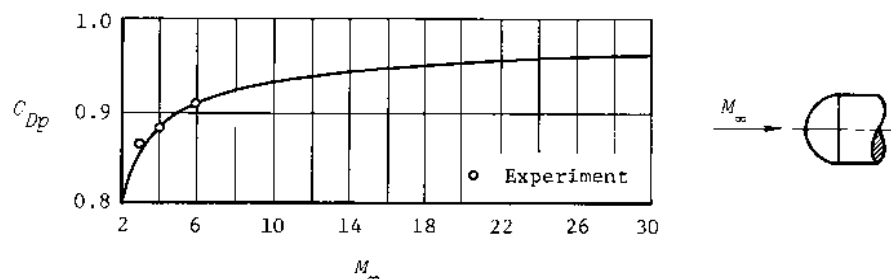


Fig. 207--Pressure drag coefficient of a hemisphere

dissociation and ionization into account. Particularly in approximate calculations, it is possible to find the density ratio $\bar{\rho} = \rho_{\infty}/\rho_2$ behind the normal portion of the shock by considering the physical-chemical changes and to compute the pressure coefficient from Eq. (20.34).

It should be noted that the calculations indicated are made on the assumption of equilibrium dissociation and ionization behind the shock wave. Strictly speaking, they are inapplicable in cases where flows of real gases are accompanied by relaxation processes.

Detachment Distance and Shape of the Shock Wave

The value of the detachment distance s_0 can be determined from Eq. (20.24), which was derived for the case of very large velocities, when it can be assumed that $R_{s0} = R_N$, and for which experiments indicate that $\bar{\rho} \leq 0.1$. However, the same equation can be used for lesser velocities (larger $\bar{\rho}$) when $R_{s0} > R_N$, but in this case the relative value of the detachment distance $\tilde{s}_0 = s_0/R_{s0}$ is derived from Eq. (20.24). To determine the absolute value of s_0 , it is necessary to find R_{s0} . For given conditions of the incident flow, R_{s0} is a function of the radius of the sphere, and research shows that it is a linear function of R_N . If it is assumed that the shock is concentric with the sphere at the axis, $\tilde{R}_{s0} = R_{s0}/R_N = 1/(1 - \tilde{s}_0)$. Experiments indicate, however, that the radii are not concentric, particularly at the lower Mach numbers. Better results are obtained if the following relation is used:

$$\tilde{R}_{s0} = \frac{R_{s0}}{R_N} = \frac{1}{(1 - \tilde{s}_0)^2}. \quad (20.37)$$

Then the detachment distance relative to the radius of the spherical nose can be calculated from the equation

$$\bar{s}_0 = \frac{s_0}{R_N} = \tilde{s}_0 R_{s0} = \frac{\tilde{s}_0}{(1 - \tilde{s}_0)^2}. \quad (20.38)$$

Figure 208 gives the results of calculations from Eqs. (20.38) and (20.24).

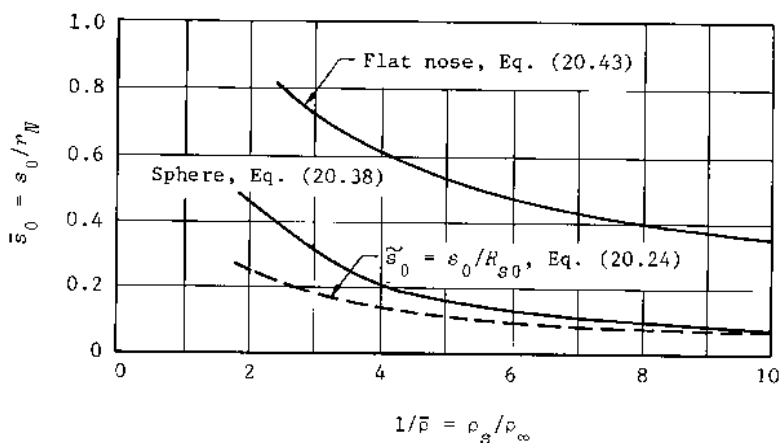


Fig. 208--Dimensionless shock-detachment distance for a sphere and a flat nose

For values of $\bar{\rho} < 0.5$, the relative detachment distance can be calculated approximately from the empirical relation⁽⁵⁾

$$\bar{s}_0 = \frac{2}{3} \frac{\bar{\rho}}{1 - \bar{\rho}}. \quad (20.39)$$

To construct the shock in front of a blunt nose, it is necessary to know the shape of the shock wave as well as its standoff distance. Studies show that it can be assumed, with sufficient accuracy, that the shock has the shape of a circle with radius R_{s0} or a parabola

$$x = -s_0 + \frac{r^2}{2R_{s0}}.$$

A shock wave constructed in this way agrees closely with experimental shapes for a wide range of Mach numbers, and the approximation improves as the Mach number increases. The curve for the change in the radius, R_{s0} , as calculated from Eqs. (20.37) and (20.24), is given in Fig. 209.[†]

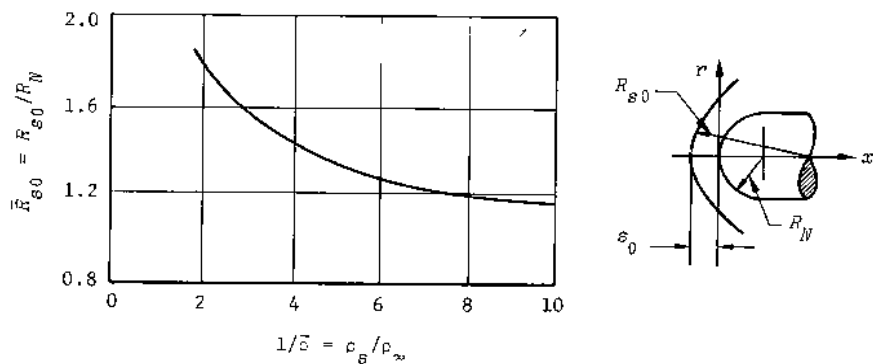


Fig. 209--Radius of curvature of a shock wave ahead of a sphere

Knowing the shape of the shock wave, it is possible to determine the parameters directly behind it at any point. For example, the distribution of M_2 can be found, and from this the point where $M_2 = 1$ can be located. For a dissociable gas, a series of values are assigned to $\omega = \pi/2 - \theta_s$, and the solution for an oblique shock is obtained for each of these values, accounting for dissociation. At the same time, the local values of V_2 and a_2 , and therefore M_2 , are determined. The value $M_2 = 1$ will correspond to one of the given angles $\omega = \omega'$. The distance from the axis to the point on the shock wave at which $M_2 = 1$ is approximately equal to $r = R_{s0} \sin \omega'$. Ordinary oblique shock theory, particularly Eq. (4.29), can be used to estimate the value of r . By choosing

[†]Editor's note: Recent calculations by Inouye⁽⁶⁾ for equilibrium flow about spheres have indicated that the following equations give better correlations than the formulas in the text:

$$\bar{s}_0 = \bar{\rho}/(1 + \sqrt{8\bar{\rho}/3}), \quad \bar{R}_{s0} = 0.78\bar{\rho}, \quad \bar{R}_{s0} = 0.78(1 + \sqrt{8\bar{\rho}/3}).$$

The first equation is from Hayes and Probstein⁽⁷⁾ and the second is from Seiff.⁽⁸⁾

a series of angles θ_s , we can find the value of θ_s for which $M_2 = 1$ as a function of M_∞ . A graph of the variation of θ_s for $\gamma = 1.4$ calculated by this method is presented in Fig. 203.

FLAT NOSES

Pressure Distribution and Drag Coefficient

Calculations of the pressure distribution over a flat nose in symmetric flow, made on an electronic computer, are compared with experimental results in Fig. 210. An analysis of these results enables us to

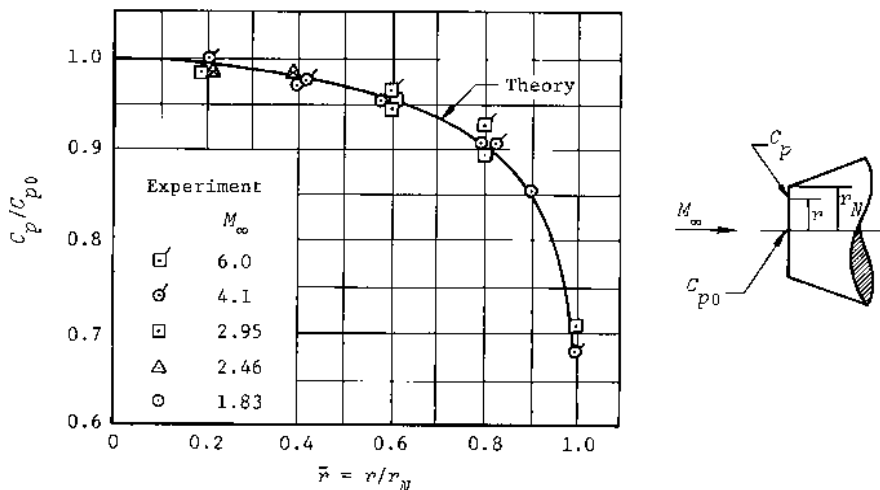


Fig. 210--Pressure distribution on a flat nose

determine the general relation for the variation of the pressure coefficient in the form $C_p = C_{p0}f(\bar{r})$. The dimensionless quantity \bar{r} is equal to the ratio of the radial distance r to an arbitrary point on the flat surface to the nose radius r_N ; $f(\bar{r})$ is a universal function varying only with \bar{r} , and C_{p0} is the pressure coefficient at the center of the nose, which coincides with the stagnation point. According to this rule, the

ratio C_p/C_{p0} is independent of the flow conditions in the free stream and of the absolute dimensions of the nose, and is determined only by the relative coordinate \bar{r} . With these results, the pressure drag coefficient of the flat nose can be derived from

$$C_{Dp} = C_{p0} \int_0^1 f(\bar{r}) d\bar{r}^2.$$

Assuming that the universal function $f(\bar{r})$ is applicable for any velocity and is given in the form of the curve in Fig. 210, we can compute the integral and obtain the following relation:

$$C_{Dp} = 0.915 C_{p0}. \quad (20.40)$$

As is evident, the drag coefficient of the flat nose is almost twice as large as that of the hemisphere. Equation (20.40) is plotted in Fig. 211, where the effects of dissociation have been included in the calculation of C_{p0} . The available experimental results (see Fig. 211) confirm the accuracy of Eq. (20.40). Unfortunately, there are no valid data for very high velocities, but it is expected that the theoretical results from Eq. (20.40) will be satisfactory for such velocities.

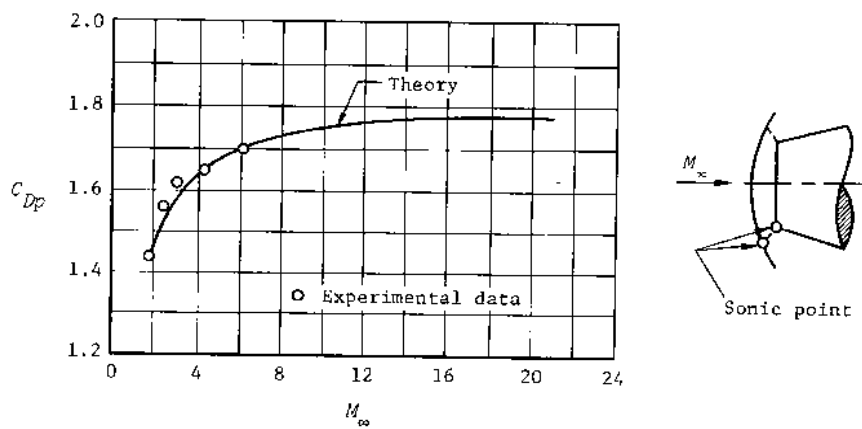


Fig. 211--Pressure drag coefficient of a flat nose

In addition to Eq. (20.40) for very high velocities, other approximate theoretical relations for the pressure coefficient and the pressure drag can be derived from an analysis of the pressure distribution directly behind the shock wave. The results of the analysis show that the pressure distributions behind the shock and on the surface are similar for comparatively low velocities, although in a small peripheral region the pressure directly behind the shock wave is somewhat lower than at corresponding points on the body surface.

The curves for pressure distribution converge with an increase in Mach number as the difference in the pressures caused by the additional compression from the shock to the body is decreased. This difference has been shown to be given by the ratio $C_{p0}/C_{ps} = (2 - \bar{\rho})/2(1 - \bar{\rho})$ on the axial streamline.

The difference disappears in the hypothetical case of $\gamma \rightarrow 1$ and $M_\infty \rightarrow \infty$, when the shock lies next to the surface of the nose. Thus, in this case, the conditions are identical for all the points on the flat surface. It can be assumed that these identical conditions are approximately maintained for a real flow at very high velocities. Consequently, the pressure coefficients on the flat surface, compared with their values at corresponding points directly behind the shock, are increased by the factor C_{p0}/C_{ps} .

Using Eq. (20.13) and assuming that the shock surface is spherical, we obtain the pressure coefficient:

$$C_p = (2 - \bar{\rho}) \left(1 - \frac{\bar{r}^2}{\bar{R}_{s0}^2} \right). \quad (20.41)$$

This expression is identical with Eq. (20.35) for a curved nose when $R_{s0} = R_N$. From Eq. (1.6), the pressure drag coefficient is

$$C_{Dp} = (2 - \bar{\rho}) \left(1 - \frac{1}{2\bar{R}_{s0}^2} \right). \quad (20.42)$$

In the limiting case of $\gamma \rightarrow 1$ and $M_\infty \rightarrow \infty$, the shock lies next to the surface, and $R_{s0} = \infty$ and $\bar{\rho} = 0$. Then $C_p = C_{Dp} = 2$, which agrees with the results of Newtonian theory. For actual flow conditions, it is

necessary to know the radius of curvature of the shock at the axis for the calculation of C_p and C_{Dp} . The determination of this radius is examined below.

The Detachment Distance and Shape of the Bow Shock Wave

Measurements of the detachment distance in various aerodynamic facilities have shown that it is proportional to the radius of the flat nose, r_N , as well as being a function of the free-stream velocity and the state of the gas. The latter factors determine the density variation behind the shock wave.

In the general case of a dissociated and ionized gas, it can be assumed that the distance from the shock to the body, relative to the radius r_N , will be a function of the density ratio across the normal part of the shock, $\bar{\delta} = \rho_\infty / \rho_s$, as in the case of a spherical nose. However, the standoff distance from a flat face is greater than that from a sphere. A preliminary estimate leads to the conclusion that, if the value of $\bar{s}_0 = s_0 / r_N$ is of the order of the density ratio $\bar{\delta}$ for a spherical nose, its value in the case of a flat face is $\bar{s}_0 \sim \sqrt{\bar{\delta}}$.

An empirical expression for the relative detachment distance can be established from experimental data in the form⁽⁵⁾

$$\bar{s}_0 = \frac{s_0}{r_N} = 1.03 \sqrt{\bar{\delta}/(1 - \bar{\delta})}. \quad (20.43)$$

The radius of curvature of the shock wave at the axis, which determines its shape in the vicinity of the flat nose, is also proportional to the radius of the flat face. The relative value of the radius of curvature $\bar{R}_{s0} = R_{s0} / r_N$ can be written as $(\bar{R}_{s0})_f = (\bar{s}_0 / \tilde{s}_0)_f$, where $\tilde{s}_0 = s_0 / R_{s0}$ and the subscript f denotes parameters for a flat nose. The analogous relation for a sphere is $(\bar{R}_{s0})_{\text{sph}} = (\bar{s}_0 / \tilde{s}_0)_{\text{sph}}$. Experimental studies show that the values of the relative detachment distances \tilde{s}_0 for a sphere and a flat nose are approximately the same, so that the ratios \bar{s}_0 / \bar{R}_{s0} will also be the same. Thus, the dimensionless radius of curvature for the flat nose is related to that for a sphere by the following equation:

$$(\bar{R}_{s0})_f = \frac{(\bar{s}_0)_f}{(\bar{s}_0)_{\text{sph}}} (\bar{R}_{s0})_{\text{sph}}. \quad (20.44)$$

The detachment distance for a flat nose is obtained from Eq. (20.43), and the quantities $(\bar{s}_0)_{\text{sph}}$ and $(\bar{R}_{s0})_{\text{sph}}$ are determined from Eqs. (20.39) and (20.37), respectively.

Equation (20.44) can be simplified if it is assumed that the shock wave is concentric with the sphere, in which case

$$(\bar{R}_{s0})_{\text{sph}} = 1 + (\bar{s}_0)_{\text{sph}}.$$

Using Eqs. (20.39) and (20.43), we find for the flat face

$$\bar{R}_{s0} = 0.52 \frac{3 - \bar{\rho}}{\sqrt{\bar{\rho}(1 - \bar{\rho})}}. \quad (20.45)$$

This relation is plotted in Fig. 212. It is apparent from Eq. (20.45) that as $\bar{\rho} \rightarrow 0$ the value of $\bar{R}_{s0} \rightarrow \infty$, because the shock wave comes into contact with the flat surface of the nose in the limit.[†]

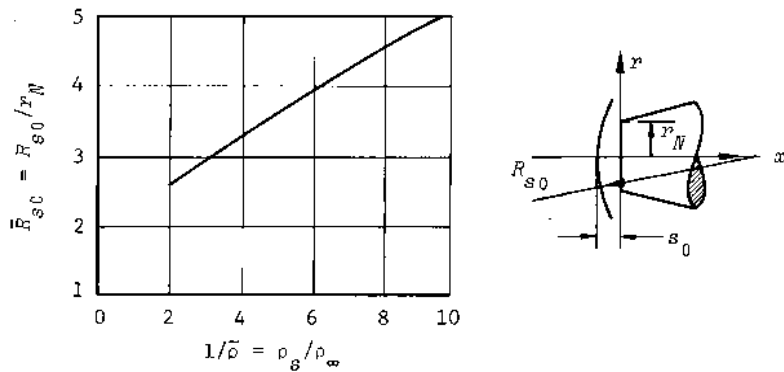


Fig. 212--Radius of curvature of a shock wave ahead of a flat nose

[†]Editor's note: See comments in Introduction to chapter.

The location of the sonic point on the shock wave can be determined by the methods discussed earlier for the flow around a sphere. The location of this point on the surface of the flat face can be found from the following considerations: Assume that the flow around the nose occurs in a convergent channel bounded by the shock wave and by the nose surface, and that the flow is subsonic since the sonic point on the shock wave is located outside the edge of the flat face. Therefore, the velocity of the gas in the converging channel increases. Since the narrowest section of the channel is bounded by the sharp corner of the nose, the flow at points lying on this corner will attain the velocity of sound. Experimental studies confirm this conclusion.

Since the velocity is sonic at the shoulder, the local Mach number is $M = 1$ and the pressure can be determined at this point. If it is assumed that the flow is isentropic along the streamline between the stagnation point and the sonic point, the expression for pressure is

$$\frac{p^*}{p'_0} = \left(\frac{2}{\gamma_2 + 1} \right)^{\gamma_2 / (\gamma_2 - 1)},$$

where γ_2 is the ratio of specific heats calculated for conditions behind a normal shock. At small velocities, $\gamma_2 = \gamma_1$ and the pressure can be determined from the usual equation for p^* at a sonic point. At large velocities, it is necessary to take into account the variation in specific heats. If it is assumed that $\bar{\rho} = (\gamma_2 - 1) / (\gamma_2 + 1)$, the approximate expression for the ratio of the pressure coefficients can be presented in the form

$$\frac{C_p^*}{C_{p0}} = \frac{1 - \bar{\rho}}{2}.$$

According to this equation, the pressure coefficient at the corner of the flat nose is about one-half that at the stagnation point.

The Velocity Gradient at the Stagnation Point

The heat flux to the surface at the stagnation point is a function of the velocity gradient. It has been shown that the velocity gradient

for a sphere is inversely proportional to the radius of curvature of the surface R_N . Therefore, the velocity gradient decreases with an increase in this radius and is zero in the limit for flat blunting. However, studies show that the value of the gradient at the stagnation point of a flat nose differs from zero. On this basis, it can be assumed that the flat face has an influence on the flow that is similar to that of a spherical surface with a radius of curvature R_{Ne} . This is confirmed by observations of the shape of the shock wave. It is possible to select an equivalent radius, R_{Ne} , for which the curvature of the shock at the axis will be approximately identical with that in front of a flat nose. Thus,

$$r_N(\bar{R}_{s0})_f = R_{Ne}(\bar{R}_{s0})_{\text{sph}},$$

and the equivalent radius is

$$R_{Ne} = r_N \frac{(\bar{R}_{s0})_f}{(\bar{R}_{s0})_{\text{sph}}}. \quad (20.46)$$

From Eq. (20.27a), the velocity gradient at the stagnation point of a sphere with an equivalent radius R_{Ne} is:

$$\left(\frac{\partial V}{\partial x} \right)_{x=0, y=0} = \frac{1}{J} \frac{r_N}{R_{Ne}}, \quad (20.47)$$

where

$$J = \frac{r_N}{\sqrt{(2p'_0/z'_0)(1 - p_\infty/p'_0)}}.$$

The value of the velocity gradient determined from Eq. (20.47) is assumed to be the same as that at the stagnation point of the flat nose. This assumption, of course, is not exact and should be checked additionally by means of experimental research. The scanty data (Fig. 213) indicate that Eq. (20.47) gives a fairly accurate solution at high velocities.[†]

[†]Editor's note: See comments in Introduction to Chapter.

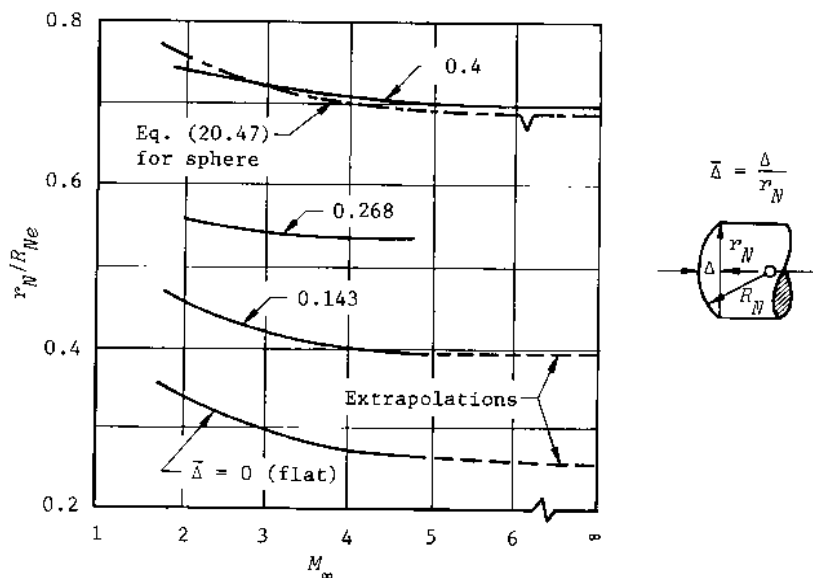


Fig. 213--Equivalent radius of a blunt nose

OTHER BLUNT NOSE SHAPES

Pressure Distribution and Drag

The spherical and flat-face blunting examined above should be considered as two limiting types of blunting between which lie noses of an intermediate form. For example, one can consider flat blunting with a curved bevel (rounded off) (see Fig. 12, p. 28) and blunting by means of a spherical segment with a radius larger than that of a hemisphere (see Fig. 10, p. 27). Studies show⁽⁹⁾ that the shape and radius of curvature of the corner of the body exert an influence on the pressure distribution upstream into the subsonic region.

For flat noses with rounded edges, the effective parameter is the relative radius of curvature $\bar{r} = r/r_N$; for a nose composed of a spherical segment, it is the dimensionless radius of the sphere $\bar{R} = R_N/r_N$ (or the dimensionless height of the segment $\bar{\Delta} = \Delta/r_N$). For the second type of nose, the position of the corner influences the flow, since the sonic point is located there.

Typical pressure distributions are shown in Fig. 214, from which it is evident that the effect of the curvature results in a reduction in pressure in comparison with a flat nose, even for the nose with a partial flat portion. It is also possible to determine the pressure variation on a spherical-segment nose compared with that on a flat face and on a hemisphere. As the radius of curvature of the segment decreases, the pressure distribution approaches that for a hemisphere. However, sonic velocity must be maintained at the sharp corner, so that the pressure distribution is a function of both the local shape of the body and the location of the sonic point.

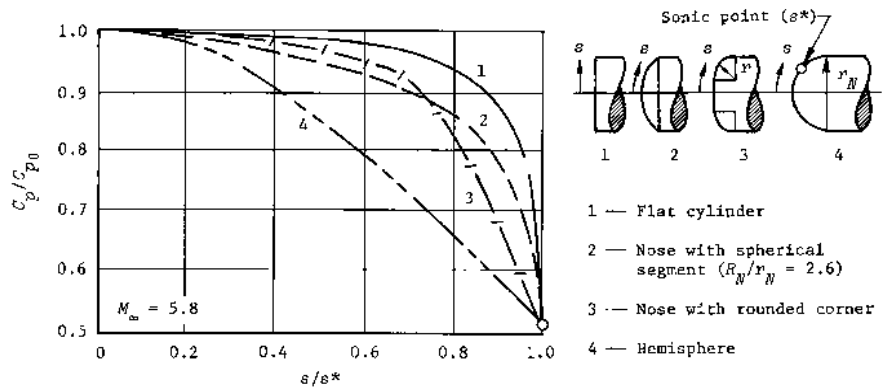


Fig. 214--Pressure distributions on blunt noses of various shapes

When the surface at the corner point has the same slope as it has at the sonic point on a hemisphere, i.e., an angle of approximately 45° , the pressure distribution is identical with that on the similar portion of a hemisphere. The character of the pressure distribution does not change with a further decrease in the radius of the segment, since perturbations will not penetrate into the subsonic region from the corner where the velocity is now supersonic.

The ratio of the pressure coefficients given in Fig. 214 depends relatively weakly on the free-stream Mach number. This was evident

earlier in the examples of flow around a hemisphere and a flat face. Curves based on experimental data are shown in Fig. 215 for the pressure distribution over the surface of a spherical segment with an angle of 26.21° for $M_\infty = 2.01$ and 4.76 .⁽⁹⁾ The sonic point is located at the corner for this nose.

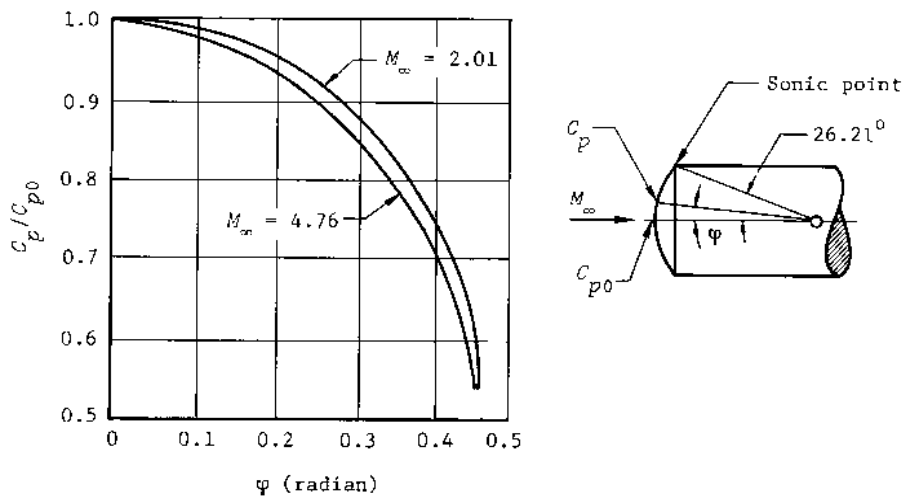


Fig. 215--Pressure distribution on a spherical segment

Experimental studies at medium Mach numbers indicate that the pressure drag coefficient for a flat nose with rounded corners is a linear function of the parameter \bar{x} and can be represented in the form

$$C_{Dp} = \langle C_{Dp} \rangle_f - [(\langle C_{Dp} \rangle_f - \langle C_{Dp} \rangle_{sph})\bar{x}] \quad (20.48)$$

It can be assumed that this relation is also valid at high velocities. Equation (20.48) can be extended approximately to blunt nose bodies in the form of a spherical segment with a radius of curvature greater than r_N , and also to bodies in the shape of an ellipse, although, strictly speaking, the experiments show some deviation from the linear relation.

In using Eq. (20.48) in these two cases, we must replace the parameter \bar{r} by $\bar{\xi}$ and $\bar{\delta}$, respectively.

Detachment Distance and Radius of Curvature of the Shock

Similar linear relations can be written for the relative detachment distance of the shock wave in front of a rounded-off nose. The variation of the dimensionless standoff distance $\bar{s}_0 = s_0/r_N$ with the blunting parameter $\bar{r} = r/r_N$ for $M_\infty = 5.8$ is shown in Fig. 216, based on experimental data. It is evident that the shape of the body surface in the sonic region has a strong influence on the detachment and curvature of the shock wave.

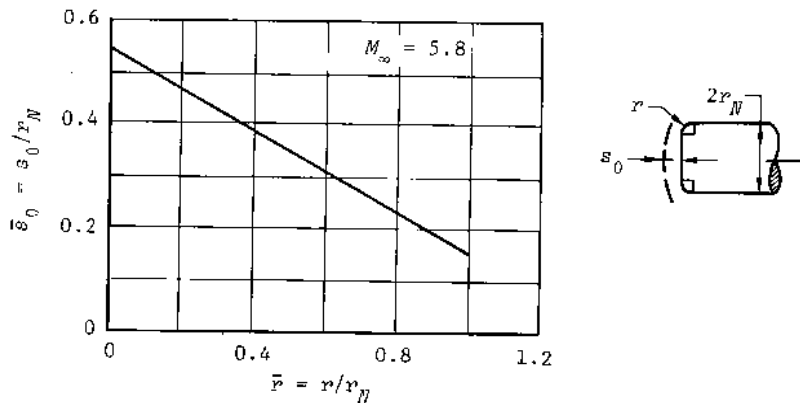


Fig. 216--Dimensionless shock-detachment distance for a flat nose with a curved bevel

Assuming that this variation is valid for arbitrary values of M_∞ , we can write a general expression for estimating the detachment distance as follows:

$$\bar{s}_0 = (\bar{s}_0)_f - [(\bar{s}_0)_f - (\bar{s}_0)_{\text{sph}}]\bar{r}. \quad (20.49)$$

A similar type of variation is observed for blunt noses consisting of spherical segments. In Fig. 217 are shown experimental data obtained

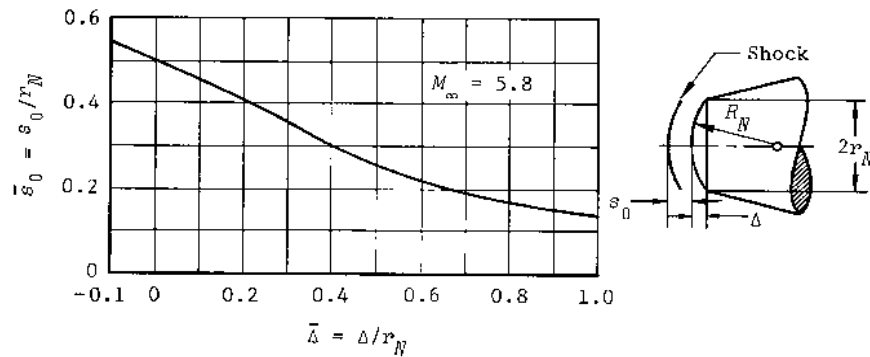


Fig. 217--Dimensionless shock-detachment distance for a blunt spherical segment

at $M_\infty = 5.8$ on models with both convex and concave noses. It is apparent that there is a practically linear relation for values of $\bar{\Delta}$ between -0.1 and 0.45. In this range of $\bar{\Delta}$, the flow velocity is sonic at the corner, and the nose is similar to a flat nose. As the value of $\bar{\Delta}$ increases, a continually greater part of the spherical surface is located downstream of the sonic point, the effect of the nose shape on the detachment distance is reduced, and the variation becomes nonlinear.

On the basis of these results, an approximate relation for the relative detachment distance in the range $-0.1 \leq \bar{\Delta} \leq 0.45$ can be presented in the following form:

$$\bar{s}_0 = (\bar{s}_0)_f - \frac{20}{9} [(\bar{s}_0)_f - A]\bar{\Delta}, \quad (20.50)$$

where A is the value of the relative detachment distance at $\bar{\Delta} = 0.45$. According to experimental data, this quantity can be assumed to be approximately equal to $A = 2(\bar{s}_0)_{\text{sph}}$.

Experimental studies also enable us to establish the approximate nature of the relation for the radius of curvature of the shock at the axis. For bodies with a rounded corner, this relation is of a hyperbolic character in the entire region $0 \leq \bar{r} \leq 1$. The corresponding empirical relation is

$$\bar{R}_{s0} = \frac{R_{s0}}{r_N} = \frac{(\bar{R}_{s0})_f (\bar{R}_{s0})_{\text{sph}}}{(\bar{R}_{s0})_{\text{sph}} + [(\bar{R}_{s0})_f - (\bar{R}_{s0})_{\text{sph}}] \bar{r}}. \quad (20.51)$$

For blunting in the shape of a spherical segment, the relative radius is an inverse function of the parameter $\bar{\delta}$ for the case of an almost flat nose ($-0.1 \leq \bar{\delta} \leq 0.45$). In this range of $\bar{\delta}$, the radius of curvature can be represented in the form

$$\bar{R}_{sc} = \frac{9(\bar{R}_{s0})_f^B}{9B + 20[(\bar{R}_{s0})_f - B]\bar{\delta}}, \quad (20.52)$$

where B is the value of \bar{R}_{s0} at $\bar{\delta} = 0.45$ and is approximately equal to 1.8 to 2 times $(\bar{R}_{s0})_{\text{sph}}$.

The Equivalent Spherical Radius and the Velocity Gradient at the Stagnation Point

The equivalent spherical radius and the velocity gradient are computed in the same way as in the study of flow around a flat nose. The equivalent radius of a sphere corresponding to a given nose is determined from Eq. (20.46), in which the numerator can be calculated from Eqs. (20.51) or (20.52).

The velocity gradient at the stagnation point is determined from Eq. (20.47) after the equivalent radius is found. Because of the many assumptions, these results are only approximate, and it is recommended that they be checked and refined with experiments. Results of such studies at low Mach numbers are presented in Fig. 213. Here, it is evident that Eq. (20.47) agrees well with the experimental data for a spherical segment with $\bar{\delta} = 0.4$, although in this case the flow is still sonic at the corner. (The largest value of $\bar{\delta}$ for which the corner velocity is sonic is 0.45.) The available data show that Eq. (20.47) can be used to calculate the velocity gradient at the stagnation point of spherical-segment noses for values of $\bar{\delta}$ up to about 0.3 to 0.35.[†]

[†]Editor's note: See comments in Introduction to Chapter.

§ 21. HYPERSONIC FLOW AROUND SLIGHTLY BLUNTED CYLINDRICAL
AND CONICAL BODIES

ANALOGY WITH THE UNSTEADY MOTION OF A PISTON

Effect of Small Blunting

STUDIES SHOW THAT THE INFLUENCE of a slight amount of blunting on the flow around the entire body is not the same for different conditions and is particularly a function of the free-stream velocity. Thus, it can be established from experiments that this effect is insignificant at moderate Mach numbers and affects only a small area of the body in the vicinity of the nose. The effect of blunting increases substantially at hypersonic flight velocities, as can be illustrated by comparing the order of magnitude of the drag of a blunt tip with a diameter $2R_N$ and the drag of the remaining portion of the body, e.g., a cone with a length L and a cone angle δ_c .

According to Newtonian theory, the drag of the spherical tip is of the order of $\rho_\infty V_\infty^2 (2R_N)^2 / 2$, and the drag for the remaining part of the body is of the order of $\rho_\infty V_\infty^2 (\delta_c L)^2 \delta_c^2 / 2$. For both portions of the body to have the same drag, the dimensions of the body must be of the order of $L/2R_N \sim 1/\delta_c^2$.[†] These considerations indicate the sizable influence of slight blunting on the character of the flow in a perturbed region tens and hundreds of blunting diameters in length. The thinner the body, the farther this region extends and, consequently, the more important is the blunting influence.

It should be noted that the blunting effect is also a function of the type of body; for example, the effect is significantly greater for

[†]Editor's note: In other words, the ratio of the nose radius to the cone base radius, R_N/r_{mid} , need only be of the order of $\delta_c/2$.

two-dimensional profiles than for three-dimensional bodies of revolution. The drag of a blunt two-dimensional profile always increases in comparison with a pointed profile, and this increase can be extremely large. However, the drag of bodies of revolution may not only not increase but, to the contrary, may even decrease.

It follows from physical considerations that the character of the flow around the body will be a function of the degree of blunting, which can be described by means of the ratio $2R_N/L$. It is obvious that the degree of blunting and the corresponding effect for a specific shape must agree with the methods of analysis for flow around blunt bodies. However, if the blunting parameter is small ($2R_N/L \ll 1$), the analysis can be carried out on the assumption that the body remains pointed and the effect of bluntness is replaced by the effect on the surrounding flow of the concentrated force acting on the blunted portion.

Professor G. G. Chernyi⁽¹⁰⁾ solved the problem by using the analogy between steady flow around a cone and the unsteady motion of the gas behind the cylindrical shock wave originating in front of a piston. According to this analogy, the perturbed flow around a cone is equivalent (in a lateral plane stationary with respect to the body) to the gas flow in front of a piston. For observers located in this plane, the flow is similar to the flow that originates in the propagation of an explosion wave.

Thus, the perturbed flow around a cone is analogous to the flow generated in the explosion of a long linear cylindrical charge at a moment of time, $t = 0$. In the case of a cone, the initial energy of the gas is assumed equal to its value in the unperturbed flow, since the pointed nose does not exert a strong force on the gas in front of the explosion (or in front of the piston). However, when the body is blunt, the force is not negligible, but is equal to the pressure drag of the blunt nose. This force acts on the gas to produce work and transmits to the gas an energy E . Thus, the initial energy per unit length of the linear charge is identified with the nose drag.

For axially symmetric flow about a blunt body, the equivalent problem of the motion of a cylindrical piston can be formulated in the following way: In an undisturbed gas, an explosion occurs along a straight line at an initial moment of time; as a result, a specific energy E is

transmitted to the gas. At the same moment of time, a cylindrical piston starts expanding radially in the gas from the line of the explosion with a velocity V . The problem is solved by determining the resultant motion of the gas ahead of the piston, which gives the shape of the shock wave in front of the blunt cone and also the pressure distribution on its surface for the equivalent problem of steady flow.

To convert from one problem to the other, it is necessary to assume

$$E = D = C_{DN} \frac{\rho_\infty V_\infty^2}{2} \pi R_N^2, \quad t = \frac{x}{V_\infty}, \quad \gamma = V_\infty \tan \delta_c, \quad (21.1)$$

where C_{DN} is the drag coefficient of the blunt portion.

Thus, in the general case, the problem of flow around a blunt cone amounts to the problem of an explosion with the subsequent expansion of a piston. It should be noted that this analogy relates to a flow region not too close to the nose of the body, where the perturbed velocity in the longitudinal direction is small and, therefore, the law of plane sections is valid.

The System of Equations

Problems of the type discussed above can be solved more conveniently by using equations in the Lagrangian form rather than in the Euler form (see Chap. I). In this form, the equations correspond to the motion of a discrete particle. If, as in our case, one-dimensional radial motion of a piston is being considered, the solution of these equations determines the coordinates r and the parameters of state of the particle for any moment of time t .

If the coordinate of the particle is r_1 at the initial moment of time $t = 0$, the instantaneous coordinate r will be a function of time t and of the initial value r_1 , i.e., $r = f(r_1, t)$. The parameters of state for their known initial values (e.g., density ρ_∞ , pressure p_∞ , entropy S_∞ , etc.) are also functions of the initial coordinate r_1 and the time t . The basic equations can be derived in Lagrangian form using Fig. 30 (p. 67). If we equate to zero the sum of the inertial forces $(\partial V_p / \partial t) \rho (2\pi r dr \cdot 1)$ and the pressure $(\partial p / \partial r) (2\pi r \cdot 1)$ that are acting on a particle with a volume $2\pi r dr \cdot 1$, we obtain the equation of motion:

$$\frac{\partial V_r}{\partial t} = \frac{\partial^2 r}{\partial t^2} = -\frac{1}{\rho} \frac{\partial p}{\partial r}. \quad (21.2)$$

The continuity equation is derived from the condition of the conservation of mass of a particle in motion. According to this condition, if the mass was $\rho_\infty(2\pi r dr \cdot 1)$ at the initial moment of time, it will remain the same at any time t ; therefore

$$2\pi r \rho dr = 2\pi r_1 \rho_\infty dr_1.$$

Since this condition is valid at any moment of time, the total derivative dr/dr_1 can be replaced by the partial derivative $\partial r/\partial r_1$. The continuity equation takes the form

$$\frac{\partial r}{\partial r_1} = \frac{\rho_\infty r_1}{\rho r}. \quad (21.3)$$

If the Lagrangian variable $m = \rho_\infty r_1^2/2$ is introduced, the equations of motion and continuity become

$$\frac{\partial V_r}{\partial t} = -r \frac{\partial p}{\partial m}, \quad (21.2a)$$

$$\frac{\partial p}{\partial m} = \frac{1}{\rho r}. \quad (21.3a)$$

These equations are solved for the condition of isentropic flow ahead of the piston. In mathematical form, the condition of constant entropy of the particle is stated as

$$\frac{\partial S}{\partial t} = 0 \quad \text{or} \quad \frac{\partial}{\partial t} \left(\frac{p}{\rho^\gamma} \right) = 0. \quad (21.4)$$

The first expression pertains to the more general case in which physical-chemical changes can occur in the gas; the second expression corresponds to isentropic flow with constant specific heats.

The energy equation relative to the same conditions behind a cylindrical shock wave must be added to these equations. It is written

on the basis of the law of conservation of energy. If the motion of gas ahead of a piston after an explosion is considered, the total (kinetic and internal) energy of the flowing gas at each moment of time is equal to the sum of the energy produced per unit length of the explosion E , the initial energy E_1 , and the work of expansion of the piston. Thus,

$$\int_{r_0}^r \left(\frac{V^2}{2} + u \right) p(2\pi r dr) = E + \int_0^r \rho u_\infty (2\pi r dr) + \int_0^r p(2\pi r dr), \quad (21.5)$$

where u and u_∞ are the specific internal energies, with dimensions of the square of the velocity; p is the pressure of the gas on the piston; and r_0 and r are the distances to the piston and shock wave, respectively.

For the case of constant specific heats, $u = c_v T = [1/(\gamma - 1)]p/\rho$. Noting that $V_r = \partial r/\partial t$ and $r_1 \rho_\infty dr_1 = r_0 dr$, we find

$$\int_{r_0}^r \left[\frac{1}{2} \left(\frac{\partial r}{\partial t} \right)^2 + \frac{1}{\gamma - 1} \frac{p}{\rho} \right] \rho r dr = \frac{E}{2\pi} + \frac{p_\infty r^2}{2(\gamma - 1)} + \int_0^r p r dr. \quad (21.5a)$$

The momentum equation, together with the energy equation, is particularly useful in solving the problem of the motion of gas ahead of a cylindrical piston, and can be obtained from Eq. (21.2) in the form

$$\rho r \frac{\partial V}{\partial t} dr = - \frac{\partial P}{\partial r} r dr.$$

After integration across the thickness of the perturbed layer, we find

$$\int_{r_0}^r \frac{\partial V}{\partial t} \rho r dr = - \int_{P_\infty}^P r dp. \quad (21.6)$$

FLOW AROUND A BLUNT CYLINDER

The solution of the equivalent problem of the unsteady motion of a cylindrical piston enables us to calculate the flow around a blunt cylinder. In the statement of the problem, it is assumed that the

explosive charge distributed along the straight line transmits an initial energy E to the gas. The motion of the gas originating as a result of this explosion corresponds to the condition when the piston velocity is $V = 0$. In general, the parameters that define this motion behind the shock wave are the initial pressure p_∞ , the initial density ρ_∞ , the explosion energy E (the work with respect to a unit length), the ratio of specific heats γ , the distance r from the line of the explosion, and the time t . The dimensionless characteristics of the perturbed flow (e.g., the relative pressure) will be functions of dimensionless combinations of these parameters.

One of these parameters, the adiabatic ratio γ , is already a dimensionless quantity, so the dimensionless combinations must be composed of the remaining five parameters. Since there are three independent dimensions, it is possible to construct two independent dimensionless combinations, i.e., $p_\infty^{\frac{1}{2}}r/E^{\frac{1}{2}}$ and $p_\infty t/(p_\infty E)^{\frac{1}{2}}$.

Thus, the flow parameters behind the shock wave, in dimensionless form, will be functions of these three dimensionless parameters. The latter two can be transformed by using Eq. (21.1), and the system of dimensionless parameters takes the form

$$\gamma, \quad \frac{1}{M_\infty \sqrt{C_{DN}}} \frac{r}{D_N}, \quad \frac{1}{M_\infty^2 \sqrt{C_{DN}}} \frac{x}{D_N}. \quad (21.7)$$

Hence, it follows that the shape of the bow wave in front of a blunt cylinder is determined by the following general functional relation:

$$\frac{1}{M_\infty \sqrt{C_{DN}}} \frac{r_s}{D_N} = R\left(\gamma, \frac{1}{M_\infty^2 \sqrt{C_{DN}}} \frac{x}{D_N}\right). \quad (21.8)$$

The general relation for the pressure distribution on the surface of a cylinder is found from the condition $r = 0$ and has the form

$$\frac{\Delta p}{p_\infty} = P\left(\gamma, \frac{1}{M_\infty^2 \sqrt{C_{DN}}} \frac{x}{D_N}\right). \quad (21.9)$$

Equations (21.8) and (21.9) have been obtained on the basis of dimensional analysis, and do not give specific expressions for the quantities involved. Nevertheless, they are of great practical value since they reveal an extremely important relation between these quantities, and the dimensionless parameters can be considered as similarity parameters. Therefore, the relations presented are used as the theoretical foundation for experimental studies, in which it is assumed that the similarity parameters are

$$\frac{1}{M_\infty^2 \sqrt{C_{DN}}} \frac{x}{D_N} \quad \text{and} \quad \gamma.$$

The existence of such parameters permits the generalization of particular experimental results to include a group of similar flows around cylindrical blunt bodies.

As an example, experimental data⁽¹¹⁾ on the pressure distribution obtained in a wind-tunnel test of a cylindrical model with a hemispherical nose at $M_\infty = 7.7$ and $\gamma = 1.4$ are shown in Fig. 218a. To generalize these data, the parameter $(x/D_N)/M_\infty^2 \sqrt{C_{DN}}$ is calculated, where C_{DN} is that for a hemisphere at $M_\infty = 7.7$. The pressure ratio is plotted against this similarity parameter in Fig. 218b, which can be used for pressure calculations for arbitrary Mach numbers. An analogous graph that generalizes the experimental results of a study of shock-wave shape made at the same conditions ($\gamma = 1.4$, $M_\infty = 7.7$) is presented in Fig. 219.

In certain cases, the general Eqs. (21.8) and (21.9) can be converted to a more specific form. This is possible, for example, for very high velocities when the initial gas pressure p_∞ is negligibly small compared with the pressure behind a very strong shock wave. In this case, p_∞ can be dropped from the similarity parameters, and the pressure on the cylinder can be represented in the form

$$\Delta p \approx p = P(\gamma, \rho_\infty, F, t).$$

It is apparent that the last three functional parameters contain the three independent dimensions and it is possible to form a dimensionless

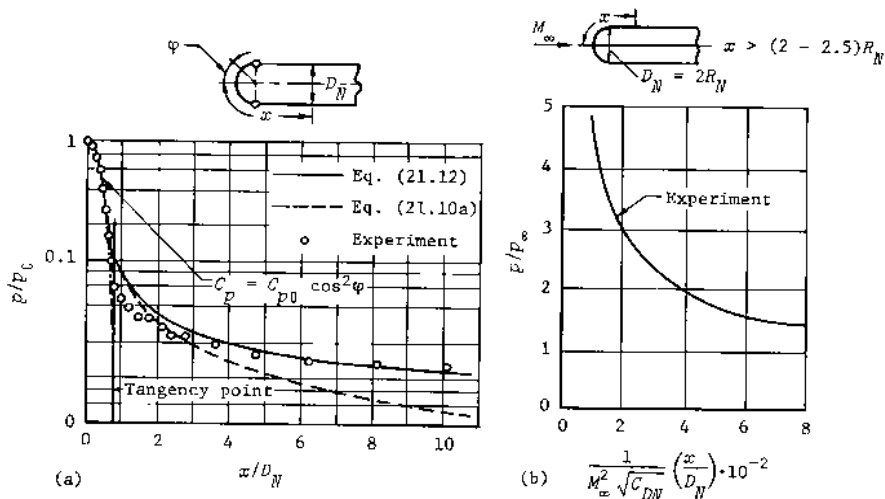


Fig. 218—Pressure distribution on a cylinder with a hemispherical nose

combination from them. If the techniques of dimensional analysis are used, the relation is

$$\Delta p = f_1(\gamma) \rho_\infty^x E^y t^z,$$

where $f_1(\gamma)$ is a function depending on the ratio of specific heats. After making substitutions from Eqs. (21.1) for E and t , we can write this expression as

$$\Delta p = f(\gamma) c_\infty^x \left(C_{DN} \frac{\rho_\infty V_\infty^2}{2} \frac{\pi D_N^2}{4} \right)^y \left(\frac{x}{V_\infty} \right)^z.$$

The exponents are determined by comparing the exponents on each side of the functional equation, i.e.,

$$ML^{-1} T^{-2} = [ML^{-3}]^x [MLT^{-2}]^y [T]^z,$$

where M , L , and T are the independent dimensions of mass, length, and

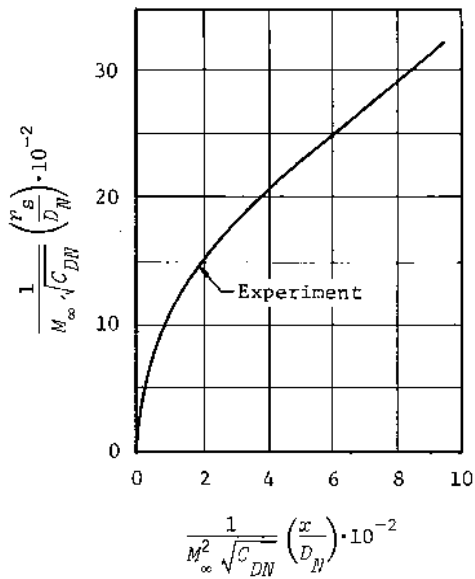


Fig. 219--Shape of the shock wave ahead of a cylinder with a hemispherical nose

time, respectively. Hence, we find that $x = y = \frac{1}{2}$ and $z = -1$. Therefore,

$$\frac{2\Delta p}{c_\infty^2 V_\infty^2} = C_p = f(\gamma) \sqrt{C_{DN}} \left(\frac{D_N}{x} \right). \quad (21.10)$$

An analogous relation can be obtained for the coordinates of the shock wave. After first writing the general expression for the radial distance to the shock in the form $r_s = R(\gamma, \rho_\infty, E, t)$, we can use dimensional analysis in the same way as before. Thus, the radial dimension of the shock wave is written as

$$r_s = \varphi_1(\gamma) \rho_\infty^x E^y t^z,$$

where $\varphi_1(\gamma)$ is a function of γ . The equation for r_s in dimensionless coordinates is

$$\frac{r_s}{D_N} = \varphi(\gamma) C_{DN}^{\frac{1}{4}} \left(\frac{x}{D_N} \right)^{\frac{1}{2}}. \quad (21.11)$$

The functions $f(\gamma)$ and $\varphi(\gamma)$ in Eqs. (21.10) and (21.11) can be determined from the exact solution of the problem of the strong explosion of a linear charge. The numerical values obtained for these functions are presented graphically in Fig. 220. If this curve for $\gamma = 1.4$ and

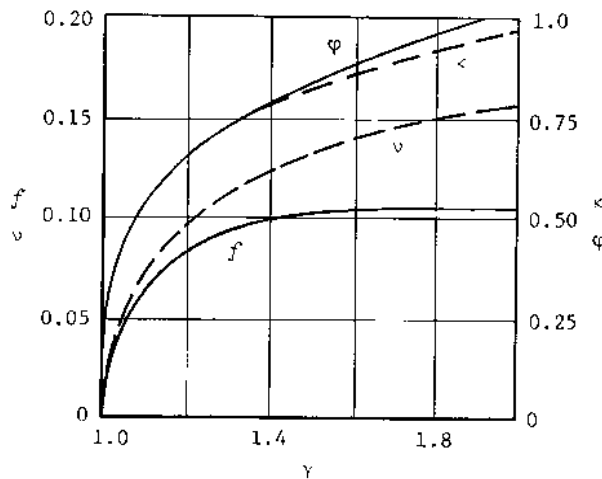


Fig. 220—Coefficients for calculating the pressure distribution and shock-wave shape

a value of $C_{DN} = 0.94$ in Eq. (21.10) are used, the expression for the pressure ratio becomes

$$\frac{p}{p_\infty} = 0.066 M_\infty^2 \left(\frac{D_N}{x} \right). \quad (21.10a)$$

It should be kept in mind that this equation, as well as the more general Eq. (21.10), is a first approximation, since the effect of the initial pressure is not considered. Attempts have been made to take this effect into account,⁽¹²⁾ and a more accurate equation is

$$\frac{P}{P_\infty} = 0.066 M_\infty^2 \left(\frac{D_N}{x} \right) + 0.405 + \frac{0.155}{M_\infty^2} \left(\frac{x}{D_N} \right). \quad (21.12)$$

As is evident from Fig. 218, the calculation from this equation agrees better with the experiment.

Equation (21.12), relating to a cylinder with a spherical nose, can be extended to a cylindrical body with an arbitrary form of blunting. For the case of $\gamma = 1.4$, the generalized equation will have the form

$$\frac{P}{P_\infty} = 0.069 M_\infty^2 \sqrt{C_{DN}} \left(\frac{D_N}{x} \right) + 0.405 + 0.150 \frac{1}{M_\infty^2 \sqrt{C_{DN}}} \left(\frac{x}{D_N} \right). \quad (21.13)$$

If the cylinder has a spherical nose for which $C_{DN} = 0.94$, this equation reduces to Eq. (21.12).

Analogous relations are obtained for determining the shape of the shock wave. For the value of $\varphi(\gamma)$ for $\gamma = 1.4$ from Fig. 220 and for $C_{DN} = 0.94$, as previously, we obtain from Eq. (21.11) the equation for the first approximation for the radial distance to a point on the shock wave around a cylinder with a spherical nose:

$$\frac{r_s}{D_N} = 0.78 \sqrt{x/D_N}. \quad (21.11a)$$

A more accurate relation, taking into account the effect of the back pressure, ⁽¹²⁾ is written as

$$\frac{r_s}{D_N} = 0.78 \sqrt{x/D_N} \left[1 + \frac{1.62}{M_\infty^2} \left(\frac{x}{D_N} \right) - \frac{6.17}{M_\infty^4} \left(\frac{x}{D_N} \right)^2 \right]. \quad (21.14)$$

For the general case when the blunting in front of the cylinder is of arbitrary shape, the relation is

$$\frac{r_s}{D_N} = 0.795 C_{DN}^{\frac{1}{4}} \sqrt{x/D_N} \left[1 + \frac{1.57}{M_\infty^2 \sqrt{C_{DN}}} \left(\frac{x}{D_N} \right) - \frac{5.80}{M_\infty^4 C_{DN}} \left(\frac{x}{D_N} \right)^2 \right]. \quad (21.15)$$

In using Eqs. (21.10) through (21.15), it should be remembered that

they give satisfactory results starting at about one body radius behind the end of the nose. Corresponding values of x measured from the stagnation point of the nose (Fig. 218) should be selected so that x/R_N is greater than about 2 to 2.5.

FLOW AROUND A SLENDER CONE WITH SMALL BLUNTING

The Basic Equations and the Method of Solution for Infinite Mach Number

The flow around a slender cone at hypersonic velocity can be studied by using the analogy from the problem of unsteady motion of a gas with a cylindrical shock wave.⁽¹⁰⁾ If it is assumed that at these velocities the gas layer between the piston and the shock is extremely thin, the energy equation, Eq. (21.5a), can be simplified somewhat:

$$\frac{r^2}{4} \rho_\infty \left(\frac{\partial r}{\partial t} \right)^2 + \frac{(r^2 - r_0^2)p}{2(\gamma - 1)} = \frac{E}{2\pi} + \frac{p_\infty r^2}{2(\gamma - 1)} + \int_0^r pr_0 dr_0. \quad (21.5b)$$

The momentum equation, Eq. (21.6), can also be simplified. Since the perturbed layer is assumed to be thin, this equation is written as

$$\rho_\infty \frac{\partial r}{\partial t} \frac{r^2}{2} = \int_0^t (p - p_\infty)r dt. \quad (21.6a)$$

In these equations, let us assume that the quantity $\partial r/\partial t = \dot{r}$ is constant in the entire perturbed region and is equal to the velocity of the particles directly behind the shock wave, keeping in mind that this velocity can be determined from shock-wave theory. In steady shock-wave theory, the relative change in velocity is determined by the expression

$$\frac{V_\infty - V_2}{V_\infty} = \frac{2}{\gamma + 1} \left(1 - \frac{a_\infty^2}{V_\infty^2} \right).$$

Reversing the motion so that the shock wave travels into the steady flow with a velocity $V_\infty = D = \dot{r}_s$, we find the equation for the velocity of the particles behind the shock:

$$\dot{r} = V_\infty - V_2 = \frac{2}{\gamma + 1} \left(\dot{r}_s - \frac{\alpha_\infty^2}{\dot{r}_s} \right), \quad (21.16)$$

which takes into account the initial pressure of the gas.

Furthermore, since the perturbed layer is thin, it can be assumed that the coordinate r equals the distance to the shock r_s . The radius of the piston is $r_0 = Ut$, where U is the velocity of expansion of the piston. Using Eq. (21.16) for \dot{r} in Eqs. (21.5b) and (21.6a) and assuming that $r = r_s$ and $r_0 = Ut$, we can convert the resulting equations to dimensionless form by defining a characteristic length $L = (E/\pi\rho_\infty U^2)^{1/2}$ and a characteristic time L/U . Thus,

$$\begin{aligned} & \frac{1}{2} r_s^2 \left(\frac{2}{\gamma + 1} \right)^2 \left(\dot{r}_s - \frac{1}{K_1^2 \dot{r}_s} \right)^2 + \frac{r_s^2 - t^2}{\gamma - 1} \left(\Delta p + \frac{1}{\gamma K_1^2} \right) \\ &= 1 + \frac{r_s^2}{\gamma - 1} \frac{1}{\gamma K_1^2} + 2 \int_0^t \left(\Delta p + \frac{1}{\gamma K_1^2} \right) dt, \end{aligned} \quad (21.17)$$

$$\frac{2}{\gamma + 1} r_s^2 \left(\dot{r}_s - \frac{1}{K_1^2 \dot{r}_s} \right) = 2 \int_0^t r_s \Delta p dt, \quad (21.18)$$

where $\Delta p = (p - p_\infty)/(\rho_\infty U^2)$, and K_1 is the similarity parameter defined as $M_\infty \tan \delta_C = U \sqrt{\rho_\infty/\gamma p_\infty}$. In general, the solution of these equations for arbitrary values of t can be obtained by numerical integration.

Let us consider the limiting case when $K_1 \rightarrow \infty$. It will be assumed that the time t is small, so that the initial energy of the gas in the perturbed region and the work of expansion of the piston will also be small compared with the energy released in the explosion. In this case, Eqs. (21.17) and (21.18) are simplified still further:

$$\frac{1}{2} \left(\frac{2}{\gamma + 1} \right)^2 r_s^2 \dot{r}_s^2 + \frac{r_s^2}{\gamma - 1} \Delta p = 1, \quad (21.17a)$$

$$\frac{2}{\gamma + 1} r_s^2 \dot{r}_s = 2 \int_0^t r_s \Delta p dt. \quad (21.18a)$$

Eliminating Δp from these equations results in a single equation:

$$\frac{1}{2} \left(\frac{2}{\gamma + 1} \right)^2 r_s^2 \dot{r}_s^2 + \frac{r_s}{\gamma - 1} \frac{d(r_s^2 \dot{r}_s)}{dt} = 1. \quad (21.19)$$

This equation has the solution

$$r_s = \left[\frac{4(\gamma + 1)^2(\gamma - 1)}{3\gamma - 1} \right]^{\frac{1}{4}} t^{\frac{1}{2}}, \quad (21.20)$$

from which the coordinates of the shock wave can be computed. The pressure can be found by substituting Eq. (21.20) into Eq. (21.17a):

$$\Delta p = \left[\frac{\gamma - 1}{4(3\gamma - 1)} \right]^{\frac{1}{2}} \frac{1}{t}. \quad (21.21)$$

Converting to dimensional parameters and using Eq. (21.1), we obtain the relations for the shape of the shock wave and the pressure distribution on the cone surface:

$$\frac{r_s}{D_N} = \kappa C_{DN}^{\frac{1}{4}} \left(\frac{x}{D_N} \right)^{\frac{1}{2}}, \quad (21.20a)$$

$$C_p = \frac{2(p - p_\infty)}{\rho_\infty V_\infty^2} = v \sqrt{C_{DN}} \left(\frac{D_N}{x} \right), \quad (21.21a)$$

in which the coefficients are

$$\kappa = \frac{1}{2} \left[\frac{8(\gamma + 1)^2(\gamma - 1)}{3\gamma - 1} \right]^{\frac{1}{4}}, \quad v = \left[\frac{\gamma - 1}{8(3\gamma - 1)} \right]^{\frac{1}{2}}.$$

It is apparent that Eqs. (21.20a) and (21.21a) differ from the corresponding relations for a cylindrical body only by the values of the coefficients κ and v , which are graphically presented in Fig. 220.

Equation (21.21a) can be used to determine some of the characteristics of the pressure variation on a blunt cone. According to this equation, the pressure coefficient has an infinitely large value at the

stagnation point, but decreases rapidly with distance from the nose, and at some distance the pressure is considerably less than that on a pointed cone. These trends are observed, for example, on a cone with a spherical nose. For comparison, assume that the pressure coefficient on a pointed cone is given by Newtonian theory as $C_p = 2\delta^2/c$, and the drag coefficient of the spherical nose is $C_{DN} = 1$. Assuming that $\nu = 0.125$ for $\gamma = 1.4$, we obtain

$$\frac{C_p}{C_{pc}} = \frac{0.0625}{\delta^2} \left(\frac{D_N}{x} \right).$$

If the cone angle is 0.1 radian, then $C_p/C_{pc} = 6.25(D_N/x)$, and the pressure on a blunt cone becomes less than on a pointed cone at a distance $x > 6.25D_N$ from the nose. This qualitative characteristic for the limiting case $K_1 = \infty$ is also maintained, as research shows, for finite values of the parameter K_1 , even for values of K_1 of the order of unity.

Equation (21.21a) is not valid along the entire surface of a cone and only applies for comparatively small values of x , corresponding to a small time t . Analytical research and experimental data show that at large values of t , i.e., at a considerable distance from the nose, both the pressure coefficient and the shock angle tend toward the values for a pointed cone.

The peculiarities noted in the pressure distribution are evident in Fig. 221, where the results of wind-tunnel tests⁽¹³⁾ at $M_\infty = 6.85$ are presented for a blunt, flat-nosed cone with $\delta_c = 10^\circ$. It can be noted that the minimum pressure is attained at a distance of approximately 10 bluntness diameters downstream, and the restoration of pressure to the value on a pointed cone occurs at a length 10 times greater.

The slope of the shock wave also varies according to the character noted for the pressure distribution. The shock-wave angle at the same experimental conditions is presented in Fig. 222, where it is evident that, at a length of approximately $20D_N$, the angle reaches a minimum and, at distances of approximately $50D_N$, the slope of the shock wave becomes the same as that on a pointed cone.

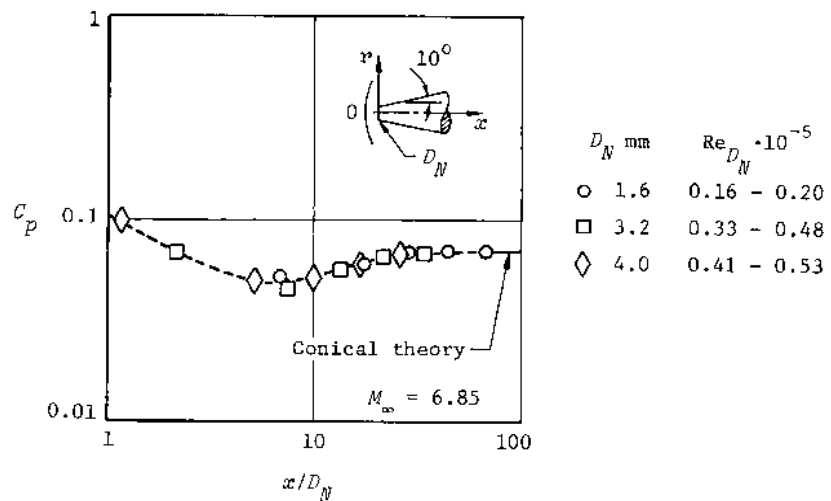


Fig. 221--Pressure distribution on a cone with a flat nose

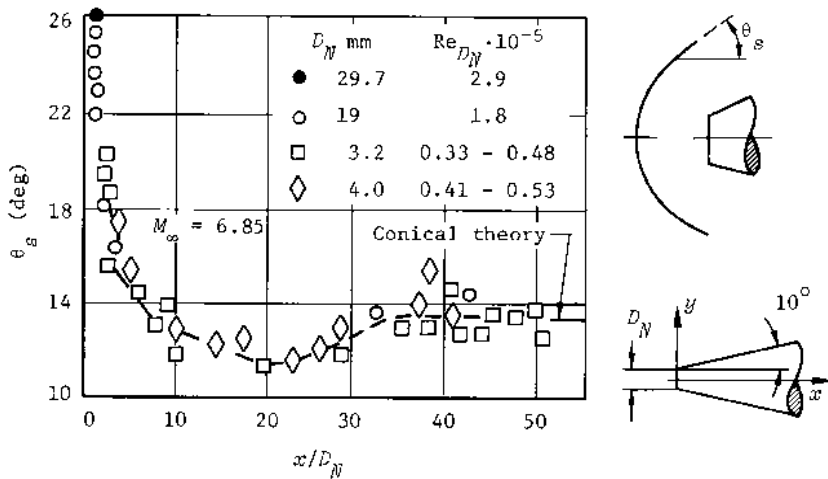


Fig. 222--Shock angle for a cone with a flat nose

The decreased pressure on a substantial part of the blunt cone can result in less drag than for a pointed cone. In Fig. 223, a graph is presented for the calculation of the drag of a blunt cone.⁽¹⁰⁾ It is evident from the graph that the drag becomes minimum at a certain cone length. The reason for the existence of a minimum drag can be visualized. As the length of the body is decreased from that for the minimum, the drag will increase because of the growing influence of the blunt nose. As the length is increased, the drag will approach that for a sharp cone. If the drag is less than the sharp cone value at some intermediate point, a minimum must exist.

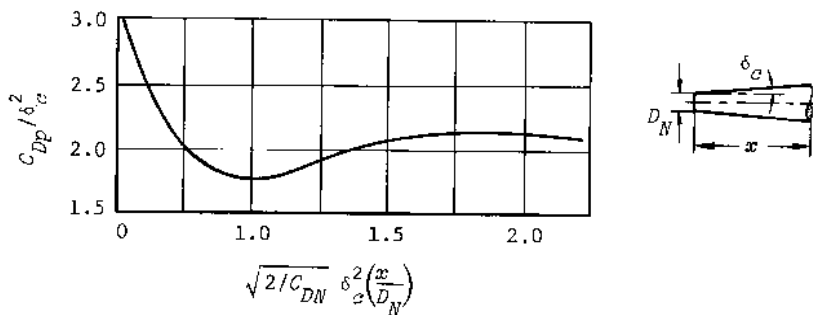


Fig. 223--Drag coefficient of a slender blunt cone

According to the data of Fig. 223, a minimum in the drag curve occurs at a relative cone length of

$$\frac{x}{D_N} = \frac{0.96}{\delta_c^2} \sqrt{C_{DN}/2}.$$

For example, for a cone with a spherical nose ($C_{DN} = 1$) and an angle $\delta_c = 0.1$, a minimum is located at $x/D_N = 68$, and the minimum drag is approximately 10 percent less than that for a pointed cone. When the cone is not extremely long, the drag of slightly blunt cones at hypersonic velocities is practically the same as for pointed cones.

The Similarity Law for Arbitrary Mach Numbers

The considerations presented above concerning the character of flow around blunt bodies can be used to develop the similarity law for the flow around blunt cones. The general relations for the flow around a blunt cylinder were derived by using the dimensionless parameters in Eq. (21.7). For a slender blunt cone it is necessary to include the cone angle δ_C in the set of parameters that define the motion. As in the case of flow around a pointed cone, this can be done by adding the similarity parameter $K_1 = M_\infty \delta_C$ to the number of dimensionless parameters on which the flow depends. These dimensionless parameters then determine the dimensionless characteristics of the flow.

From Newtonian theory, the order of magnitude of the excess pressure on the cone is $p - p_\infty \sim \rho_\infty V_\infty^2 \delta_C^2$, and the actual value of the excess pressure can be defined as $p - p_\infty = \rho_\infty V_\infty^2 \delta_C^2 \tilde{P}$, where \tilde{P} is a dimensionless characteristic parameter for pressure. Therefore, the pressure coefficient on the cone surface is given by the general relation

$$\frac{C_p}{\delta_C^2} = \frac{2(p - p_\infty)}{\rho_\infty V_\infty^2 \delta_C^2} = P(x_*, K_1, \gamma), \quad (21.22)$$

where the function P is equal to $2\tilde{P}$ and is a function of γ , K_1 , and a parameter

$$x_* = \frac{1}{M_\infty^2 \sqrt{C_{DN}}} \left(\frac{x}{R_N} \right) = \frac{1}{K_3} \left(\frac{x}{R_N} \right), \quad (21.23)$$

which can be considered as a dimensionless longitudinal coordinate. As previously noted, the longitudinal station must be at least one nose radius downstream of the end of the blunt tip. Henceforth, the coordinate x will be measured along the axis of the body from the base of the blunt tip for conical blunt bodies, so that it can be assumed that $x > R_N$.

In analogy to Eq. (21.8), the similarity law for the radial coordinate of the shock wave is

$$\frac{1}{M_\infty^2 \sqrt{C_{DN}}} \frac{1}{\delta_c} \frac{r_s}{D_N} = e(x_*, K_1, \gamma), \quad (21.24)$$

where the limits of validity of the similarity law can be extended by replacing δ_c by $\tan \delta_c$.

According to the similarity law for flow around slightly blunted cones having different values of δ_c and D_N , the dimensionless quantities in Eqs. (21.22) and (21.24) will be identical for equal relative coordinates x/D_N if the value of the following similarity parameters are maintained the same:

$$K_1 = M_\infty \tan \delta_c, \quad K_3 = M_\infty^2 \sqrt{C_{DN}}.$$

Thus, the parameter K_3 represents the specific characteristics of the flow around a blunt nose.

The similarity law can be extended to blunt bodies of arbitrary shape that are related by an affine transformation. In this case, instead of the angle δ_c , it is necessary to introduce another parameter representing the relative thickness of the body.

To obtain a more specific relation for the general forms given in Eqs. (21.22) and (21.24), experimental results for some particular conditions must be used. Data for the pressure distribution around cones with spherical noses and cone angles from 10° to 40° are presented in Fig. 224 for $\gamma = 1.4$ and $M_\infty = 6$. However, according to the similarity law, the five curves can be reduced to a single curve if selected new variables are introduced. The similarity law of Eq. (21.22) serves as a guide in selecting these variables. Of course, the equation obtained on the basis of experimental data may differ from its form in Eq. (21.22), since the theoretical form was based on a series of assumptions. Analysis of the experimental data shows that $K_1^{0.2} C_p / (\tan \delta_c)^{1.8}$ should be used for the pressure parameter, and the argument should be expressed as

$$\tilde{x} = \frac{K_1^{3/2}}{M_\infty^2 \sqrt{C_{DN}}} \left(\frac{x}{D_N} \right).$$

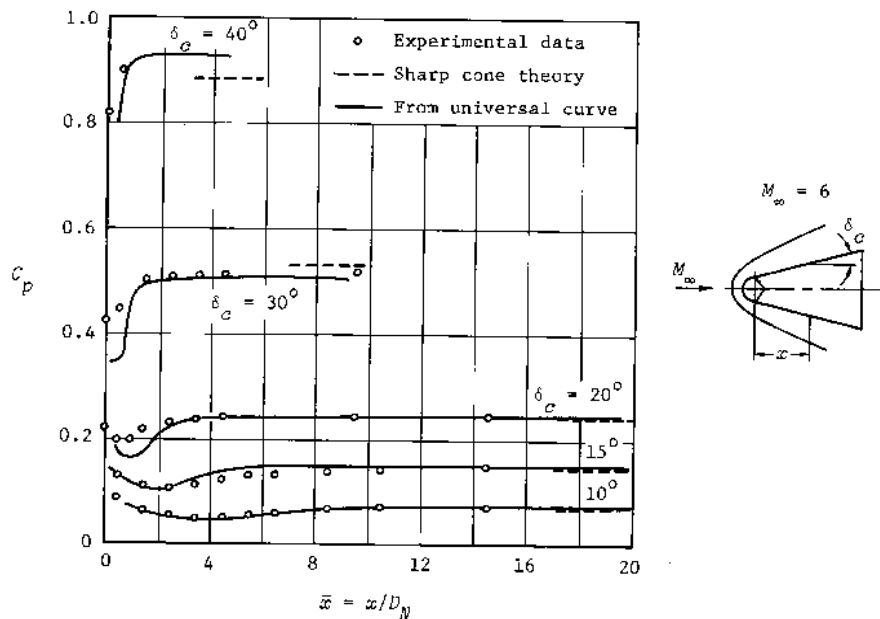


Fig. 224--Pressure distribution on a cone with a spherical nose

Thus, the expression for the similarity law is written in the form

$$\frac{K_1^{0.2} C_p}{(\tan \delta_c)^{1.8}} = P(\tilde{x}), \quad (21.25)$$

where \tilde{x} can be treated as a conditional relative coordinate. It is evident that this expression differs significantly from the general relation given by Eq. (21.22).

In the special case under consideration, $C_{DN} = 0.91$ for $M_\infty = 6$ (see Fig. 207) and $M_\infty^2 \sqrt{C_{DN}} = 34.4$. Thus,

$$\frac{K_1^{0.2} C_p}{(\tan \delta_c)^{1.8}} = P(\tilde{x}) = P\left(\frac{K_1^{1.3}}{34.4} \frac{x}{D_N}\right). \quad (21.26)$$

The average universal curve, constructed on the basis of this relation and using the experimental data presented in Fig. 224, is shown in Fig. 225. According to the similarity law, this curve can be used for the calculation of pressure, not only on the surface of a spherically blunted cone, but also for blunting in the form of a flat face. In the latter case, the correct value of the nose drag coefficient should be chosen.

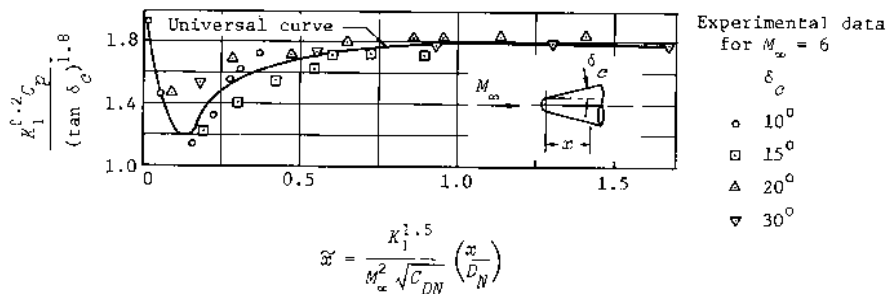


Fig. 225--Universal curve for the pressure distribution on blunt cones

Pressures on cones with different blunting can be compared by using this curve. For example, let us consider the same case of a 10° cone at a free-stream Mach number of 6. Since $C_{DN} = 0.91$ for the spherical nose and $C_{DN} = 1.7$ for the flat face, the corresponding values of $K_1^{1.5}/M_\infty \sqrt{C_{DN}}$ are 0.0317 and 0.0232. For a station on the body with the relative coordinate $\bar{x} = x/D_N = 10$, the conditional coordinate $\bar{x} = 0.317$ and 0.232. Then from the curve in Fig. 225, the values of $K_1^{0.2} C_p / (\tan \delta_c)^{1.8}$ are 1.55 and 1.40. Since $K_1^{0.2} / (\tan \delta_c)^{1.8} = 23$, the pressure coefficients will be 0.0675 and 0.0608, respectively. From this example, it is evident that the pressure at corresponding points on a blunt cone with a flat nose is somewhat less than on a cone with a spherical nose.

Results are presented in Figs. 224 and 226 for the theoretical calculation of the pressure coefficient using the universal curve for cones with spherical noses and flat noses. The experimental data are also plotted for comparison. The data presented in these graphs pertain to cones at a fixed Mach number with different cone angles. The effect of

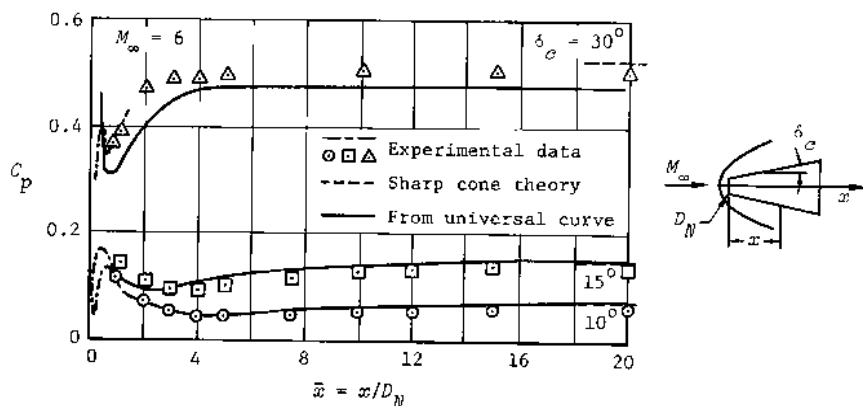


Fig. 226--Pressure distribution on a cone with a flat nose

Mach number on the pressure distribution around a specific cone is shown in Fig. 227. It is apparent that the larger the velocity, the more significant is the region of reduced pressures compared with the pointed cone. This indicates a basic advantage in the use of blunt bodies at very high Mach numbers: The decrease in local density associated with the reduction in pressure contributes to a large decrease in heat flux. In addition, the decrease in pressure aids in reducing the drag.

The similarity law derived above relates to cones with blunt noses of arbitrary shape. However, it is not valid for the entire surface of the body; for example, in the vicinity of the nose the results deviate considerably from the experimental data. Nevertheless, in the vicinity of a spherical nose the similarity law and, in particular, the universal curve, correctly specify the general character of the pressure change, according to which the pressure decreases gradually beginning at the stagnation point of the nose, reaches a minimum at some point downstream, and increases again to approach the value for a pointed cone.

On the other hand, a more complex phenomenon, which cannot be represented by the similarity law, is observed in flow around a cone in the vicinity of a flat face. Observations show that flow separation occurs directly behind the corner, and as a consequence a stagnant region develops (Fig. 228). The supersonic flow is diverted around this zone

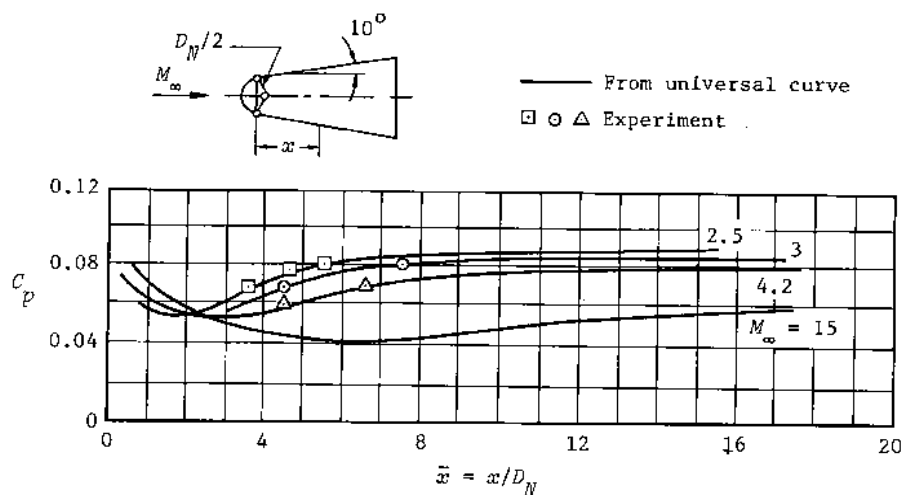


Fig. 227--Pressure distribution on a cone with a spherical nose

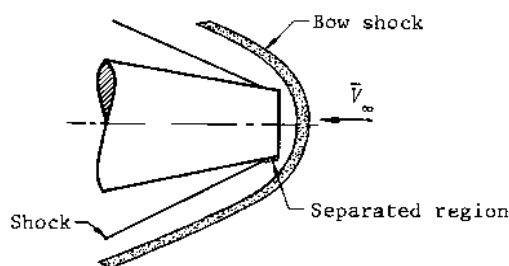


Fig. 228--Flow around a cone with a flat nose

and eventually reattaches itself to the surface. The deflection is accompanied by the development of a local shock wave. This illustrates one of the peculiar features of flow around a body with a flat nose.

It is natural that such a peculiarity leads to a change in the character of the pressure distribution in comparison with that on a spherical nose (see Fig. 226). The pressure decrease due to the expansion of flow directly behind the corner changes to a rapid increase, as the flow

passes through the local shock wave. After achieving some maximum, the pressure begins to decrease again. From this point on, the pressure variation is of the same character as that on a cone with a spherical nose. Thus, with the exception of a small region in the vicinity of the nose, the pressure distributions for both forms of blunting are similar, which permits the use of only one similarity law.

For convenience in practice, the similarity law can be applied arbitrarily to the region indicated, since this region is comparatively small for a sufficiently long body and the effect on the total pressure drag is very small.

The total pressure drag is calculated as the sum of the nose drag and the drag of the remainder of the body, i.e.,

$$D = \frac{1}{2} \rho_\infty \gamma^2 \pi R_N^2 C_{DN} + 2\pi \int_{r_N}^{r_{mid}} (p - p_\infty) r dr, \quad (21.27)$$

where C_{DN} is the nose drag coefficient calculated from Eq. (20.36). From this equation, the drag is calculated for the portion of the sphere extending to a central angle of $\varphi = \arcsin(r_N/R_N)$, which in turn can be determined by the radial coordinate to the junction of the spherical nose and the aft part of the body. Thus, the total drag coefficient is

$$C_D = C_{DN} \bar{R}_N^2 + 2 \int_{\bar{r}_N}^1 C_p \bar{r} d\bar{r}, \quad (21.28)$$

where $\bar{R}_N = R_N/r_{mid}$, $\bar{r} = r/r_{mid}$, and $\bar{r}_N = r_N/r_{mid}$. Introducing into Eq. (21.28) the expression for C_p obtained from Eq. (21.26) and substituting

$$\bar{r} = \bar{r}_N(1 + 2\bar{x} \tan \delta_c),$$

where $\bar{x} = x/D_N$, we obtain

$$C_D = C_{DN} \bar{R}_N^2 + 4\bar{r}_N^2 \frac{(\tan \delta_c)^{2.8}}{K_1^{0.2}} \frac{M_\infty^2 \sqrt{C_{DN}}}{K_1^{1.5}} \left(\int_0^{\bar{x}} P d\bar{x} + \frac{M_\infty^2 \sqrt{C_{DN}}}{K_1^{1.5}} \tan \delta_c \int_0^{\bar{x}} P d\bar{x}^2 \right). \quad (21.29)$$

In the case of a spherical nose, the coordinate \tilde{x} is calculated from the length x measured from its junction point with the cone. In this same case, the dimensionless radius $\tilde{r}_N = \bar{R}_N \cos \delta_c$, but for a flat nose it should be assumed that $\tilde{R}_N = \tilde{r}_N$. The integrals

$$\int_0^{\tilde{x}} P \, d\tilde{x}, \quad \int_0^{\tilde{x}^2} P \, d\tilde{x}^2,$$

which enter into Eq. (21.29), can be computed graphically from the universal curve of Fig. 225. The drag coefficients given by Eq. (21.29) for the special case of a cone with an angle $\delta_c = 10^\circ$ and $M_\infty = 6$ are presented in Fig. 229. The experimental data are also plotted for comparison.

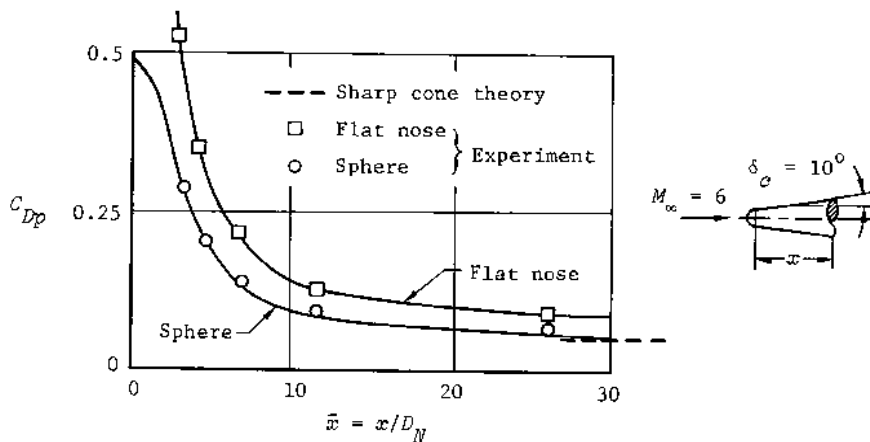


Fig. 229—Pressure drag coefficient of blunt cones

An analysis of the experimental results indicates the difference in the pressure variation for flow around slender and thick blunt bodies (see Figs. 224 and 226). In the case of slender bodies, the pressure on the cone section is considerably less than that on a pointed cone and it recovers comparatively slowly to the pressure on the pointed cone as the distance from the nose increases. However, for flow around a thick cone, the difference in pressure is sharply reduced, and the recovery process is practically completed close to the blunted portion.

This is quite evident in Fig. 224, for example, where experimental data are presented for $M_\infty = 6$ around a 40° cone with a spherical nose. At a distance somewhat larger than the blunting diameter from the stagnation point, the pressure on the conical section almost equals its value on a pointed cone. This indicates the practical possibility of estimating the pressure on the conical part of the body from the theory of flow around a pointed cone.

It is evident from the data presented in Fig. 230 that modified Newtonian theory ($C_p = C_{p0} \cos^2\varphi$) gives a good approximation to the experimental data both on the spherical nose and on the small conical portion in its vicinity.⁽¹⁴⁾

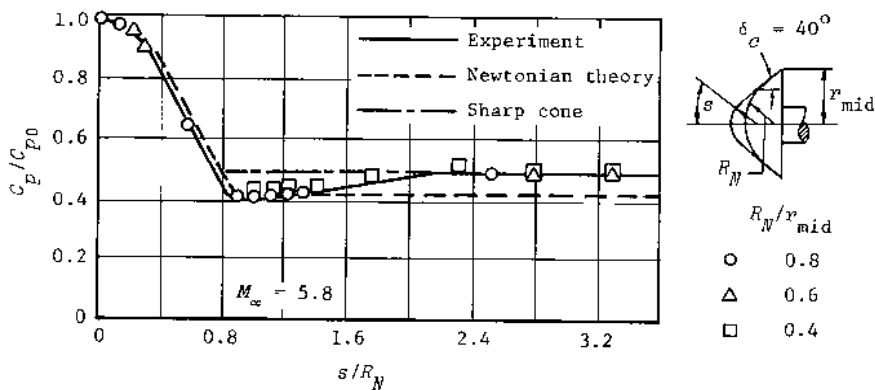


Fig. 230--Pressure distribution on a blunt cone with a spherical nose

§ 22. APPLICATION OF THE METHOD OF CHARACTERISTICS TO THE CALCULATION
OF FLOW AROUND BLUNT BODIES OF REVOLUTION

THE CHARACTERISTICS EQUATIONS

THE THEORETICAL METHODS discussed above are applicable to the study of hypersonic flow around blunt bodies, but in practical cases it is also necessary to calculate the flow in the supersonic region downstream of the blunt nose. The method of characteristics can be used in this region, provided that the equations include the effects of the vorticity created by the curved shock wave in front of the body.

Therefore, Eqs. (9.9) and (9.10) are the basic equations for the conjugate characteristics of the supersonic rotational flow. In principle, for given boundary conditions, it is possible to calculate the flow parameters numerically and step-by-step in the region between the body surface and the shock wave. However, the method of characteristics has been extremely difficult to apply to practical computations, and because of the great expenditure of time for calculations, it had not been used widely in practice until recently. With the advent of electronic computers, this is no longer a problem. It has been shown, however, that the use of computers for solving the universally accepted equations (Eqs. (9.9) and (9.10)) for the characteristics was ineffective. These equations were not adapted to machine calculation, since a whole series of functions (e.g., exponential and trigonometric) entered into them and these required an additional expenditure of machine time in their computation. In addition, the programming was complicated. Thus, it became necessary to modify the basic equations and adapt them to effective machine calculation. P. T. Chushkin⁽¹⁵⁾ accomplished this work and also carried out machine calculations for supersonic flow around a series of conical bodies with spherical noses.

To modify Eqs. (9.9) and (9.10), it is advantageous first to convert them to the new variables

$$\beta = \cot \mu = \sqrt{M^2 - 1}, \quad \xi = \tan \delta, \quad S = \log \left(\frac{\tilde{p}}{\tilde{\rho}} \right),$$

where

$$\tilde{\rho} = \frac{\rho}{\rho_\infty}, \quad \tilde{p} = \frac{p}{\rho_\infty \alpha^2}.$$

Then Eqs. (9.9) and (9.10) for the conjugate characteristics in the physical plane and the hodograph plane are written as

First family:

$$\frac{dx}{dr} = \frac{\beta - \xi}{\beta \xi + 1} \equiv m, \quad (22.1)$$

$$d\xi + K d\beta + L dr - P dS = 0; \quad (22.2)$$

Second family:

$$\frac{dr}{dx} = \frac{\beta \xi - 1}{\beta + \xi} \equiv n, \quad (22.3)$$

$$d\xi - K d\beta - N dx + P dS = 0, \quad (22.4)$$

where

$$K = - \frac{2\beta^2(\xi^2 + 1)}{(\gamma + 1)(\beta^2 + 1)(\xi\beta^2 + 1)}, \quad L = \frac{\xi(\xi^2 + 1)}{r(\beta\xi + 1)},$$

$$N = \frac{\xi(\xi^2 + 1)}{r(\beta + \xi)}, \quad P = \frac{\beta(\xi^2 + 1)}{\gamma(\gamma - 1)(\beta^2 + 1)},$$

and $\epsilon = (\gamma - 1)/(\gamma + 1)$.

It is convenient in the calculation of the entropy term to express

it by the stream function Ψ , at the same time rewriting Eq. (3.25) and the entropy relation in terms of the new variables β and ξ . In addition, it is useful to replace Ψ by a modified stream function ψ , defined by

$$d\psi = (\gamma e^S)^{1/(\gamma-1)} d\Psi.$$

If the differential $d\Psi$ is written in the form

$$d\Psi = \psi_x dx + \psi_r dr,$$

and Eq. (3.25) is substituted for the partial derivatives ψ_x and ψ_r , the equation for the modified stream function in terms of the variables β and ξ is

$$\frac{d\psi}{dx} = - \frac{r \sqrt{(\beta^2 + 1)(\xi^2 + 1)}}{(\beta + \xi)(\epsilon\beta^2 + 1)^{1/2}} \equiv q. \quad (22.5)$$

Since isentropic flow is considered, both ψ and the entropy are constant on a given streamline, so that the relation between ψ and S obtained from the conditions behind the shock wave can be used.

The system consisting of Eqs. (22.1) through (22.5) and the equation relating S and ψ can be solved numerically. Each of the equations is represented, as already noted, in a finite-difference form, and the equations can then be solved by the method of successive approximations.

The solution of the two basic cases illustrated in Fig. 80 is the same as for the ordinary method of characteristics described in Chap. III. The third problem, concerned with the computation of the point H on the shock wave (see Fig. 82), can be solved in the following manner. At point H , the location of which is as yet unknown, an arbitrary value of the shock wave angle θ_{SH} is selected, somewhat less than at the adjacent point F . Then from the relations behind the shock wave, the following values can be determined:

$$\bar{\rho}_H = \frac{\bar{\rho}_0 \tan^2 \theta_{SH}}{1 - \epsilon \bar{\rho}_0 + \tan^2 \theta_{SH}}, \quad \bar{\epsilon}_0 = \frac{(\gamma + 1)M_\infty^2}{2 + (\gamma - 1)M_\infty^2},$$

$$\beta_H^2 = \frac{\bar{v}_0 (\tan^2 \theta_{SH} + \bar{v}_H^2) - \bar{v}_H^2 (1 + \tan^2 \theta_{SH})}{\bar{v}_H^2 (1 + \tan^2 \theta_{SH}) - \bar{v}_0 (\tan^2 \theta_{SH} + \bar{v}_H^2)},$$

$$\epsilon_H = \frac{(\bar{v}_H - 1) \tan \theta_{SH}}{\tan^2 \theta_{SH} + \bar{v}_H},$$

$$S = \log \left\{ \frac{1}{\bar{v}_H^\gamma} \left[\frac{2}{\gamma + 1} \frac{\bar{v}_0 \tan^2 \theta_{SH}}{1 + \tan^2 \theta_{SH}} - \frac{\gamma - 1}{2\gamma} (1 - c\bar{v}_0) \right] \right\}.$$

The coordinates x_H and r_H are found from an iterative solution of the equation for the first family of characteristics, in the form $\Delta x = m\Delta r$, and a parabolic equation representing the shock segment FH . The approximation is completed when the equation for the first-family characteristic is satisfied:

$$\epsilon_H - \epsilon_N + K_N (\beta_H - \beta_N) + L_N (r_H - r_N) - P_N (S_H - S_N) = 0.$$

The modified stream function at point H is

$$\psi_H = \psi_F + \gamma^{1/(\gamma-1)} \frac{\bar{v}_0^{\frac{1}{2}}}{4} \left(\exp \frac{S_F}{\gamma - 1} + \exp \frac{S_H}{\gamma - 1} \right) (r_H^2 - r_F^2).$$

BOUNDARY CONDITIONS

It is necessary to know the flow parameters on an initial curve to determine all the parameters in the flow field in the region between this curve, the surface of the body, and the shock wave. The shock shape is gradually constructed during the solution. For a body with a spherical nose, the initial data may be known along the normal to the spherical surface (AB) located in a completely supersonic region close to the sonic line CD (Fig. 231). These data can be determined by various methods; one of the most accurate is the method of integral relations described earlier.

An approximate method can also be used, in which a shock wave is

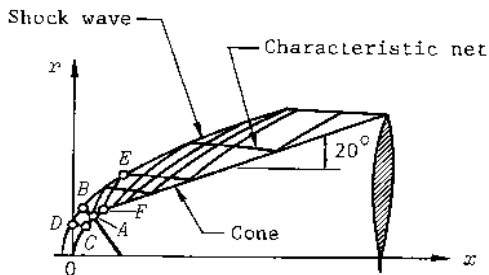


Fig. 231--Characteristics net for a blunt cone

constructed around the spherical nose with the equation $r^2 = 2R_{ss}(x + s_0)$. Then, close to the sonic point on the sphere, an arbitrary point A is selected through which passes a normal to the surface, AB (Fig. 232). The distribution of a parameter along the normal can be approximated by the polynomial

$$\Pi = \sum_{n=0}^N a_n \bar{y}^n, \quad (22.6)$$

in which $\bar{y} = y/s$, and s is the thickness of the shock layer at the section in question. The independent variable \bar{y} varies from zero at the wall to unity at the shock wave.

At sufficiently high velocities and, therefore, small shock-layer thicknesses, the polynomial can be limited to three terms, i.e., a quadratic relation

$$\Pi = a_0 + a_1 \bar{y} + a_2 \bar{y}^2. \quad (22.6a)$$

The coefficient a_0 is determined from the wall condition at $\bar{y} = 0$, where the parameters at the wall can be calculated approximately from modified Newtonian theory or found experimentally. The two other coefficients can be determined from the shock-wave conditions at $\bar{y} = 1$ and the known value of the derivative $\partial\Pi/\partial\bar{y}$ at point B ($\bar{y} = 1$) or A ($\bar{y} = 0$). This derivative enables us to find the coefficient $a_1 = (\partial\Pi/\partial\bar{y})_{\bar{y}=0}$.

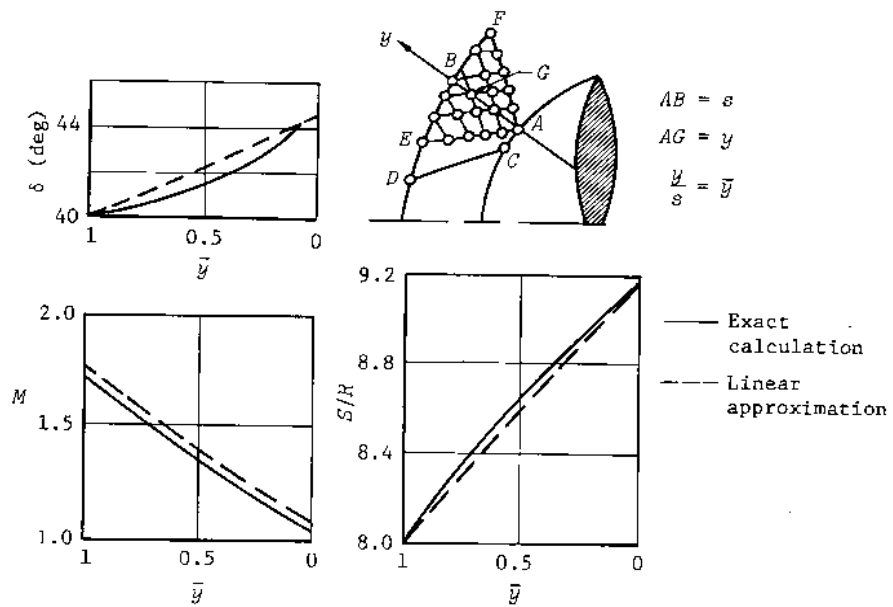


Fig. 232--Distribution of flow parameters across the shock layer

Results of the calculation of the distribution of some of the parameters are shown in Fig. 232, e.g., the Mach number, flow angle, and the dimensionless entropy S/R . It is evident that these results are close to those obtained from the parabolic relations given by Eq. (22.6a).

If the velocity of the incident flow is very large, the shock layer is very thin and the distribution is almost linear, so that it can be assumed that $a_2 = 0$ in Eq. (22.6a). In this case, the coefficient a_1 is equal to the value of the parameter in question at point B on the shock wave.[†] In Fig. 232, where data are presented for $M_\infty = 20$, it is evident that the parameters actually do approach a linear variation:

$$R = a_0 + a_1 \bar{y}.$$

[†]Editor's note: The coefficient a_1 is actually equal to the difference between the values behind the shock and on the surface.

The method of characteristics can be used directly to determine the initial data along a normal by choosing a row of points along an arbitrary arc, EF , of the given shock wave (Fig. 232). Since the parameters are known at each of these points, the equations for the characteristics can be solved to determine the grid in this region. The flow parameters at the junctions of the grid are then known in the region between the arc EF and the conjugate characteristics EA and FA , and the parameters can be found along the normal AB . The results presented in Fig. 232 were obtained in this way.

METHOD OF COMPUTATION AND SOME RESULTS

When a row of points has been determined along the selected normal, and at each of these points the flow parameters are known, the finite-difference form of the characteristics equations can be used to compute the parameters at the points of the first row close to the normal. The upper point of this row is located at the intersection of a first-family characteristic with the shock-wave surface, and the lower point lies at the intersection of the second-family characteristic with the body surface. All the remaining points lie at the intersection of the conjugate characteristics issuing from the adjacent points on the normal. The coordinates and parameters at the points of the following row are found in a similar way. Calculations on an electronic computer were produced by the method described for flow around a series of cones with spherical noses and different velocities. The cone angles were $\delta_c = 0^\circ, 20^\circ, 30^\circ, 40^\circ$, and the Mach numbers were $M_\infty = 3, 4, 6, 10$, and ∞ . The normal segment AB was divided into 48 spaces. Figure 231 shows a flow diagram around a blunt cone with a cone angle of 20° at $M_\infty = 6$ and gives some idea of the shape of the shock wave and of the characteristics network.

The calculation by the method of characteristics, accompanied by the construction of a network of characteristics, enables us not only to obtain the quantitative results but also to explain some phenomena observed in experiments. Among these is the frequent appearance of a second shock between a spherically blunted body and the bow shock wave. Shadowgraphs show that this discontinuity is, as it were, suspended above the surface, which is also indicated by the calculations, since

characteristics of the same family, issuing from points on the surface located close to one another, intersect at the place where the discontinuity originates. The surface points lie in the vicinity of the junction between the nose cap and the body.

This discontinuity is caused by the appreciable compression of the supersonic flow as it passes from a curved to a straight surface. Thus, the accumulation of the perturbations results in the development of a local "hanging" shock, which is apparent in the shadowgraphs.

In Fig. 231, the first-family characteristic issuing from the junction point of the sphere and the cone is EF , which is a boundary for that part of the flow directly affected by the flow around the spherical nose. Behind this part of the flow, there begins a region resulting from not only the influence of the sphere but also the basic part of the body. Thus, in many ways, the characteristic EF is analogous to the characteristic KS in Fig. 82, which separated the conical flow from that around a curved surface.

The pressure distribution on a 20° spherically blunt cone was computed on an electronic computer by the method of characteristics for three Mach numbers and the results are given in Fig. 233. The pressure

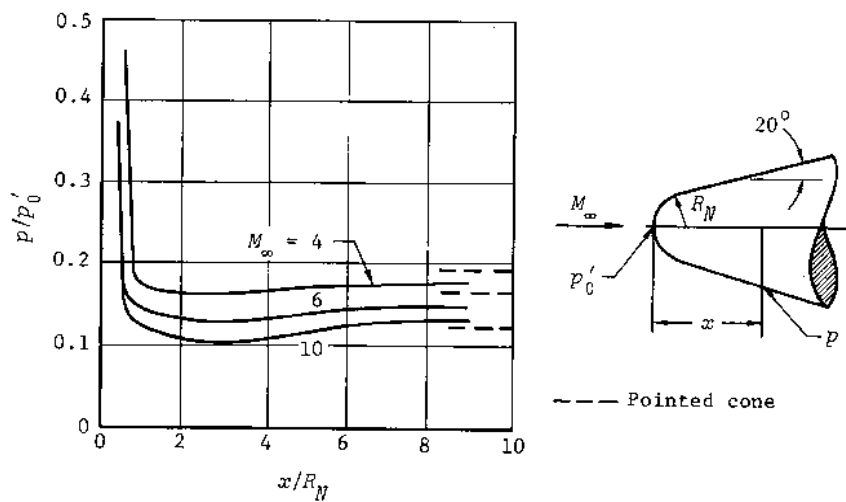


Fig. 233--Pressure distribution on a blunt cone

on a pointed cone is indicated by the dashed line for comparison. It is evident that blunting decreases the pressure over part of the cone, and the relative magnitude of the reduction increases with Mach number.

For low velocities, the flow around the conical part of the body differs little from flow over a pointed cone. This indicates the possibility of calculating the drag of a blunt cone by using the sum of the drag of the blunt nose and the remainder of the cone, on which the pressure is assumed to be equal to that on a pointed cone.

The same conclusion can also be reached in the case of a thick blunt body, for which the pressure distribution differs little at any velocity from the corresponding distribution on a pointed body, if we exclude the small area of the conical surface immediately behind the nose where the pressure changes considerably.

§ 23. EFFECT OF ANGLE OF ATTACK

STUDIES OF THE FLOW around blunt cones at angle of attack show that the basic characteristics of the pressure variation along different meridian planes are the same as those for zero angle of attack. This is evident, for example, from the experimental results⁽¹⁴⁾ for a cone with a spherical nose at $M_\infty = 5.8$ and angles of attack of 4° and 8° (Fig. 234). On the upper and lower meridians of the cone, the pressure gradually decreases from the stagnation point, reaching a minimum at some distance from the nose. After this it increases to a value close to that which occurs in flow around a pointed cone.

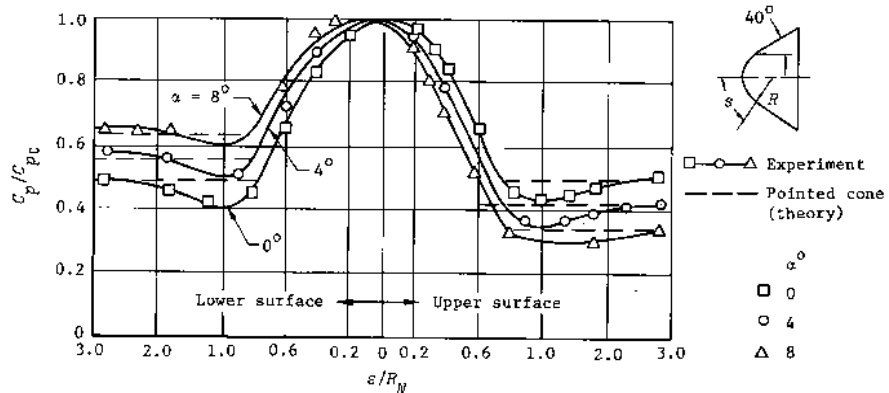


Fig. 234--Pressure distribution for asymmetric flow around a cone with a spherical nose

It is worth noting that the coordinates of the minimum in the pressure for small angles of attack are approximately identical with those for symmetric flow. This permits us to assume that the similarity law for the symmetric case can be used as the basis for the study of asymmetric flow.

Two universal curves have been constructed from the experimental data for blunt cones at $\alpha = 4^\circ$ for two values of the meridian angle, $\phi = 0$ and π (Fig. 235). Approximate equations can be written for these curves in the form⁺

$$P = P_{\alpha=0} - \alpha B \cos \phi + \alpha^2 (C \cos 2\phi + D) + \dots \quad (23.1)$$

Since the coefficients B , C , and D are independent of the angle of attack, known results of measurements or the calculations of the pressure distribution along three arbitrary meridians at a given angle of attack can be used for their determination. Equation (23.1) is simplified if it is applied only to meridian angles of zero, $\pi/2$, and π , since the coefficient D can be neglected compared with C for these cases. The coefficients B and C have been calculated from the experimental data shown in Fig. 235 by solving Eq. (23.1) for the meridians $\phi = 0$ and $\phi = \pi$ and assuming that $D = 0$.

Equation (23.1) can be used as an approximation for asymmetric flow, but it should be noted that the pressure distribution for flow around blunt cones at high velocities is quite sensitive even to small angles of attack. For a 10° blunt cone, an angle of attack of 0.5° results in a pressure change of 15 percent, compared with 10 percent for a pointed cone. The angle of attack of 4° used above is large enough to obtain reliable values of the coefficients from Eq. (23.1), although some improvement in the results is attained by retaining the other nonlinear term in the equation. The coefficients B and C are presented in Fig. 236, and these values can be used for preliminary estimates of the pressure. However, it is advisable to refine the coefficients when additional accurate experimental or theoretical data are available.

⁺Editor's note: The parameter P is as defined in Eq. (21.25). It is plotted versus \tilde{x} in Fig. 235, where \tilde{x} is defined in connection with Eq. (21.25). $P_{\alpha=0}$ is presented in Fig. 225.

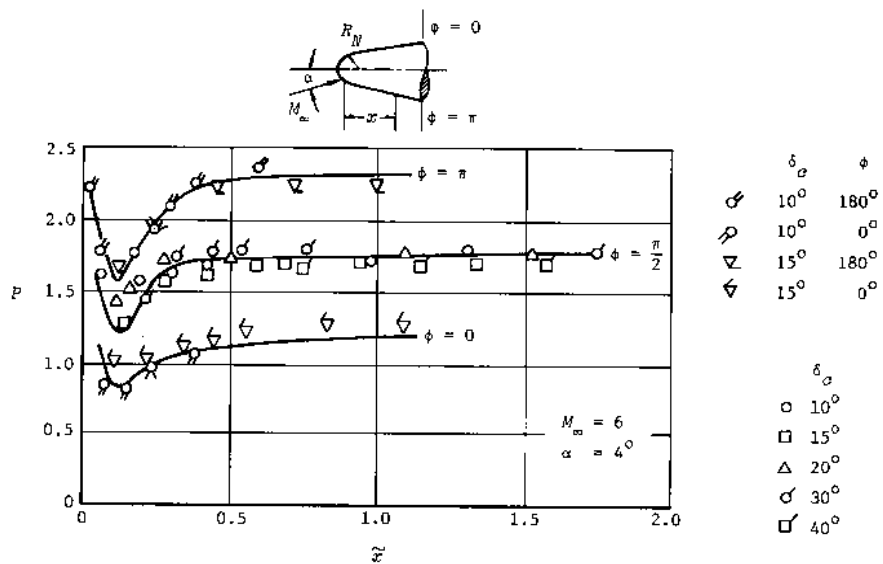


Fig. 235--Universal curves for the pressure distribution at angle of attack on blunt cones with spherical noses

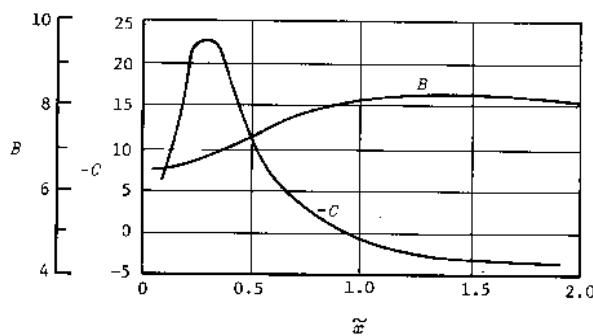


Fig. 236--Coefficients for calculating the pressure distribution at angle of attack

The accuracy of the results is increased as the angle of attack approaches zero. For very small values of α , only the second term in Eq. (23.1) is necessary, resulting in

$$P = P_{\alpha=0} - \alpha B \cos \phi. \quad (23.2)$$

This equation together with the data in Fig. 236 for B makes it possible to estimate very simply, for example, the location of the center of pressure. It will be assumed that the pressure distribution on the blunt tip in asymmetric flow does not have much influence on the change in the location of the center of pressure. Thus, the coordinate x will be measured from the beginning of the conical part of the body. Equations (1.12) and (1.19) are used for the normal force and moment coefficients, and Eq. (1.22) for the center of pressure. Making the following substitutions

$$r = r_N + x \tan \delta_c,$$

$$C_p = \frac{(\tan \delta_c)^{1.8}}{K_1^{0.2}} P(\tilde{x}),$$

we obtain for the center-of-pressure coefficient

$$\bar{x}_{cp} = \frac{3F_1 N^2 \tan \delta_c + 6F_2 N(1 + \tan^2 \delta_c) + 4F_3 \tan \delta_c (2 + \tan^2 \delta_c)}{12(F_1 N + F_2 \tan \delta_c) \tilde{x}}, \quad (23.3)$$

where

$$N = \frac{K_1^{1.5}}{M_\infty^2 \sqrt{C_{DN}}}, \quad (23.4)$$

$$F_1 = \int_0^{\tilde{x}} B d\tilde{x}, \quad F_2 = \int_0^{\tilde{x}^2} B d\tilde{x}^2, \quad F_3 = \int_0^{\tilde{x}^3} B d\tilde{x}^3. \quad (23.5)$$

The integrals of Eq. (23.5) can be determined numerically or graphically from the data of Fig. 236.[†]

For small cone angles ($\tan \delta_c \ll 1$), Eq. (23.3) is simplified:

$$\bar{x}_{cp} = \frac{3F_2^2 N + 4F_3 \delta_c}{6(F_i N + F_2 \delta_c)} \bar{x} \quad (23.3a)$$

The calculated variation of the center-of-pressure coefficient with length for blunted cones is compared with experiment in Fig. 237.

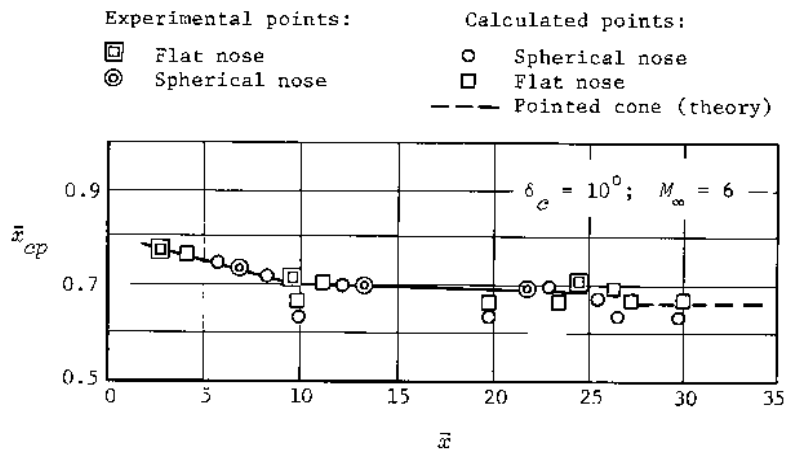


Fig. 237--Center of pressure of a blunt cone

The center of pressure of a blunt nose at hypersonic speeds can be determined from Newtonian theory, still retaining the assumption that the blunt tip exerts a negligibly small influence. Then the nose length l_N will be measured from the base of the blunt tip. If the radius of the initial cross section at this point is designated by r_N , the expressions for the normal force and moment coefficients of the blunt nose, corresponding to Eqs. (18.31b) and (18.45b), will be

[†]Editor's note: The definition of \tilde{x} in the above equations is that given with Eq. (21.25), i.e., $\tilde{x} = Nx/D_N$. It must not be confused with that used in Eqs. (1.12) and (1.19), where \tilde{x} is defined as x/l .

$$C_{NP} = \alpha \tilde{p}(\gamma) \left(1 - \frac{r_N^2}{r_{mid}^2} \right),$$

$$C_{mp} = \alpha \tilde{p}(\gamma) \left(1 - \frac{W_N}{l_N S_{mid}} \right). \quad (23.6)$$

The relation for the center of pressure becomes

$$\bar{x}_{cp} = \frac{1 - W_N/l_N S_{mid}}{1 - r_N^2/r_{mid}^2}. \quad (23.7)$$

This equation applies not only to a thin slender conical nose but also to a slender body of arbitrary shape. For a thick body, the general expression, Eq. (1.23), must be used for \bar{x}_{cp} .

§ 24. FLOW AROUND BLUNT BODIES OF CURVED SHAPETHE GENERAL SOLUTION

THE PROBLEM OF FLOW around certain blunt bodies with curved profiles, such as those defined in the form of a power law (Eq. 1.41), can be solved theoretically. The solution can be obtained by using the law of plane sections, the equation for which results from the analogy with the unsteady motion of a gas around a cylindrical piston. The general form of this one-dimensional motion is described by Eqs. (21.2a) and (21.3a). The solution of the equations can be found by expanding the required function into a power series in $\epsilon = (\gamma - 1)/(\gamma + 1)$, as shown by Chernyi.⁽¹⁰⁾ For an explanation of this method, let us return to the equations that determine the gas parameters behind the shock wave.

As was shown in §4, these relations, particularly Eq. (4.12) for pressure, express the required parameters in terms of the density ratio ρ_1/ρ_2 . With an increase in velocity the density ratio decreases, and in the limiting case as $M_\infty \rightarrow \infty$, the value of $\rho_1/\rho_2 = \epsilon$ for constant specific heats.

If the physical-chemical changes behind the shock wave are taken into account, the value of ρ_1/ρ_2 will be even less. Thus, a layer of compressed gas develops between the shock wave and the body in which the perturbed parameters will be of the same order of magnitude as those immediately behind the shock; i.e., the density ratio in the free stream is the determining parameter. The larger the velocity, the stronger the shock and the thinner the layer in which the compression occurs.

This perturbed region of gas behind the shock can be examined as a type of boundary layer, in which basic changes occur in the pressure of the gas. In the special case of infinitely large compression in this layer, i.e., $\rho_1/\rho_2 = 0$, the excess gas pressure behind the wave

is $p_2 - p_1 = \rho_\infty V_\infty^2 \sin^2\delta$, and agrees with the value obtained from Newtonian theory. The thickness of the layer becomes infinitesimally small. In reality, the pressure differs from this limiting case, and the criterion of the difference is the parameter ρ_1/ρ_2 . Therefore, it is possible to seek the solution of the problem of gas flow in the thin layer near the shock in the form of a power series in the parameter ρ_1/ρ_2 . The value of the small parameter can be assumed to be $\rho_1/\rho_2 = \epsilon$ for an ideal gas with constant specific heats. Incidentally, it can be seen from the equations of §4 that the gas parameters behind the shock wave are completely defined by the parameter ϵ .

The solutions to Eqs. (21.2a), (21.3a), and (21.4) can be obtained by using the expansions[†]

$$r = r_0 + \epsilon r_1 + \dots,$$

$$p = p_0 + \epsilon p_1 + \dots, \quad (24.1)$$

$$\rho = \frac{\rho_0}{\epsilon} + \rho_1 + \dots,$$

Using these series and designating $\partial r_0/\partial t = \dot{r}_0$ and $\partial^2 r_0/\partial t^2 = \ddot{r}_0$, we obtain a new set of equations:

$$\frac{\partial r_0}{\partial m} = 0, \quad \ddot{r}_0 = -r_0 \frac{\partial p_0}{\partial m}, \quad \frac{\partial}{\partial t} \left(\frac{p_0}{\rho_0^\gamma} \right) = 0, \quad (24.2)$$

which determine the form of the functions r_0 , p_0 , and ρ_0 . Integrating the equations, we get

$$r_0 = r_0(t), \quad p_0 = P(t) - \frac{\ddot{r}_0}{r_0} m, \quad p_0^{1/\gamma} = \zeta_0(m) \rho_0, \quad (24.3)$$

where $r_0(t)$, $P(t)$, and $\zeta_0(m)$ are arbitrary functions. From these results, we obtain another set of equations that r_1 , p_1 , and ρ_1 must satisfy:

[†]Editor's note: It should be noted that the r_1 used here is simply the second coefficient in the expansion, whereas r_1 denotes the initial condition for r in §21.

$$\frac{\partial r_1}{\partial m} = \frac{1}{r_0^2 r_0}, \quad r_0 \frac{\partial p_1}{\partial m} = \frac{\ddot{r}_0}{r_0} r_1 - \frac{\partial^2 r_1}{\partial t^2}, \quad \frac{\partial}{\partial t} \left(\frac{p_1}{p_0} - \gamma \frac{p_1}{r_0} \right) = 0. \quad (24.4)$$

The integration of these equations gives the following expressions for these functions:

$$r_1 = \frac{1}{r_0} \int_{m^*}^m \frac{\zeta_1(m)}{p_0^{1/\gamma}} dm + r_1^*(t), \quad p_1 = \frac{p_0}{\gamma} \left[\frac{p_1}{p_0} - \zeta_1(m) \right], \quad (24.5)$$

$$p_1 = \frac{\ddot{r}_0}{r_0^2} \int_{m^*}^m r_1 dm - \frac{1}{r_0} \int_{m^*}^m \frac{\partial^2 r_1}{\partial t^2} dm + p_1^*(t),$$

where $r_1^*(t)$, $p_1^*(t)$, and $\zeta_1(m)$ are arbitrary functions; the lower limit of the integrals (m^*) is also selected arbitrarily.

The conditions on the shock wave and on the surface of the piston must be used to determine the arbitrary functions. The conditions on the shock wave, moving with the velocity D with respect to the undisturbed flow, have the form

$$m = \frac{1}{2} \rho_\infty r_s^2, \quad (24.6)$$

$$p_s = (1 - \varepsilon) \rho_\infty D^2 - \varepsilon p_\infty,$$

$$\rho_s = \frac{\rho_\infty}{\varepsilon + (1 - \varepsilon) \alpha_\infty^2 / D^2}.$$

The correct choice of $r_0(t)$ is such that it agrees with the law of shock-wave propagation; i.e., it is given by $r_0 = r_s(t)$. The velocity of this propagation will be $D = \partial r_s / \partial t = \dot{r}_s$. For this choice, obviously, the function $r_1 = 0$ on the shock wave.

The conditions on the shock wave that the other terms in the expansion must satisfy are obtained if Eqs. (24.6) for p_s and ρ_s are equated to their respective values in Eq. (24.1). As a result, we obtain

$$\begin{aligned} p_0 &= \rho_\infty \dot{r}_s^2, & p_1 &= -p_\infty = \rho_\infty \dot{r}_s^2, \\ p_0 &= \frac{\epsilon \rho_\infty}{\epsilon + (1 - \epsilon) \alpha_\infty^2 / \dot{r}_s^2}, & p_1 &= 0. \end{aligned} \quad (24.7)$$

The arbitrary functions in Eqs. (24.3) and (24.5) can now be determined from these conditions. For example, if we substitute $p_0 = \rho_\infty \dot{r}_s^2$ and $m = \rho_\infty r_s^2/2$ into the second expression of Eq. (24.3), we find the following function:

$$P(t) = \rho_\infty \dot{r}_s^2 + \frac{1}{2} \rho_\infty r_s \ddot{r}_s.$$

The other functions can be found in a similar manner. After substituting these functions into Eq. (24.3) and after simple transformations, we can determine the quantities p_0 and ρ_0 :

$$\begin{aligned} p_0 &= \rho_\infty \dot{r}_s^2 + \frac{1}{2} \rho_\infty r_s \ddot{r}_s - \frac{\dot{r}_s}{r_s} m, \\ \rho_0 &= \rho_\infty \frac{(p_0/\rho_\infty \dot{r}_s^2)^{1/\gamma}}{1 + 2\alpha_\infty^2/(\gamma - 1)\dot{r}_s^2}, \end{aligned} \quad (24.8)$$

where $\dot{r} = \partial r/\partial \tau$ is a function of the new variable τ . If t corresponds to the instant in time when the particle crosses the shock wave, so that $m = m^* = \rho_\infty r_s^2/2$, τ is defined as the instant in time when the particle is at a distance r from the axis and the Lagrangian variable m is given by $m = \rho_\infty r^2/2$.

Equations for the functions r_1 , p_1 , and ρ_1 are obtained in the same way and have the form

$$r = \frac{1}{r_s} \int_{m^*}^m \frac{[1 + 2\alpha_\infty^2/(\gamma - 1)\dot{r}^2] \dot{r}^{2/\gamma} dm}{\rho_\infty (\dot{r}_s^2 + r_s \ddot{r}_s/2 - m \ddot{r}_s/\rho_\infty r_s)^{1/\gamma}}, \quad (24.9a)$$

$$p_1 = \frac{\dot{r}_s}{r_s^2} \int_m^m r_1 dm - \frac{1}{r_s} \int_m^m \frac{\partial^2 r_1}{\partial t^2} dm = p_\infty - \rho_\infty r_s^2, \quad (24.9b)$$

$$\rho_1 = \frac{\rho_0}{\gamma} \left(1 + \frac{p_1}{p_0} + \frac{\alpha_\infty^2}{\gamma r_s^2} \right). \quad (24.9c)$$

Since the shape of the body is usually specified by the law for the motion of the piston, $r_N(t)$, it is necessary to relate r_s to r_N by an additional condition. Neglecting terms of the second and higher orders, we obtain

$$r = r_s + \epsilon r_1 = r_N,$$

so that

$$r_s = r_N - \epsilon \left| r_1 \right|_m^0, \quad (24.10)$$

where $\left| r_1 \right|_m^0$ is determined from Eq. (24.9a) by setting the upper limit of the integral equal to zero (the condition on the piston). Note that in Eq. (24.9a) the quantity r_s on the right side can be replaced by r_N , since when Eq. (24.10) is substituted for r_s , a term of order ϵ^2 results, which can be neglected.

FLOW AROUND A POINTED CONE

It is evident from the relations presented above that the solution is found in the form of functions that can be determined in turn by the law of motion of the shock wave, i.e., by the relation for r_s . An expression for this law for flow around a cone can be obtained by dimensional analysis.

Analysis of the phenomenon of shock-wave propagation indicates that the shock-wave velocity $D = \partial r_s / \partial t$ is a function of the variable t and of the dimensional variables p_∞ and ρ_∞ , i.e.,

$$\frac{\partial r_s}{\partial t} = f(t, p_\infty, \rho_\infty).$$

It is apparent that all of these quantities have independent dimensions, so that it is possible to write

$$\frac{\partial r_s}{\partial t} = At^n p_\infty^m k,$$

where A is a constant. It can be shown by dimensional analysis that the exponents n , m , and k are equal to $n = 0$, $m = 0.5$, and $k = -0.5$. Thus, the shock is propagated with a constant velocity

$$\frac{\partial r_s}{\partial t} = D = A \sqrt{p_\infty / \rho_\infty}.$$

If t is replaced by x/V_∞ in agreement with the law of plane sections, $\partial r_s / \partial x = D/V_\infty$. Thus, a shock-wave velocity equal to D corresponds to flow around a pointed cone with an attached shock wave whose angle is given by

$$\frac{\partial r_s}{\partial x} = \tan \theta_s = \frac{D}{V_\infty}.$$

The law of motion for the shock wave is expressed in the form $r_s = Dt$, where $D = V_\infty \tan \theta_s$. The form of the law of motion for the piston must correspond to the equation of the cone, $r = x \tan \delta_c$, and is given by $r = Ut$, where the velocity of the piston is $U = V_\infty \tan \delta_c$. If we substitute the expressions $r_s = Dt$ and $r = Ut$ into Eq. (24.8), we find a relation for p_0 and ρ_0 :

$$p_0 = \rho_\infty D^2, \quad \rho_0 = \frac{\rho_\infty}{1 + 2x_\infty^2/(\gamma - 1)D^2}. \quad (24.11)$$

A similar substitution into Eq. (24.9) gives the following relation for r_1 :

$$r_1 = \frac{Dt}{2} \left(1 + \frac{2}{\gamma - 1} \frac{\alpha_\infty^2}{D^2} \right) (\bar{m} - 1) = \frac{Dt}{2} \left(1 + \frac{2}{\gamma - 1} \frac{\alpha_\infty^2}{D^2} \right) \left(\frac{r^2}{r_s^2} - 1 \right), \quad (24.12)$$

where $\bar{m} = m/m^*$. Noting that $m^* = \rho_\infty D^2 t^2 / 2$, we can compute the second derivative:

$$\frac{\partial^2 r_1}{\partial t^2} = \frac{2m}{Dt^3 v_\infty} \left(1 + \frac{2}{\gamma - 1} \frac{a_\infty^2}{D^2} \right).$$

Substituting this derivative into Eq. (24.9) for p_1 and using the definitions $m = \rho_\infty r^2/2$ and $m^* = \rho_\infty r_s^2/2$, we obtain

$$p_1 = \frac{\rho_\infty D^2}{4} \left(1 + \frac{2}{\gamma - 1} \frac{a_\infty^2}{D^2} \right) \left(1 - \frac{r_s^4}{r_1^4} \right) - p_\infty - \rho_\infty D^2. \quad (24.13)$$

Finally, with Eqs. (24.11) and (24.13), Eq. (24.9c) gives a relation for r_1 :

$$r_1 = \frac{v_\infty}{4\gamma} \left(1 - \frac{r_s^4}{r_1^4} \right). \quad (24.14)$$

To determine the relation between the velocities of the piston U and of the wave D , we must first set $m = 0$ in Eq. (24.12), resulting in

$$r_1 = -\frac{Dt}{2} \left(1 + \frac{2}{\gamma - 1} \frac{a_\infty^2}{D^2} \right).$$

Substituting this result with $r_s = Dt$ and $r = Ut$ into Eq. (24.12), we obtain

$$U = D \left[1 - \frac{\gamma - 1}{2(\gamma + 1)} \left(1 + \frac{2}{\gamma - 1} \frac{a_\infty^2}{D^2} \right) \right]. \quad (24.15)$$

This relation can be converted to an expression for the relation between the cone angle and the shock angle for hypersonic flow velocities, since

$$\frac{U}{a_\infty} = \frac{V_\infty}{a_\infty} \tan \delta_c = K_1, \quad \frac{D}{a_\infty} = \frac{V_\infty}{a_\infty} \tan \theta_s = K_0.$$

Thus,

$$K_1 = K_0 \left[1 - \frac{\gamma - 1}{2(\gamma + 1)} \left(1 + \frac{2}{\gamma - 1} \frac{1}{K_0^2} \right) \right]. \quad (24.16)$$

This equation agrees with the relation derived previously in Eq. (17.4a), and the expression for the pressure coefficient on the cone (obtained

from $p = p_0 + \epsilon p_1$ by substituting Eqs. (24.11) and (24.13)) is identical with Eq. (17.11).

The relations for the dimensionless gas parameters at an arbitrary point between the wave and the cone are determined only as a function of the ratio r/r_s (see Eqs. (24.13) and (24.14)). Thus, unsteady motion ahead of a cylindrical piston, which is equivalent to steady flow around a cone, possesses the characteristic that the spatial distribution of the flow parameters remains the same with changes in time. This type of motion is called similar. It is evident from the discussion that, in the given case, similar motion also occurs when the initial pressure of the gas, p_∞ , is included.

FLOW AROUND A POWER LAW BODY

In the example of flow around a cone, it was possible to obtain a closed-form solution. In the equivalent problem of the expansion of a piston, this solution describes the similar motion behind a cylindrical shock wave, which accounts for the ambient pressure p_∞ . In addition, an analytical solution can be obtained for another form of similar motion that corresponds to the flow around a body with a particular curved shape.

Let us assume that the pressure in front of the shock wave can be neglected at hypersonic velocities, for which $a_\infty/D \ll 1$. The shock velocity is determined by the expression

$$\frac{\partial r_s}{\partial t} = f(t, p_\infty)$$

and

$$\frac{\partial r_s}{\partial t} = B t^n p_\infty^m,$$

where B is a constant. The product of this constant and p_∞^m is also constant and can be designated by C_1 . Then the propagation velocity of the shock is written as

$$\frac{\partial r_s}{\partial t} = D = C_1 t^n,$$

and the law of motion is

$$r_s = \frac{C_1}{n+1} t^{n+1}. \quad (24.17)$$

It should be noted that the constant C_1 has the dimensions $[L]/[T]^{n+1}$.

In analogy to the expression for r_s , the relation for the law of piston expansion is

$$r_N = \frac{C}{n+1} t^{n+1}. \quad (24.18)$$

Replacing t by x/V_∞ , we obtain the equation for the profile of the body:

$$r_N = \frac{C}{n+1} \left(\frac{x}{V_\infty} \right)^{n+1}. \quad (24.18a)$$

In the special case of $n = 0$, we obtain the equation for a cone.

Using Eq. (24.17) for r_s and the corresponding relation

$$r = \frac{C_1}{n+1} \tau^{n+1}, \quad (24.17a)$$

we can evaluate the functions that are represented in general form by Eqs. (24.8) and (24.9). Assuming that a_∞/D is negligible, we obtain

$$\begin{aligned} p_0 &= \rho_\infty D^2 \left[1 + \frac{n}{2(n+1)} (1 - \bar{m}) \right], \\ \rho_0 &= \rho_\infty^{(\gamma-1)/\gamma} \left(\frac{p_0}{C_1^{2/\gamma} 2^n} \right)^{1/\gamma}. \end{aligned} \quad (24.19)$$

The relations given by Eq. (24.9) are obtained in a similar manner:

$$r_1 = - \frac{r_s}{2} J(\bar{m}), \quad (24.20a)$$

$$p_1 = \rho_\infty D^2 \left\{ \bar{m}^2 J'(\bar{m}) - \frac{1}{2} \left(\frac{n}{n+1} + \frac{3}{2} \right) \bar{m} J(\bar{m}) - \left[\frac{n}{2(n+1)} + \frac{3}{2} \right] \int_{\bar{m}}^1 J(\bar{m}) d\bar{m} \right\}, \quad (24.20b)$$

$$\rho_1 = \frac{\rho_0}{\gamma} \left(\frac{p_1}{p_0} + 1 \right), \quad (24.20c)$$

where

$$J(\bar{m}) = \int_{\bar{m}}^1 \left[\frac{\bar{m}^{n/(n+1)}}{1 + \frac{n}{2(n+1)}(1 - \bar{m})} \right]^{1/\gamma} d\bar{m}, \quad (24.21)$$

and $J'(\bar{m}) = dJ/d\bar{m}$. It is evident from Eqs. (24.19) and (24.20) that the motion under consideration is, in fact, of a similar character because all the dimensionless parameters are determined by the one dimensionless quantity \bar{m} .

The laws of piston motion and of shock-wave motion are related by the coefficients C and C_1 , which can be obtained from Eq. (24.10) and Eq. (24.20):

$$\frac{r_N}{r_s} = \frac{C}{C_1} = 1 - \frac{\epsilon}{2} J(0). \quad (24.22)$$

Equation (24.22) gives the ratio between the coordinates of the body surface and the shock wave and is plotted in Fig. 238.

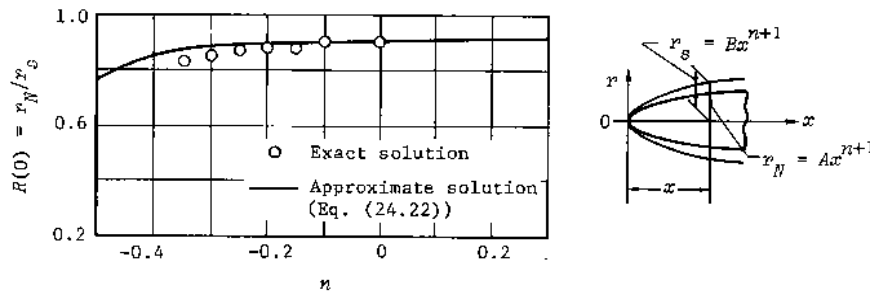


Fig. 238--Ratio of the coordinates for a power law body and its shock wave

Relations for the flow parameters in the perturbed layer between the shock wave and the body can be found by using Eqs. (24.19), (24.20), and (24.1). For example, the pressure at the surface ($\bar{m} = 0$) is

$$p_N = p_\infty D^2 \left[1 + \frac{n}{2(n+1)} - \frac{\epsilon}{2} \left(\frac{n}{n+1} + 3 \right) \int_0^1 J(\bar{m}) d\bar{m} \right] = p_s P(0), \quad (24.23)$$

where the pressure directly behind the shock wave is

$$p_s = \frac{2}{\gamma + 1} \rho_\infty D^2,$$

and the function $P(\bar{m}) = P(0) = p_N/p_s$. This pressure ratio is presented in Fig. 239. The drag of a power law body can be determined from the equation

$$C_D q S = 2\pi \int_0^{r_N} p_N r_N dr_N$$

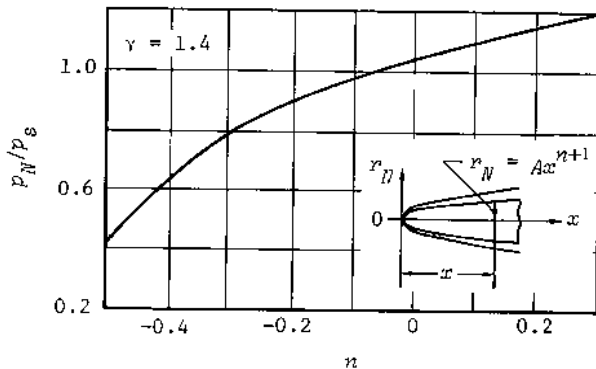


Fig. 239--Ratio of the surface pressure on a power law body to the pressure behind the shock wave

and the expression for pressure

$$p_H = p_s P(0) = \frac{2}{\gamma + 1} \rho_\infty D^2 P(0) = \frac{2}{\gamma + 1} \rho_\infty C_1^2 t^{2n} P(0).$$

The product $C_1^2 t^{2n}$ can be replaced by a function of r_s and r_N by using Eqs. (24.17) and (24.18). Then, performing the integration indicated above, we obtain

$$C_D q S = \frac{4\pi}{\gamma + 1} \rho_\infty C^2 \frac{P(0)}{R^2(0)} \left(\frac{n+1}{C} \right)^{2n/(n+1)} \frac{n+1}{2(2n+1)} r_N^{2+2n/(n+1)} \Big|_0^{r_N}, \quad (24.24)$$

where $R(\bar{m}) = R(0) = r_N/r_s$ is the function calculated from Eq. (24.22). To calculate the drag, it is necessary to know not only the free-stream flow parameters, but also the shape of the power law body. The latter is specified by the maximum radius r_{mid} , the exponent n , and the constant C . The fineness ratio $\lambda_N = l_N/2r_{\text{mid}}$ can be used instead of C , so that the equation for the body is written as

$$r_N = Ax^{n+1} = \frac{x^{n+1}}{2\lambda_N^{n+1}(2r_{\text{mid}})^n}.$$

After determining the value of A from this equation, the coefficient C is obtained from Eq. (24.18a) as $C = A(n + 1)V_\infty^{n+1}$.

It follows from Eq. (24.24) that solutions do not exist for all values of the exponent n in Eq. (24.17), i.e., for all power law shapes. In particular, it is evident that the value of the integral

$$\int_0^{r_N} r^{2+2n/(n+1)} dr$$

diverges for $n/(n + 1) \leq -1$ and the drag becomes infinite, which is not valid. The drag given by Eq. (24.24) will be finite for bodies with values of $n > -\frac{1}{2}$, and for $n < -\frac{1}{2}$ a similar solution does not exist. This means that the distribution of parameters in transverse planes between the body and the shock wave does not possess the property of similarity, and, therefore, it is impossible to express the pressure, density, and velocity in the form

$$\frac{P(r)}{P(0)} = f\left(\frac{r}{r_s}\right).$$

In this case the flow at a given station must be, to some degree, a function of the previous history of the flow, which in turn must be determined by the geometric shape of the body.

It follows from Eq. (24.18a) that, for $n > -\frac{1}{2}$, this equation represents both pointed bodies ($n \geq 0$) and blunt bodies. Since solutions were assumed to be given by the series in Eq. (24.1) and were limited to the

first order in $\epsilon = (\gamma - 1)/(\gamma + 1)$, Eq. (24.24) is approximate and can be used only for values of n somewhat larger than $-\frac{1}{2}$. This is evident in Fig. 240, in which a curve is plotted for the variation of the drag coefficient

$$C_D = \frac{1}{\gamma + 1} \frac{(n+1)^3}{2n+1} \frac{P(0)}{R^2(0)} \frac{1}{\lambda^2}, \quad (24.25)$$

where the reference area is $S = \pi r_N^2$, and the fineness ratio $\lambda = l_N/2r_N$. Equation (24.25) is derived from Eq. (24.24) by setting the integral equal to zero at the lower limit and choosing the constant to be

$$C = (n+1) \frac{r_N}{t^{n+1}} = (n+1)r_N \left(\frac{V_\infty}{x} \right)^{n+1}.$$

A comparison with the results of the exact solution (see Fig. 240) indicates that the accuracy of Eq. (24.25) decreases near values of $n = -\frac{1}{2}$. The same situation can be noted with respect to the shape of the shock wave as given by Eq. (24.22), which is compared with exact theory in Fig. 238.

The results in Fig. 240 indicate that the minimum value of $C_D \lambda^2$

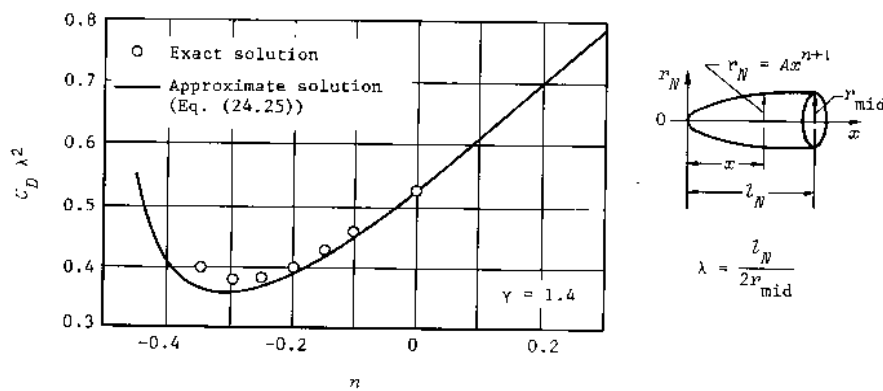


Fig. 240--Drag coefficients of power law bodies

is equal to 0.38 at approximately $n = -0.29$, and for a cone $C_D \lambda^2 = 0.52$, which is larger by 37 percent. Thus, at very high velocities, a blunt body of revolution with a curved generatrix, which is better from the standpoint of heating, is also advantageous in having less drag than a cone.

The relations obtained above pertain to the case in which terms of the order of ϵ are taken into account in Eq. (24.1). Of course, these relations are simplified if only the main terms are used.⁽¹⁶⁾ For example, Eqs. (24.22) and (24.23) take the form

$$R(0) = \frac{r_N}{r_s} = \frac{C}{C_1} = 1, \quad (24.22a)$$

$$p_N = \rho_\infty D^2 \left[1 + \frac{n}{2(n+1)} \right] = p_s P(0), \quad (24.23a)$$

and Eq. (24.25) for the drag coefficient is

$$C_D = \frac{(n+1)^2}{4(2n+1)} \frac{3n+2}{\lambda^2}. \quad (24.25a)$$

The minimum C_D for a fixed fineness ratio λ is obtained for $n = -\frac{1}{3}$. The minimum

$$C_D = \frac{1}{3\lambda^2} \quad (24.26)$$

is less than that given for a cone by Newtonian theory, $C_D = \frac{1}{2}\lambda^2$.

THE APPLICATION OF THE NEWTONIAN EQUATION

The pressure given by Eq. (24.23) applies to points on the surface of a power law body located at some distance from the blunt nose. Another method must be used for points on the blunt nose. It was noted that modified Newtonian theory gives satisfactory results in calculating the pressure distribution around a spherical nose. Research shows that these results can be applied to bodies of any curved shape. This is particularly evident in Fig. 241, where experimental data for the pressure

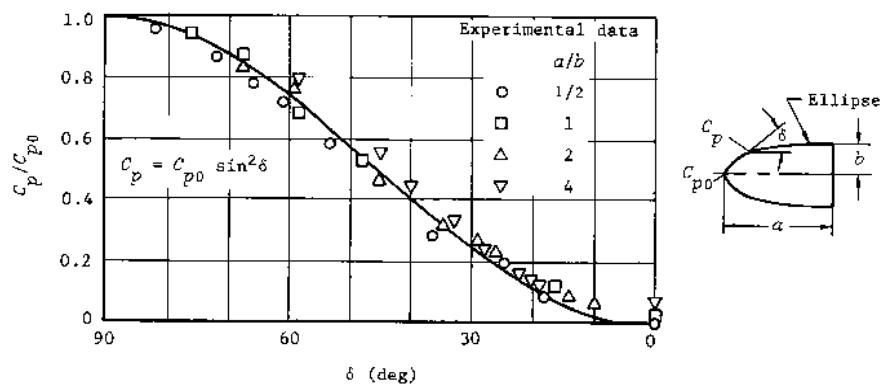


Fig. 241--Comparison of the theoretical and experimental pressure distributions around an ellipsoid

distribution over a symmetric ellipsoid are compared with the results of calculations by the equation $C_p = C_{p0} \sin^2 \delta$.

The Newtonian equation can also be applied with the same success to blunt power law bodies. Comparison shows that better agreement of the experimental and theoretical results is observed for large supersonic velocities. However, Newtonian theory gives an approximation sufficiently satisfactory for practical purposes even for comparatively small velocities, as is verified by the data obtained in wind tunnels at $M_\infty = 4$ in Fig. 241.

The data indicate that the pressure measured at the rear of the nose is relatively large. The calculated results can be improved somewhat by "splicing" the pressure distribution obtained from the Newtonian equation on the forward part of the body to a pressure distribution over the aft part from a Prandtl-Meyer expansion. The Prandtl-Meyer theory can also be spliced to the calculation based on the law of plane sections, i.e., with Eq. (24.23).

§ 25. NONEQUILIBRIUM EFFECTS ON INVISCID FLOW AROUND BLUNT BODIES

NONEQUILIBRIUM FLOW IN REGIONS OF GREAT OVEREXPANSION
AND SMALL PRESSURE GRADIENTS

Flow Regions around Blunt Bodies

THREE DIFFERENT REGIONS can be distinguished in the flow over a blunt body (Fig. 242). The first of these regions is directly adjacent to the blunt nose between the axis and the sonic line. The pressure in this region is almost constant, and is approximately equal to the stagnation pressure. Initially, the gas will be in a state of nonequilibrium dissociation after passing through the shock wave, but it will be assumed that it can return rapidly to an equilibrium state specified by an average value of pressure and enthalpy in this region. We shall consider nonequilibrium flow in this region in somewhat more detail later in this section.

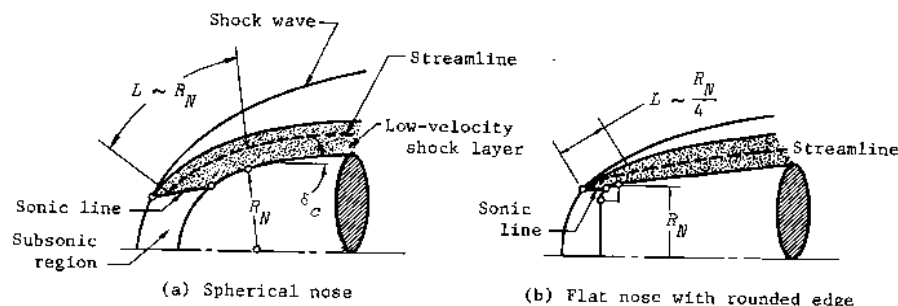


Fig. 242--Diagram of flow around blunt bodies

The second flow region begins at the sonic line and is characterized by a rapid decrease in pressure. It terminates behind the nose in a flow with a positive, zero, or negative pressure gradient, depending on the shape of the body. In the region of significant expansion, the state of the dissociating gas does not have time to reach equilibrium. Therefore, thermodynamic nonequilibrium is an important characteristic of the gas flow in this region.

Finally, in the third flow region over the aft part of the body, the pressure changes are small, and the gas tends toward equilibrium.

Thus, the nonequilibrium state must be considered in calculating inviscid flow. However, research has shown that there is little difference in the pressure between the nonequilibrium and the equilibrium state. Therefore, the effects of nonequilibrium molecular dissociation on such inviscid flow parameters as the degree of dissociation, the density, and the temperature can be estimated by assuming that the pressure distribution is independent of the dissociated state of the gas.

Calculation of Nonequilibrium Flow

The calculation of the flow parameters requires the integration of the system of equations given in Eqs. (4.64) through (4.67) for certain given constants and boundary conditions. The results presented below⁽¹⁷⁾ were obtained using the values $C = 6 \cdot 10^{14} \text{ cm}^3/\text{g sec}$ and $\rho_d = 125 \text{ g/cm}^3$. The boundary conditions for the integration of the equations were the conditions on the sonic line, which were determined for a given flight velocity V_∞ and altitude H on the basis of equilibrium flow in the region of the stagnation point.

The streamline along which the nonequilibrium flow parameters were computed was located downstream of the sonic region. It was assumed that the pressure on this streamline was determined by a one-dimensional expansion as given by Prandtl-Meyer theory. It was also assumed that the length of the streamline having this pressure distribution would be of the order of the radius of a spherical nose, or one-fourth the radius of a flat face (or of a slightly curved face). The dimension assumed for the initial supersonic expansion also determines the characteristic length in Eq. (4.68) for $\bar{\varphi}$.

The pressure distribution is shown in Fig. 243, calculated on the basis of Prandtl-Meyer theory for a streamline passing through an expansion fan originating at the sonic point. In the present case, the radius of curvature of the streamline is assumed to be constant and approximately equal to the radius of curvature of the surface; the expansion angle is $\nu = \bar{x} = x/R_N$.

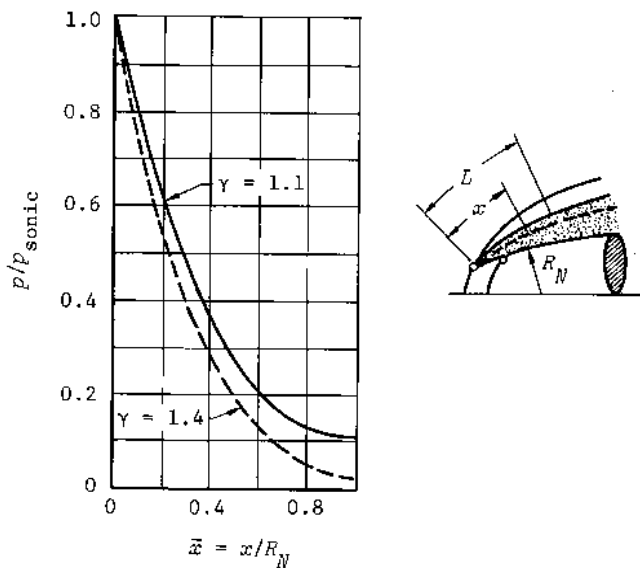


Fig. 243--Pressure distribution along a streamline for a Prandtl-Meyer expansion

Some results of the numerical integration of Eqs. (4.64) through (4.67) for various altitudes and flight velocities⁽¹⁷⁾ are presented in Figs. 244 through 248. In each case the calculations were made for several values of the characteristic length L (corresponding to different values of the parameter $\bar{\psi}$).

The character of the variation in nonequilibrium dissociation can be determined from Fig. 244. In addition, curves are shown for the variation in the equilibrium degree of dissociation for real air (B) and a model of a diatomic gas (A). It should be noted that the values of the

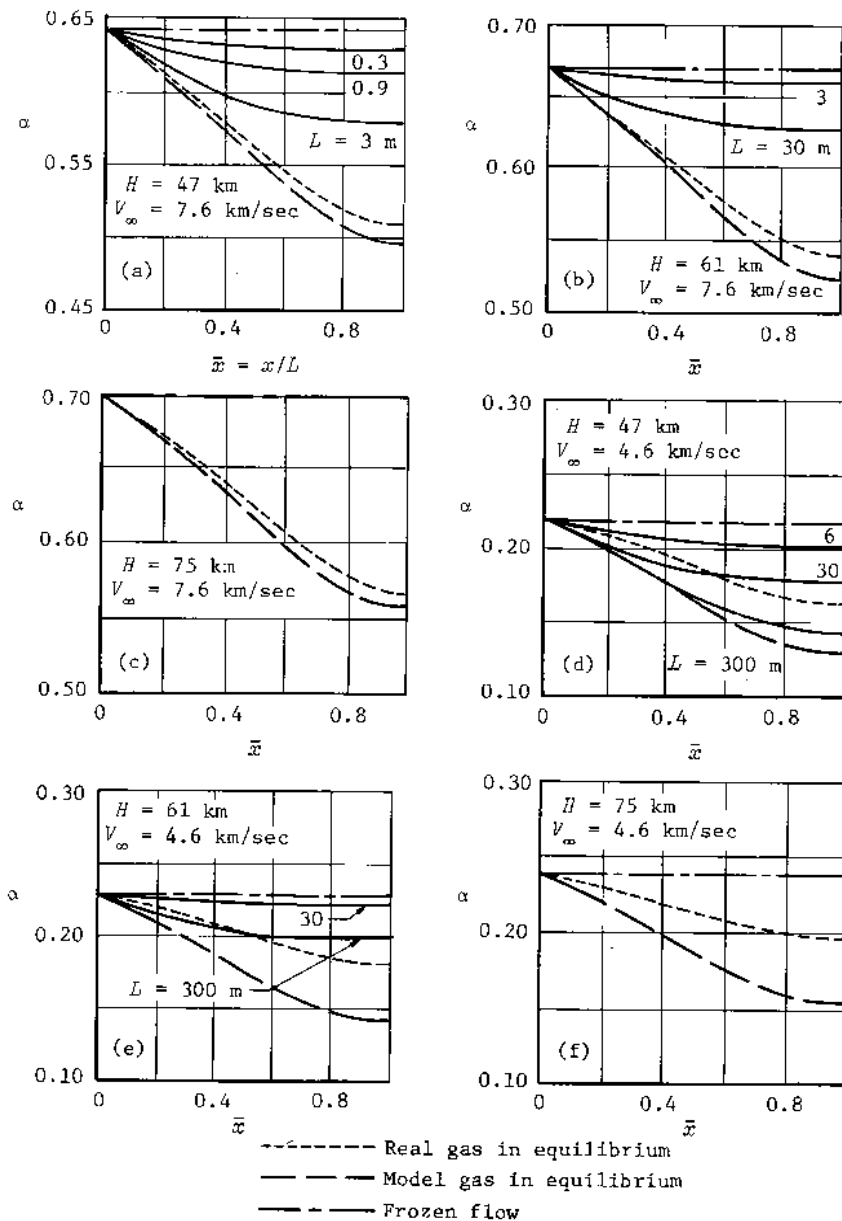


Fig. 244—Nonequilibrium effects on the degree of dissociation along a streamline

equilibrium degree of dissociation for the model gas are in good agreement with those for air at the higher velocity (7.6 km/sec). In the case of the nonequilibrium calculations, the change in the degree of dissociation along the streamline compared with the initial equilibrium value α_{0e} is generally quite small even for rather large values of L . This state of the gas is referred to as being close to "frozen." The frozen state is characterized by the fact that no reactions occur in the gas, and therefore its chemical state does not change.

In practical cases, the flow can be considered frozen if the state of the gas differs from the initial state by no more than about 5 percent. The state of the gas can also be defined by comparing the change in the degree of dissociation with the maximum possible change. If α_1 is the nonequilibrium degree of dissociation at the end of the region of expansion, the gas can be assumed to be in the frozen state if

$$\tilde{\alpha}_1 = \frac{\alpha_1 - \alpha_{1e}}{\alpha_{0e} - \alpha_{1e}} \geq 0.95,$$

where α_{1e} is the equilibrium degree of dissociation at the end of the same region. If $\tilde{\alpha}_1$ is less than about 0.05, the flow can be considered to be in equilibrium.

Returning to Fig. 244, it should be noted that flow in the expansion region near a blunt body will be practically frozen at altitudes higher than 47 km for flight velocities of 5 to 8 km/sec. For a fixed flight velocity and length L the flow becomes more frozen as the altitude increases, and for a fixed altitude and length the flow becomes more frozen with a decrease in velocity. An increase in freezing is also observed for a decrease in the characteristic length L . This is due to the decrease in the time a particle of gas remains in the expansion zone, during which time only a few atoms succeed in recombining.

From the results presented in Figs. 245 and 246, it follows that the deviation from equilibrium is caused by a reduction in density and an increase in temperature, which also leads to substantial changes in the local Reynolds number. However, the calculations show that the deviation from equilibrium flow has a small effect on the pressure.

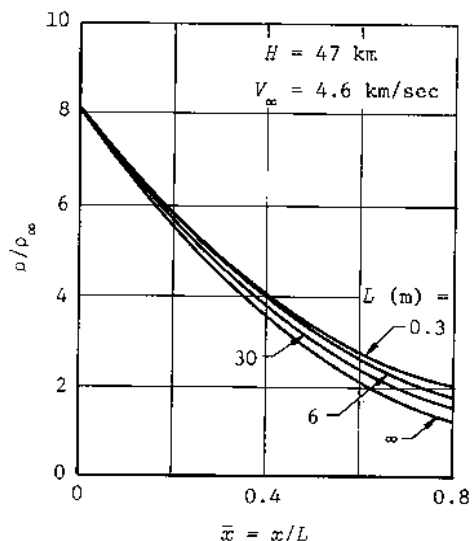


Fig. 245--Density ratio for nonequilibrium flow of a diatomic gas

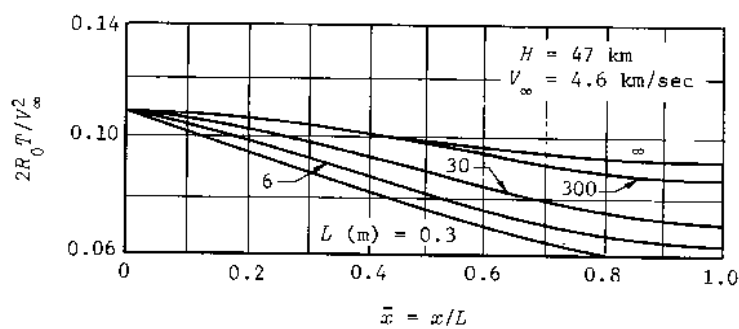


Fig. 246--Temperature distribution for nonequilibrium flow of a diatomic gas

Curves for the nonequilibrium dissociation parameter $\tilde{\alpha}_1$ as a function of $\bar{\varphi}$ are presented in Fig. 247. For the frozen state $\bar{\varphi} < 0.001$, and for the equilibrium state $\bar{\varphi} > 1$.

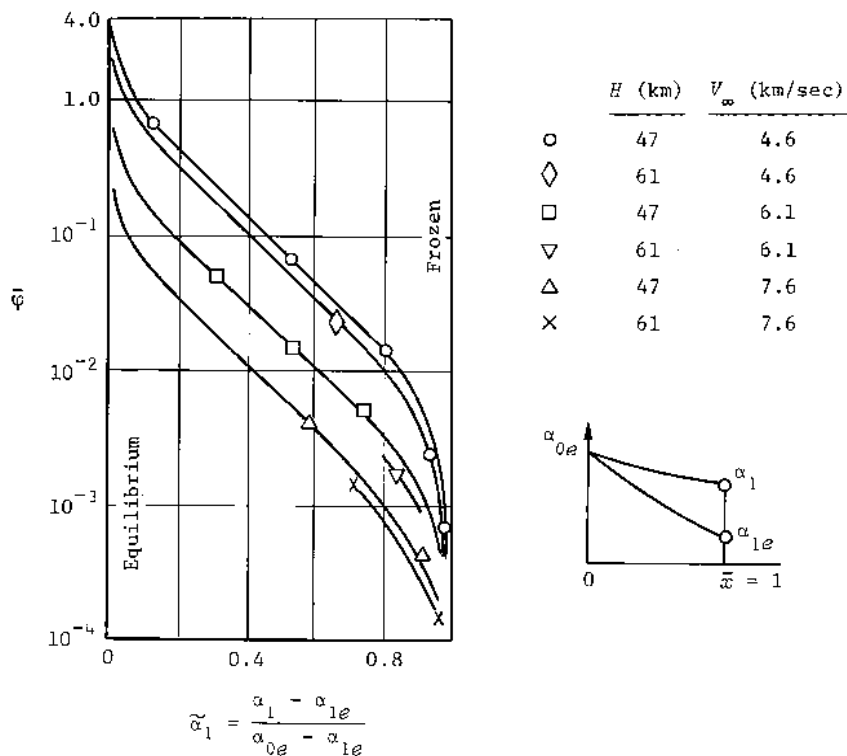


Fig. 247--The nonequilibrium dissociation parameter for various flow conditions

After the expansion, the flow enters a region of slowly changing pressure, which to simplify the analysis can be assumed to be a region of constant pressure. If a conical section lies behind the blunt nose, the pressure is actually almost constant. In this region of constant pressure, the gas particles are able to return to an equilibrium state, with constant values of enthalpy and pressure. During this transition the nonequilibrium parameters can be determined from the integration of Eq. (4.67). The initial conditions can be considered to be the frozen parameters at the end of the section of supersonic expansion discussed above (the length is measured from that station). The results show that, at velocities of 4.6 to 7.6 km/sec, the flow in the section behind the nose continues to remain frozen at a distance of more than 6 to 9 m.

This distance corresponds to an altitude of 45 to 47 km and increases for higher altitudes. For example, at $H = 61$ km, L increases to 30 m.

Some results of the calculation for an altitude of 47 km are presented in Fig. 248. It is evident that the approach to equilibrium conditions occurs more rapidly at the higher velocities.

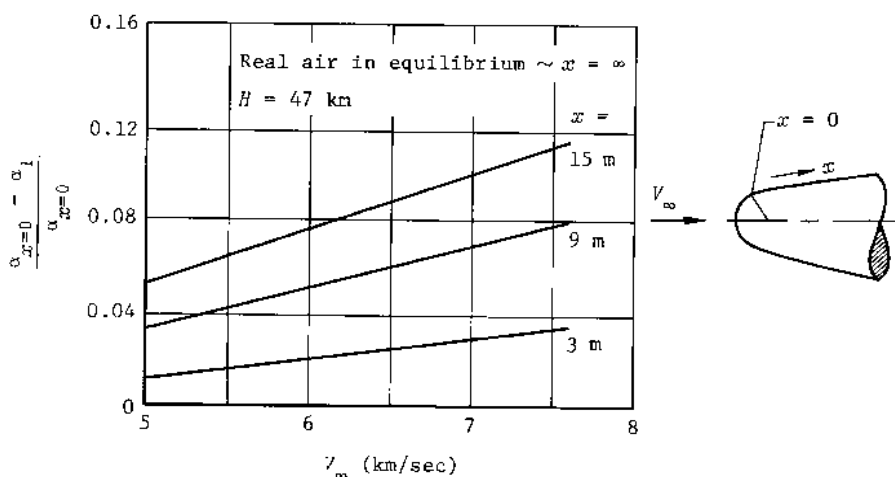


Fig. 248—Degree of dissociation along a streamline near a conical surface with constant pressure

The phenomenon of frozen flow is observed not only in the region with a zero pressure gradient but to an even greater degree in flow with a negative pressure gradient, such as that over a cylinder following a blunt nose. This is because the pressure reduction is accompanied by a decrease in density, and the term on the right side of Eq. (4.67) that represents recombination varies approximately proportionally to the square of the density.

The following conclusions can be reached from this discussion of nonequilibrium flow around a blunt body. Since the entire region of flow stemming from the strong part of the shock wave continues to remain frozen along almost the whole length of a blunt body, the inviscid flow parameters along a streamline in this shock layer can be calculated from isentropic flow conditions for $\gamma_2 = 1.1$ to 1.2 (the exact value of

γ_2 can be calculated for the stagnation conditions). The temperature and density at a given point can be found from the expressions

$$\frac{T}{T_0'} = \left(\frac{p}{p_0'} \right)^{(\gamma_2 - 1)/\gamma_2}, \quad \frac{\rho}{\rho_0'} = \left(\frac{p}{p_0'} \right)^{1/\gamma_2}. \quad (25.1)$$

These approximate results for nonequilibrium flow around blunt bodies can be used in the calculation of friction and heat transfer parameters. It is apparent that the local temperature in the boundary layer will be higher, and the density and Reynolds number will be lower, than the corresponding values for equilibrium flow.

ESTIMATES OF NONEQUILIBRIUM EFFECTS IN THE VICINITY OF BLUNT BODIES

Nonequilibrium Effects between a Normal Shock and the Stagnation Point

We assumed above that thermodynamic equilibrium was established in the vicinity of the blunt nose. Strictly speaking, this premise is only valid for specific flight conditions and pertains to that part of the decelerated flow that is adjacent to the blunt surface.

In the region close to the shock wave, the flow will always be in a nonequilibrium state. It is necessary to estimate the extent of this region and to determine whether it includes the stagnation region on the body. For this purpose, the relaxation length x_D can be used. It is evident from Fig. 47 that equilibrium is attained at approximately $\bar{x} = 1$. Therefore, an expression for the relaxation length can be obtained from the second part of Eq. (2.31):

$$x_D = \int_0^1 V t_D d\bar{x}.$$

If average values of V and t_D are assumed on the portion of the streamline between the shock and the body, the relaxation length is

$$x_D = V t_D. \quad (25.2)$$

The time t_D can be determined from Eq. (2.31), if it is assumed that

$\rho_d = 130 \text{ g/cm}^3$ for a diatomic model of air. Then the product $C\rho_d$ is

$$\bar{C} = C\rho_d = 6 \cdot 10^{14} \cdot 130 \text{ sec}^{-1} = 7.8 \cdot 10^{16} \text{ sec}^{-1}.$$

The density can be assumed equal to the average value $\bar{\rho} = 0.5(\bar{\rho}_2 + \bar{\rho}_e)$, where $\bar{\rho}_2$ and $\bar{\rho}_e$ are the dimensionless densities behind the shock (for $\alpha = 0$) and for equilibrium, respectively.[†] Finally, setting $\alpha = 0.5\alpha_e$ in Eq. (2.31), we obtain an approximate estimate of the relaxation time:

$$t_D = \frac{2.8 \cdot 10^{-7} (1 - \alpha_e)}{\alpha_e (3 - \alpha_e) [f_p(H)\tilde{\rho}]^2}, \quad (25.3)$$

where $f_p(H) = \rho_{\infty H}/\rho_{\infty SL}$ is a function of altitude, and the density ratio $\tilde{\rho} = \rho/\rho_{\infty H}$ is determined as the average $\tilde{\rho} = 0.5(\tilde{\rho}_2 + \tilde{\rho}_e)$. The time t_D given by Eq. (25.3) is also called the characteristic reaction time.

As an example, let us calculate t_D for flight conditions at an altitude of 30 km and a velocity of 8.1 km/sec, for which it was shown in §4 that $\tilde{\rho}_e = 14$ and $\alpha_e = 0.735$. Then $\bar{\rho} = 0.5(14 + 6) = 10$ and the altitude function $f_p(H) = 1.45 \cdot 10^{-2}$, so that

$$t_D = \frac{2.8 \cdot 10^{-7} (1 - 0.735)}{0.735 (3 - 0.735) (1.45 \cdot 10^{-2} \cdot 10)^2} = 2.1 \cdot 10^{-6} \text{ sec.}$$

The relaxation time of nitrogen and oxygen can be estimated approximately with the aid of Fig. 25 or Eq. (2.32), with the temperature T computed as an average between the values directly behind the shock ($\alpha = 0$) and in the equilibrium state ($\alpha = \alpha_e$).

To determine the relaxation length, we assume that the average velocity along the axial streamline $V = 0.5V_0$, where V_0 is the velocity directly behind the normal portion of the detached shock. Therefore,

$$x_D = 0.5V_0 t_D. \quad (25.2a)$$

[†]Editor's note: Here $\bar{\rho}$ is defined as in §4, i.e., $\bar{\rho} = \rho/\rho_d$. In §20, recall that $\bar{\rho} = \rho_{\infty}/\rho$, which is defined here as $1/\tilde{\rho}$.

If this length is less than the distance s_0 between the shock and the body, the relaxation zone is located close to the wave and does not include the body surface.

Thus, the condition of equilibrium in the vicinity of the nose will be $x_D \ll s_0$ or $0.5V_0 t_D \ll s_0$. This can also be expressed as an inequality $t_D \ll 2s_0/V_0$, where the term on the right represents the characteristic time t_{s0} that the particles remain in the region of nonequilibrium reaction (the "dwell" time). If this time is substantially larger than the characteristic reaction time, i.e., if $t_{s0} \gg t_D$, the gas particle attains equilibrium before it reaches the surface.

To illustrate, let us turn to the earlier example. For a value of $\tilde{\rho} = 10$, the dimensionless detachment distance is given by Eq. (20.39) as $\tilde{s}_0 = 0.074$.[†] If it is assumed that $R_N = 0.5$ m, the absolute distance between the shock and the body is $s_0 = 37$ mm. The velocity behind the shock wave^{††} is $V_0 = 1350$ m/sec from Eq. (4.11), so that the characteristic dwell time is

$$t_{s0} = \frac{2s_0}{V_0} = \frac{2 \cdot 37 \cdot 10^{-3}}{1350} = 5.5 \cdot 10^{-5} \text{ sec.}$$

Thus, in this example, the relaxation time is approximately 26 times less than the dwell time. In other words, the extent of the relaxation zone is about 1/26 of the distance between the shock and the body and extends for only about 1.5 mm behind the shock wave.

It is apparent from Eq. (25.3) that the relaxation time increases with an increase in altitude and, thus, the extent of the nonequilibrium zone is increased; e.g., with an increase in altitude to 40 km, the time t_D increases by a factor of 23 and the relaxation length is 35 mm.

The basic parameter for estimates of the flow regime is the ratio of the relaxation time to the dwell time, i.e., $\bar{t}_D = t_D/t_{s0}$. Since $t_{s0} = 2s_0/V_0$ and $s_0 = \tilde{s}_0 R_N$, the ratio of the characteristic times is

$$\bar{t}_D = \frac{t_D V_0}{2\tilde{s}_0 R_N}. \quad (25.4)$$

[†]Editor's note: See the previous note.

^{††}Editor's note: Calculated for $\tilde{\rho} = 6$.

The parameter $\bar{s}_0 = s_0/R_N$ is a function of the density ratio behind and ahead of the normal shock, as given, for example, by Eq. (20.39).

The quantity $R_N \bar{t}_D$ is shown in Fig. 249 as a function of Mach number and altitude, as calculated from Eqs. (25.3) and (25.4) for oxygen, if it is assumed that the dissociation of O_2 occurs at a wall temperature of 1500°K . Thus, the quantity $R_N \bar{t}_D$ can be determined as a function of M_∞ and H and then, for a given radius of sphere in meters, the flow regime can be estimated. For example, if \bar{t}_D is less than 0.1 to 0.01, the region can be assumed to be in equilibrium.

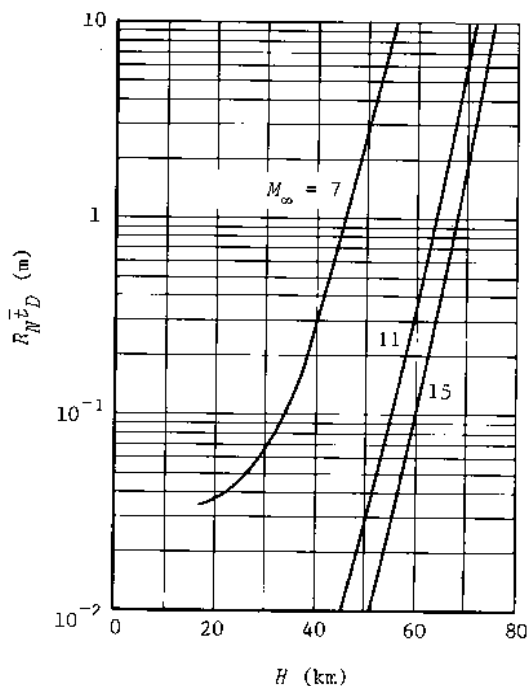


Fig. 249--Ratio of the relaxation time to the dwell time in the reaction zone

It must be kept in mind that the data in Fig. 249 represent a rather rough approximation even for oxygen, since the average temperature between the body and the shock is higher than T_w . Therefore, these data

can be used only to establish a qualitative picture of the flow. Similar graphs can be constructed taking into account all of the factors, which can then be used for quantitative estimates of the nonequilibrium effects.

Effects of Nonequilibrium on the Position and Shape of the Shock Wave

A hot gas layer will exist between the shock and the body for all cases of high velocity flow over a blunt body, and some region of non-equilibrium flow will always occur. This region will affect the shape and location of the shock wave. After examining the following two limiting cases, a qualitative estimate of this effect can be given.

The first case is characterized by completely frozen flow behind the shock wave; the gas behaves as a medium with constant specific heats corresponding to the instant accommodation of the vibrational degrees of freedom behind the shock wave. However, the greatest effect results if these degrees of freedom remain undisturbed. In the second limiting case, the gas is in a compressed layer under conditions of equilibrium dissociation. In the first case the shock lies farthest from the stagnation point and in the second case it is located closest to that point. Real nonequilibrium flows are bounded by these limiting cases, and the shock waves are located at intermediate positions.

These flows can be described by a nonequilibrium parameter that can be determined in the following way. From Eq. (4.67) it follows that, for flow conditions behind a normal shock, the quantity $1/C_{P_\infty}$ can be considered as a time scale for dissociation, and the parameter V_∞/C_{D_∞} as a scale of length for the flow. Then, the ratio of a linear dimension of the body to the linear scale of the flow can be used as a dimensionless parameter for nonequilibrium flow.

The linear dimension for a sphere can be chosen as its diameter D_N , and the nonequilibrium parameter in this case is

$$\Lambda = \frac{D_N C_{D_\infty}}{V_\infty}. \quad (25.5)$$

If Λ equals zero, the flow is undissociated (frozen), which results from an infinitely slow chemical reaction. Large values of Λ correspond to rapid reactions and, therefore, dissociation begins close to the shock

and includes almost the entire region between the shock and the body. For $\Lambda \rightarrow \infty$, equilibrium is reached immediately behind the shock.

To analyze the flow between the shock wave and the body, a local value of Λ can be used, calculated from the local velocity on the zero streamline; i.e.,

$$\lambda = \frac{D_N C_{p_\infty}}{V}. \quad (25.5a)$$

At the stagnation point, where $V = 0$, we obtain $\lambda = \infty$, and the dissociation is in equilibrium. This is because of the very low velocity near the stagnation point, which allows sufficient time for thermodynamic equilibrium to be established.

The extent of the nonequilibrium region can be estimated from the average velocity along the zero streamline, as was done above. If it is assumed that there is equilibrium flow on the body surface, the distribution of the concentrations of the atomic components along the normal to the wall are represented qualitatively by a gradual decrease in the direction of the shock wave, where the degree of dissociation is set equal to zero.

A theoretical profile of the concentrations can be calculated by a simultaneous solution of the flow equations and Eq. (4.67) in the vicinity of the stagnation point. Profiles for several special cases are presented in Fig. 250.

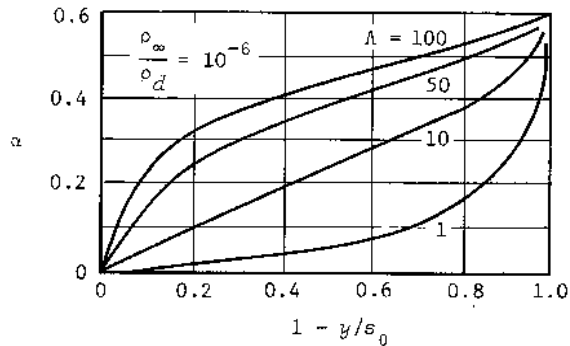


Fig. 250--Degree of dissociation along the axial streamline between the shock wave and the stagnation point

One of the results of the solution is the determination of the distance from the shock to the body. The variation in the relative displacement distance as a function of the nonequilibrium parameter Λ is presented in Fig. 251. It can be noted that the displacement in the two limiting cases, i.e., in frozen and equilibrium flows, can differ by a factor of two. The variation in the radius of curvature of the shock wave at the axis has approximately the same character.

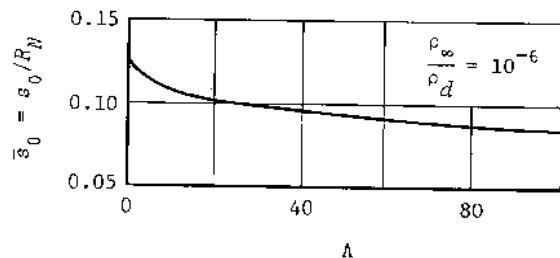


Fig. 251--Dimensionless shock-detachment distance as a function of the nonequilibrium parameter

The Case of Nonequilibrium at the Surface

The ratio of the characteristic times can be used for a preliminary estimate of the conditions for which chemical reactions occur at the wall. It is obvious that these reactions occur only for $\bar{t}_D \geq 1$, i.e., when the atoms reach the surface before they react. To estimate the extent of the length along the surface where chemical reactions take place, it is necessary to compare the characteristic time of the reaction with the characteristic dwell time of the particles in the nonequilibrium region in question. The dwell time is also a function of da/dt , which determines the rate of change in the degree of dissociation resulting from the disappearance of atoms due to recombination. The time of this disappearance is equal to the characteristic dwell time in the reaction zone and is determined from the equation

$$\frac{dt}{da} = \frac{1}{V} \frac{dx}{da}.$$

For an approximate estimate, it can be assumed that $dx/d\alpha \sim L/\alpha_0$, where α_0 is the nonequilibrium degree of dissociation at the stagnation point. Therefore, the dwell time can be represented in the form $L/\alpha_0 V$, where V is the velocity of a particle along the surface near the stagnation point. Assuming that this velocity is of the same order of magnitude as the average velocity between the wave and the body, $0.5V_0$, we get the ratio of the characteristic times:

$$\bar{t}_L = \frac{t_D V \alpha_0}{L} = \frac{t_D V_0 \alpha_0}{2L}, \quad (25.6)$$

which can be rewritten as

$$\bar{L} \bar{t}_L = \bar{t}_D \alpha_0 \bar{s}_0, \quad (25.6a)$$

where $\bar{L} = L/R_N$. In the zone of reaction, $\bar{t}_L \geq 1$, and the length of this region from the stagnation point is given by

$$\bar{L} = \bar{t}_D \alpha_0 \bar{s}_0. \quad (25.7)$$

As an illustration, the example used previously can be analyzed for an altitude of 50 km instead of 30 km. The density ratio (or the altitude function f_p) is decreased by a factor of 19 compared with that for 30 km, and the relaxation time is increased by the factor $(19)^2 = 361$. Therefore, the ratio of the characteristic times is $\bar{t}_D = 361/26 = 14$. For $\bar{s}_0 = 0.074$ and $\alpha_0 = 0.5$, we obtain $\bar{L} = 14 \cdot 0.5 \cdot 0.074 = 0.52$, and the length of the nonequilibrium zone is $L = 0.26$ m for a sphere with $R_N = 0.5$ m.

Over this length of the surface, atoms enter the boundary layer without having entered into chemical reactions. The process of recombination is completed in the boundary layer, producing well-known effects on the friction and heat transfer. However, it should be stressed that, in general, the pressure distribution is not altered by the nonequilibrium effects.

A more accurate definition of the flow regime in the stagnation zone (at the stagnation point and in some region downstream) provides

an estimate of the change in density and temperature if the flow in this region is not in equilibrium. The temperature increases and the density decreases at the outer edge of the boundary layer compared with the equilibrium state. It can be assumed that, despite the temperature increase, the heat flux to the surface decreases somewhat due to the lower density.

All of the calculations so far have been made on the assumption that the recombination-rate parameter k_R is not a function of temperature. However, temperature actually has considerable influence on this parameter, and according to some experimental data for oxygen⁽¹⁷⁾

$$k_R = 8.4 \cdot 10^{14} \left(\frac{3500}{T} \right)^2 \text{ cm}^6/\text{mole}^2 \text{ sec.} \quad (25.8)$$

This temperature factor can be applied to the expression for the relaxation time, resulting in a corrected relaxation time:

$$\bar{\tau}'_D = \bar{\tau}_D \left(\frac{T}{3500} \right)^2. \quad (25.9)$$

Relaxation Effects for Expansion from Equilibrium Conditions
at the Stagnation Point

In the case considered above, the nonequilibrium region included part of the surface of the body. Another case of interest is that for which the air in the vicinity of the stagnation point is in thermodynamic equilibrium. However, this equilibrium can be disturbed as the flow expands over the surface, because the inert degrees of freedom will not have time to adjust to the rapid changes in temperature and pressure.

This type of nonequilibrium flow will be frozen in the sense that the expansion occurs only with the participation of the active degrees of freedom and with fixed (frozen) thermodynamic parameters, i.e., with the specific heat and degree of dissociation established by the condition of thermodynamic equilibrium at the stagnation point. Therefore, the temperature of the isentropic expanding flow is determined by the translational and rotational degrees of freedom and will be less than for equilibrium conditions. As the particles continue on their paths,

relaxation effects in the gas will increase the internal energy as the inert degrees of freedom begin to adjust, and the temperature will increase compared with that for frozen flow. Since the heat input is irreversible, this process is accompanied by an increase in entropy.

An equilibrium flow of gas can also be maintained for a slow flow over the surface in the vicinity of the stagnation point, i.e., when the relaxation times of the inert degrees of freedom are small compared with the characteristic times of the process. The characteristic time can be written in the form

$$\Delta t = \frac{dt}{dT} T. \quad (25.10)$$

This expression represents a quantity inversely proportional to the rate of change of temperature in an adiabatic flow of a gas along a streamline.

If Δt is considerably larger than the maximum relaxation time t_D of the inert degrees of freedom, equilibrium can be maintained. The condition for maintaining equilibrium can be given, for example, in the form of an inequality $t_D/\Delta t < 10^{-3}$.

To determine the equilibrium region in the vicinity of the stagnation point, it is necessary to calculate the ratio $t_D/\Delta t$ for various points on the surface and to compare it with the value above. For this purpose, the temperature distribution as well as the velocity along the surface are calculated for equilibrium conditions.

Assuming that the velocity varies approximately linearly with time, we can find the variation of temperature with time and, therefore, compute the value Δt at each point. The distribution of $t_D/\Delta t$ is presented in Fig. 252 for flow around a sphere with $R_N = 0.61$ m. The gas used was nitrogen at $M_\infty = 24$ for conditions corresponding to an altitude of 37 km. For a maximum value of $t_D/\Delta t = 10^{-3}$, it is apparent that equilibrium flow for both the inert degrees of freedom, vibration, and recombination occurs only up to values of the central angle φ less than 30° . For larger values, equilibrium is not possible, and the gas flows as a frozen medium.

Calculations show that the local Reynolds number and Mach number of the frozen and equilibrium flows differ little, although the temperature in the frozen flow is 20 percent less than in equilibrium flow for the example in question.

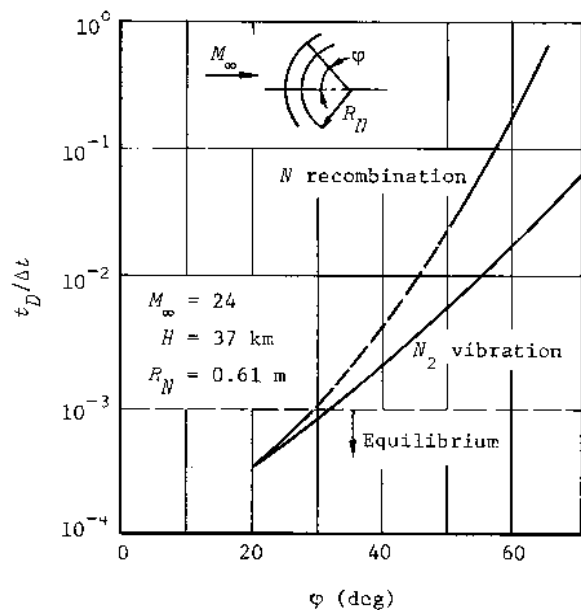


Fig. 252--Equilibrium and frozen flow regions around a sphere

Chapter VIII

SKIN FRICTION AND HEAT TRANSFER ON BLUNT BODIES

Editor's Introduction

MOST OF THE FIRST SECTION (§ 26) of this chapter consists of a summary of the analysis of Moeckel⁽¹⁾ on the effects of bluntness in delaying boundary layer transition. The results provide an estimate of the bluntness required to delay transition to the point at which the thickness of the boundary layer and the entropy layer are equal. Wilson (J. Spacecraft and Rockets, July-August 1965) has solved the more general problem of the growth of a laminar boundary layer on a blunted cone, giving results for the effect of blunting on skin friction, heat transfer, and the flow conditions at the outer edge of the boundary layer. The local skin friction and heat transfer are reduced significantly by the slight blunting of the nose. The decay of the entropy layer far back on the body (discussed qualitatively at the end of Section 26) is also calculated by Wilson, and the effect of this decay on the heat transfer and skin friction is evaluated (discussed briefly on pp. 723-724).

Formulas for heat transfer at the stagnation point are given in Section 27, and the effects of nonequilibrium chemistry are discussed briefly on pp. 690-691. Tong (AIAA J., April 1965) shows that the non-equilibrium-flow Stanton numbers for noncatalytic and fully catalytic surfaces lie on the same curve if the enthalpy at the wall is defined as $i_w = i_{deW} + (i_w)_o$, where $(i_w)_o$ is the wall enthalpy with no dissociation. Tong gives correlation curves for determining the atom concentration c_w for a noncatalytic wall. Inger (J. Spacecraft and Rockets, March 1966) presents a relatively simple analytical method for predicting the effects of nonequilibrium dissociation on heat transfer to bodies with arbitrary surface catalyticity. The method is applicable downstream on the body as well as at the stagnation point.

Radiative heat transfer from the high temperature shock layer about the nose of a blunt body has been the subject of extensive study in recent years, particularly with regard to radiation cooling and self-absorption of radiation in shock layers. Representative of these studies are those of Hoshizaki and Wilson (AIAA J., January 1967) and Hoshizaki and Lasher (AIAA J., August 1968). They show that the combined effects of radiation cooling and self-absorption result in a significant reduction in the radiative flux to the surface, but have little effect on convective heat transfer; the total heating rate at the surface is almost

independent of nose radius. Ablation products of typical ablator materials (particularly carbon atoms) can produce a substantial reduction in radiative heat transfer at the surface. Anderson (AIAA J., November 1968) has published a simple and reasonably accurate method for estimating radiative heat transfer with radiation cooling and self-absorption.

A very general computer solution for the laminar boundary layer has been developed by Smith and co-workers and described in a series of papers; see for example, Smith and Clulter (AIAA J., April 1965) and Smith and Jaffe (AIAA J., April 1966). The method is valid for nonequilibrium dissociating air with finite reaction rates for axisymmetric or two-dimensional flow over surfaces with arbitrary catalyticity.

Experimental data for turbulent heat transfer on blunt and sharp-nosed bodies of revolution have been correlated by Zoby and Sullivan (NASA TN D-3802, January 1967); the results confirm the validity of Eqs. (27.76) to (27.78). Simple empirical formulas based on the results of Ref. 9 have been proposed by Arthur, Schultz, and Guard (J. Spacecraft and Rockets, October 1966).

Experimental results for the drag of blunted cones at high Mach numbers have been used by Whitfield and Griffith (AIAA J., October 1964) to evaluate theoretical estimates of viscous contributions to the drag. The major contributions resulted from the usual skin friction drag and the effects of transverse curvature, boundary layer displacement effects being small.

§ 26. CHANGES IN FLOW CHARACTERISTICS DUE TO BLUNTINGTHICKNESS OF THE INVISCID LAYER AT LOW VELOCITIES

AS HAS BEEN MENTIONED previously, the most important effect of blunting appears as a decrease in local Reynolds numbers, resulting in an aft movement of the transition point from laminar to turbulent flow, and thus in a reduction in friction and heat transfer.

The decrease in Reynolds number is caused by the fact that the boundary layer is located in a flow region of lesser velocity than on a pointed body due to the strong shock wave in front of the blunt body. Since this causes the transition point to shift toward the base of the body, the heat flux will be less. If the maximum reduction in heat transfer were required, the blunting would have to be such that the laminar layer completely covered the surface, i.e., such that the transition point lay at the base of the body. It should be noted that a large length of laminar flow is only possible for absolutely smooth surfaces.

The location of the transition point is determined by the transition Reynolds number Re_{tr} , which in turn can be determined from the velocity V_δ at the outer edge of the boundary layer. Therefore, for completely laminar flow, the blunting should be sufficient so that the flow in the high-entropy "inviscid" layer[†] (covering the boundary layer) has the necessary value of V_δ at the end of the body.

Studies⁽¹⁾ have shown that the outer edge of the high-entropy inviscid layer lies approximately on the streamline passing through the sonic point on a detached shock wave (Fig. 196). The location of the sonic point on the shock can be calculated for the general case including dissociation, as was discussed earlier. If the radial coordinate

[†]Editor's note: This is often called the entropy layer in American literature. We will continue to use the Russian term.

of this point is r_S , the rate of flow of gas through a cross section with an area πr_S^2 will be $\rho_\infty V_\infty \pi r_S^2$. The same amount of gas flows through the low Reynolds number layer having a thickness Δ (Fig. 196). In what follows we will neglect the effect of the boundary layer on the extent of the high-entropy layer. The thickness Δ corresponds to a section of the body with a radius r , so that

$$\rho_\infty V_\infty r_S^2 = 2\rho V r \Delta,$$

whence the thickness of the inviscid layer is

$$\Delta = \frac{1}{2} \frac{\rho_\infty}{\rho} \frac{r_S^2}{r} \frac{V_\infty}{V}, \quad (26.1)$$

where ρ and V are the density and velocity at the section under consideration, calculated for inviscid flow along the surface. Although these parameters should be determined including the effect of blunting, the calculations can sometimes be simplified if the pressure at some distance from the blunt nose is assumed to be the same as that on a pointed body. This was evident in the case of flow around a blunt cone.

The local density, temperature, enthalpy, and speed of sound can be determined at a given cross section from the local pressure and entropy behind the normal part of the shock wave by using the graphs or tables of the thermodynamic functions of air. Next, using the equation $i_0 = i + V^2/2$, we can compute the local velocity and Mach number. Thus, the influence of dissociation or the variation of the specific heat of the gas on passing through the shock wave can be considered.

The gasdynamic and thermodynamic parameters at stations far downstream from the nose can be computed with sufficient accuracy by using the relations for isentropic gas flow with constant specific heats. In this case, the equations for velocity, Mach number, and density have the following form:

$$\frac{V^2}{V_\infty^2} = \frac{1 - \left(\frac{\rho}{\rho_0} \frac{P_0}{P_0'}\right)^{(\gamma-1)/\gamma}}{1 - \left(\frac{P_\infty}{P_0}\right)^{(\gamma-1)/\gamma}}, \quad (26.2)$$

$$M^2 = \frac{2}{\gamma - 1} \left[\left(\frac{P'_0}{P_0} \frac{P_0}{P} \right)^{(\gamma-1)/\gamma} - 1 \right], \quad (26.3)$$

$$\frac{P}{P_\infty} = \frac{\frac{c_0}{c_\infty} \frac{P'_0}{P_0}}{\left(1 + \frac{\gamma-1}{2} M^2 \right)^{1/(\gamma-1)}}. \quad (26.4)$$

To increase the accuracy of the calculations, the stagnation pressure can be selected as an average between the values at the points *B* and *S* (Fig. 196, p. 545), the first of which is located directly behind the normal part of the shock wave and the second at the sonic point.

It is apparent that the difference in the values of the parameters on the surfaces of pointed and blunt bodies is caused by unequal losses in total pressure through the shock wave. Since the shock in the vicinity of the nose is stronger in front of a blunt body, the value of P'_0 will be less than for a pointed body. Then the local velocities, Mach numbers, and densities will also be less, as can be determined from Eqs. (26.2) through (26.4). The local Mach numbers on a blunt cone have been calculated from Eq. (26.3) assuming that the pressure is the same as on a pointed conical surface; the results are shown in Fig. 253.

If the relations for velocity and density are introduced into Eq. (26.1), the thickness of the low Reynolds number layer can be determined as a function of the body station provided the location of the sonic point on the shock wave is known. The cross-sectional area of this layer is equal to $2\pi r\Delta$. Shown in Fig. 254 is the ratio of the areas

$$\frac{F_S}{F_{SN}} = \frac{2\pi r\Delta}{r r_{SN}^2} = \frac{r_S^2}{r_{SN}^2} \frac{\rho_\infty}{\rho} \frac{V_\infty}{V}, \quad (26.1a)$$

where r_{SN} is the radial coordinate of the sonic point on the surface of a spherical nose. It was assumed in these calculations that the radius to this point is twice as large as that to the sonic point on the shock wave; i.e., the ratio r_S^2/r_{SN}^2 in Eq. (26.1a) is equal to 0.25.

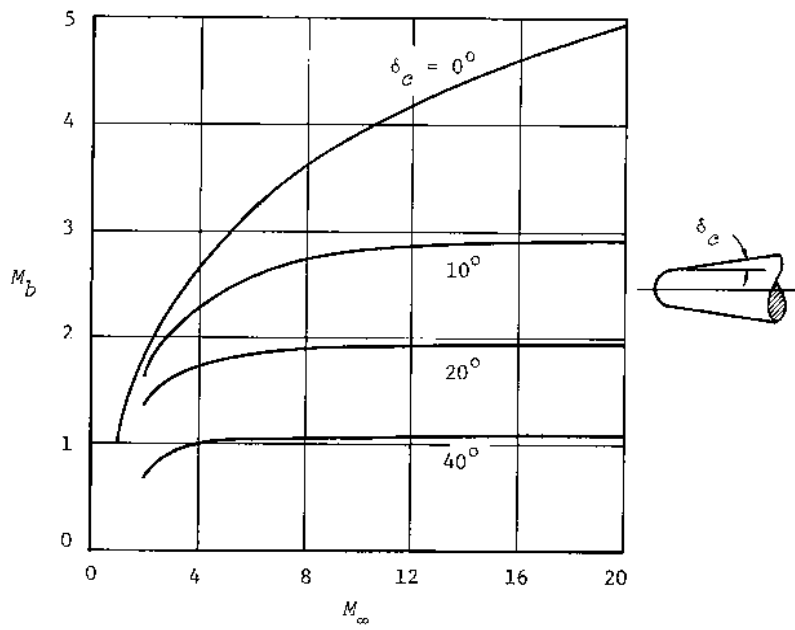


Fig. 253--Mach number on the surface of blunt cones in inviscid flow

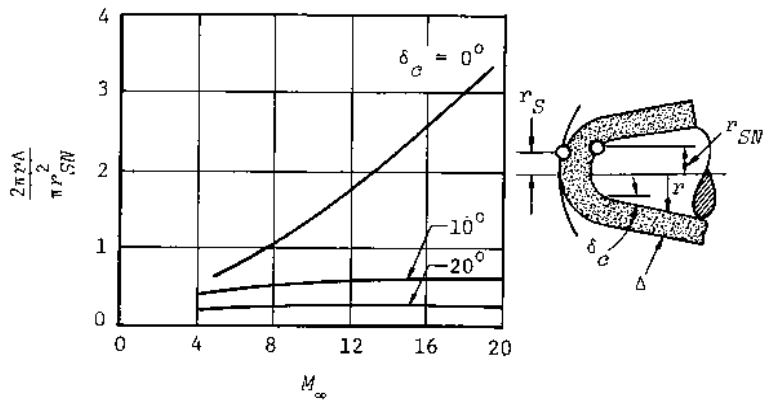


Fig. 254--Ratio of the area of the low-velocity layer on cones to the area πr_{SN}^2

It is evident from Fig. 254 that, for the assumptions made, the area ratio represented by this expression is of the order of unity for spherically blunted cones with small angles δ_g . If cones with flat noses are considered, it is clear from physical considerations that the low-velocity layer will be somewhat thicker. If it is assumed that the co-ordinates of the sonic points on the flat nose and the shock wave are approximately identical, i.e., $r_S = r_{SN} = R_N$, the area ratio F_S/F_{SN} will be four times larger than for a cone with a spherical nose, according to Eq. (26.1a). Thus, for the calculation of the thickness of the low-velocity layer, Eq. (26.1) can be used or, if the relation for the area ratio F_S/F_{SN} is given, it can be determined from

$$\Delta = \frac{F_S}{F_{SN}} \frac{r_{SN}^2}{2r}. \quad (26.5)$$

THE CALCULATION OF THE REQUIRED BLUNTING

The bluntness required (in terms of the radius r_{SN}) to maintain laminar flow to a given station can be estimated by imposing the condition that the thickness of the laminar layer at the transition point, i.e., for the required transition Reynolds number, be equal to the thickness of the inviscid low-velocity layer. Therefore, the conditions are

$$\delta_L = \frac{1}{2} \frac{\rho_\infty}{\rho} \frac{r_S^2}{r_{tr}} \frac{V_\infty}{\gamma}, \quad (26.6)$$

$$\delta_L = \frac{F_S}{F_{SN}} \frac{r_{SN}^2}{2r_{tr}},$$

where r_{tr} is the radius of the blunt cone at the transition point.

In particular, it follows from the second equation of Eq. (26.6) that if $F_S/F_{SN} \approx 1$, the coordinate r_{SN} should be of the order of $\sqrt{2r_{tr}\delta_L}$, which is the geometric mean of the diameter of the body and the thickness of the boundary layer at the transition point.

The thickness of the laminar layer at the transition point on the surface of a blunt cone can be determined from the transition Reynolds number Re_{tr}^* and the equation for a flat plate

$$\frac{\delta_L^{pl}}{x_{tr}} = \frac{4.64}{\sqrt{Re_{tr}^*}},$$

in which x_{tr} is the distance to the transition point, and the transition Reynolds number $Re_{tr}^* = Vx_{tr}^p/\nu^*$ is calculated in the general case from the effective parameters of inviscid flow. Since the transition Reynolds number is usually assumed to be a known quantity, the length of the laminar portion can be calculated as $x_{tr} = \nu^* Re_{tr}^* / V_0^*$, and the thickness of the boundary layer at the transition point is

$$\delta_L = \frac{1}{\sqrt{3}} \delta_L^{pl} = \frac{1}{\sqrt{3}} x_{tr} \left(\frac{\delta_L^{pl}}{x_{tr}} \right). \quad (26.7)$$

For the case of constant specific heats, the equation for the calculation of the required blunting takes the form

$$\Pi = \frac{r_{SN}^2}{x_{tr} r_{tr}} = \frac{16.1}{\sqrt{Re_{tr}^*}} \frac{p'_0}{p_0} \left(\frac{1 + \frac{\gamma - 1}{2} M_\infty^2}{1 + \frac{\gamma - 1}{2} M^2} \right)^{\frac{\gamma+1}{2(\gamma-1)}} \frac{M}{M_\infty} \frac{r_{SN}^2}{r_S^2}. \quad (26.8)$$

As was indicated, Re_{tr}^* is usually given in this equation and the ratios p'_0/p_0 , r_{SN}^2/r_S^2 , and the Mach number M on the blunt cone are determined from the known value of M_∞ . In the case of rough calculations, r_{SN}/r_S can be assumed equal to 2 and 1, respectively, for a spherical and a flat nose.

The radius r_{tr} in Eq. (26.8) can be written in the form

$$r_{tr} = r_N + x_{tr} \sin \delta_c,$$

where r_N is the radius of the body at the tangency point between the spherical tip and the conical afterbody. In turn, the coordinate x_{tr} is determined from the given transition Reynolds number. To simplify

the calculations, it is possible to use the inviscid flow parameters obtained without considering the effective temperature instead of the effective parameters μ^* and ρ^* .

After determining the quantity Π and the coordinate x_{tr} , we can compute the required blunting r_{SN} or, more precisely, the coordinate of the sonic point on the nose, from

$$r_{SN}^2 = \Pi x_{tr} (r_N + x_{tr} \sin \delta_c). \quad (26.8a)$$

For a flat nose, this coordinate gives the magnitude of the radius of the flat surface, since $r_{SN} = r_N$, but for a spherical nose the radius is found from $R_N = r_{SN}/\sin \varphi$, where the angle φ is the location of the sonic point on a sphere (see Fig. 203, p. 565).

THE INFLUENCE OF BLUNTING ON THE EXTENT OF THE LAMINAR BOUNDARY LAYER

It is of interest to estimate the relative movement of the transition point due to blunting, if we assume that the transition Reynolds numbers are identical for pointed and blunt bodies (denoted by the subscripts p and b). For equal Reynolds numbers,

$$\left(\frac{V_{ox}}{\mu} \right)_p = \left(\frac{V_{ox}}{\mu} \right)_b,$$

and the relative shift of the transition point is

$$\frac{(x_{tr})_b}{(x_{tr})_p} = \left(\frac{V_p}{\mu} \right)_p \left(\frac{\mu}{V_b x} \right)_b,$$

where all the parameters entering into this equation pertain to the transition point. However, for conical bodies the local flow parameters are constant along the surfaces, so the right-hand side of the previous expression simply represents the ratio of the local Reynolds numbers at a given station x :

$$\frac{(x_{tr})_b}{(x_{tr})_c} = \left(\frac{V_{ox}}{\mu} \right)_c \left(\frac{\mu}{V_{bx}} \right)_b = \frac{Re_c}{Re_b}. \quad (26.9)$$

The subscripts *c* and *b* now refer to pointed and blunt cones, respectively. Thus, the ratio of the transition points with and without blunting is directly proportional to the ratio of the local Reynolds numbers for the pointed and blunt cones:

$$\frac{Re_c}{Re_b} = \frac{V_c}{V_b} \frac{\rho_c}{\rho_b} \frac{u_b}{u_c}$$

Let us assume that $u_b/u_c = (T_b/T_c)^n$ and that the pressures on the pointed and blunt cones are identical, so that $\rho_c/\rho_b = T_b/T_c$. Noting that

$$T = \frac{T_0}{1 + \frac{\gamma - 1}{2} M^2},$$

we obtain for the ratio of the Reynolds numbers

$$\frac{Re_c}{Re_b} = \frac{M_c}{M_b} \left[\frac{1 + \frac{\gamma - 1}{2} M_c^2}{1 + \frac{\gamma - 1}{2} M_b^2} \right]^{n+\frac{1}{2}}. \quad (26.10)$$

The reciprocal of this ratio, which indicates the decrease in local Reynolds number due to blunting, is presented in Fig. 255. It is evident that a substantial decrease in local Reynolds number and, consequently, a considerable aft movement of the transition point, are characteristic of slender cones, and these effects are more significant for large Mach numbers. For example, according to the data in Fig. 255 for a blunt 10° cone at $M_\infty = 8$ and 15, the extent of the laminar boundary layer is increased by a factor of approximately 10 to 30.

SOME DATA ON THE TRANSITION REYNOLDS NUMBER

As we have seen, it is necessary to know at least a tentative value of the transition Reynolds number for the calculation of the required blunting. Unfortunately, there are as yet no theoretical methods for calculating this value, because at present the very nature of turbulence is not clear. Therefore, the estimation of Re_{tr} must be based

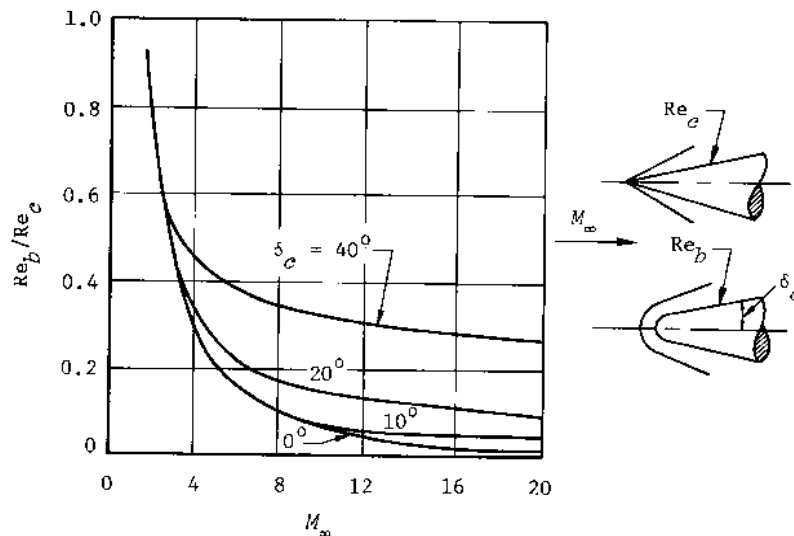


Fig. 255--Ratio of the Reynolds numbers on blunt and pointed cones

on available experimental data, which enable us to make a quantitative estimate and also to analyze, qualitatively, the phenomenon of laminar boundary layer stability and the process of transition to turbulence.

For example, it has been established that one of the main reasons for turbulence is the instability of the laminar boundary layer at large Reynolds numbers. The accidental formation of perturbations in the boundary layer due to the turbulence of the external flow or the roughness of the surface are not damped at large Reynolds numbers, making the boundary layer turbulent. Therefore, to maintain laminar flow, it is advisable to maintain a smooth surface.

If it is taken into account that the turbulence of the external flow under flight conditions in the atmosphere is negligibly small, it is possible to increase the transition Reynolds number considerably for a smooth wall. Nevertheless, an unstable condition remains, and it is desirable to take other measures to stabilize the laminar boundary layer. It has been noted that if the wall is cooled, the stability of the layer increases, because the density of the gas increases with a reduction in the gas temperature close to the surface and, consequently, the kinetic energy

of the gas increases. It is apparent that particles with large energy are less subject to the influence of perturbing pulsations. At the same time, it is worth noting that at very high velocities the Reynolds number plays a less significant role as the criterion of stability compared with such parameters as the relative temperature of the wall T_w/T_δ (T_w/T_∞ or T_w/T_r) and the Mach number M_δ at the outside edge of the boundary layer (or for a given body, M_∞).

Theoretical studies⁽¹⁾ enable us to determine the values of the relative wall temperature and local Mach number required for complete stability of the laminar boundary layer (Fig. 256). It is evident from

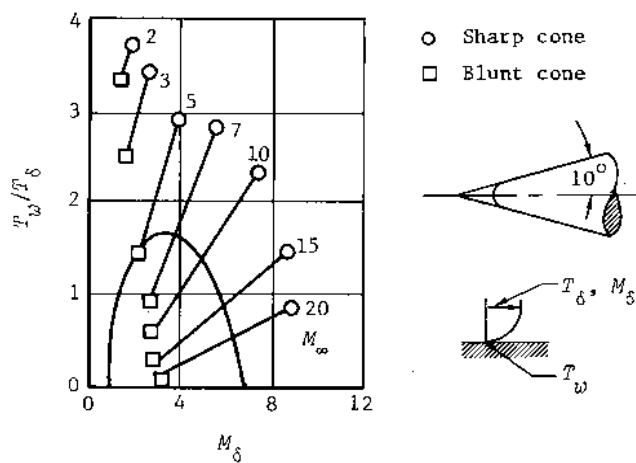


Fig. 256—Effect of blunting on the stability of the laminar boundary layer

Fig. 256 that the boundary layer cannot be stabilized at $M_\delta > 8$ irrespective of the intensity of the cooling. It can also be noted that the stability boundaries are broadened with a decrease in the ratio T_w/T_δ . Hence it follows that a decrease in speed of the local external flow, which is accompanied by a decrease in M_δ and an increase in T_δ , will be a stabilizing influence (if, at the same time, the wall temperature remains constant due to proper cooling). It was mentioned above that this can occur when a blunt instead of a pointed body is used.

Thus, blunting is an important means of stabilizing a laminar boundary layer, since it shifts the conditions at the external edge of the boundary layer from the unstable region toward the zone of stability, as Fig. 256 shows.

It should be noted that the region of instability located outside the curve in Fig. 256 is not necessarily a region of complete turbulence. Turbulent bursts are characteristic of the laminar layer in this region. Their formation is related to the inception of transition from laminar to turbulent flow. The transition is completed at the transition Reynolds number.

The experimental results obtained by Van Driest⁽²⁾ for a fixed Reynolds number are presented in Fig. 257. The experimental model was a

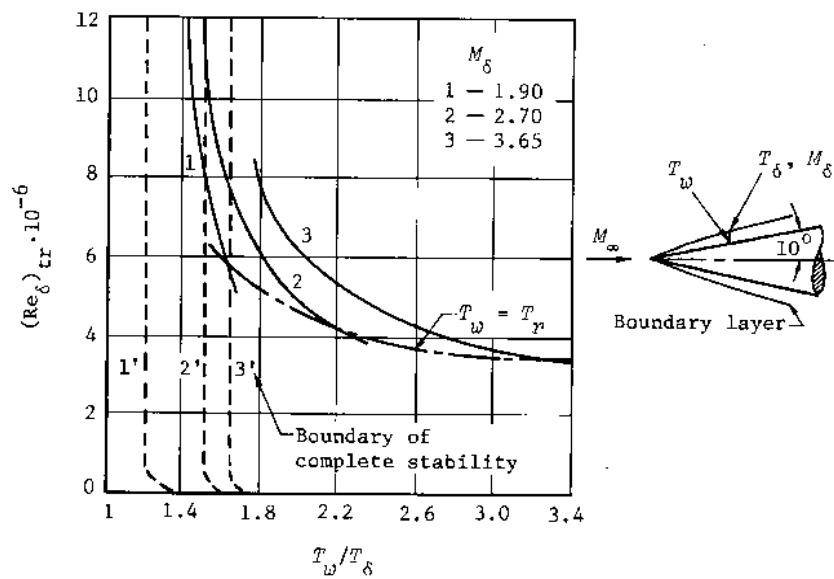


Fig. 257--Experimental data on the transition Reynolds number

pointed cone and was cooled from within, which ensured a variation in the ratio T_w/T_δ . The tests were conducted for various Mach numbers. Also presented in Fig. 257 are the theoretical curves 1', 2', and 3' for the variation in the critical Reynolds numbers, corresponding to

the boundaries of complete stability. An analysis of the curves shows that the transition Reynolds number increases with a decrease in the wall temperature, while the character of this variation is a function of M_δ .

To show this relation, the curves are replotted in Fig. 258 so that the ratio T_w/T_r is represented as a parameter. First, it should

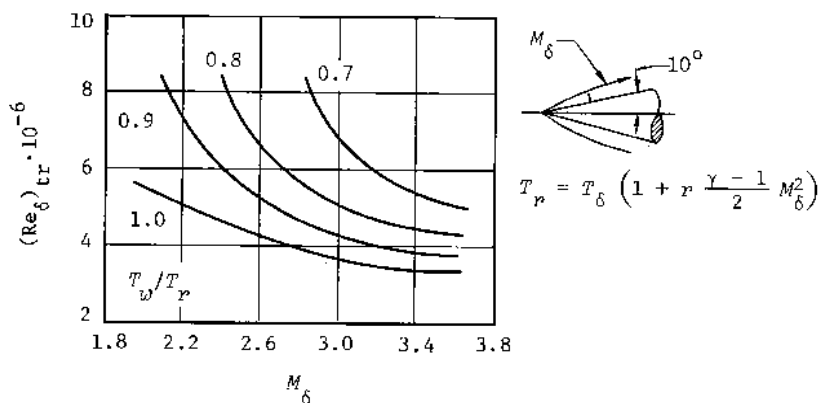


Fig. 258—Experimental data on the transition Reynolds number

be noted that the transition Reynolds number remains practically constant for M_δ greater than about 3.8. For a cooled surface ($T_w/T_r < 1$), the transition Reynolds number increases, and the estimate of the variation in Re_{tr} can be based on the fact that it is approximately inversely proportional to the relative temperature of the wall T_w/T_r , which can in turn be determined from the expression

$$\frac{T_w}{T_r} = \frac{T_w/T_\delta}{1 + r \frac{\gamma - 1}{2} M_\delta^2}.$$

The pressure gradient along the wall is known to have an influence on Re_{tr} . For example, a negative gradient is favorable for an increase in stability and, thus, for an increase in the critical and transition

Reynolds numbers. On the other hand, with a pressure increase in the direction of flow (i.e., a positive gradient), conditions are created for premature turbulence and the value of Re_{tr} decreases. The curve in Fig. 259 is for subsonic velocities and allows an estimate of the influence of the longitudinal pressure gradient on the transition Reynolds number. This curve is calculated from the empirical equation

$$\frac{(Re_{tr})_p}{(Re_{tr})_0} = \frac{1}{(1 - 0.048\lambda)^2},$$

where $\lambda = -18\pi dC_{p\delta}/dx$, and the pressure coefficient at the edge of the layer is $C_{p\delta} = 2p/\rho_\delta V_\delta^2$.

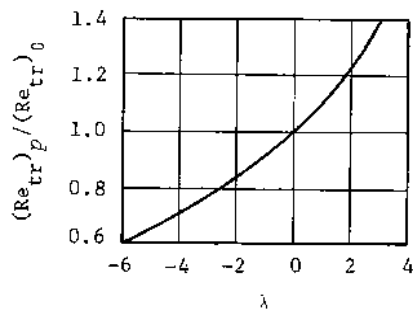


Fig. 259--Effect of longitudinal pressure gradient on the transition Reynolds number

If we consider flow around a blunt body (e.g., a cone), we find regions with various types of pressure variation on the surface. Directly behind the stagnation point, the pressure decreases and, therefore, a negative pressure gradient is established, favorable to stabilization of the laminar boundary layer. A deceleration of the flow begins at some distance from the nose, resulting in a positive pressure gradient. Generally speaking, this leads to a decrease in stability, although in practice the effect is small. Nevertheless, it is expedient to allow for this influence in the final selection of the blunting dimension by increasing it compared with the calculated dimension.

EXAMPLE

Let us calculate the location of the transition point for $M_\infty = 10$ on the smooth surface of a spherically blunted 10° cone. The Mach number on the blunt cone is determined from Fig. 253 as $M_B = 2.8$. From Fig. 258 the transition Reynolds number is $8.7 \cdot 10^6$, if it is assumed that the relative wall temperature $T_w/T_r = 0.7$, which corresponds to the ratio

$$\frac{T_w}{T_\delta} = 0.7 \left(1 + \frac{\gamma - 1}{2} r M_B^2 \right) = 0.7 [1 + 0.169(2.8)^2] = 1.58.$$

The location of the transition point on a sharp 10° cone is determined from the equation

$$x_{tr} = Re_{tr} \left(\frac{M_\infty}{M_c} \frac{v_\infty}{V_\infty} \right) \left[\frac{1 + \frac{\gamma - 1}{2} M_c^2}{1 + \frac{\gamma - 1}{2} M_\infty^2} \right]^{\frac{\gamma+1}{2(\gamma-1)} - n} \quad (26.11)$$

For a 10° cone, the local Mach number is $M_c = 7.6$. For flight at an altitude of approximately 24 km, the kinematic viscosity coefficient is given in Appendix A as $v_\infty = 0.2991 \cdot 10^{-3}$. Assuming that $n = 1$, we obtain the value $x_{tr} = 0.438$ m from Eq. (26.11).

To determine the corresponding length for the blunt cone, the decrease in the local Reynolds number can be estimated from Fig. 255, i.e., $Re_b/Re_c = 0.071$. Then the transition point on the blunt cone is located at

$$x_{tr} = \frac{0.438}{0.071} = 6.2 \text{ m.}$$

The radial coordinate of the sonic point on the shock wave (r_S) can be obtained from the equation for the shock wave, $x = -s_0 + r^2/2R_{s0}$, giving

$$\frac{r_S}{R_N} = \frac{R_{s0}/R_N}{(dr/dr)_S}.$$

The dimensionless radius of curvature of the shock, R_{s0}/R_N , is a function of the static density ratio ρ_s/ρ_∞ across a normal shock. For low altitudes at $M_\infty = 10$, the density ratio $\rho_s/\rho_\infty = 7.4$, including the effects

of dissociation (Fig. 41). The shock wave curvature is obtained from Fig. 209 or from the approximate equation in the footnote on p. 572 as $P_{S0}/R_N = 1.20$. The shock wave angle at the sonic point is determined from Fig. 203 as $\delta_S = 67.5^\circ$, and $(dr/dx)_S = \tan \delta_{SS} = 2.41$. Therefore, $r_S/R_N = 1.2/2.41 \approx 0.5$. From Fig. 203, the angular coordinate of the sonic point on the sphere is $\varphi_{SN} = 42.5^\circ$, from which the dimensionless radial coordinate to the sonic point on the body is obtained as $r_{SN}/R_N = \sin \varphi_{SN} = 0.676$. Thus, the ratio of the coordinates of the sonic points is $r_{SN}/r_S = 0.676/0.5 = 1.35$.

The stagnation pressure ratio p'_0/p_0 can be assumed to be the average between the values at the apex and at the sonic point on the shock. Using Eq. (4.33a) and Mach number components normal to the shock of $M_\infty = 10$ and $M_\infty \sin \theta_s = 10 \sin 67.5^\circ = 9.24$, we can compute the ratio of the stagnation pressure behind the shock to that in front as the average:

$$\frac{p'_0}{p_0} = \frac{3.14 + 4.52}{2} \cdot 10^{-3} = 3.83 \cdot 10^{-3}.$$

As a result of substituting these values into Eq. (26.8), we find the value of the function Π :

$$\Pi = \frac{r_{SN}^2}{x_{tr} r_{tr}} = 5.95 \cdot 10^{-3}.$$

The radius of the body at the tangency point is related to the radius at the sonic point by $r_N = r_{SN} \cos \delta_c / \sin \varphi_{SN}$. Substituting this expression into Eq. (26.8a) and solving the result for r_{SN} , we obtain the radial coordinate to the sonic point on the spherical nose:

$$r_{SN} = \frac{\pi x_{tr} \cos \delta_c}{2 \sin \varphi_{SN}} + \sqrt{\left(\frac{\pi x_{tr} \cos \delta_c}{2 \sin \varphi_{SN}} \right)^2 + \pi x_{tr}^2 \sin \delta_c}.$$

Using the numerical values calculated above, we obtain $r_{SN} = 22.9$ cm. The radius of the spherical blunting is then

$$R_N = \frac{r_{SN}}{\sin \varphi_{SN}} = 33.9 \text{ cm.}$$

The body radius at the transition point is 1.4 m, and the ratio of the cross-sectional area of the blunt nose to the cross-sectional area of the cone at the transition point is approximately $\bar{S}_{\text{sph}} = 0.06$. If the transition point is located at the base, the entire surface of the cone is covered by the laminar boundary layer, and the total heat flux corresponds to that for completely laminar flow.

This example can be simplified if part of the shock wave is represented in the form of a circular arc with a radius R_{s0} . Obviously, the accuracy of this approximation increases with an increase in Mach number. In this case,

$$r_S = R_{s0} \sin \omega_S = R_{s0} \cos \theta_{sS}, \quad r_{SN} = R_N \sin \varphi_{SN}.$$

Therefore,

$$\frac{r_{SN}}{r_S} = \frac{R_N}{R_{s0}} \frac{\sin \varphi_{SN}}{\cos \theta_{sS}} = 1.47.$$

The blunting parameters then can be calculated from these data.

INFLUENCE OF THE BOUNDARY LAYER

The required blunting computed by the method described above can be refined if the effect of the displacement thickness of the boundary layer is taken into account. In fact, it follows from physical considerations that the effect of viscosity on the flow can be accounted for, as was noted earlier, if we consider inviscid flow around an arbitrary body with the lateral dimensions increased by a displacement thickness δ_L^* . Thus, the low-velocity layer is displaced by a value of δ_L^* , and the calculation of the required blunting must be based on

$$\Delta = \delta_L - \delta_L^*.$$

The estimation of the displacement thickness can be based on the relation for boundary layer thickness; i.e., it is assumed that on a cone

$$(\delta_L^*)^c = \frac{1}{\sqrt{3}} (\delta_L^*)^{pl}.$$

In turn, the displacement thickness $(\delta_L^*)^{pl}$, calculated from the effective parameters, can be found from the equation for incompressible flow; i.e.,

$$(\delta_L^*)^{pl} = \frac{3}{8} \delta_L^{pl}. \quad (26.12)$$

Thus, if the influence of the displacement thickness is taken into account, the relation for a blunt cone is given by

$$\Delta = \delta_L - \delta_L^* = 0.361x_{tr} \left(\frac{\delta_L^{pl}}{x_{tr}} \right). \quad (26.13)$$

Comparing this with Eq. (26.7), we can conclude that the required blunting is decreased by the effects of the boundary layer displacement.

EFFECTS OF VARIOUS ASSUMPTIONS IN THE THEORY OF THE INVISCID LAYER

A number of assumptions have been made to simplify the study of the flow processes involved in the important concept of the high-entropy, low-velocity, inviscid layer. One of these assumptions is based on the fact that the velocities and other flow parameters across a given section of the high-entropy layer are taken as constants. Actually, all these parameters vary and, strictly speaking, the influence of this variation on the formation of the boundary layer should be taken into account, particularly the influence of the velocity gradient occurring in the high-entropy layer. The assumption of constant flow properties is warranted in those cases where the thickness of the low-velocity inviscid layer is small compared with the boundary layer thickness, and, therefore, the influence of the transverse velocity gradient is insignificant. In this case the boundary layer develops in that section of the inviscid layer where the flow parameters are almost constant.

The second assumption results from the neglect of the interaction between the inviscid high-entropy layer and the viscous boundary layer. This assumption is warranted for those regions where the boundary layer

thickness is small. However, as was shown, this interaction can be taken into account by a simple method if the concept of the relative displacement thickness is used.

It was noted above that we estimated the effect of blunting on the location of the transition point assuming that the transition Reynolds number for pointed and blunt cones remained identical. There are very few experimental data to support this assumption, although what data do exist tend to confirm the hypothesis to some degree. However, there are still insufficient experimental data to validate any assumptions in the calculation of transition Reynolds numbers. The results available show that on a blunt surface, the transition point varies with the longitudinal pressure gradient and with surface roughness.

Finally, let us indicate one more premise, concerned with the invariability of the profile shape in the inviscid layer. In reality, a deformation of this profile occurs downstream and is caused by the decay of the low-velocity inviscid layer due to the continual entry into it of a large amount of air with low entropy. This decay of the high-entropy flow is equivalent to an effective decrease in blunting. Thus, the flow conditions at a great distance from the nose should approach those for the flow behind the conical shock existing for zero blunting. Therefore, the heat transfer must increase downstream. In regions closer to the nose, the predominant stagnation conditions are those behind a normal shock, and the heat transfer is low.

The approximate picture of the velocity variation along the body is presented in Fig. 260, where the velocity at the outer edge of the boundary layer has been calculated for various conditions. The dashed curves result from conditions behind conical and normal shocks. The velocities computed by considering the curvature of the shock are shown by solid lines and were calculated in the following way. The mass flow of gas through a section of the boundary layer was found on the basis of an approximate estimate of the thickness of the layer at the given station. The portion of the curved shock wave corresponding to this mass flow was determined, and the average value of the stagnation pressure was calculated. The velocity was computed from this average and the value of the local static pressure.

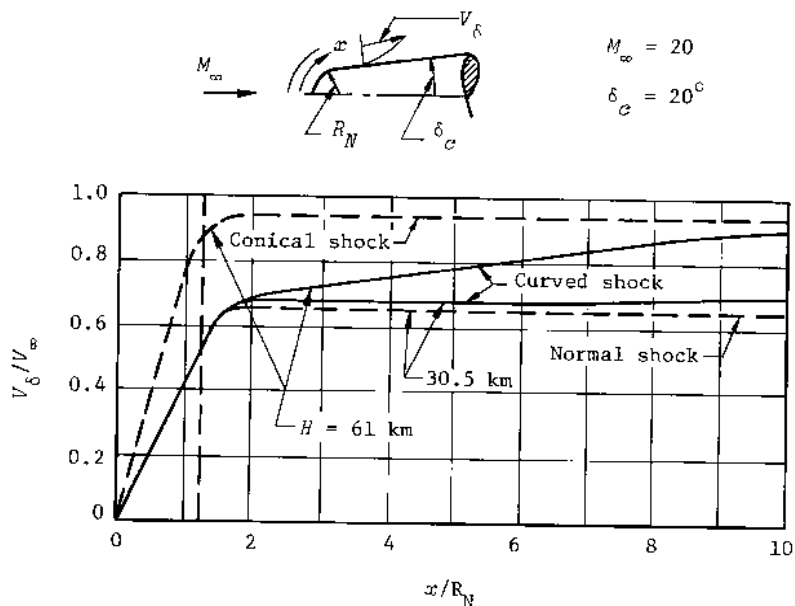


Fig. 260--Velocity distribution at the outer edge of the boundary layer for a spherically blunted cone

It is evident from Fig. 260 that, for an altitude of 30.5 km and a conical surface length of $x = 10R_N$, the velocity differs little from that calculated using the normal part of the shock. However, when the altitude is doubled, the difference becomes substantial, and the velocity computed by the indicated method is almost equal to that on a pointed cone. Here also the dissipation effect emerges, essentially leading to a decay of the inviscid layer of low velocities. If this effect were taken into account in practical calculations of optimum blunting, the blunting initially obtained would be increased somewhat.

Several studies have indicated that, for flight at comparatively low altitudes, dissipation of the low-velocity layer can be neglected for lengths of the laminar boundary layer of the order of 1000δ .

From this discussion, it is apparent that the results of the calculation of the low-velocity inviscid layer will differ somewhat from the actual values because of the simplifying assumptions used in the

calculations. Therefore, the quantitative estimate presented above for the thickness of the inviscid layer and for the coordinate of the transition point should be considered preliminary and, before making final practical recommendations, the calculated parameters obtained should be tested experimentally.

§ 27. HEAT FLOW ON A BLUNT NOSEGENERAL SOLUTION FOR THE LAMINAR BOUNDARY LAYER ON THE CURVED SURFACE OF A NOSE FOR EQUILIBRIUM DISSOCIATION

FLOW CONDITIONS on a blunt nose are characterized by low velocities due to the abrupt deceleration of the flow through the bow shock. Negative pressure gradients are also characteristic of the flow. Therefore, the boundary layer in the majority of practical cases is laminar, and the heat transfer is defined by the processes in a laminar layer.

In the case of thermodynamic equilibrium, heat transfer is caused only by molecular thermal conductivity and, therefore, the heat flow to the surface is

$$q = \frac{k_w}{c_{pw}} \left(\frac{\partial T}{\partial y} \right)_w. \quad (27.1)$$

This expression applies to an arbitrary point on the surface of a spherical nose, including the stagnation point. The value of the heat flux at the point in question is a function of the local inviscid wall parameters and of the processes occurring in the boundary layer itself. The longitudinal pressure gradient also has considerable influence. In addition, the heat transfer is determined by processes that occur in the boundary layer upstream of the section under consideration. In other words, the heat flow to the wall is related to the previous history of the motion of the gas.

To take this previous history into account, it can be shown⁽³⁾ that it is advantageous to introduce a new variable:

$$\xi = \int_0^x \rho_\delta V_\delta \mu_\delta r^2 dx. \quad (27.2)$$

Since ξ is a measure of the distance along the surface from the stagnation point, the parameters at a given section of the boundary layer will be functions of ξ . The heat transfer is determined by the variation of these parameters with thickness, as are the integral (or average) characteristics of the boundary layer.

The integral $\int_0^y (\rho/\rho_\delta) dy$ is introduced as a relative coordinate corresponding to the coordinate y at a point in the cross section of the boundary layer. Based on the dependence of the parameters in the boundary layer on the processes in the preceding sections of flow, it is necessary to relate $\int_0^y (\rho/\rho_\delta) dy$ to ξ by defining a new variable:

$$\eta = \frac{r \rho_\delta V_\delta}{\sqrt{2\xi}} \int_0^y \frac{\rho}{\rho_\delta} dy. \quad (27.3)$$

Studies have shown that similar solutions can be found representing a family of velocity and enthalpy profiles depending only on the parameter η . For example, if we introduce the stream function, which is defined by

$$\frac{\partial \Psi}{\partial y} = \rho V_x r, \quad \frac{\partial \Psi}{\partial x} = -\rho V_y r, \quad (27.4)$$

and convert to the variables ξ and η , it can be shown that the stream function will depend on these new variables in the following way:

$$\Psi(\xi, \eta) = \sqrt{2\xi} f(\eta). \quad (27.5)$$

The relation for the velocity ratio V_x/V_δ is determined from Eqs. (27.4) and (27.5),

$$\frac{V_x}{V_\delta} = \frac{df}{d\eta} = f'(\eta), \quad (27.6)$$

and the enthalpy ratio is defined by a function $g(\eta)$:

$$\frac{i_0}{i_p} = g(\eta), \quad (27.7)$$

where

$$i_0 = i + \frac{V^2}{2}.$$

Using these results, we can transform the equations of motion, Eq. (3.33), and energy, Eq. (3.41), to the new variables ξ and η (neglecting the concentration gradient):

$$(Cf'')' + ff'' + \beta \left[\frac{\rho_\delta}{\rho} - (f')^2 \right] = 0, \quad (27.8)$$

$$\left(\frac{Cg'}{\text{Pr}} \right)' + fg' + \frac{V_\delta^2}{2i_r} \left[2C \left(1 - \frac{1}{\text{Pr}} \right) f' f'' \right]' = 0, \quad (27.9)$$

where

$$C = \frac{\rho \mu}{\rho_\delta \mu_\delta}, \quad \beta = \frac{2\xi}{V_\delta} \frac{dV_\delta}{d\xi}.$$

For large supersonic velocities, it can be assumed that the density ratio $\rho_\delta/\rho \approx g(\eta)$, and that C is equal to unity. The study is also simplified if we assume that $\text{Pr} \approx 1$ and that β , which is a function of the velocity gradient, is constant. Based on these assumptions, Eqs. (27.8) and (27.9) are simplified:

$$f''' + ff'' + \beta [g - (f')^2] = 0, \quad (27.8a)$$

$$g'' + fg' = 0. \quad (27.9a)$$

Thus, the equations obtained reflect local similarity, in the sense that the dimensionless velocity V_x/V_δ and enthalpy i_0/i_r are identical at points in different flows for which the parameter η , the similarity parameter, is the same.

Solving the system of ordinary differential equations, Eqs. (27.8a) and (27.9a) (for the proper boundary conditions), we can find the functions $f(\eta)$ and $g(\eta)$ and their derivatives and thereby determine the flow parameters V_x/V_δ , i_0/i_r , etc.

Specifically, studies have shown that the value of the derivative $g'(\eta)$ on a cooled wall, i.e., for $\eta = 0$, in the case of very high velocities can be expressed with sufficient accuracy by the relation[†]

$$g'(0) = \frac{1}{2} \text{Pr}^{\frac{1}{3}}, \quad (27.10)$$

in which the Prandtl number is an average value for the given section of the layer. The cooled wall is characterized by the fact that the density ratio $\rho_w/\rho_\delta \gg 1$ on the surface.

The equation for heat flow, Eq. (27.1), can be transformed to the variable η and, with Eqs. (27.7) and (27.10), written as

$$q = \frac{k_w}{\bar{\sigma}_{pw}} i_r \left(\frac{\partial q}{\partial \eta} \right)_w \left(\frac{\partial \eta}{\partial y} \right)_w = \frac{1}{2} \frac{k_w}{\bar{\sigma}_{pw}} \frac{\rho_w V_\delta r i_r}{\sqrt{2\xi}} \text{Pr}^{\frac{1}{3}}. \quad (27.11)$$

Assuming that $\rho_w u_w = \rho_\delta u_\delta$, we obtain

$$\frac{\rho_\delta u_\delta}{\rho'_0 u'_0} = \frac{p}{p'_0} \frac{u_\delta}{u'_0}, \quad (27.12)$$

where $\omega = \mu/RT$. At high temperatures, the value of this function varies little with the thickness of the boundary layer, and it can be assumed that the values at the edge of the boundary layer and at the stagnation point are identical, i.e., $\omega_\delta = \omega'_0$. Therefore, only the ratio p/p'_0 is a variable on the right side of Eq. (27.12).

Using Eq. (27.2) for ξ and taking into account that $\text{Pr} = \bar{\sigma}_{pw} u_w / k_w$, we obtain the heat flow as follows:

$$q = \frac{1}{2 \text{Pr}^{\frac{2}{3}}} \sqrt{V_\infty \rho'_0 u'_0} i_r F(x), \quad (27.13)$$

where

$$F(x) = \frac{\sqrt{2}}{2} \frac{(p/p'_0)(V_\delta/V_\infty)r}{\left[\int_0^x (p/p'_0)(V_\delta/V_\infty)r^2 dx \right]^{\frac{1}{2}}}. \quad (27.14)$$

[†]Editor's note: The more precise expression is $g'(0) = 0.47 \text{Pr}^{\frac{1}{3}}$.

It will be observed that the dimensions of i_r in Eq. (27.13) should be kcal m/kgf sec² to allow the proper units for the heat transfer rate.

STAGNATION POINT

Equilibrium Dissociation

Calculations of the heat transfer over the surface of a blunt nose are dependent on the determination of the heat transfer rate at the stagnation point. Conditions at this point are also of particular interest because the heat transfer rate is usually greater at the stagnation point than at any other point on the nose. The heat transfer rate at the stagnation point is given by Eq. (27.13), where $F(x)$ is computed for conditions in the vicinity of the stagnation point:

$$V_\delta = \tilde{\lambda}x = \frac{\tilde{\lambda}V_\infty x}{D_N}, \quad \frac{p}{p_0'} = \text{const} \approx 1, \quad r = x.$$

The absolute value of the function is

$$|F(x)|_0 = \sqrt{2\tilde{\lambda}/V_\infty},$$

and Eq. (27.13) has the form

$$q_0 = \frac{0.664}{Pr^{\frac{2}{3}}} (\tilde{\lambda}p'_0 u'_0)^{\frac{1}{2}} i_r. \quad (27.15)$$

This expression is obtained for a supercooled surface on which the temperature T_w and the enthalpy i_w are negligibly small compared with the corresponding values of T_r and i_r . In cases where the cooling does not ensure a sufficiently low wall temperature, e.g., for the dissipation of heat by radiation only when a comparatively high equilibrium radiation temperature is established, it is necessary to account for i_w . Studies have shown⁽⁴⁾ that for the case of a heated wall, the equation for q_0 retains basically the same form as Eq. (27.15), but the quantity $(i_r - i_w)$ enters into the new equation instead of i_r , as well as the supplementary coefficient

$$\left(\frac{\rho_w u_w}{\rho'_0 u'_0}\right)^{\frac{1}{10}} = (\bar{\rho}_w \bar{u}_w)^{\frac{1}{10}},$$

which takes into account the variation of the parameters across the boundary layer in the vicinity of the stagnation point. Moreover, it has been established that better results are obtained if the coefficient 0.664 is changed to 0.763. If these changes are made, then, in the general case of a heated wall, the equation for the heat transfer can be presented in the following form:

$$q_0 = \frac{0.763}{Pr^{\frac{1}{10}}} (\bar{\lambda} c'_0 \mu'_0)^{\frac{1}{10}} (i_r - i_w) (\bar{\rho}_w \bar{u}_w)^{\frac{1}{10}}. \quad (27.16)$$

The variation in the quantity $1/\bar{\rho}_w \bar{u}_w$ as a function of wall temperature is shown in Fig. 261. It is apparent that the heat flux does not increase significantly over its value for a cooled surface even for an insulated wall (for which $T_w = T_r$), since the heat transfer varies only with the $\frac{1}{10}$ power of the parameter.

Equation (27.16) indicates that at high velocities, when dissociation has a considerable influence on heat transfer processes, the heat

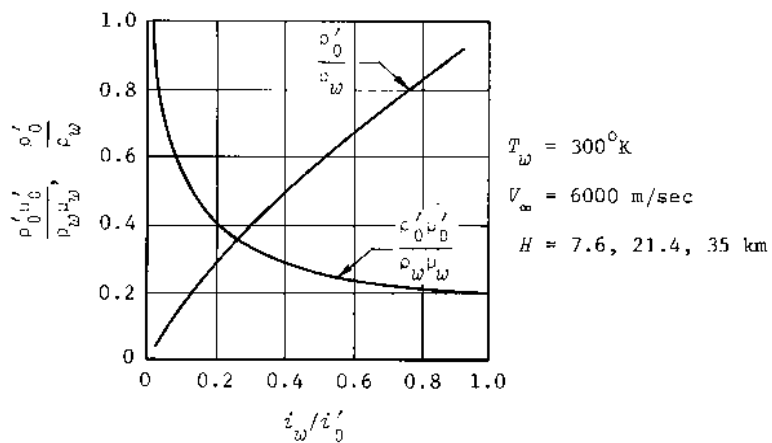


Fig. 261--Variation in density and the product ρu in the boundary layer near the stagnation point

transfer is a function of the enthalpy rather than the temperature. At these velocities, the recovery enthalpy i_r can be computed from $i_r = V_\infty^2/2$. In a wind tunnel, the enthalpy is determined from the gas temperature in the stagnation chamber and, in a shock tube, from the equation $i_r = u_s^2$, in which u_s is the velocity of the shock wave. In Eq. (27.16), it is possible to convert from an enthalpy difference to a temperature difference if we substitute

$$i_r - i_w = \bar{c}_{pw}(T_r - T_w),$$

where the specific heat \bar{c}_{pw} is calculated as an average between the values on cooled and insulated walls having temperatures of T_w and T_r , respectively.

It should be noted that the equations for the calculation of the heat transfer rate pertain to the case of steady motion of a body on a trajectory. If the velocity is not constant, the expression

$$\frac{d\bar{q}_0}{dt} = h_l(T_r - T_w)_l = q_{0l} \quad (27.17)$$

can be used for an approximate estimate of the heat flux at a point l on the trajectory, where q_{0l} is given by Eqs. (27.15) or (27.16), for example. The total amount of heat transferred to the stagnation point during an interval of time $t_2 - t_1$ is

$$\tilde{q}_0 = \int_{t_1}^{t_2} \frac{d\bar{q}_0}{dt} dt = \int_{t_1}^{t_2} h_l(T_r - T_w)_l dt. \quad (27.18)$$

It follows from the equations presented that the heat flow to the wall is a function of the parameters at the external edge of the boundary layer. The parameters are determined from the flow conditions at the stagnation point of the spherical nose.

With an increase in flight velocity, it becomes increasingly necessary to consider the effects of dissociation of the gas in front of the blunt body. At very high Mach numbers, a large part of the kinetic energy of the moving gas is converted into heat in the vicinity of the stagnation point. For example, at a velocity of 8 km/sec, almost 8000

kcal are generated by 1 kg of air, i.e., an amount sufficient for the dissociation of a large portion of the nitrogen and oxygen molecules.

Of course, the variation in the chemical composition of air at high temperatures changes the heat transfer conditions. The chemical composition must be considered in the calculation of the parameters at the outer edge of the boundary layer, e.g., the longitudinal velocity gradient $\tilde{\lambda}$, the density ρ' , and the viscosity ν'_0 . These calculations are similar to the computation of these parameters behind a normal shock. Knowing the entropy on the zero streamline and the stagnation enthalpy, we can compute p'_0 , T'_0 , ρ'_0 , and the other parameters at the stagnation point necessary in Eqs. (27.15) or (27.16).

An analysis of the numerical results of the calculation for hypersonic velocities enables us to obtain the following approximate equation for the calculation of the heat flux at the stagnation point:⁽⁵⁾

$$q_0 = \frac{31,500}{\sqrt{R_N}} \sqrt{\frac{\rho_{\infty H}}{\rho_{\infty SL}}} \left(\frac{V_{\infty}}{V_C} \right)^{3.25} \left(1 - \frac{i_w}{i_r} \right)^3 \text{ kcal/m}^2 \text{ sec}, \quad (27.19)$$

in which V_C is the orbital velocity, equal to 7.93 km/sec; $\rho_{\infty H}$ and $\rho_{\infty SL}$ are the atmospheric densities at altitude H and at sea level, respectively; and R_N is the radius of the sphere in meters. The recovery enthalpy can be assumed equal to the stagnation enthalpy.

Equation (27.19) is obtained on the assumption of equilibrium dissociation in the boundary layer. However, research has shown that it can also be used at high velocities where the flow in the boundary layer on a catalytic surface is in a nonequilibrium state. In this case, the recombination of atoms is accelerated by the catalytic effect of the wall (e.g., a metal skin) and is accompanied by the generation of heat that is almost equal to the heat of dissociation. At the same time, the processes occurring in the boundary layer, although not in equilibrium, are nevertheless close to equilibrium. Thus, Eq. (27.19) accounts not only for heat conduction but also for the transfer of heat by diffusion due to the recombination of atoms at the wall.

If the surface of the sphere is noncatalytic (e.g., a nonmetallic

surface), Eq. (27.19) will give values of the heat flux that are too high. In this case, the equation will become increasingly inaccurate as the altitude increases, i.e., as the gas deviates from the equilibrium state.

From a practical viewpoint, the use of a noncatalytic surface can be advantageous since it decreases the heat transfer. In this case, the low rate of recombination peculiar to these chemical reactions under ordinary conditions is not affected by the noncatalytic surface, and the heat absorbed by the dissociation process can be considerable.

In calculations in which these equations are used, it is assumed that the enthalpy or wall temperature is known. For example, a specific value can be assigned, thus setting a cooling requirement. In particular, it is possible to examine the case of a strongly cooled surface when the quantity i_w/i_r can be neglected in comparison with unity. In other cases, it is possible to assign a maximum allowable skin temperature. In addition, the heat flux to the surface can be calculated, assuming that it is equal to the heat emitted by radiation from the surface. By selecting a value for the emissivity of the surface (ϵ) and a surface temperature, which in this case will be the equilibrium temperature, we can determine the flight velocity and altitude necessary for thermal equilibrium. The radiative heat flux, $\epsilon\sigma T_w^4$, is set equal to the heat flux given by Eq. (27.19), from which a relation between velocity and density (therefore, altitude) is obtained. Under these flight conditions, cooling occurs due to thermal radiation from the heated surface. This so-called radiative cooling plays an important role in the reduction of the net heat flow.

EXAMPLE

Let us determine the heat transfer at the stagnation point of a spherical nose with a radius $R_N = 0.25$ m for flight at an altitude $H = 30$ km with a velocity corresponding to $M_\infty = 15$; the wall temperature is $T_w = 1000^\circ\text{K}$. We will use Eq. (27.15), in which it will be assumed that the Prandtl number is equal to 0.71.

The sequence and the results of the calculations are presented in Table 19, in which part of the data is taken from Table 4. To simplify the calculations, the inviscid parameters at the stagnation point are assumed equal to those behind a normal shock wave. As is evident from Table 19, the heat flux is 1200 kcal/m² sec, and the heat transfer coefficient is $h = 0.27$ kcal/m² sec deg.

Now, let us estimate the heat transfer parameters at the stagnation point of a body with a flat nose. The equivalent radius can be determined from Eq. (20.46), and the heating rate at the stagnation point can then be calculated just as at the stagnation point of a sphere with a radius R_{Ne} .

As an example, let us compute the value of q_0 for the conditions given above assuming that the radius of the flat nose is $r_N = 0.25$ m. From the known density ratio $\rho'_0/\rho_\infty = 11$ and the curves in Figs. 209 and 212, it can be determined that the radii of curvature of the shocks are $(\bar{R}_{s0})_{sph} = 1.14$ and $(\bar{R}_{s0})_f = 5.25$. Therefore, the equivalent nose radius is $R_{Ne} = 0.25 \cdot 5.25 / 1.14 = 1.15$ m, i.e., 4.6 times larger than the radius of the sphere. According to Eq. (20.27a), the value of $\tilde{\lambda}$ for a flat nose will be less than that for a sphere by the same factor. It follows from Eq. (27.15) that the heating rate is reduced by $\sqrt{4.6} = 2.15$ times and is approximately 560 kcal/m² sec.

Calculations using the effective parameters give almost the same result when the effective enthalpy at the stagnation point is calculated from

$$i^* = \frac{1}{2} (i_r + i_w).$$

The more accurate heat flux is only 3 percent larger.

Experimental measurements of the heating rate at the stagnation point of a flat face indicate that

$$(q_0)_f = (0.55 \pm 0.05)(q_0)_{sph},$$

i.e., equal to half the value at the stagnation point of a sphere with the same radius as the flat nose. This corresponds quite well to the calculated value above.

Table 19
CALCULATION OF HEAT TRANSFER AT THE STAGNATION POINT

1	2	3	4	5	6	7	8
M_∞	H km	$\frac{P_{\infty H}}{P_{\infty SL}}$	$\frac{P_{\infty H}}{P_{\infty SI}}$	$\frac{\alpha_{\infty SL}}{\alpha_{\infty H}} = \sqrt{\frac{T_{\infty SL}}{T_{\infty H}}}$	g m/sec ²	γ_m m/sec	$T_{\infty H}$ °K
Assumed						$340 \frac{M_\infty}{(S)}$	$\frac{288}{(S)^2}$
15	30	0.0118	0.0145	1.11	9.72	$4.61 \cdot 10^3$	234
9	10	11	12	13	14	15	
$i_{\infty H}$ kcal/kgf	$\frac{V_\infty^2}{2}$	i_r kcal/kgf	$\bar{\lambda}$	$\tilde{\lambda}$	$\frac{p'_0}{p_{\infty H}}$	$\frac{p'_0}{p_{\infty H}}$	
0.24-234	$\frac{(7)^2}{2}$	$\frac{(10)^2}{427g} + (9)$	Fig. 201	$\bar{\lambda} \frac{V_\infty}{D_N}$	Eq. (3.46)	Fig. 42	
56.2	$10.6 \cdot 10^6$	2586	1.15	$1.06 \cdot 10^4$	11	280	
16	17	18	19	20			
$T'_0/T_{\infty H}$	p'_0 kgf sec ² /m ⁴	$T'_0/T_{\infty SL}$	$\mu'_0/\mu_{\infty SL}$	τ'_0 kgf sec/m ²			
Fig. 40	$0.125 \cdot (4) \cdot (14)$	$(16)/(5)^2$	Eq. (2.3) and Fig. 13	$1.82 \cdot 10^{-6} \cdot (19)$			
23	0.02	18.8	7.85	$1.43 \cdot 10^{-5}$			
21	22	23	24	25	26		
p'_0 kgf/cm ²	T_w °K	i_w kcal/kgf	q'_0 kcal/m ² sec	T_r °K	h kcal/m ² deg sec		
(3) · (15)	Assumed	(21), (22), and Fig. 15	Eq. (27.16)	(21), (11), and Fig. 15	$\frac{q_w}{T_r - T_w}$		
3.31	1000	250	1200	5430	0.27		

NOTE: The italic numbers in parentheses indicate the column of the specified value.

The Effect of Vorticity in the External Flow

The relation presented for the heat flow is obtained on the assumption that the flow in the inviscid layer adjacent to the wall is steady and that there are no velocity gradients across the layer due to vorticity. In reality, the velocity is not constant but increases from its value at the wall, corresponding to stagnation conditions behind a normal shock, to a higher value at the edge of the inviscid layer; thus, vorticity appears in the flow field. The effect of vorticity is apparent at each point on the surface, including the stagnation point, where the ratio of the heating rate including vorticity, q_{0v} , to that with no vorticity depends on a series of factors including the free-stream Mach number and the flight altitude.

For example, calculations showed that the ratio q_{0v}/q_0 was 1.3 and 1.04 at the stagnation point of a hemisphere for $M_\infty = 20$ and altitudes of 90 and 60 km, respectively. Thus, in practice, it is possible to disregard the vortex effect in dense layers of the atmosphere, whereas it is advisable to increase somewhat the calculated heat transfer in a rarefied medium.

The most important parameter determining the effect of vorticity on heat transfer is the Reynolds number calculated from the radius of the sphere and the gasdynamic characteristics at the stagnation point:

$$Re = \frac{R_N^{0'} C \sqrt{i_r}}{\nu'_0}.$$

In this expression, it should be noted that at high velocities it can be assumed that $i_r \approx V_\infty^2/2$.

Experimental data are presented in Fig. 262 for the ratio q_{0v}/q_0 for Mach numbers of 8 and 20, which can be used to correct the calculated values of the heat flow. It is obvious that the vortex effect is considerably less for $M_\infty = 8$ than for $M_\infty = 20$. The data in Fig. 262 are obtained for a stagnation point temperature of $T'_0 = 2000^\circ\text{K}$. The effect of vorticity increases with temperature, but even for a considerable temperature increase the effect is not great. Thus, for example, heat transfer due to vorticity increases, in all, by 3 to 4 percent for a temperature increase of 1000°K .

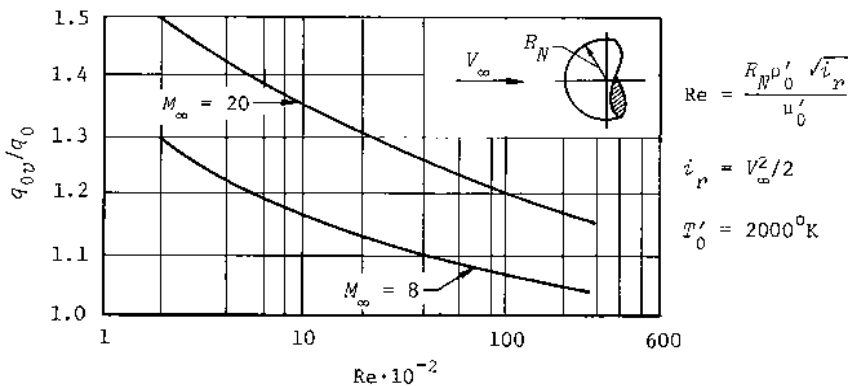


Fig. 262--Effect of vorticity on stagnation point heat transfer

Radiation from a Heated Shock Layer

At very high flight velocities, the significant temperature increase behind the shock wave changes the physical character of the air. In particular, it ceases to be transparent and therefore becomes a source of radiative heat flow to the surface. The opacity of the air results chiefly from a significant increase in the concentration of nitric oxide at high temperatures.

If the optical properties are characterized by a parameter ϵ representing the emissivity of a unit thickness of the radiative layer, where ϵ has the dimensions L^{-1} , the quantity ϵs_0 will be the dimensionless characteristic of the radiation of the gas between the shock and the body, having a thickness s_0 . This quantity is called the effective emissivity of the gas. According to the Stefan-Boltzmann law, the heat radiated by a black body is $q = \sigma T^4$. To take transparency into account in this equation, it is necessary to introduce a function, $f(\epsilon s_0)$, that depends on the effective emissivity. Thus, the general relation for the determination of the radiative heat flow to the wall will have the form

$$q = f(\epsilon s_0) \sigma (T'_0)^4, \quad (27.20)$$

where T'_0 can be assumed equal to the temperature at the stagnation point of the nose. It must be kept in mind that Eq. (27.20) refers to the case

in which the surface does not radiate and its temperature is less than 3000°K .

The curve presented in Fig. 263 shows the variation in the function $f(\varepsilon s_0)$ under real flight conditions at a very high velocity. At sufficiently high values of εs_0 , the air practically behaves as an opaque medium and the heat transfer due to radiation can be considerable. Thus,

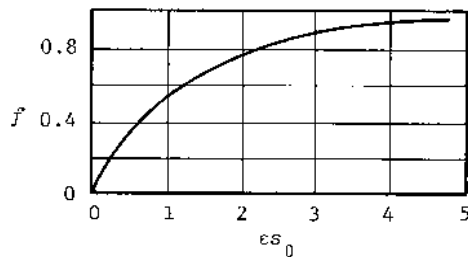


Fig. 263—Variation of $f(\varepsilon s_0)$ for radiative heat flow at the stagnation point

the farther the shock wave is displaced, i.e., the thicker the radiative layer, the larger in value will be the radiative heat flow corresponding to the same flight velocity ($\varepsilon = \text{const}$). The curve shown in Fig. 263 can be approximated by the equation

$$f = 1 - \exp(-\varepsilon s_0), \quad (27.21)$$

which gives an error of not more than 20 percent. As one would expect, the function $f = 0$ when $\varepsilon = 0$, i.e., when the air is transparent, which occurs at low flight velocities. At high velocities $f \rightarrow 1$; i.e., for practical purposes the gas becomes absolutely black.

The results of physical studies can be used for practical conditions, which show that the parameter ε is a function of the temperature and density of the air. This is evident in Fig. 264, where a family of experimentally determined curves is presented. Each curve represents the dependence of the quantity $\log(\varepsilon)$ on air temperature for a constant density ratio, where the units of ε are cm^{-1} . In the temperature range

of $8000^{\circ}\text{K} \leq T \leq 16,000^{\circ}\text{K}$, this set of curves can be well approximated by the equation

$$\varepsilon = 0.138 \left(\frac{\rho}{\rho_{\infty SL}} \right)^{1.28} \left(\frac{T}{10^4} \right)^{6.54} \text{ cm}^{-1}. \quad (27.22)$$

If this equation is used to calculate the radiation to the stagnation point of a blunt nose, the density ρ and temperature T of the gas must be assumed equal to their corresponding values ρ'_0 and T'_0 at this point. The calculation of the temperature T'_0 can be simplified if an approximate relation is used:

$$T'_0 = 1.34 \left(\frac{\rho'_0}{\rho_{\infty SL}} \right)^{0.0667} \left(\frac{V_{\infty}}{10^4} \right)^{1.333} {}^{\circ}\text{K}, \quad (27.23)$$

where V_{∞} is in m/sec.

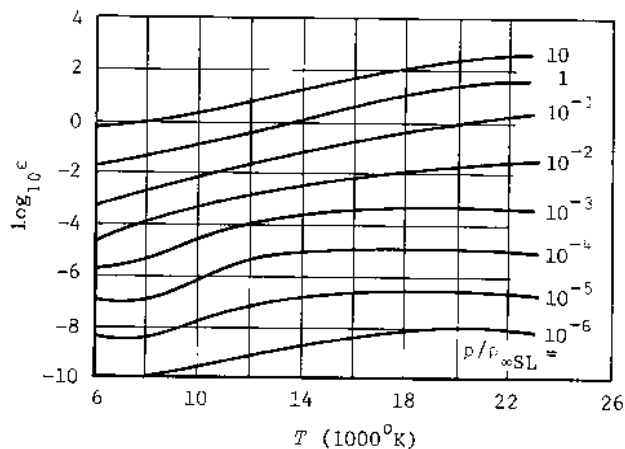


Fig. 264--Experimental data on the emissivity of a gas

On the basis of experimental studies, the following empirical relation was also obtained for the radiative heat flux at the stagnation point:

$$q_{\text{rad}} = 2.12 \cdot 10^7 R_N \left(\frac{V_\infty}{10^4} \right)^{0.5} \left(\frac{\rho_{\infty H}}{\rho_{\infty SL}} \right)^{1.6} \text{ kcal/m}^2 \text{ sec}, \quad (27.24)$$

where R_N is in meters and V_∞ is in meters per second.

A typical distribution of the radiative heat flow q_{rad} and the aerodynamic heat flow q_{aer} for a certain trajectory is presented in Fig. 265. It should be noted that the radiant heat flow has large values at low altitudes. The largest value of q_{rad} corresponds to the maximum aerodynamic heat transfer and is about one-third of that value.

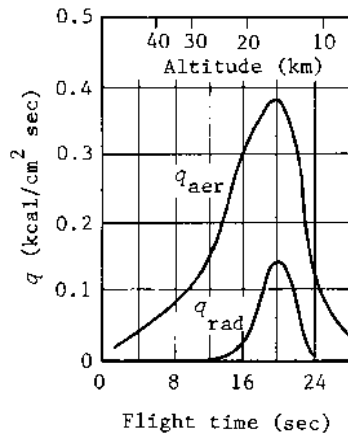


Fig. 265--Convective and radiative heat flow near the stagnation point of a spherically blunt body

THE EFFECT OF DIFFUSION ON HEAT TRANSFER

The Mechanism of Heat Transfer

One of the characteristics of the heat transfer process in the boundary layer for very high flow velocities is based on the fact that atoms and ions, created as the result of dissociation and ionization, take part in the transfer of heat by diffusing into regions with lesser atomic and ionic concentrations.⁽³⁾ Diffusion, accompanied by the recombination of the atoms and ions, leads to the evolution of additional heat. The total heat flux is increased, because a certain amount of

heat due to recombination of the atoms taking part in the diffusion is added to the heat from ordinary molecular thermal conductivity.

Thus, the total heat flow to the wall will be determined by the expression

$$q = q_T + q_D = - \left[\lambda_w \left(\frac{\partial T}{\partial y} \right)_w + \rho_w \bar{D} i_R \left(\frac{\partial c}{\partial y} \right)_w \right], \quad (27.25)$$

in which \bar{D} is the diffusion coefficient of a binary mixture of air consisting of atoms and molecules, and q_T and q_D are the heat flows due to molecular thermal conductivity and diffusion, respectively. Obviously, it is possible to assume that air can be represented by such a binary mixture since the transfer coefficients, i.e., viscosity, thermal conductivity, and diffusion, as well as the atomic weights of oxygen and nitrogen, are close to one another. Moreover, the concentration of nitric oxide is low and its influence on the transfer of energy is negligible. For the same reason, it is possible to neglect the effects of ionization, which begin to appear only for $M_\infty > 25$.

With the enthalpy of the mixture defined by Eq. (3.40a), the heating rate at the wall can be written

$$q = - \frac{\lambda_w}{\bar{c}_{pw}} \left[\left(\frac{\partial i}{\partial y} \right)_w - i_R \left(\frac{\partial c}{\partial y} \right)_w + \frac{\rho_w \bar{D} \bar{c}_{pw}}{\lambda_w} i_R \left(\frac{\partial c}{\partial y} \right)_w \right]. \quad (27.25a)$$

In the limiting case of local thermodynamic equilibrium, it can be assumed that the degree of dissociation does not vary within the thickness of the boundary layer and is equal to its value at the outer edge, so that the concentration gradient $\partial c / \partial y = 0$. If the enthalpy gradient at the wall is assumed to be of the order of magnitude of

$$\left(\frac{\partial i}{\partial y} \right)_w \sim \frac{i_r - i_w}{\delta},$$

the thermal flux in the equilibrium boundary layer is of the order of

$$q_T \sim \frac{1}{\delta} \frac{\lambda_w}{\bar{c}_{pw}} (i_r - i_w). \quad (27.26)$$

In this case, the heat transfer is due to molecular thermal conductivity involving the transfer of kinetic, vibrational, and rotational energy. Actually, the flow in the boundary layer is not in equilibrium, and a concentration gradient exists. Therefore, in addition to molecular thermal conductivity, heat transfer occurs due to the chemical energy produced by recombination. In general, part of this energy is liberated in the boundary layer and part at the wall as a result of catalytic reaction.

In the limiting case of local equilibrium, the reaction occurs only in the boundary layer. In the other limiting case of frozen flow, recombination occurs only at the catalytic surface.

The total heat flow to the wall can be estimated from Eq. (27.25a) as

$$q \sim q_T [(1 - \bar{i}_w) + Le_w \bar{i}_w], \quad (27.27)$$

where

$$\bar{i}_w = \frac{i_R(c_\delta - c_w)}{i_r - i_w},$$

and $Le_w = \rho_w \bar{C}_{pw} / k_w$. If the surface temperature is low enough that there is no dissociation at the wall, the concentration of atoms is zero at the wall and the difference $c_\delta - c_w$ should be replaced by c_δ .

The first term in the parentheses in Eq. (27.27) determines the heat transfer due to thermal conductivity and the second gives that due to diffusion. The heat flux caused by thermal conductivity is different from its value for equilibrium flow because of the presence of concentration gradients. It should be noted that the concentration gradient is essentially equivalent to the enthalpy gradient of the atomic component of the binary mixture.

It is evident from Eq. (27.27) that the relative value of each component of the heat flux is determined by the Lewis-Semenov number and by the parameter \bar{i}_w . At very high velocities, nonequilibrium becomes the deciding factor in heat transfer. In this case, the relative value of \bar{i}_w is close to unity because practically all of the gas in the boundary layer is dissociated, and the entire heat flow is caused by diffusion.

The magnitude of this flow, as is evident from Eq. (27.27), is of the order of $q \sim q_T Le_w$. If $Le_w = 1$, the heat flux at any velocity is determined by the value for the case of total thermodynamic equilibrium and is independent of the heat transfer mechanism.

The Frozen Boundary Layer

To obtain a quantitative estimate of the diffusion effect, it is convenient to examine frozen flow when thermodynamic equilibrium exists at the edge of the boundary layer. In this case, the effects of diffusion are contained in a very thin layer next to the catalytic wall. The heat flow due to thermal conductivity can thus be determined separately by solving the equations for the equilibrium boundary layer; e.g., the heat transfer at the stagnation point can be calculated from Eq. (27.15).

The second component of the total heat transfer, resulting from diffusion, must be determined on the basis of the diffusion equation, Eq. (3.29). As a result of its solution, the concentration gradient of the atomic component at the wall can be found, which then determines the diffusional flow of matter by Eq. (2.34). For the required solution, let us convert Eq. (3.29) to the new variables ξ and η to obtain⁽⁶⁾

$$2\xi \frac{\partial z}{\partial \xi} f' - fz' - \left(\frac{C}{Sc} z' \right)' = 0, \quad (27.28)$$

where the variable z represents the dimensionless concentration of atoms, $z = c/c_\delta$, the prime indicates differentiation with respect to η , and the Schmidt number is defined as $Sc = \mu/\rho D = Pr/Le$. The remaining notation is the same as that in Eqs. (27.8) and (27.9).

Equation (27.28) is to be solved for specified boundary conditions at the wall. For the function f , the condition $f(0) = f'(0) = 0$ must be satisfied. At the outer edge of the boundary layer ($\eta \sim \infty$), the concentration ratio $z(\infty) = 1$, and the boundary condition at the wall is obtained from Eq. (2.35a). Assuming that $m = 1$ in Eq. (2.35a), we can write this condition in terms of the new variables ξ and η as

$$z'(0) = \left(\frac{\partial z}{\partial \eta} \right)_w = \frac{\sqrt{2\xi}}{rV_\delta \rho_w D} z(0).$$

Close to the stagnation point, we can compute ξ from Eq. (27.2) assuming that $r \approx x$, $V_\delta = \tilde{\lambda}x$, and $\rho_\delta u_\delta = \text{const}$. Furthermore, assuming that $\rho_\delta u_\delta = c'_0 u'_0$, we find the boundary condition

$$z'(0) = \sqrt{\frac{\rho'_0 u'_0}{2\tilde{\lambda}}} \frac{k_w}{\rho_w \bar{D}} z(0). \quad (27.29)$$

For this same region, it can be assumed that the concentration profile is independent of x . Furthermore, a good approximation for C is given by $C \approx 1$. This assumption is accurate for a low-temperature boundary layer but is worse at high temperatures. However, it has been established that the heat transfer is almost independent of the parameter C because of the weak dependence of the enthalpy gradient on this parameter at the wall. The parameter C has exactly the same minor influence on the concentration gradient and, therefore, on the heat transfer due to diffusion. In view of this discussion, Eq. (27.28) can be simplified and written in the form

$$\text{Sc } fz' + z'' = 0. \quad (27.28a)$$

Integrating this equation twice, we obtain

$$z(\eta) - z(0) = z'(0) \int_0^\eta \exp \left[- \int_0^{\eta'} \text{Sc } f(\eta) d\eta \right] d\eta. \quad (27.30)$$

Numerical calculations have shown that for $\eta \sim \infty$ the value of the integral is approximately $1/0.47 \text{ Sc}^{\frac{1}{3}}$. Thus, we can write

$$z'(0) = 0.47 \text{ Sc}^{\frac{1}{3}} [1 - z(0)]. \quad (27.31)$$

Introducing the quantity $z'(0)$ from Eq. (27.29), we obtain the dimensionless concentration at the wall:

$$z(0) = \frac{c_w}{\sigma_\delta} \left[\left(\frac{\rho'_0 u'_0}{2\tilde{\lambda}} \right)^{\frac{1}{2}} \frac{k_w}{0.47 \text{ Sc}^{\frac{1}{3}} \rho_w \bar{D}} + 1 \right]^{-1}. \quad (27.32)$$

It follows from Eqs. (27.29) and (27.32) that for the case of infinitely rapid catalysis ($k_w \sim \infty$), the dimensionless concentration at the wall

$z(0) = 0$ and the derivative $z'(0) = 0.4/\text{Sc}^{\frac{1}{3}}$. In the other limiting case of infinitely slow catalytic reaction ($k_w = 0$), the concentration at the wall remains the same as that at the outside edge of the layer, i.e., $z(0) = 1$, and the derivative is $z'(0) = 0$.

The heat flux generated by recombination at the wall can be obtained if we substitute the concentration gradient from Eq. (27.31) into Eq. (2.34), using Eq. (27.32) for $z(0)$. This results in

$$q_D = 0.664 (\rho'_0 \mu'_0 \lambda)^{\frac{1}{2}} \text{Sc}^{-\frac{2}{3}} i_R c_\delta \varphi, \quad (27.33)$$

where the so-called catalytic coefficient is

$$\varphi = \left[1 + \frac{0.664 \text{Sc}^{-\frac{2}{3}} (\rho'_0 \mu'_0 \lambda)^{\frac{1}{2}}}{\rho_w k_w} \right]^{-1}. \quad (27.34)$$

This coefficient takes into account the influence of the finite recombination rate, because the parameter k_w enters into the expression. In the limiting case of $k_w \sim \infty$, the coefficient $\varphi = 1$, which corresponds to the release of the maximum amount of heat in recombination. In the other limiting case of an infinitely slow reaction ($k_w = 0$), the catalytic coefficient is $\varphi = 0$, corresponding to the liberation of no additional heat.

The total heat flux to the wall can be determined if the diffusional heat is added to the heat due to thermal conductivity. As a result, we obtain

$$q = q_T \left[1 + (\text{Le}^{\frac{2}{3}} \varphi - 1) \frac{i_D}{i_r} \right], \quad (27.35)$$

where q_T is the heat transfer without diffusion, and $i_D = i_R c_\delta$ is the dissociation enthalpy.

Introducing the Nusselt and Reynolds numbers

$$\text{Nu}_w = \frac{q \bar{c}_{pw} x}{\lambda_w (i_r - i_w)}, \quad \text{Re}_w = \frac{V_\delta \bar{c}_w x}{\mu_w},$$

and determining the thermal heat transfer rate from Eq. (27.16), we find

the expression for the heat transfer parameter:[†]

$$\frac{Nu_w}{\sqrt{Re_w}} = \frac{0.763 Pr^{\frac{1}{3}}}{(\bar{\rho}_w \bar{v}_w)^{0.4}} \left[1 + (\text{Le}^{\frac{2}{3}} \varphi - 1) \frac{i_D}{i_p} \right]. \quad (27.36)$$

For a more detailed study of the effect of recombination, we can examine the ratio of the heat transfer with a finite recombination rate to that with infinitely rapid catalysis ($k_w \rightarrow \infty$). This ratio is

$$\bar{q} = \frac{q}{q(k_w \rightarrow \infty)} = 1 - \frac{\text{Le}^{\frac{2}{3}} \tilde{i}_D}{1 + (\text{Le}^{\frac{2}{3}} - 1) \tilde{i}_D} (1 - \varphi), \quad (27.37)$$

where $\tilde{i}_D = i_D/i_p$. It is evident from Eq. (27.34) that the catalytic coefficient φ is a function not only of the recombination rate but also of the flow velocity. Therefore, the heat transfer ratio \bar{q} from Eq. (27.37) is plotted in Fig. 266 with the variables k_w and V_∞ . For conditions of thermodynamic equilibrium at the edge of the boundary layer, these data

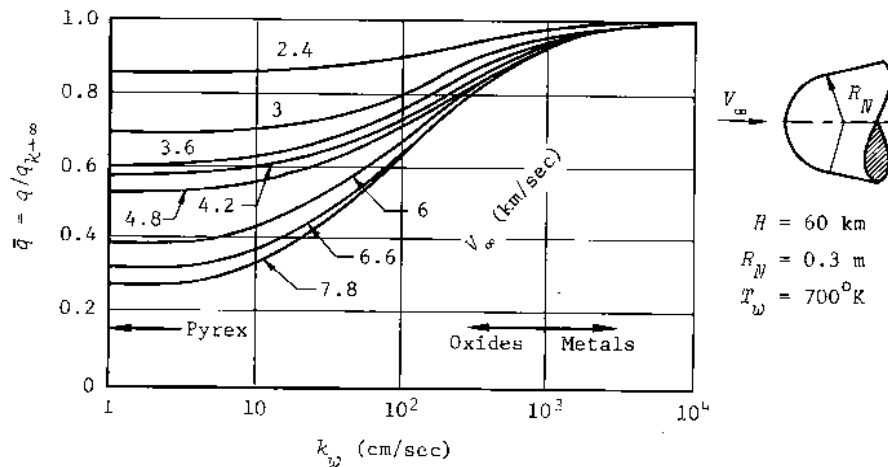


Fig. 266--Variation of heat transfer with flight velocity and recombination rate

[†] Editor's note: The equation in the Russian text is in error and has been corrected.

reveal how important it is to take into account the finite recombination rate. In addition, the results indicate the possibility of decreasing the heat transfer at the stagnation point through use of a nonmetallic skin, since recombination does not occur close to this type of surface. The net heat flow is decreased since nonequilibrium dissociation absorbs a significant amount of thermal energy. In the limiting case of $\varphi = 0$, the heat transfer is determined from

$$q = q_T \left(1 - \frac{i_D}{i_r} \right). \quad (27.38)$$

The values of $\bar{q} = q/q_T$ calculated from Eq. (27.35) are shown in Fig. 267 as a function of the catalytic parameter

$$x = \frac{p_w k_w}{0.664 Sc^{\frac{2}{3}} (\rho'_0 \mu'_0 \lambda)^{\frac{1}{2}}} \quad (27.39)$$

for various Lewis-Semenov numbers. It is obvious that the parameter x is related to the coefficient φ by $x = \varphi/(1 - \varphi)$.

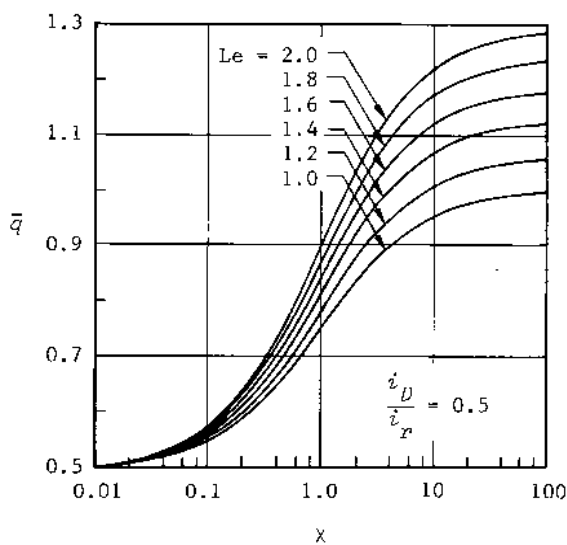


Fig. 267--Heat transfer as a function of the Lewis-Semenov number and the recombination parameter at the wall

The calculations shown in Fig. 267 pertain to the case in which the ratio $i_D/i_r = 0.5$ at the stagnation point and the nose surface is strongly cooled in the vicinity of that point, so that the concentration $c_w = 0$. If the wall remains sufficiently heated, chemical reactions will occur until the establishment of thermodynamic equilibrium with a finite final concentration $c_w \neq 0$, leading to a decrease in the heat flux. The corresponding value of the catalytic coefficient in Eq. (27.35) is determined by

$$\varphi = \frac{x}{1+x} \left(1 - \frac{c_w}{c_\delta} \right). \quad (27.40)$$

The quantity i_D in Eq. (27.35) must then be calculated from the expression

$$i = i_R(c_\delta - c_w),$$

where, for a binary mixture, it can be assumed that $c_\delta = \alpha_\delta$ and $c_w = \alpha_w$. In addition, in the case of a heated wall, it is necessary to replace i_r by $i_r - i_w$ in Eq. (27.35).

Factors That Decrease Diffusional Heat Transfer

In addition to the catalytic recombination rate k_w , a number of other factors tend to decrease diffusional heat transfer.

1. The velocity gradient $\tilde{\lambda} = V_\delta/x$ appears in Eq. (27.33) and varies inversely with the radius of the spherical nose. Therefore, a decrease in the nose radius will reduce the catalytic coefficient and thereby lower the heat transfer.[†]

2. With an increase in flight velocity, the total heat transfer increases, but that due to diffusion is decreased in the actual case of a finite recombination rate. As the total heat transfer increases, the portion of heat expended on dissociation is increased, and the part of

[†]Editor's note: This statement is in agreement with the original reference(6) but is incorrect. It is true that an increase in $\tilde{\lambda}$ reduces the catalytic coefficient φ . But $\tilde{\lambda}$ also enters directly into the expression for q_D (see Eq. (27.33)), and the net result is an increase in diffusional heat transfer with increasing $\tilde{\lambda}$. Thus, a large nose radius is desirable to decrease the heating rate.

the energy released as a result of chemical reaction at the wall is decreased.

3. The wall temperature also has an effect on the diffusional heat transfer. It is evident from Eq. (27.34) that the catalytic coefficient ϕ is a function of the product $\rho_w k_w$, which in turn is determined by T_w . The recombination rate may be a strong function of wall temperature (e.g., for some types of glass $k_w \sim T_w^{\frac{3}{2}}$), but the density variation is less pronounced. Thus, the quantity $\rho_w k_w$ will be approximately proportional to the wall temperature in this case, and it follows that the coefficient ϕ will decrease with a decrease in T_w . This means that low surface temperatures prevent the release of a large amount of chemical energy. However, it should be noted that other effects appear, e.g., a large heat flow to the wall due to convection.

The Quasi-equilibrium Boundary Layer

To determine the heat transfer in the case of local equilibrium in the boundary layer from Eq. (27.25a), it is necessary to know the concentration gradient and the enthalpy gradient at the wall. The first quantity is calculated from the condition of an equilibrium value of concentration near the wall using the tables or graphs of thermodynamic functions. To calculate the enthalpy gradient, it is necessary to solve the energy equation, Eq. (3.41), including the diffusion term. Converting this equation to the variables ξ and η , we obtain

$$\frac{\partial}{\partial \eta} \left[\frac{C}{Pr} (1 + d) \frac{\partial g}{\partial \eta} \right] + f \frac{\partial g}{\partial \eta} = 0, \quad (27.41)$$

where the parameter d is defined as

$$d = (Le - 1)(i_A + i_M) \left(\frac{\partial c_A}{\partial \xi} \right)_p. \quad (27.42)$$

The Lewis-Semenov number is assumed to be identical for all components, and the subscript p designates differentiation at constant pressure.

Equation (27.41) is to be solved with boundary conditions as given in the following expressions:

$$f(0) = 0, \quad \frac{\partial f(0)}{\partial \eta} = 0, \quad \frac{\partial f(\infty)}{\partial \eta} = 1, \quad g(0) = g_w, \quad g(\infty) = 1.$$

The parameters C and d are determined with the aid of the thermodynamic tables or graphs for air in thermodynamic equilibrium.

Using the solution of this equation and assuming that $Le = 1$, we can find the heat rate without diffusion, q_T . The effect of a Lewis-Semenov number different from unity can be taken into account by the approximate equation

$$q = q_T \left[1 + (Le^{0.52} - 1) \frac{i_D}{i_r} \right]. \quad (27.43)$$

The somewhat larger exponent of the Lewis-Semenov number in Eq. (27.35), compared with that in the present case of an equilibrium boundary layer, is explained physically by the fact that diffusion through the thickness of the frozen layer has a more important influence on heat transfer. Despite the difference indicated in the values of the exponents, the total heat flux differs little.

The Effect of the Recombination Rate

The case of a finite recombination rate in the boundary layer is the most realistic, because actually there are neither frozen nor equilibrium flows.

The results of calculations⁽⁴⁾ are presented in Fig. 268 for the heat transfer parameter

$$\frac{Nu_w}{\sqrt{Re_w}} = \frac{0.71q}{(i_r - i_w)(\lambda_{p_w} \mu_w)^{\frac{1}{2}}} \quad (27.44)$$

as a function of the recombination rate parameter C given by Eq. (2.29). In one case the wall was catalytic; in the other, noncatalytic.

Curve 1 in Fig. 268 shows the total heat transfer parameter to a catalytic surface, which is practically independent of the recombination rate parameter. This equality of the heat flow is due to the catalytic effect of the wall at small recombination rates (frozen flow) and by the small catalytic effect of the surface in the equilibrium boundary layer

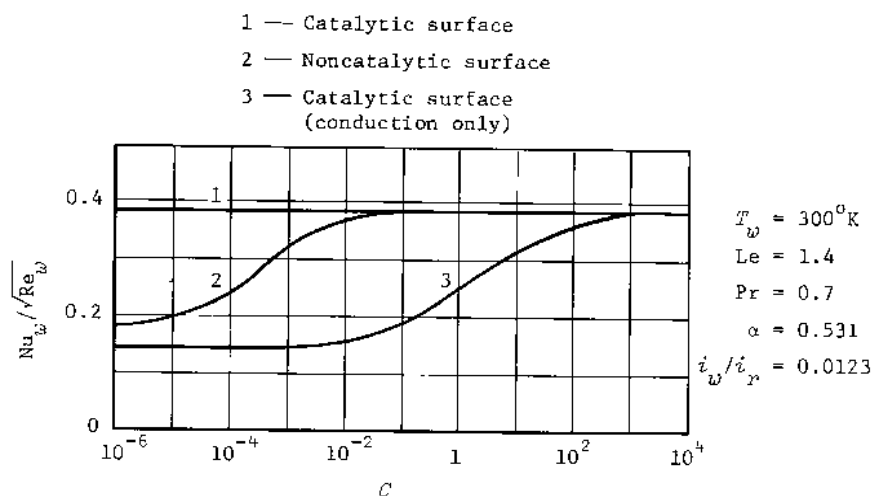


Fig. 268--Heat transfer as a function of the recombination rate

for large recombination rates. In the latter case, the atoms do not succeed in reaching the wall by diffusion but recombine in the boundary layer itself. Thus, as already noted, the calculation of the heat transfer to a catalytic wall can be carried out in practice without considering dissociation.

By comparing curve 1 in Fig. 268 with curve 3, which represents the heat transfer to a catalytic wall due to thermal conductivity alone, we can determine the fraction of the heat flow to a catalytic surface that is caused by diffusion. For large values of the parameter C , corresponding to high recombination rates, the process in the boundary layer is close to equilibrium, and the effect of diffusion toward the wall decreases. In this case, the major part of the heat is supplied by thermal conductivity.

Curve 2 represents the heat transfer parameter to a noncatalytic wall. It is evident that a much smaller value of C is required to produce a frozen boundary layer than for the catalytic wall. This is due to the fact that a much greater number of atoms accumulates near the noncatalytic wall, and a low value of C is required to create frozen flow.

The parameter C varies with the square of the density for a given temperature T'_0 . Thus, if the flow in the boundary layer is in equilibrium for atmospheric conditions near sea level where the parameter C is relatively large, it is in a frozen state at high altitudes. If we assume that these two limiting conditions represent a range of values of C approximately equal to 10^4 , we must reduce the density 100 times for transition to the frozen state.

The heat transfer at the stagnation point for the flow of a dissociable gas can be calculated from Eq. (27.43) for an equilibrium layer and from Eq. (27.35) for a frozen layer. The heat transfer depends mainly on the product $\rho'_0 u'_0$ at the outer edge of the boundary layer, where the values of ρ'_0 and u'_0 are those for the inviscid parameters at the stagnation point. If the wall is catalytic, the variation in $\rho'_0 u'_0$ across the boundary layer due to dissociation has no effect on the heat flux, which remains practically the same as in an undissociated boundary layer. If the wall is not catalytic, the total heat transfer can be reduced when the importance of the recombination rate is less than that of the diffusion rate in the boundary layer.

The Enthalpy of Equilibrium Dissociation

If air is examined as a mixture of two components, nitrogen and oxygen, the dissociation enthalpy of the mixture is

$$i_D = \sigma_d \frac{\sum_{k=N,0}^{N_1,0} (ci_R)_k}{\sum_{k=N,0} c_k} = (i_R c)_{O_2} + (i_R c)_{N_2}, \quad (27.45)$$

where the dissociation enthalpy of the k th component is given by Eq. (2.11) as $i_{Rk} = D_k / 2m_k = u_{dk}$. The values of i_{Rk} are given in Tables 2 and 3 and the concentrations are plotted in Fig. 14. For a diatomic gas, $i_D = \alpha u_d = \alpha i_R$, where α is the degree of dissociation of the gas, and $u_d = i_R$ is the characteristic energy of dissociation.

In practical calculations, it is possible to assume that all the oxygen is dissociated by the beginning of the nitrogen dissociation. In this case, the atomic concentration is caused only by the dissociation of oxygen and, therefore, $c = \alpha = 0.2346$. Thus,

$$i_D = 0.2346(i_R)_{O_2}.$$

If the conditions are such that the dissociation of the oxygen is incomplete, $i_D < 0.2346(i_R)_{O_2}$, and the concentration (the degree of dissociation of the mixture) is $c = \alpha < 0.2346$.

At high temperatures and low pressures, the nitrogen dissociates after the oxygen. The enthalpy of the dissociation of the mixture is

$$i_R^c = i_R^\alpha = i_D = 0.2346(i_R)_{O_2} + (c - 0.2346)(i_R)_{N_2}. \quad (27.46)$$

Tables or graphs of the thermodynamic functions can be used for rough estimates of the magnitude of i_D . In this case, the enthalpy i_r at the stagnation point is found from the temperature T and the pressure p , and i_D is determined from

$$i_D = i_r - i_{\alpha=0},$$

where $i_{\alpha=0}$ is the enthalpy at the same temperature but without dissociation. For approximate calculations of the enthalpy, the equation

$$i_{\alpha=0} = c_{p0} T \left(\frac{T}{T_0} \right)^\varphi$$

can be used, in which the exponent $\varphi = 0.1$ for $T > 1000^\circ K$, and the specific heat c_{p0} is assumed equal to 0.24 kcal/kgf deg for $T_0 = 273^\circ K$.

As an example, let us estimate the maximum value of the heat transfer for infinitely rapid catalysis and for $M_\infty = 15$ and $p_\infty = 0.1 \text{ kgf/cm}^2$, which corresponds to an altitude of approximately 16 km. The stagnation pressure for these conditions is

$$p'_0 = C_{p0} p_\infty \frac{\gamma M_\infty^2}{2} = 30 \text{ kgf/cm}^2.$$

The value of the enthalpy at this point is

$$i_r = \frac{AV_\infty^2}{2g} = \frac{\alpha_\infty^2 M_\infty^2 A}{2g} = 2430 \text{ kcal/kgf}$$

for $A = 1/427$ kcal/kgf m. For these values of i_r and p'_0 , the temperature is obtained from Fig. 15 as $T_r = 5500^\circ\text{K}$. The enthalpy of an undissociated gas at this temperature is $i_{\alpha=0} = 1780$ kcal/kgf. Therefore, the dissociation enthalpy is $i_D = 2430 - 1780 = 650$ kcal/kgf, and the ratio $i_D/i_r = 0.267$.

If it is assumed that $\text{Le} = 1.45$, the effect of diffusion is given by Eq. (27.35) (with the catalytic reaction coefficient equal to unity) as $q/q_T = 1.075$. In this case, the heat flux due to diffusion amounts to 7.5 percent of the total.

The effect of diffusion increases with an increase in velocity, and at very large velocities the ratio i_D/i_r is very close to unity. If it is assumed that $i_D/i_r = 1$, the maximum value of the heat transfer ratio is

$$\frac{q}{q_T} = \text{Le}^{\frac{2}{3}}.$$

For a Lewis-Semenov number of 1.45, this ratio is 1.28, so that the greatest possible increase in heat flux is only 28 percent.

CURVED SURFACES

Thermodynamic Equilibrium

Let us examine some of the relations for calculating the heat transfer at an arbitrary point on a curved surface under conditions of thermodynamic equilibrium.⁽³⁾ The general form of the function that determines the ratio of the heat flow q at an arbitrary point to its value q_0 at the stagnation point is

$$\frac{q}{q_0} = \frac{F}{F_0} = \frac{(p/p'_0)V_\delta r}{2 \sqrt{\lambda} \left[\int_0^x (p/p'_0)V_\delta r^2 dx \right]^{\frac{1}{2}}} \quad (27.47)$$

Hemispheres. Studies have shown that the distribution of heat transfer over a spherical surface calculated by Eq. (27.47) with a Newtonian pressure distribution, $C_p = C_{p0} \cos^2 \varphi$, agrees satisfactorily with experimental data even for $M_\infty < 2$.

To calculate the heat flow, it should be recalled that the velocity

varies almost linearly with the central angle φ for values of φ up to 75° or 80° . Therefore, it can be assumed that the velocity at the outer edge of the boundary layer is $V_\delta = \tilde{\lambda} R_N \varphi$. Furthermore, since

$$dx = R_N d\varphi, \quad r = R_N \sin \varphi,$$

and the pressure ratio for high velocities is given by the Newtonian equation

$$\frac{p}{p_0} = \cos^2 \varphi + \frac{p_\infty}{p_0} \sin^2 \varphi = \cos^2 \varphi + \frac{1}{\gamma_\infty M_\infty^2} \sin^2 \varphi,$$

Eq. (27.47) can be written in a form more suitable for calculation:

$$\frac{q}{q_0} = \frac{2\varphi \sin \varphi}{\sqrt{D(\varphi)}} \left[\left(1 - \frac{1}{\gamma_\infty M_\infty^2} \right) \cos^2 \varphi + \frac{1}{\gamma_\infty M_\infty^2} \right], \quad (27.48)$$

where the function $D(\varphi)$ is defined as

$$D(\varphi) = \left(1 - \frac{1}{\gamma_\infty M_\infty^2} \right) \left(\varphi^2 - \frac{\varphi \sin 4\varphi}{2} + \frac{1 - \cos 4\varphi}{8} \right) + \frac{4}{\gamma_\infty M_\infty^2} \left(\varphi^2 - \varphi \sin 2\varphi + \frac{1 - \cos 2\varphi}{2} \right). \quad (27.49)$$

When $1/\gamma_\infty M_\infty^2 \ll 1$, a simpler expression can be used to estimate the distribution of the heating rate:

$$\frac{q}{q_0} = \frac{2\varphi \sin \varphi \cos^2 \varphi}{\left(\varphi^2 - \frac{\varphi \sin 4\varphi}{2} + \frac{1 - \cos 4\varphi}{8} \right)^{\frac{1}{2}}}. \quad (27.50)$$

It is apparent that this expression determines the heat transfer exactly in the limiting case of $M_\infty = \infty$. Furthermore, Eq. (27.50) can probably be used for $M_\infty > 10$, as is shown in Fig. 269, which gives curves calculated from Eqs. (27.48) and (27.50). It was assumed in the calculations that the wall temperature was constant and that $T_w/T_\delta \ll 1$. The heat transfer is a maximum at the stagnation point and decreases with distance,

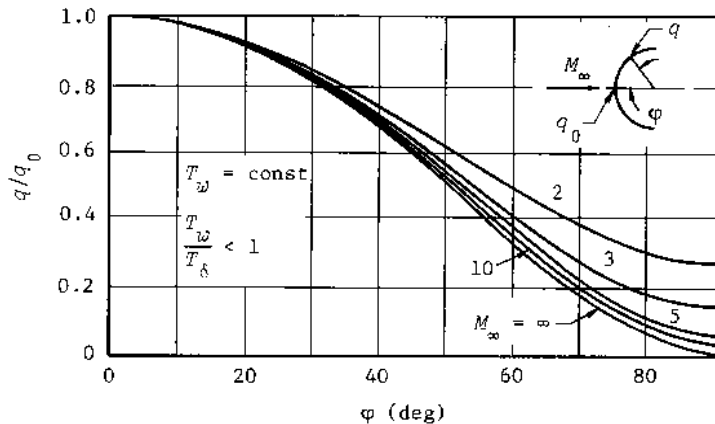


Fig. 269--Heat transfer distribution on a sphere with a laminar boundary layer

because the pressure decreases, and thus the product $p_\delta \mu_\delta$ decreases.

Equation (27.48) represents very well the actual distribution of heat transfer. However, this applies for high Mach numbers, for which $p_\infty/p'_0 = 1/\gamma M_\infty^2$. Moreover, for the portion of the surface near $\phi = 90^\circ$, the actual value of the heat transfer is larger than that obtained theoretically from Eq. (27.48). This is because the static pressure is somewhat higher there than the free-stream pressure, which is the value predicted by the approximate Newtonian equation.

To refine Eq. (27.48), let us assume the following pressure distribution for the sphere:

$$\frac{p}{p'_0} = 1 - \left(1 - \frac{p'}{p'_0}\right) \sin^2 \phi, \quad (27.51)$$

where p' is the pressure at $\phi = 90^\circ$. Then Eq. (27.48) takes the form

$$\frac{q}{q_0} = \frac{(1 - \zeta \sin^2 \phi) \phi \sin \phi}{[F_1(\phi) - \zeta F_2(\phi)]^{1/2}}. \quad (27.52)$$

The following notation is introduced into this equation:

$$\xi = 1 - \frac{p'}{p'_0},$$

$$F_1(\varphi) = \varphi^2 - \varphi \sin 2\varphi + \sin^2 \varphi, \quad (27.53)$$

$$F_2(\varphi) = \frac{1}{2} \left[\frac{3}{2} \varphi^2 - \varphi \sin 2\varphi \left(\frac{3}{2} + \sin^2 \varphi \right) + \frac{3}{2} \sin^2 \varphi + \frac{1}{2} \sin^4 \varphi \right].$$

The experimental dependence of ξ on M_∞ is presented in Fig. 270. It is evident that for $M_\infty > 6$, ξ is practically constant, and the greatest variation is observed for $M_\infty < 3$. Therefore, the ratio q/q_0 also varies considerably at these velocities.

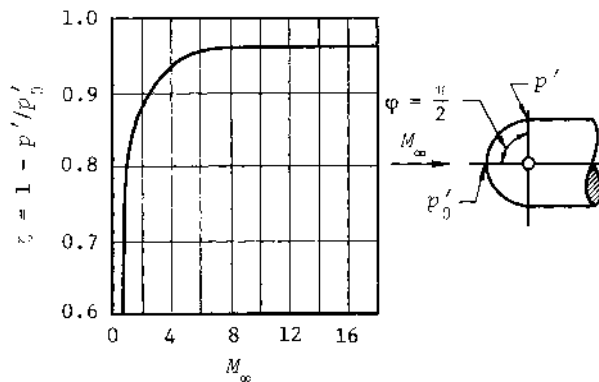


Fig. 270--Relation between the pressure parameter ξ and the Mach number

Comparison with experimental data shows that Eq. (27.52), with the values for ξ presented in Fig. 270, gives satisfactory results for $M_\infty \geq 1$. These results are presented in the form of curves in Fig. 271, where the curve for $M_\infty = 7$ represents the practical limiting value for q/q_0 at very high velocities. The limiting values are independent of Mach number.

The average values of q_{sph}/q_0 for blunting can be computed from the heat transfer distribution around a sphere and are shown as a function of M_∞ in Fig. 272.

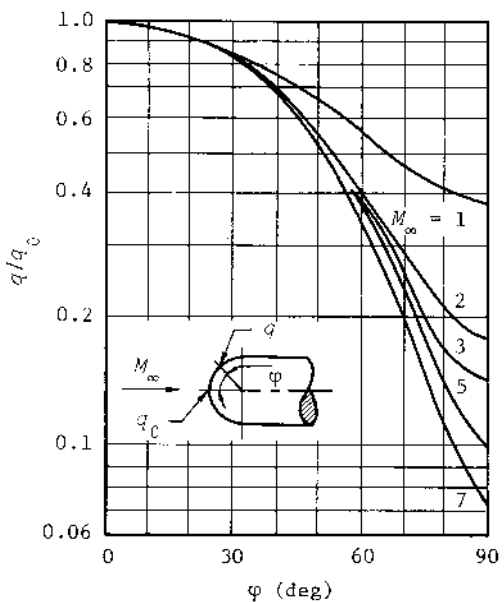


Fig. 271--Distribution of laminar heat flow
on a sphere for various Mach numbers

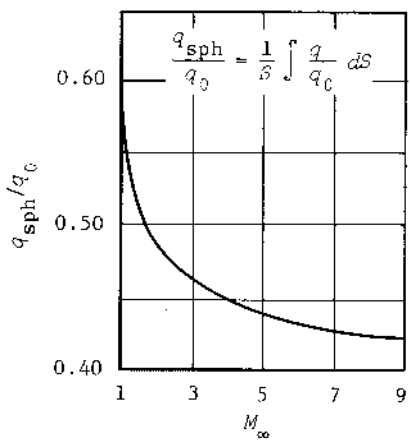


Fig. 272--Average value of heat transfer
for laminar flow over a hemisphere

Let us compute the total heat transfer to a sphere with a radius $R_N = 0.25$ m at $M_\infty = 15$ and a flight altitude of 30 km. The temperature of the wall is constant and equal to $T_w = 1000^\circ\text{K}$. On the spherical nose, the total thermal flux is determined from the equation

$$q = r^2 R_N^2 q_0 \int_0^{\bar{\varphi}} \frac{q}{q_0} \sin \varphi d\bar{\varphi}, \quad (27.54)$$

in which the variable is $\bar{\varphi} = 2\varphi/\pi$, and q/q_0 is calculated from one of the equations presented above or from the curves in Fig. 271. The integral in Eq. (27.54) can be calculated numerically or graphically. For example, the upper limit for a hemisphere is $\bar{\varphi} = 1$, and for the given conditions the value of the integral is 0.248. For these conditions, the heat transfer per unit area at the stagnation point was calculated above as $q_0 = 1200$ kcal/m² sec. Thus, the total heat transfer to the surface of a hemispherical nose is given by Eq. (27.54) as 182 kcal/sec.

Flat Noses. The heat transfer on a flat face can be assumed to be constant and equal to its value at the stagnation point. If we use the conditions for the preceding example, $q_0 = 560$ kcal/m² sec and the total heat rate is $Q = \pi R_N^2 q_0 = 110$ kcal/sec. As is evident, the heat flow to a flat surface is considerably less than that to a spherical surface. This is explained not only by the smaller surface area of a flat face but also by the greater deceleration of the flow, which leads to a considerable decrease in velocity at the outer edge of the boundary layer. In addition, there is a reduction in heat flow at the stagnation point of the flat nose because of the decrease in the velocity gradient $\tilde{\lambda}$ compared with that on a sphere.

An accurate analysis shows that the reduction of the total heat flow is less than that indicated in this example, because on a large part of the peripheral surface of the flat face the heat transfer is higher than at the stagnation point. This phenomenon is due to the fact that the pressure decreases more slowly than the velocity increases, moving away from the stagnation point. If the distribution of these parameters is known, the approximate character of the variation in the ratio q/q_0 can be determined from Eq. (27.47), in which it must be assumed

that $r = x$. In Fig. 273, the results of the calculation of this variation are presented for several values of ρ_∞/ρ'_0 . The pressure decrease can have a decisive influence near the sharp corner at comparatively small flow velocities and, in spite of a velocity increase, the heat transfer begins to decrease after reaching a maximum value.

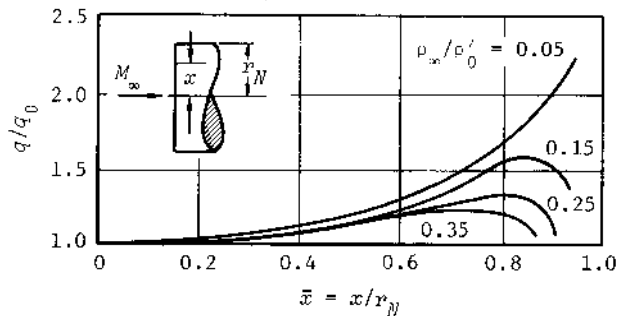


Fig. 273--Distribution of laminar heat flow on a flat face

Equation (27.47) enables us to estimate, approximately, the heat flow distribution around an arbitrary blunt surface. In Fig. 274, the results of such a calculation⁽⁷⁾ are compared with experimental data for a flat nose with a beveled edge having a radius of $r = 0.25r_N$. As is evident, the curved surface modified the distribution of the heat transfer somewhat compared with that of a flat nose, although an increase in heating rate with distance from the stagnation point can be noted, as is characteristic for a flat nose.

Ellipsoids of Revolution. Equation (27.47) can be used to calculate the laminar heat transfer around other bodies of revolution. For example, Fig. 275 shows the results of calculations⁽⁸⁾ of the variation in q/q_0 as a function of the pressure ratio on ellipsoids with different ratios of the semiaxes a/b . Small values of the ratio a/b correspond to blunt noses with increased drag, whereas the large values refer to bodies with decreased drag.

The heat flux at the stagnation point of an ellipsoid can be computed, for example, from Eq. (27.19) in which $\sqrt{R_N}$ is replaced by $\sqrt{b^2/a}$.

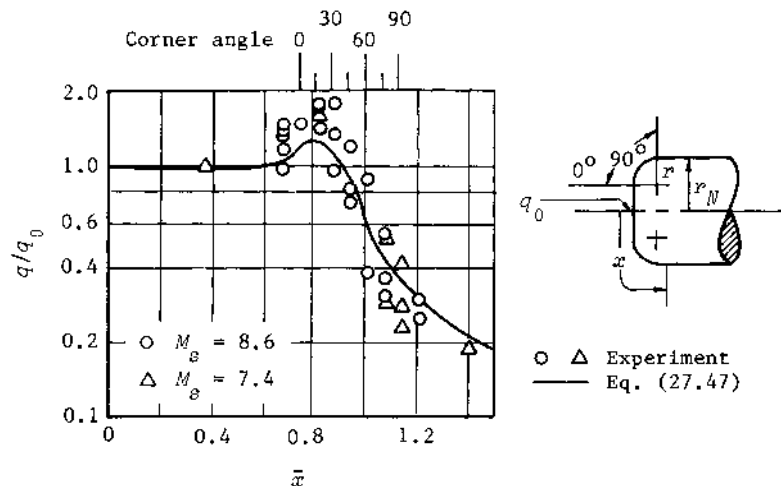


Fig. 274--Distribution of laminar heat flow on a flat face with beveled edges

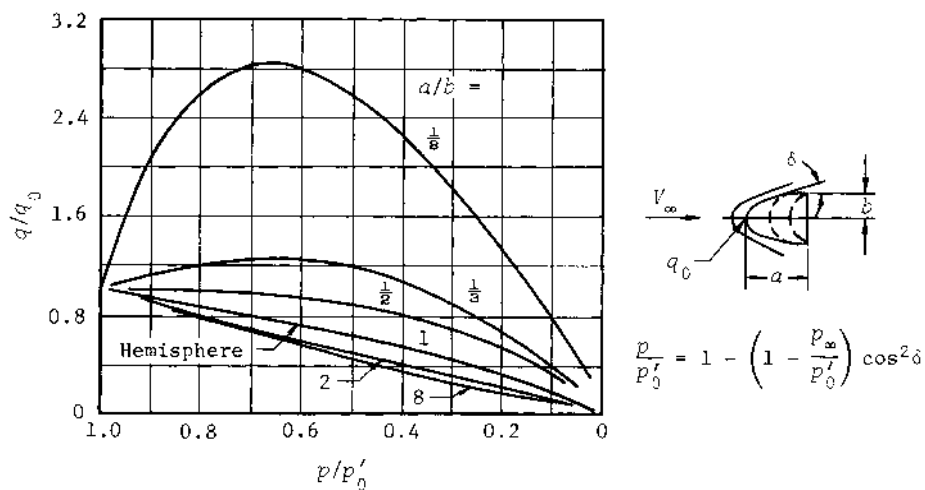


Fig. 275--Heat transfer on an ellipsoid of revolution

Then the heat transfer at an arbitrary point on the surface can be found from Fig. 275. The pressure ratio at this point is determined from Newtonian theory or from experimental data.

Conical Surfaces. Let us examine the calculation of the thermal flow on the surface of a spherically blunted cone.⁽³⁾ It will be assumed that the inviscid gas parameters on the conical surface are constant and equal to their corresponding values at the end of the sphere. For example, the velocity is

$$V_\delta = \tilde{\lambda} R_N \varphi_c = \tilde{\lambda} R_N \left(\frac{\pi}{2} - \delta_c \right),$$

and the pressure ratio is

$$\frac{p}{p'_0} = \cos^2 \varphi_c + \frac{1}{\gamma_\infty M_\infty^2} \sin^2 \varphi_c.$$

The radial coordinate of an arbitrary point on the cone surface is $r = x_c \sin \delta_c$, in which x_c is the distance along the surface from the imaginary apex of a pointed cone. This distance can be determined from

$$\frac{x_c}{R_N} = \cot \delta_c + \frac{x}{R_N} - \left(\frac{\pi}{2} - \delta_c \right).$$

These relations for V_δ , p/p'_0 , and r can now be substituted into Eq. (27.47). The integral in the denominator is computed as the sum of two integrals: one with limits of 0 to $x = R_N \varphi_c$ (or for angles from 0 to φ_c) and the other with limits from $R_N \cot \delta_c$ to x_c . The first integral corresponds to the value of the heat transfer at the end of the spherical section (i.e., at the beginning of the conical surface). Of course, the distribution of heat transfer on the spherical tip is the same as that previously obtained for a sphere. The second integral is

$$\int_{R_N \cot \delta_c}^{x_c} G x_c^2 dx_c = \frac{G}{3} (x_c^3 - R_N^3 \cot^3 \delta_c),$$

where the function is

$$G = \tilde{\lambda} R_N \Psi_C \sin^2 \varphi_C \left(\cos^2 \varphi_C + \frac{1}{\gamma_\infty M_\infty^2} \sin^2 \varphi_C \right),$$

and $\varphi_C = \pi/2 - \delta_C$. This angle (or the cone angle δ_C) is the characteristic parameter on which the value and distribution of the heat flux on a conical surface depend.

After the necessary transformations, we obtain the equation

$$\frac{q}{q_0} = \frac{A \bar{x}_C}{\sqrt{B + \bar{x}_C^3}}, \quad (27.55)$$

in which

$$A(\delta_C) = \frac{\sqrt{3}}{2} \left\{ \left[\left(1 - \frac{1}{\gamma_\infty M_\infty^2} \right) \sin^2 \delta_C + \frac{1}{\gamma_\infty M_\infty^2} \right] \left(\frac{\pi}{2} - \delta_C \right) \right\}^{\frac{1}{2}}, \quad (27.56)$$

$$B(\delta_C) = \frac{(3/16)D(\varphi_C)/\Psi_C}{\left(1 - \frac{1}{\gamma_\infty M_\infty^2} \right) \sin^4 \delta_C + \frac{1}{\gamma_\infty M_\infty^2}} - \cot^3 \delta_C. \quad (27.57)$$

The function $D(\varphi_C)$ in the last equation is determined from Eq. (27.49) for $\varphi = \varphi_C$. The dimensionless quantity \bar{x}_C in the basic equation, Eq. (27.55), is defined as x_C/R_N . It should be noted that this relation is valid only on the cone, i.e., for values of $\bar{x}_C \geq \cot \delta_C$.

On the basis of these equations, it is possible to calculate the distribution of the heat transfer in the limiting case of $M_\infty \rightarrow \infty$. The relations corresponding to this case for the functions $A(\delta_C)$ and $B(\delta_C)$ take the form

$$A(\delta_C) = \frac{\sqrt{3}}{2} \sqrt{\pi/2 - \delta_C} \sin \delta_C, \quad (27.56a)$$

$$B(\delta_C) = \frac{3}{16 \sin^4 \delta_C} \left[\frac{D(\varphi_C)}{\Psi_C} \right] - \cot^3 \delta_C. \quad (27.57a)$$

In actual cases, these equations can be used for $M_\infty \sin \delta_C \gg 1$.

In Fig. 276, results are plotted of calculations⁽³⁾ based on Eqs. (27.55) through (27.57) for a strongly cooled surface ($T_w \ll T_\delta$). The same figure presents results of the calculation from the equation

$$q_c = \frac{0.608 i_r}{Pr^{\frac{2}{3}}} \left(\frac{\sigma_{c,i} V_c}{x_c} \right)^{\frac{1}{2}}, \quad (27.58)$$

which is obtained from Eq. (27.55) for $\bar{x}_c \gg 1$. Equation (27.58) gives the value of the heat flow on the surface of the so-called equivalent pointed cone, for which the surface velocity is determined by the expression $V_c = \tilde{\lambda} R_N \varphi_c$. It is evident from Fig. 276 that the heat transfer

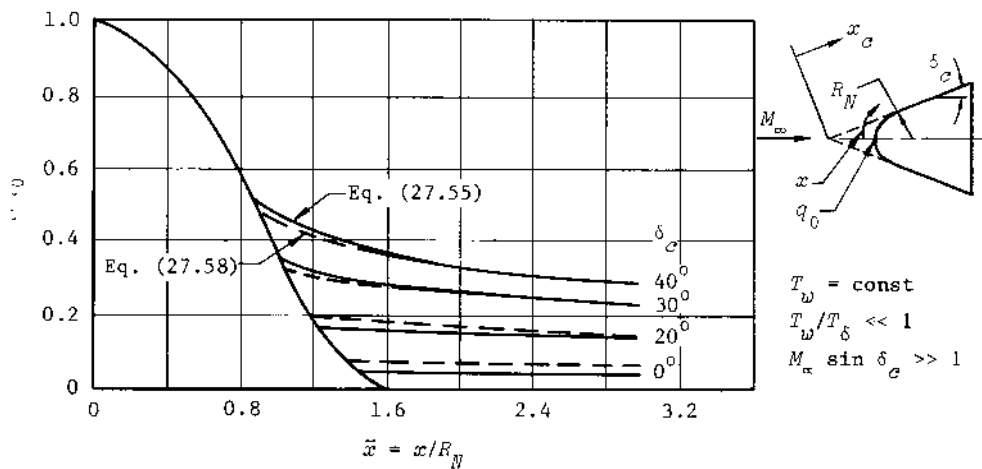


Fig. 276--Laminar heat transfer on the surface of a blunt cone

distribution is almost the same on the blunt and on the equivalent pointed cones for the 30° and 40° cone angles, whereas the heat flow to the slender blunt bodies is less than that for the corresponding equivalent cones.

Equation (27.55) shows that the heat flux far downstream of the stagnation point is approximately proportional to $1/\sqrt{\bar{x}_c}$. Therefore, it is possible to present the heat transfer in a form that is independent of x and R_N by introducing the parameter $(q/q_0) \sqrt{x/R_N}$. This parameter is a function of the local inclination of the surface δ and the free-stream

Mach number. Using the curves presented in Fig. 277, we can determine very simply the heat transfer both on the surface of the blunt nose and on the conical afterbody. Comparison with experimental data and more exact calculations shows that the results obtained from Fig. 277 are better for regions far from the nose on thick bodies. For example, satisfactory results were obtained for cone angles of $\delta_c > 30^\circ$ if the stations were located at a distance of the order $x > 20R_N$ from the nose.

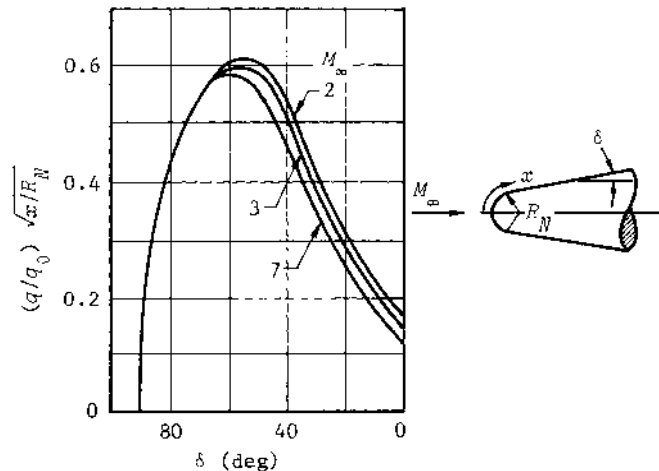


Fig. 277--Laminar heat transfer parameter

The relations presented above, as well as the conclusions, apply to the case in which dissipation in the low-velocity inviscid layer can be neglected. Actually, dissipation does occur and, as indicated earlier, it reduces the effect of blunting. Therefore, the local heat flow will be higher than the calculated value.

The effects of dissipation are a function of the velocity variation at the outer edge of the boundary layer. Thus, the heat flow equals the calculated flux near the nose but increases with distance downstream, approaching the value on a pointed cone. The calculations can be corrected by computing the parameters at the outer edge of the boundary layer including the effect of curvature of the shock wave.

The effect of dissipation can be determined approximately if the heat transfer calculated for a blunt body close to the nose and for a pointed body at a distance from the nose are plotted on a sketch, and then, after assigning a certain length, an interpolation curve is drawn. A longer length must be chosen for dense atmospheres than for rarefied atmospheres.

Cylindrical Surfaces. If a spherical nose has a cylindrical after-body, the heat transfer distribution can be calculated from Eq. (27.47) for $p/p'_0 = 1/\gamma_\infty M_\infty^2$ and $V_\delta = \pi \tilde{\lambda} R_N / 2$; i.e., the parameters are assumed to be the same as at the end of the sphere, where $\varphi = \pi/2$.

Since $r = R_N$ on the cylinder, Eq. (27.47) for the heat transfer takes the form

$$\frac{q}{q_0} = \frac{\pi / \gamma_\infty M_\infty^2}{\left[D\left(\frac{\pi}{2}\right) + \frac{4\pi}{\gamma_\infty M_\infty^2} \bar{x}'_{cyl} \right]^{\frac{1}{2}}}, \quad (27.59)$$

where $\bar{x}'_{cyl} = x'_{cyl} / R_N$ and x'_{cyl} is measured from the beginning of the cylindrical section. The function $D(\pi/2)$ is determined from Eq. (27.49) for $\varphi = \pi/2$:

$$D\left(\frac{\pi}{2}\right) = \frac{\pi^2}{4} + \frac{1}{\gamma_\infty M_\infty^2} \left(\frac{3\pi^2}{4} + 4 \right). \quad (27.60)$$

If it is assumed that $p/p'_0 = \rho_\delta u_\delta / \rho_0 L_C$ and that the heat transfer at the stagnation point (q_0) is given by Eq. (27.16), then for sufficiently distant points on the cylinder (for which $\bar{x}_{cyl} \gg 1$) the heating rate is

$$q = \frac{0.27i}{Pr^{\frac{2}{3}}} r' \sqrt{\frac{\rho_\delta u_\delta u_\delta}{x'}}, \quad (27.61)$$

which agrees with the equation for the heat transfer on a flat plate for an equivalent velocity of $u_\delta = \pi \tilde{\lambda} R_N / 2$. Experimental research shows that the heat transfer on a cylinder approaches that on a flat plate somewhat sooner than theory predicts, in fact as far forward as the corner point. If it is assumed that $Pr = 0.71$ and $u_\delta \approx V_\delta$, then according to Eq. (27.61)

the heat transfer parameter is

$$St \sqrt{Re} = 0.34,$$

which agrees with the value for incompressible flow.

Calculation of the Heat Flux from the Effective Enthalpy

It was indicated that to obtain Eq. (27.15) we assumed that the product $\rho \mu$ remained constant across the boundary layer. This assumption is valid if the wall is strongly cooled, but in other cases it is necessary to assume that $\rho \mu$ is variable. Such a complication can be avoided if the product of the density and the dynamic viscosity coefficient is assumed equal to the product of the corresponding effective parameters, i.e., to the quantity $\rho^* \mu^*$, where ρ^* and μ^* are functions of the effective enthalpy (Eq. (5.21)). The corresponding expression for heat flow can be obtained from Eq. (27.13), in which the function $F(x)$ is found from the effective parameters; i.e., it is assumed that $F(x) = F^*(x)$. If i_r is replaced by $i_r - i_w$, the heat transfer at an arbitrary point on the surface is given by

$$q^* = \frac{(i_r - i_w) F^*(x)}{2 \Pr^{\frac{2}{3}}} \sqrt{V_\infty \rho'_0 \mu'_0}. \quad (27.62)$$

In this equation, the function $F^*(x)$ is determined from Eq. (27.14), in which p/p'_0 is replaced by $\rho^* \mu^* / \rho'_0 \mu'_0$:

$$F^*(x) = \frac{\sqrt{2}}{2} \frac{(\rho^* \mu^* / \rho'_0 \mu'_0) (V_\delta / V_\infty)_r}{\left[\int_0^x (\rho^* \mu^* / \rho'_0 \mu'_0) (V_\delta / V_\infty)^{n^2} dx \right]^{\frac{1}{2}}}. \quad (27.63)$$

Relating Eqs. (27.62) and (27.63) to stagnation conditions and denoting the corresponding parameters by the subscript 0, we obtain the ratio of the heat flux at an arbitrary point to that at the stagnation point:

$$\frac{q^*}{q_0} = \frac{F^*}{F_0}. \quad (27.64)$$

The Effect of Vorticity

In the study of heat transfer at the stagnation point, it was established that the effect of vorticity resulted in increased heat transfer. The same result is observed at an arbitrary point on the surface. The results of a study of the effect of vorticity under various conditions are presented in Fig. 278. Using these curves and values for the heat transfer at the stagnation point, we can construct a preliminary curve for the estimation of the heat flow at an arbitrary surface point, accounting for the effect of vorticity.

1 — $H = 60 \text{ km}$, $M_\infty = 20$, $\text{Re} = 1470$

2 — $T'_0 = 2900^\circ\text{K}$, $M_\infty = 8$, $\text{Re} = 1000$

3 — $T'_0 = 2000^\circ\text{K}$, $M_\infty = 8$, $\text{Re} = 3570$

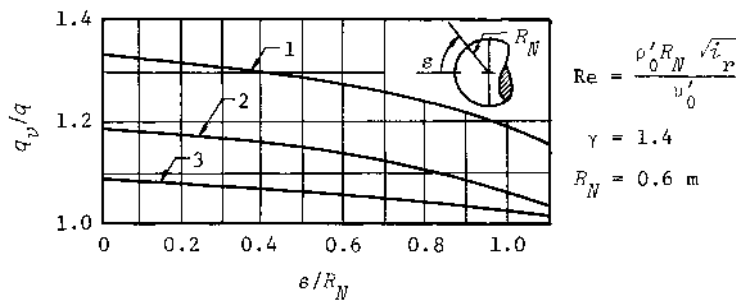


Fig. 278--Effects of vorticity on the local heat transfer to a spherical surface

The Effect of Diffusion

So far, we have presented equations for the calculation of heat transfer on the afterbody of blunt bodies neglecting the effect of diffusion. To correct the calculations for the effect of diffusion, a relation can be used similar to that used in the analysis of heat transfer at the stagnation point. One such equation is

$$q = q_T \left[1 + (\text{Le}^\beta - 1) \frac{i_D}{i_r - i_w} \right], \quad (27.65)$$

in which q_T is the heat transfer without diffusion, and the superscript β depends on the flow conditions in the boundary layer. It was shown earlier that at the stagnation point $\beta = \frac{2}{3}$ for frozen dissociation and $\beta = 0.52$ for equilibrium. There are no exact data for the value of β for downstream regions of the surface. Rough calculations show that, in the case of frozen flow, it can be assumed that $\beta = \frac{2}{3}$ for a strongly cooled flat plate. If the data for the stagnation point and a flat plate are compared, it appears that $\beta = \frac{2}{3}$ can be used for an approximate estimate of the effect of diffusion on heat transfer for all parts of the surface of a body.

The expression in the square brackets of Eq. (27.65) can also be interpreted as a correction to the friction coefficient for the effect of diffusion. Therefore,

$$c_f = c_{f0} \left[1 + (\text{Le}^\beta - 1) \frac{i_p}{i_r - i_w} \right], \quad (27.66)$$

where c_{f0} is the friction coefficient without diffusion.

HEAT TRANSFER FOR A TURBULENT BOUNDARY LAYER

Method of Calculation

In practice, some part of the aft surface of a blunt body is covered by a turbulent boundary layer. As a result, the heat transfer from the gas to the body increases considerably in this region. Experimental results are presented in Fig. 279 for a cylinder with a spherical nose.⁽⁹⁾ It is evident that the flow becomes turbulent in the Reynolds number range from $4 \cdot 10^5$ to $6 \cdot 10^5$ and the heat transfer is increased by a factor of five.

Measurements have shown that Eq. (5.34a) can be used for the calculation of turbulent heat transfer. In using this equation, we can assume that the Prandtl number is the same as for a laminar boundary layer, although it actually will be different in turbulent flow. For the case of a strongly cooled surface, we can assume that the skin friction coefficient in Eq. (5.34a) is the same as that for an incompressible fluid, using the parameters at the outer edge of the boundary layer. If the wall is cooled only slightly, it is better to use the effective parameters in calculating the skin friction and heat transfer. Nevertheless,

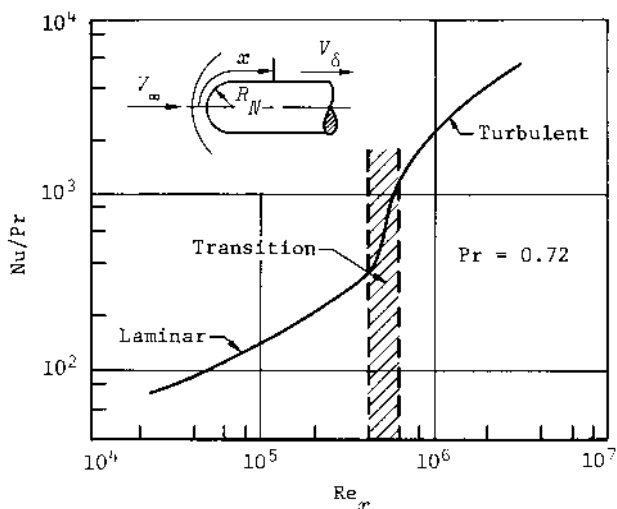


Fig. 279--Heat transfer on a cylinder with a spherical nose

the forms of the applicable relations remain the same as those for incompressible flow.

This method was tested for the laminar boundary layer and gave satisfactory results, and can be assumed to be effective in the case of the turbulent boundary layer. In fact, in such a boundary layer, there is always a thin laminar sublayer in which occur the most important changes in density and other gas parameters. These changes have a decisive influence on the friction and heat transfer. Thus, for calculating turbulent friction and heat transfer it is justifiable to use relations that are similar in external form to those used for calculating the laminar boundary layer.

The Effects of Diffusion

For a dissociated boundary layer, the presence of a concentration profile causes the diffusion of atoms toward the wall, which can be represented by a concentration of atoms at the edge of the laminar sublayer. Therefore, it can be expected that the heat transfer mechanism due to diffusion will be similar to that in a completely laminar layer, and

Eq. (27.65) can be used. However, if this equation is used for the turbulent boundary layer, a correction should be introduced to account for changes in the Lewis-Semenov number and in the exponent β . This correction would only be reliable if it were tested experimentally, but, unfortunately, there are few experimental data at the present time. Some were obtained as a result of heat transfer studies on a cylinder with a spherical nose. It was established that the quantity $(Le^\beta - 1)$ can be assumed approximately equal to 0.4, which then accounts for changes in both the Lewis-Semenov number and in β . Thus, the relation for calculating the turbulent heat transfer on a blunt surface takes the form

$$q = q_T \left(1 + 0.4 \frac{i_D}{i_r - i_w} \right). \quad (27.67)$$

This relation can be used as a basis for an equation to determine the turbulent skin friction coefficient with diffusion:

$$c_f = c_{f0} \left(1 + 0.4 \frac{i_D}{i_r - i_w} \right), \quad (27.68)$$

where c_{f0} is the skin friction coefficient without diffusion.

Useful information concerning heat transfer on a blunt surface with a small longitudinal pressure gradient (blunt cones and cylinders) can be obtained from the theory of flow over a flat plate. One of the relations for a plate that can be extended to a surface of revolution takes the form

$$q = A \rho_\delta V_\delta \text{Pr}^{-\frac{2}{3}} \frac{c_{f0}}{2} \left[2 \left(\frac{1 + \alpha_w}{1 + \alpha_\delta} \right)^{\frac{1}{\beta}} - 1 \right] \left[1 + (Le^\beta - 1) \frac{i_D}{i_r - i_w} \right] (i_r - i_w), \quad (27.69)$$

where the coefficient $A = 1.17$ for a cone.

From Eq. (27.65), it follows that the value of q_T is obtained from the expression

$$q_T = A \rho_\delta V_\delta \text{Pr}^{-\frac{2}{3}} \frac{c_{f0}}{2} \left[2 \left(\frac{1 + \alpha_w}{1 + \alpha_\delta} \right)^{\frac{1}{\beta}} - 1 \right] (i_r - i_w). \quad (27.70)$$

If the dissociation at the wall is not zero, the dissociation energy i_D in Eq. (27.69) is calculated for an atom-molecule mixture of nitrogen and oxygen:

$$i_D = (a_\delta - a_w) \frac{\sum_{k=0,N} [(c_k)_\delta - (c_k)_w] (i_R)_k}{\sum_{k=0,N} [(c_k)_\delta - (c_k)_w]} \quad (27.71)$$

The calculations are simplified for a strongly cooled surface because a_w and $(c_k)_w$ are zero. In addition, since $i_w \ll i_r$, the influence of the enthalpy of the gas at the wall can be neglected.

Heat Transfer on a Blunt Nose

A turbulent boundary layer forms on the surface of a blunt nose under certain conditions. If we know the transition Reynolds number, we can find the transition point from laminar to turbulent flow. For blunt bodies, the transition Reynolds number is usually predicted in the form of a Reynolds number based on the momentum thickness δ^{**} ; i.e.,

$$Re_{\delta^{**}} = \frac{V_\delta \rho \delta^{**}}{\mu_\delta}$$

The momentum-thickness Reynolds number can be obtained from a correlation⁽⁸⁾ of numerical solutions for the laminar boundary layer on a series of ellipsoids of revolution (including a hemisphere), resulting in the expression

$$Re_{\delta^{**}} = 11.2 \sqrt{b} \left(\frac{p_{\infty H}}{p_{\infty SL}} \right)^{0.51} \left(\frac{V_\infty}{10^3} \right)^{0.48} \psi, \quad (27.72)$$

where b , the semiaxis of the ellipse, is in meters, and V_∞ is in meters per second. The function ψ in Eq. (27.72) depends on the location of the point on the surface of the body and on the shape of the surface. Values of ψ for an ellipsoid are presented graphically in Fig. 280 as a function of p/p'_0 .

The momentum thickness corresponding to Eq. (27.72) is determined from

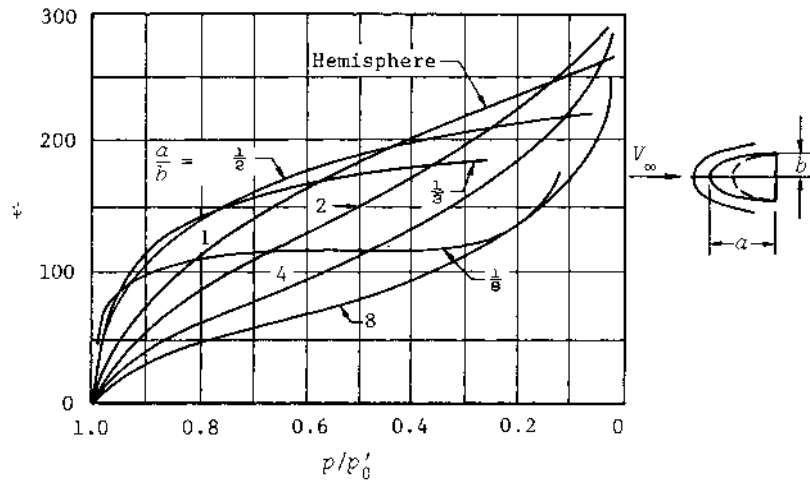


Fig. 280--Parameter for the effects of local pressure gradient and geometric shape on the transition Reynolds number

$$\delta^{**} = \frac{\sqrt{2}\xi}{\rho_{\delta} V_{\delta} r} \left[0.491(1 - 0.09\bar{\beta}^{0.4}) \left(\frac{\delta^{**}}{\nu_w} \right)^{0.39} \right], \quad (27.73)$$

where ξ is given by Eq. (27.2). The coefficient $\bar{\beta}$ is a function of the longitudinal velocity gradient and is defined as

$$\bar{\beta} = 2 \frac{d \log V_{\delta}}{d \log \xi}.$$

From Eq. (27.73), it is evident that the momentum thickness depends on the degree of cooling of the wall. This is also confirmed by experimental results obtained on a cylindrical body with a hemispherical nose (Fig. 281).

The location of the transition point can be determined by comparing the variation of $\text{Re}_{\delta^{**}}$ along the body with experimental values for the transition Reynolds number based on momentum thickness. Experimental data for Re_{tr} on a spherically blunted 30° cone are shown in Fig. 282. These results correspond to a strongly cooled wall. In general, it should be stressed that the transition Reynolds number depends considerably on the wall temperature. The effect of cooling on Re_{tr} can be

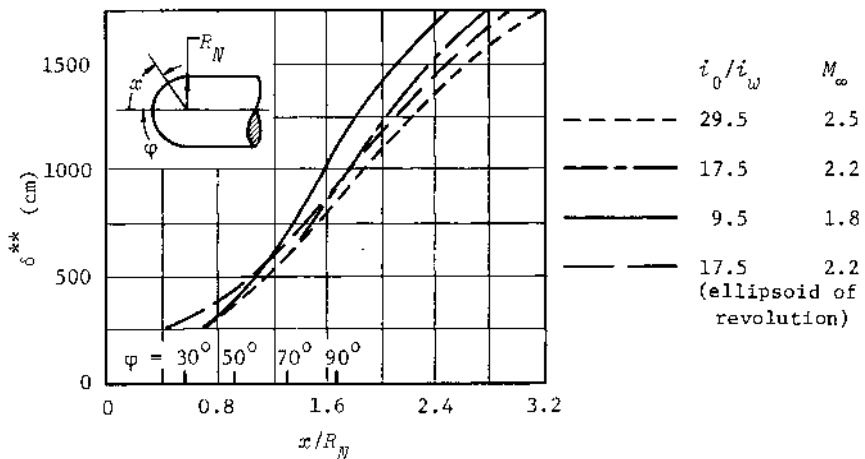


Fig. 281--Momentum thickness on a blunt body with various degrees of cooling

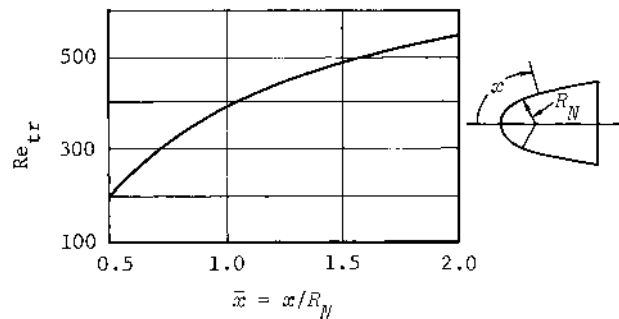


Fig. 282--Transition Reynolds number based on momentum thickness

estimated from Fig. 283, where experimental data are presented for a cylinder with a hemispherical nose. The curves in the figure can be used not only for the curved surface on the nose but also for the afterbody.

Analysis of the curves in Fig. 283 shows that the more intense the cooling of the wall, the larger the transition Reynolds number and the later transition occurs. The relation between Re_{tr} and the cooling parameter i_0/i_w is presented in another form in Fig. 284.

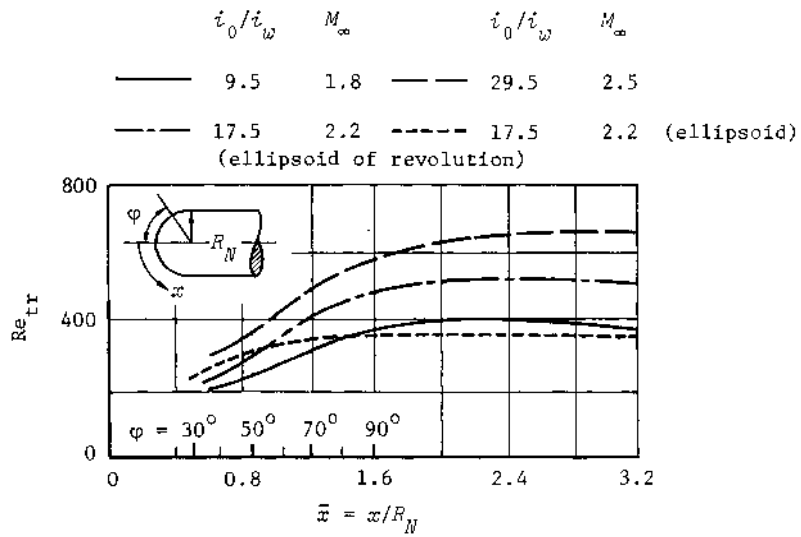


Fig. 283--Transition Reynolds number on a cooled surface

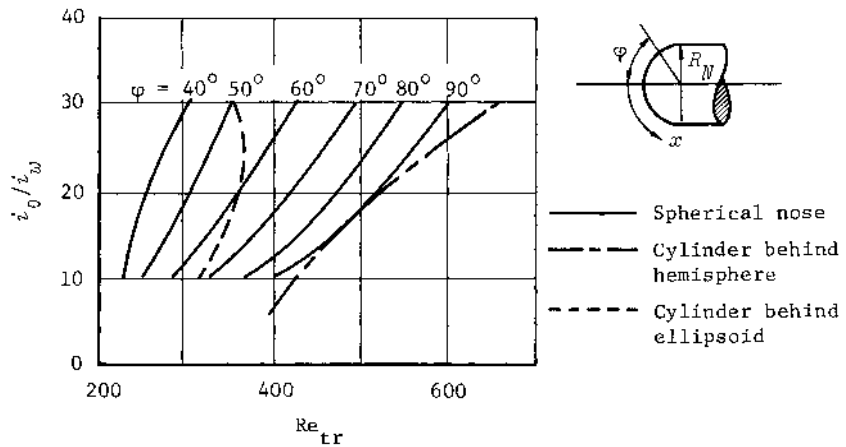


Fig. 284--Variation in transition Reynolds number with degree of cooling

It should be noted that the transition Reynolds number depends not only on the degree of wall cooling but also on the location of the point in question on the surface, i.e., on the history of the boundary layer. Indeed, the history of the boundary layer on the curved surface of the nose is the dominating influence. In the portion located on the cylindrical surface of the body, this influence is unimportant, which is evident from the fact that the transition Reynolds number for a cylinder is almost independent of the distance to the section in question, or, more accurately, of the value of x/R_N (see Fig. 283).

The calculation of the turbulent heat transfer behind the transition point must also account for the history of the boundary layer, i.e., account for the processes that occur upstream. The turbulent heat transfer equation corresponding to Eq. (27.13) for laminar heat transfer is⁽¹⁰⁾

$$\frac{\tilde{Nu}}{\tilde{Re}^{\frac{4}{5}}} = \frac{0.029 \ Pr^{\frac{1}{3}} \bar{\rho}_\delta \bar{V}_\delta^{\frac{5}{4}} \bar{\eta}_\delta^{\frac{1}{4}}}{\varphi_r^{\frac{2}{5}} \left[\int_0^{\bar{x}} \bar{\rho}_\delta \bar{V}_\delta (\bar{\rho} \bar{V}_\delta)^{\frac{5}{4}} d\bar{x} \right]^{\frac{1}{6}}}, \quad (27.74)$$

where the Nusselt number is determined from the expression

$$\tilde{Nu} = \frac{q(c_p) R_N}{\lambda_r (i_r - i_w)},$$

and the parameter \tilde{Re} is given by

$$\tilde{Re} = Re \varphi_r^{\frac{1}{2}}, \quad Re = \frac{\rho_r R_N \sqrt{i_r}}{\lambda_r}.$$

The dimensionless densities, viscosities, and velocities are defined as

$$\bar{\rho}_\delta = \frac{\rho_\delta}{\rho_r}, \quad \bar{\mu}_\delta = \frac{\mu_\delta}{\mu_r}, \quad \bar{V}_\delta = \frac{V_\delta}{\sqrt{i_r}},$$

and the parameter φ_r in Eq. (27.74) is

$$\varphi_r = \frac{p'_0}{\rho_r i_r}.$$

All quantities with the subscript r correspond to the recovery enthalpy and can be calculated approximately for stagnation conditions. The dimensionless linear parameters in this equation are based on the radius of the sphere R_N .

As is evident from Eq. (27.74), the integration begins from the conditions at the stagnation point where $\bar{x} = 0$. The solution will be valid only for those sections of the surface (or values of \bar{x}) located beyond the transition point from laminar to turbulent flow, the coordinate of which is known approximately. Results of a calculation of the turbulent heat transfer parameter from Eq. (27.74) are compared with experimental data⁽¹⁰⁾ in Fig. 285. With the exception of the transition region, the theoretical results agree satisfactorily with the experimental data.

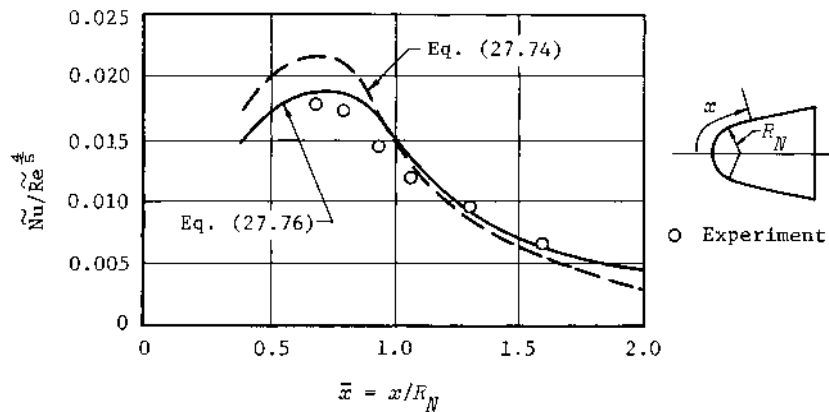


Fig. 285--Turbulent heat transfer parameter

After the heat flow is determined, the local turbulent friction coefficient can be calculated by using the Reynolds analogy:

$$q = \frac{\delta V_{\delta}}{Pr^{\frac{2}{3}}} (i_r - i_w) \frac{c_f T}{2}. \quad (27.75)$$

Studies have shown that approximate heat transfer calculations can be made if we use the relations for a flat plate and neglect the effect

of the longitudinal pressure gradient. If diffusion in the boundary layer is also neglected, the equation for the heat transfer parameter can be written as

$$\frac{\tilde{Nu}}{\tilde{Re}_x^{\frac{4}{5}}} = \frac{0.029 \Pr^{\frac{1}{3}}}{\varphi_r^{\frac{2}{5}}} \left(\frac{\bar{c}_\delta \bar{V}_\delta \bar{x}}{\bar{u}_\delta} \right)^{\frac{4}{5}} \frac{\bar{u}_\delta}{\bar{x}} \quad (27.76)$$

or

$$Nu^o \equiv (Nu)_{Le=1, G=1} = 0.029 Re_x^{\frac{4}{5}} \Pr^{\frac{1}{3}}. \quad (27.77)^+$$

Somewhat better results are obtained if the calculations are made with an effective enthalpy determined by a modified form of Eq. (5.21) that includes the Prandtl number:

$$i^* = 0.5 i_w + 0.22 \Pr^{\frac{1}{3}} i_r + (0.5 - 0.22 \Pr^{\frac{1}{3}}) i_\delta. \quad (27.78)$$

The effective parameters corresponding to this enthalpy enter into the Reynolds and Nusselt numbers:

$$Re_x = \frac{\rho^* V_\delta x}{\mu^*}, \quad Nu = \frac{q c^* x}{\lambda^* (i_r - i_w)}.$$

The use of the effective parameters in Eq. (27.76) is compared with Eq. (27.74) and the experimental data in Fig. 285.

Further refinement of these equations can be made by accounting for the effects of the longitudinal pressure gradient and diffusion. To do this, a semiempirical relation must be used:

$$\frac{(Nu)_{Le \neq 1, G \neq 1}}{Nu^o} = \frac{(q)_{Le \neq 1, G \neq 1}}{q^o} = 1.037 G(\bar{x}) \left[1 + (Le^B - 1) \frac{i_D}{i_r - i_w} \right]. \quad (27.79)$$

The function $G(\bar{x})$ determines the effect of the local pressure gradient. As is evident from Fig. 286,⁽⁸⁾ the parameter $G(\bar{x})$ depends on the pressure

[†]Editor's note: The function G in the subscript in this equation is a pressure gradient parameter defined on the next page.

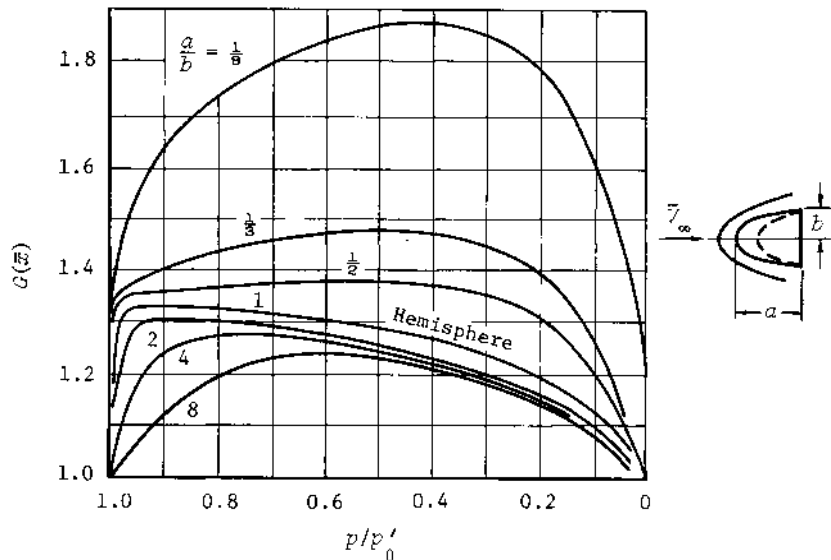


Fig. 286--Parameter for effects of pressure gradient and geometric shape on heat transfer

ratio at a given point on the surface and on the shape of the surface.[†] The quantity in the square brackets in Eq. (27.79) accounts for the effect of diffusion from the dissociating boundary layer to the wall. The quantity $Le^{\beta} - 1$ can be assumed equal to 0.58, based on experimental results.

[†]Editor's note: The function $G(\bar{x})$ can be determined from Eq. (27.74):

$$G(\bar{x}) = \left[\frac{\bar{p}_\delta \bar{V}_\delta (\bar{U}_\delta \bar{r})^{5/4} \bar{x}}{\int_0^{\bar{x}} \bar{x}^5 \bar{p}_\delta (\bar{U}_\delta \bar{r})^{5/4} d\bar{x}} \right]^{1/5}. \quad (27.79a)$$

However, Fig. 286 was obtained from Detra and Hidalgo,⁽⁸⁾ and their results were based on the formulas of Probstein, Adams, and Rose.⁽¹¹⁾ For $G(\bar{x})$, the latter authors give

$$G(\bar{x}) = \left(\frac{\bar{p}_\delta \bar{V}_\delta^{5/4} \bar{U}_\delta^{1/4} \bar{r}^{5/4} \bar{x}}{\int_{\bar{c}}^{\bar{x}} \bar{x}^5 \bar{p}_\delta^{9/4} \bar{U}_\delta^{1/4} \bar{r}^{5/4} d\bar{x}} \right)^{1/5}. \quad (27.79b)$$

COMPARISON OF HEAT FLOW ON POINTED AND BLUNT CONESConical and Spherical Noses

To estimate the effect of blunting on the total heat transfer to a body, it is of interest to first determine the difference in the heat transfer on a pointed cone and on a corresponding spherical nose (Fig. 287). The total heat transfer on a pointed cone is

$$Q_c = 2\pi \int_0^{x_c} q_c r dx,$$

which we can evaluate by using Eq. (27.58) for the local heat flow q_c to the surface of the nose. Assuming that Pr is constant, we find

$$Q_c = \frac{0.812 S_c^{\frac{1}{2}} r}{\text{Pr}^{\frac{2}{3}}} \sqrt{\frac{\sigma_e V_e}{x_c}}, \quad (27.80)$$

where the surface area of the cone is given by $S_c = \pi x_c^2 \sin \delta_c$.

The total heat transfer to the surface of an inscribed spherical segment can be calculated from

$$Q_{\text{sph}} = \frac{1}{2} S_{\text{sph}} q_0 \int_0^{\varphi_c} \left(\frac{q}{q_0} \right) \sin \varphi d\varphi,$$

in which the ratio q/q_0 can be obtained from Eqs. (27.48) or (27.52),

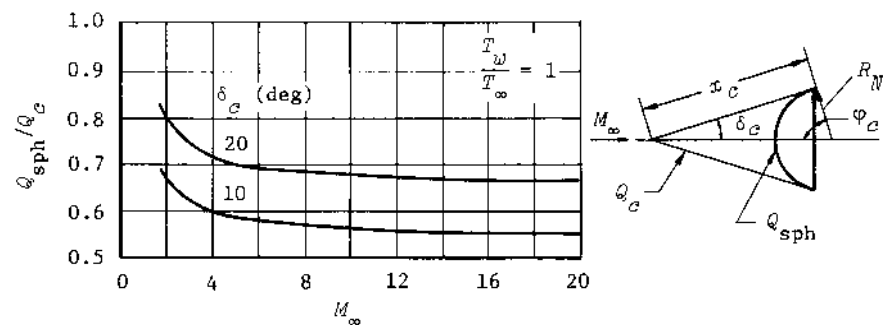


Fig. 287--Comparison of laminar heat transfer on spherically blunted and sharp conical noses

and the surface area of the sphere is

$$S_{\text{sph}} = 4\pi R_N^2 = 4\pi x_c^2 \tan^2 \delta_c.$$

The upper limit of the integral is $\phi_c = \pi/2 - \delta_c$.

The ratio of the total heat flows for the sphere and the cone, i.e., Q_{sph}/Q_c , can be determined for various flow conditions defined by the parameters M_∞ , T_w/T_∞ , and δ_c . Part of the results of such calculations⁽¹⁾ is presented in Fig. 287 for cones with half angles of 10° and 20° and for a surface cooled to the free-stream temperature. From these data, it is evident that the total heat transfer to the inscribed spherical nose is less than for the conical nose.

Conical Bodies with Pointed and Blunt Noses

We can estimate the variation in the heat transfer on a conical surface as a result of blunting by comparing the local heat flow at corresponding points on the surface of a pointed and a blunt cone. Equation (27.58) can be used, where, as before, the parameters for the blunt and the pointed cones are designated by the subscripts b and c , respectively. Assuming that, in both cases, the Prandtl numbers are identical and that $x_c \approx x_b$ for points far downstream, we obtain from Eq. (27.58)

$$\frac{q_b}{q_c} = \left(\frac{\rho_b \mu_b V_b}{\rho_c \mu_c V_c} \right)^{\frac{1}{2}} \frac{(i_r)_b}{(i_r)_c} = \left(\frac{Re_b}{Re_c} \right)^{\frac{1}{2}} \frac{\mu_b}{\mu_c} \frac{(i_r)_b}{(i_r)_c}, \quad (27.81)$$

where the ratio of the Reynolds numbers can be calculated from Eq. (26.10).

If Eq. (2.3) is used to compute the viscosity and the recovery enthalpy is calculated from the expression

$$i_r = c_p T \left(1 + r \frac{\gamma - 1}{2} M^2 \right),$$

then, assuming $c_p \approx \text{const}$, we can write Eq. (27.81) in the form

$$\frac{q_b}{q_c} = \left(\frac{M_b}{M_c} \right)^{\frac{1}{2}} \frac{1 + r \frac{\gamma - 1}{2} M_b^2}{1 + r \frac{\gamma - 1}{2} M_c^2} \left(\frac{1 + \frac{\gamma - 1}{2} M_c^2}{1 + \frac{\gamma - 1}{2} M_b^2} \right)^{\frac{1}{2}(n+\frac{3}{2})}. \quad (27.81a)$$

This equation applies to a strongly cooled surface. It indicates that, despite the increase in the local static temperature and in the recovery enthalpy for the blunt cone, the reduction in the Reynolds number leads to a decrease in heat flux on the blunt cone, although the decrease is small. For example, at $M_\infty = 20$, $r = \sqrt{0.71} = 0.845$, $\gamma = 1.4$, and $n = 1$, the decrease is only approximately 5 percent. Thus, there is little need for blunting a pointed cone if it is covered by a laminar boundary layer. The main advantage of blunting appears when a large part of the blunt cone is covered by a laminar layer, but the boundary layer is mostly turbulent on the pointed cone. To illustrate this, let us examine the relation between the friction and heat transfer coefficients for pointed and blunt cones when turbulent and laminar boundary layers, respectively, exist on their surfaces.

The ratio of the local friction coefficients is

$$\frac{(c_f)_b}{(c_f)_c} = \frac{A_b}{A_c} \frac{(c_f^{pl})_b}{(c_f^{pl})_c},$$

where $A_b = \sqrt{3}$, $A_c = 1.17$. The coefficients $(c_f^{pl})_b$ and $(c_f^{pl})_c$ can be determined from Eq. (5.5), for example, in which it is necessary to convert to the effective parameters in the more general case. If a strongly cooled surface ($i_w \ll i_r$) is considered, this transformation need not be made. However, the calculation must be made from the inviscid parameters on the cone surface. Then, we get

$$\frac{(c_f)_b}{(c_f)_c} = 16.65 \left(\frac{\text{Re}_c}{\text{Re}_b} \right)^{1/2} \frac{1}{\text{Re}_c^{3/10}}. \quad (27.82)$$

To estimate the influence of blunting on the average friction coefficient, it is necessary to replace the coefficient 16.65 by 20.4 in Eq. (27.82).

Obviously, to use this equation we must first find the Reynolds numbers for the given points on the blunt and pointed conical surfaces. We can obtain some idea of the order of magnitude of the reduction in friction by assigning anticipated values to these numbers. For example,

if it is assumed that $\text{Re}_c = 10^{10}$ on the pointed cone and $\text{Re}_b = \text{Re}_c/25$ on the blunt cone, the local and average friction coefficients on the blunt surface decrease in comparison with their values on the pointed cone by factors of 12 and 10, respectively.

Equation (27.82) can also be used with the Reynolds analogy for the estimation of the decrease in heat transfer to the blunt surface. For simplicity, it can be assumed that the Prandtl numbers for both bodies are identical. Then, if $i_w \ll i_r$, the ratio of the heating rates is

$$\frac{q_b}{q_c} = 16.65 \left(\frac{\text{Re}_b}{\text{Re}_c} \right)^{1/2} \frac{1}{\text{Re}_c^{3/10}} \frac{u_b}{u_c} \frac{(c_p)_b}{(c_p)_c} \frac{(T_r)_b}{(T_r)_c}.$$

If we assume that the last two ratios on the right side vary little, compute the coefficient of viscosity from Eq. (2.3) and Re_b/Re_c from Eq. (26.10), and choose $n = \frac{3}{4}$, we can obtain a simpler relation for the ratio of the local heat flows on the blunt and pointed cones:

$$\frac{q_b}{q_c} = 16.65 \left(\frac{M_b}{M_c} \right)^{4/5} \frac{1}{\text{Re}_b^{3/10}} \left(\frac{1 + \frac{\gamma - 1}{2} M_b^2}{1 + \frac{\gamma - 1}{2} M_c^2} \right)^{1/4}. \quad (27.83)$$

The coefficient 20.4 must be substituted for 16.65 to estimate the ratio of the average values of heat transfer.

According to Eq. (27.83), the heat transfer on the blunt body can decrease considerably. For example, for a 10° cone at $M_\infty = 20$, $M_b = 3$, and $\text{Re}_b = 10^6$, the local heat transfer is reduced by a factor of 20 and the average heat transfer by a factor of 16. Experimental research shows that these estimates are very approximate. Actually, the reduction in heat transfer is significantly less, because turbulence occurs on the blunt body before the calculated transition Reynolds number is reached. Thus, a turbulent boundary layer covers a considerable part of the surface, and the heat flow is the same in that region as it is on the pointed cone.

28. VISCOSITY EFFECTS ON THE EXTERNAL FLOW
AROUND A BLUNT BODY

ESTIMATE OF THE EFFECT OF VISCOSITY

IN A STUDY of viscosity effects on the external (inviscid) flow parameters, in particular on the static pressure distribution, it is necessary to consider the role of blunting in the formation of the boundary layer. If the free-stream Reynolds number based on the nose diameter is sufficiently large, the influence of the pressure distribution around the blunt nose dominates, i.e., the magnitude and character of the pressure distribution determine the development of the boundary layer. The reciprocal influence of the boundary layer on the external flow is unimportant in the region of the nose. However, this influence increases with distance from the nose and with a thickening of the boundary layer. Therefore, in the calculation of the flow parameters at the outer edge of the boundary layer, it is necessary to take into account the interactions caused by viscous forces.

Studies have shown that, for a body of revolution, the distance L from the blunt nose at which the additional drag (due to viscous effects on the pressure distribution) is equivalent to the drag due to blunting is given by the equation

$$\frac{L}{D_N} = b \frac{\text{Re}_{DN}}{M_\infty^2}, \quad (28.1)$$

where b is a coefficient dependent on the flow conditions. For example, it has been found from wind-tunnel tests on a thermally insulated cylindrical surface ($T_w = T_r$) at $M_\infty = 15$ that b is approximately equal to two.

The effects of viscous interaction are decreased considerably for cases in which the surface temperature is much lower than the recovery

temperature, and therefore the boundary layer is thinner than that on an insulated wall. For example, in air at $T_w = 5T_\infty$ and $M_\infty = 15$, the coefficient $b \approx 20$. Thus, viscous interaction is a function of the thermal conditions at the wall, the free-stream Mach number, and Re_{DN} . As an example, let us estimate the interaction on the surface of a sphere-cylinder with $D_N = 1$ m for flight conditions at an altitude of 82 km and a velocity corresponding to $M_\infty = 15$. For these conditions, the Reynolds number is $\text{Re}_{DN} \approx 2640$. If Eq. (28.1) is used, the ratio $L/D_N = 23$ for an insulated wall, while for a cold wall with $T_w = 5T_\infty$ and $b = 20$, the length will be 10 times larger, i.e., $L/D_N = 230$.

For this value of the Reynolds number, it is evident that the effects of viscosity on the pressure distribution can be neglected for bodies having lengths shorter than those calculated above. However, with a decrease in Reynolds number or with an increase in Mach number, the calculated value of L/D_N may be less than the relative length of the actual body, and viscous interaction will be important. For example, at $\text{Re}_{DN} = 225$, $M_\infty = 15$, and $T_r = T_w$, the additional drag due to viscous interaction becomes commensurate with the basic nose drag at a length $L = 2D_N$.

These results are valid only for large Re_{DN} and are of doubtful accuracy for small Reynolds numbers. At the moment, it is difficult to say exactly where the boundary of applicability of the interaction theory is located, i.e., as characterized by some specific value of Re_{DN} . Some data show that a preliminary estimate of the lower limit is probably $\text{Re}_{DN} \approx 100$.

THE EFFECTIVE SHAPE OF THE BODY

The computation of viscous interaction effects on the external flow parameters is based on the calculation of the inviscid flow around an effective body, which is obtained by shifting the given body contour by a quantity equal to the displacement thickness of the boundary layer. The displacement thickness can be calculated approximately on the basis of the theory of an incompressible boundary layer on a flat plate. The displacement thickness is related to the boundary layer thickness by $\delta^* = 3\delta/8$. In turn, δ can be obtained from Eqs. (5.2) and (5.5).

$$\delta = 7.2x c_{fx}.$$

Therefore,

$$\delta^* = 2.7x c_{fx}. \quad (28.2)$$

To determine the local skin friction coefficient c_{fx} , we must take into account the surface shape (cone, sphere, or plate) and also the effects of bluntness on the boundary layer flow.

Since the calculation is of an approximate nature, let us use Eq. (6.28) to estimate c_{fx} . The Stanton number in this equation can be found from the corresponding heat flow equation. Then the relation for the displacement thickness takes the form

$$\delta^* = \frac{5.4qx}{(i_r - i_w) \rho_s V_\delta^2} \text{Pr}^{\frac{2}{3}}. \quad (28.3)$$

To use this equation, the heat flow must be determined. At an arbitrary point on the surface, the heat flow can be defined as $q = \bar{q} q_0$, where the ratio \bar{q} is determined from Eq. (27.50) for a sphere, from Eq. (27.55) for a conical surface, and from Eq. (27.59) for a cylindrical surface. In addition, the corresponding graphs can be used for the calculation.

Using Eq. (27.16) for the heat transfer at the stagnation point and assuming that the Prandtl number is constant, we can write Eq. (28.3) as

$$\delta^* = 4.14 (\tilde{\lambda} F'_0 u'_0)^{\frac{1}{2}} \frac{x \bar{q}}{\rho^* V_\delta} \frac{(i_r - i_w)_0}{i_r - i_w}, \quad (28.4)$$

which contains the effective parameters. If the wall is uniformly cooled and $i_w \ll i_r$, then

$$\frac{(i_r - i_w)_0}{i_r - i_w} \approx 1.$$

Furthermore, if it is assumed that $V_\delta = \tilde{\lambda} x$, Eq. (28.4) can be simplified further:

$$\delta^* = 4.14 \left(\frac{F'_0 u'_0}{\tilde{\lambda}} \right)^{\frac{1}{2}} \frac{\bar{q}}{\rho^*}. \quad (28.4a)$$

From this equation it follows that, at the stagnation point ($\bar{q} = 1$, $\rho^* = \rho_0'$), the displacement thickness has the finite value

$$\delta^* = 4.14 \left(\frac{\mu_0'}{\lambda \rho_0'} \right)^{\frac{1}{2}}.$$

For the conditions considered in the earlier example ($M_\infty = 15$, $H = 30$ km, and $R_N = 0.25$ m, Table 19), the value of $\delta^*/R_N = 4.32 \cdot 10^{-3}$, i.e., an order of magnitude less than for a thermally insulated surface. If the value of δ^* is estimated for the same free-stream conditions at a point on a sphere corresponding to $\varphi = 80^\circ$, it turns out that the same value of δ^*/R_N is obtained as at the stagnation point. Consequently, viscous interaction on a sphere is negligible for the example in question.

The displacement thickness for points far downstream on a cone and a cylinder (for a cooled surface) can be determined from Eqs. (27.58), (27.61), and (28.3) with the general form

$$\delta^* = \frac{Ax}{\sqrt{Re_x}}, \quad (28.5)$$

where the coefficient A for a cone and a cylinder is 3.3 and 1.47, respectively. The Reynolds number is $Re_x = V_\delta \rho_\delta x / \tau_\delta$, where the velocity equals its value at the end of the spherical nose. In practical calculations, the Reynolds number can be computed from Eq. (26.10) or found from Fig. 255.

As an illustration of the application of Eq. (28.5), let us consider the calculation of the displacement thickness for a blunt 10° cone and for a cylinder, each 10 m long. It is assumed that the same flight conditions apply as in the example presented above ($M_\infty = 15$, $H = 30$ m), and that the spherical blunting has the same dimension ($R_N = 0.25$ m). The Reynolds number for these conditions is $9 \cdot 10^7$ for a sharp 10° cone of a length of 10 m. The corresponding Reynolds number for an unblunted cylinder is $5.28 \cdot 10^7$, where an unblunted cylinder can be considered a pointed cone with zero slope. The Reynolds numbers obtained are larger than the transition Reynolds number and, therefore, the boundary layer will be turbulent on the pointed bodies. Since blunting reduces the

Reynolds numbers on a cone by a factor of 30 and on a cylinder by a factor of 48, the boundary layer will be laminar over practically the entire length and, therefore, it is possible to use Eq. (28.5). Substituting the reduced values of the Reynolds numbers, we obtain $\delta^* = 19.2$ mm at the end of the cone and $\delta^* = 14.4$ mm at the end of the cylinder.

The viscous interaction will be greater in turbulent flow. To estimate the displacement thickness in this case, we can use the equation

$$\delta^* = \frac{Bx}{\text{Re}_x^{\frac{1}{2}}}, \quad (28.6)$$

in which the coefficient B for a cone and a cylinder is 0.054 and 0.046, respectively.

It should be noted that this equation gives only limiting values. One of these values corresponds to the case of a thermally insulated wall, for which the Reynolds number must be computed from the effective parameters for $T_w = T_r$. The other limiting value corresponds to the case of a highly cooled wall for which $T_w \ll T_r$. In this case, the Reynolds number must be calculated from the parameters at the external edge of the boundary layer. For the condition $T_w \ll T_r$, and if the reductions in Reynolds number due to bluntness given above are considered, the displacement thickness at the end of a cone and a cylinder is 27 and 28 mm, respectively. Hence, it can be seen that if the thickening for a cone is approximately 2 percent of the base radius, it is significantly greater for a cylinder, approximately 11 percent.

It is interesting to estimate the variation in δ^* for an insulated wall. Calculations show that the effective wall temperature will be approximately 10 times greater than that at the outer edge of the boundary layer. If the variation of σ and v with temperature is taken into account, the Reynolds number found from the effective parameters is decreased by 50 times. Thus, the displacement thickness of the laminar boundary layer is increased by a factor of 7, and that of the turbulent boundary layer by a factor of 2.2. The considerable increase in the displacement thickness is related to the decrease in local Reynolds numbers. Thus, the blunting of a body, an increase in flight altitude, or

an increase in the average temperature of the boundary layer, all promote changes in the effective shape of the body.

The results of the calculation of the displacement thickness on a blunt cylinder by another method are presented in Fig. 288 for a thermally insulated body. The displacement thickness parameter

$$\frac{\delta^*}{R_N} \sqrt{Re_{RN}}$$

has a value of 0.53 at the stagnation point and at the beginning of the cylindrical section is increased by a factor of 10.

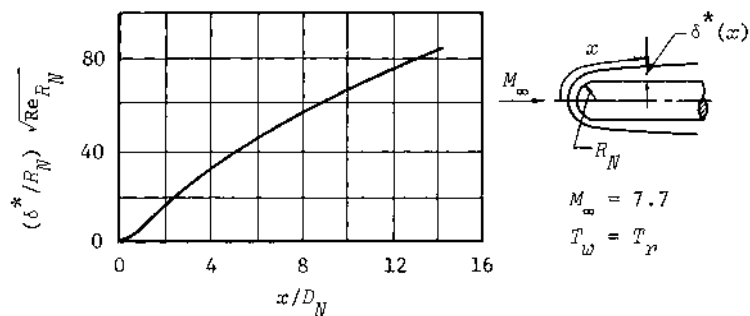


Fig. 288--Variation of the displacement thickness parameter with length on a cylindrical body

After determining the effective shape of the body by shifting the contour in a normal direction by the quantity δ^* , we can compute the pressure distribution and other inviscid parameters for this new shape. One of the characteristics of this new shape (e.g., for a cone) is its effective angle, which can be found approximately from the equation

$$\delta_c^e = \delta_c + \frac{\delta^*}{L},$$

where δ^* is the displacement thickness at a given length L . If a cylinder is considered, its effective shape can be assumed to be a cone

with an angle δ^*/L . However, the determination of the effective shape of a cone or a cylinder is more accurate if it is taken to be a modified surface of revolution with a curved profile. The effective curved shape is obtained, obviously, in all cases when the initial body shape has a curved profile. For the effective curved surfaces, the pressure calculation can be made from the Newtonian equation $C_p = C_{p0} \sin^2 \delta^e$, in which the angle δ^e is determined by the slope of the effective profile relative to the free-stream flow velocity. It is often convenient to construct the body profile to a suitable scale and to establish the required new angle δ^e graphically. In addition, Eqs. (28.5) and (28.6) can be used to compute the increment in slope of the contour, $\Delta\delta$, due to the influence of the displacement thickness for parts of the body sufficiently distant from the blunt nose. Differentiating with respect to x , we obtain

$$\Delta\delta = \frac{d\delta^*}{dx} = \frac{A}{2} (Re_x)^{-\frac{1}{2}}, \quad (28.7)$$

$$\Delta\delta = \frac{d\delta^*}{dx} = \frac{4B}{5} (Re_x)^{-\frac{1}{5}}. \quad (28.8)$$

From these values it is possible to compute the effective slope of the contour $\delta^e = \delta + \Delta\delta$.

The effect of the boundary layer on the pressure distribution is shown in Fig. 289 for the example of a power law body in helium flow. The rather considerable pressure increase due to viscous interaction (on the average approximately 20 percent) is due to the very high Mach number, the comparatively small Reynolds number, and the insulated surface.

In Fig. 290, the effect of Reynolds number on the pressure is reproduced for three points on a cylindrical surface with a spherical nose, where $Re_\infty = \rho_\infty V_\infty L_N / \mu_\infty$. The boundary layer thickness on this surface depends on the viscous flow conditions over the nose and is larger at a given section for smaller values of Re_∞ . It must be kept in mind that for sections of the cylinder far downstream this viscosity effect essentially disappears. It is practically impossible to define a thickness

for the boundary layer under these conditions, since considerable dissipation of the viscous layer occurs in the external flow, and the pressure approaches its value in the unperturbed flow.

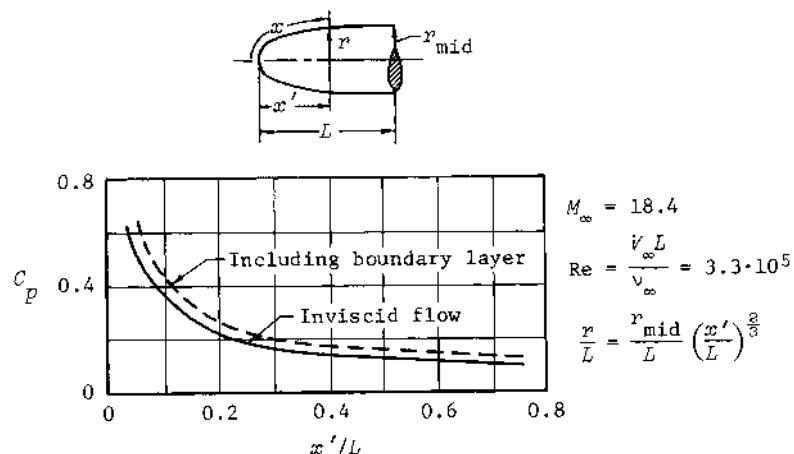


Fig. 289--Effect of the boundary layer on the pressure distribution

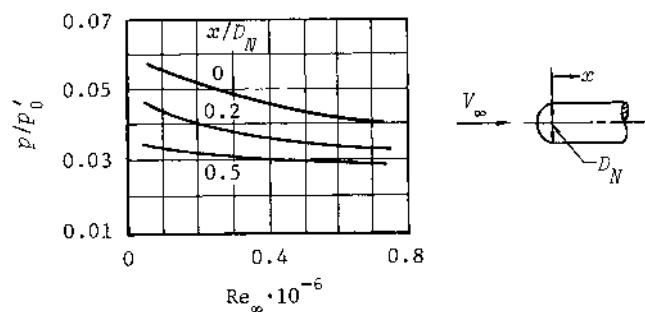


Fig. 290--Effect of Reynolds number on the pressure distribution

Chapter IX

HEAT AND MASS TRANSFER FROM THE SURFACE OF A VEHICLE

Editor's Introduction

THIS CHAPTER PRESENTS a basic treatment of the process of ablation by melting, vaporization, and sublimation. Although charring ablators have emerged in recent years as attractive materials for providing an efficient thermal protection shield, they are not discussed in the text. Swann (NASA TR R-195, June 1964) derives the equations that govern the performance of charring ablators, subject to a diffusion-controlled oxidation mechanism of char removal. A solution is presented for the case of a constant-enthalpy level, and the effects of various material properties and environmental parameters are discussed. Swann, Pittman, and Smith (NASA TN D-2976, September 1965) present an analysis of charring ablators consisting of differential equations that are expanded into finite-difference equations and are thus suitable for computerized numerical solutions. The equations provide for three layers of different materials, the first two of which may have moving boundaries.

Because of the complexity of analyzing theoretically the performance of charring ablators, digital computer programs are usually used for this purpose. Curry (NASA TN D-3150, December 1965) describes a typical program that predicts the transient thermal response of a charring ablator. The numerical results from this program are in good agreement with exact solutions and test data.

Lundell, Dickey, and Jones (AIAA J., June 1968) show that the physical model for analyzing the performance of charring ablative materials in the diffusion-controlled surface combustion regime becomes particularly simple when the surface and char-interface velocities are equal. These velocities, as well as the mass degradation rates, then depend solely upon the ratio of the surface pressure to the nose radius. The surface temperature is a function of this ratio and the enthalpy potential across the boundary layer.

An important mechanism of ablation may be the failure of a solid surface as a result of loading by aerodynamic shear or by the rapid loss of surface liquid due to the action of both shear and surface pressure gradients on a body in hypersonic flow. Graves (AIAA J., May 1966) discusses an analytical and experimental investigation of the behavior of ablation materials (pyrex, quartz, phenolic refrasil, and teflon) under conditions that are representative of hypersonic velocity at low altitude. An analysis by Schneider, Dolton, and Reed (AIAA J.,

January 1968) of elastic/plastic thermal stresses in a carbon/phenolic heat shield during reentry shows that high tangential stresses exist in the char, accompanied by high-frequency char spallation through the peak heating period. In this example, mechanical erosion accounted for two-thirds of the total reentry surface recession.

A brief discussion is given on page 776 of the desirability of low heat absorption and low heat conduction to the interior of surfaces protected by ablation materials. Gasley (Handbook of Astronautical Engineering, 1961, Chapter 10) includes the effect of conduction to the interior by defining an effective heat absorption parameter that is more general than the usual effective heat of ablation given in the text. The effective heat absorption of an ablation system is presented as a function of the fractions of heat transferred by radiation, vaporization, and conduction.

Design techniques, procedures, and example solutions for ablative heat shields are given in the Ablation Handbook, Entry Materials Data and Design, AFML-TR-66-262, November 1966. The handbook illustrates the important parameters, the problems involved, and the necessary information and sequential steps required in the design process, including mission definition, materials selection, heat shield sizing, and fabrication. Thermal, mechanical, chemical, and ablation data are also presented for a large number of ablative materials.

§ 29. GENERAL DEFINITIONSABLATION (MASS TRANSFER)

ON ENTRY INTO THE DENSE LAYERS of the atmosphere, part of the material of a satellite or of the nose section of a ballistic missile is destroyed and carried away due to the fact that the surface is exposed to extreme heating. As a result, the temperature can reach the melting point and, at very high velocities, the vaporization or sublimation temperature. The processes caused by fusion, vaporization, and sublimation are combined under the general term ablation.

Mass transfer must be considered as the most important means of thermal shielding of the remaining part of a vehicle, since a large amount of the energy arriving at its surface is absorbed and dispersed by the mass loss.

THE TWO-PHASE BOUNDARY LAYER

For the majority of usable materials, particularly vitreous materials, the ablation process begins with fusion of the surface into a thin film of molten material, which can be called the liquid phase of the boundary layer. The other phase of the boundary layer is represented by the gas stream next to the molten surface (Fig. 291). When there is insufficient heat to vaporize the liquid, there is negligible interaction between the two phases. Furthermore, since the viscosity of the molten material is much greater than that of the gas, the liquid layer flows with a very small tangential velocity compared with the gas.

For example, calculations show that the ratio of local velocities at the outer edges of the liquid and gas layers under the usual conditions of very high velocity flow is of the order of $V_{xt}/V_{x\delta} \approx 5 \cdot 10^{-4}$.

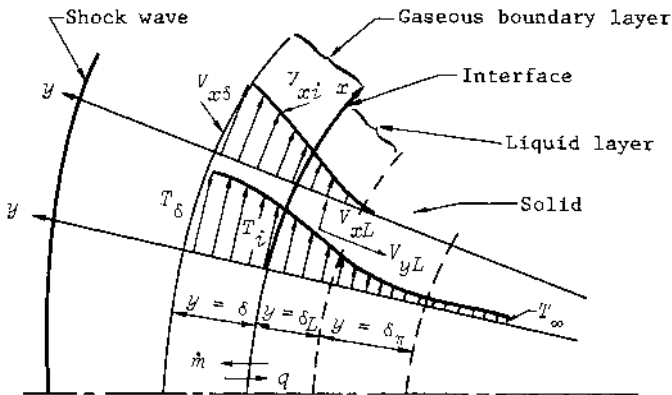


Fig. 291--The two-phase boundary layer on a blunt surface with fusion

Therefore, it can be assumed that the flow in the gaseous phase is practically independent of the liquid layer. In other words, the gas phase behaves as an ordinary boundary layer.

With an increase in heat transfer and temperature, a certain amount of the flowing liquid evaporates, and the vapor penetrates into the gas layer. As a result of this injection of vapor, an interaction occurs between the liquid film and the gaseous boundary layer that leads to a decrease in the aerodynamic heating rate and thus to a reduction in heating. If the temperature of the surface approaches the boiling point, practically the entire liquid layer vaporizes and the maximum amount of vapor enters into the gas phase.

Such is the physical mechanism of the ablation process. Since its basic effect involves the absorption of energy by mass loss, it is very important to know what this energy (heat) of ablation is. As we shall see subsequently, the amount of material lost can be calculated from the value of the heat of ablation.

THE HEAT OF ABLATION FOR VAPORIZATION (OR SUBLIMATION)

To obtain a general expression for the heat of ablation when the molten material is completely vaporized or in the case of sublimation

(for material not having a liquid phase), let us consider the heat balance equation for steady ablation.⁽¹⁾ The heat balance equation for an ablating material expresses the condition that the aerodynamic heat flow (q_i) is expended on heating and vaporization of the material and is partially radiated (q_r). Therefore,

$$q_i = m_v (c_p T_i + i_v) + q_r, \quad (29.1)$$

where m_v is the flow of mass of vaporized material, defined as the rate of mass loss or ablation; i_v is the vaporization enthalpy (latent heat of vaporization); T_i is the surface temperature; and c_p is the specific heat of the material.

The aerodynamic heat flow (q_i) absorbed during ablation is less than the amount of heat (q_0) supplied to the surface in the absence of ablation because of the injection of vaporized material into the boundary layer. The so-called transpiration cooling effect is involved in this phenomenon. The reduced heating rate can be given by $q_i = q_0 - \Delta q$, where Δq is the decrease in heat flow to the wall due to vapor injection and can be represented in the form $\Delta q = q_0(1 - \psi)$. The quantity ψ in this expression is a function of the character of the boundary layer (i.e., whether it is laminar or turbulent) of the mass loss m_v , of the velocity of the body M_∞ , and of the molecular weight of the vapor \bar{m}_v .

It has been established experimentally that the function ψ has the form⁽¹⁾

$$\psi = 1 - \frac{\beta m_v}{q_0} (i_0 - i_w), \quad (29.2)$$

where β is called the transpiration coefficient. For laminar and turbulent flows, respectively, the value of β can be determined from

$$\beta_L = N \left(\frac{29}{\bar{m}_v} \right)^{\frac{1}{3}}, \quad \beta_T = \frac{1}{3} \beta_L. \quad (29.3)$$

Equation (29.2) gives satisfactory results for $0.24 \leq \beta \leq 4.0$. From

[†]Editor's note: It should be noted that $\psi = q_i/q_0$.

experimental data, N and $\bar{\alpha}$ lie in the ranges

$$0.67 \leq N \leq 0.72, \quad 0.25 \leq \bar{\alpha} \leq 0.4.$$

In particular, for glassy materials it can be assumed that $N = 0.68$ and $\bar{\alpha} = 0.26$.

The molecular weight of the vapors (\bar{m}_v) of the more common materials such as plastic and glass coincide approximately with the molecular weight of air. If it is assumed that $\bar{m}_v = 29$ and $N = 0.7$, the coefficients determined from Eq. (29.3) will be $\beta_L = 0.7$ and $\beta_T = 0.23$.

The surface temperature T_i^* is approximately equal to the vaporization temperature. The term in parentheses in Eq. (29.1) represents the heat of ablation, and consists of the heat capacity of the material and the heat of vaporization. If it can be determined, the mass loss rate m_v can be computed. In practice, it is convenient to introduce the concept of the effective heat of ablation, defined as

$$q^* = \frac{q_0}{m_v} \text{ kcal/kgf.} \quad (29.4)$$

For steady heating, the amount of heat ($q_0 t$) supplied by the ordinary boundary layer in a certain time t is equal to the energy $q^* m_v t$ involved in the loss of mass.

From the expression for w and Eq. (29.1), the effective heat of ablation is given by

$$q^* = \frac{c_p T_i + i_v + \beta(i_0 - i_w)}{1 - q_r/q_0}, \quad (29.5)$$

where the heat flux per unit area due to radiation is $q_r = \epsilon \sigma T_i^4$. If radiation and the wall enthalpy i_w are neglected, the effective heat of ablation is

$$(q^*)^0 = c_p T_i + i_v + \beta i_0. \quad (29.6)$$

As can be seen, this quantity is a function of the stagnation enthalpy. It should be noted that Eq. (29.6) is not valid when the radiative energy

becomes commensurate with the aerodynamic heating rate. Based on Eq. (29.5), radiative cooling increases the effective heat of ablation according to the relation

$$q^* = \frac{(q^*)^o}{1 - q_r/q_0}. \quad (29.7)$$

For some materials, the heat flow to the surface will be increased due to the combustion of the vapors with the oxygen of the air diffusing into the gaseous layer. The amount of heat due to combustion in the laminar layer has been determined to be⁽²⁾

$$\Delta q_i = \frac{0.21 i_c}{i_0 - i_w} q_i \quad (29.8)$$

where i_c is the heat of combustion per unit mass of oxygen. Thus, the term q_i in Eq. (29.1) should be modified to the form

$$q_i + \Delta q_i = q_i(1 + \bar{q}_c),$$

where $\bar{q}_c = \Delta q_i/q_i$. Therefore, instead of Eq. (29.5) for calculating the effective heat of ablation, we have

$$q^* = \frac{s(i_0 - i_w) + (c_p T_i + i_v)/(1 + \bar{q}_c)}{1 - (q_r/q_0)/(1 + \bar{q}_c)}. \quad (29.9)$$

If radiation and i_w are neglected, this relation is simplified:

$$(q^*)^o = \frac{c_p T_i + i_v}{1 + \bar{q}_c} + \beta i_0. \quad (29.10)$$

SIMULTANEOUS FUSION AND VAPORIZATION

The demands associated with the necessity for materials possessing a high effective heat of ablation and a low thermal conductivity result in the use of combinations of heat resistant coatings. For example, one type of coating involves the use of a plastic in conjunction with glass, which has a high viscosity and a low thermal conductivity. A special

feature of these vitreous-plastics or, in general, of similar combination materials is that, under strong thermal action, they behave first as heat absorbers. Then, due to the low coefficient of thermal conductivity, their surface temperature rapidly increases to the level at which simultaneous melting and vaporization is possible. Observations show that in the use of fiber glass the glass component melts and flows without vaporizing, while the plastic component vaporizes.

At high surface temperatures exceeding the melting point, vaporization of part of the molten mass is characteristic for the majority of materials, among them the glassy materials. Furthermore, pyrolysis of the surface layer of the molten material precedes vaporization, as a result of which an additional amount of gas diffuses into the boundary layer. Thus, ablation in the most general case is characterized by simultaneous fusion and vaporization. This feature should be taken into account in determining the effective heat of ablation.

If the total mass loss rate is designated by m , the degree of vaporization (or the vaporization coefficient) can be defined as $\bar{m} = m_v/m$. Therefore, the quantity m_v can be replaced by $m\bar{m}$ in the term in Eq. (29.1) that depends on only the vaporized mass. The effective heat of ablation (1)

becomes

$$q^* = \frac{c_p T_i + \bar{m}[i_v + \beta(i_0 - i_w)]}{1 - q_r/q_0}, \quad (29.11)$$

in which the unknowns are the ablation temperature and the coefficient \bar{m} . The value of \bar{m} is chiefly a function of the vapor pressure and viscosity of the molten component, factors that depend, in turn, on the temperature as well as on the flow conditions. Some data are available concerning the nature of the variation in \bar{m} . For example, with an increase in pressure or a decrease in the stagnation enthalpy, \bar{m} will decrease. For a rough estimate, this coefficient can be defined as the ratio of the mass of the vaporized material to the entire mass.

Equation (29.11) takes radiation into account. If radiation is neglected, the effective heat of ablation is

$$(q^*)^0 = c_p T_i + \bar{m}[i_v + \beta(i_0 - i_w)], \quad (29.12)$$

and we can consider the influence of radiation later using Eq. (29.7).

FUSION

Fusion represents a limiting case of ablation in the same way as does vaporization. The material melts but it does not evaporate; therefore, the boundary layer is not affected by mass losses of the ablating material.

We can determine the effective heat of ablation by assuming that the vaporization coefficient $\bar{m} = 0$ in Eq. (29.12), resulting in

$$(q^*)^0 = c_p T_i. \quad (29.13)$$

If this expression is compared with Eqs. (29.6) and (29.12), it is evident that the effective heat for fusion is less than that for simultaneous fusion and vaporization, and also less than that for total vaporization (or sublimation).

In the case of fusion alone, the net heat flux ($q_0 - q_r$) must be completely absorbed by the liquid. This energy balance is expressed in the form

$$q_0 - q_r = mc_{pL} T_i = mq^*, \quad (29.14)$$

where c_{pL} is the specific heat of the liquid material. As already noted, it is possible to neglect the radiation in a first approximation.

THE FUSION TIME

In practical cases, it is of interest to estimate the time, t_1 , required for fusion to begin on the surface of the nose of a body with steady state heating. The equation that determines t_1 is written as

$$t_1 = \frac{1}{4} \frac{\pi \rho c \lambda}{q_{ave}^2} (T_m - T_0)^2. \quad (29.15)$$

In this equation, the average heat rate is

$$q_{ave} = \frac{1}{\pi r_N^2} \int q dS, \quad (29.16)$$

where S is the area of the blunt surface. In addition, the temperatures in Eq. (29.15) are defined as T_m , the fusion temperature, and T_0 , the initial temperature of the material.

In the derivation of Eq. (29.15), it is assumed that a longitudinal strip of the body is insulated with respect to the lateral surfaces, so that the heat flow is zero at the sides of the strip, and the depth of penetration of the heat in the time t_1 is considerably less than the radius of the nose r_N . Equation (29.15) enables us to compare the time t_1 of the beginning of fusion of bodies with various shapes of blunt noses and indicates that in order of magnitude $t_1 \sim 1/q_{ave}^2$. If the shape of the nose is such that the heat flow is decreased, the time t_1 will be greater. Thus, t_1 will be greater for a flat-faced cylindrical body than for a hemispherical nose.

The accuracy of the calculation from Eq. (29.15) is confirmed by the experimental data presented in Fig. 292. The rapid melting of slender bodies is explained by the increase in the average heating rate, as indicated by Eq. (29.15).

HEAT TRANSFER TO A WALL WITH ABLATION

The general expression for the calculation of heat transfer with ablation has the following form:

$$q = St \rho_\delta V_\delta (i_p - i_w) = mL + q_p. \quad (29.17)$$

The symbol L is the total variation in enthalpy of the ablating material from the solid to the vaporized state. The value of L can be determined from

$$L = c_{pS}(T_L - T_0) + i_L + c_{pL}(T_v - T_L) + i_v, \quad (29.18)$$

where i_L is the heat of fusion. The subscripts S and L designate parameters of the solid and liquid phases of the material, respectively.

Without ablation, the heat transfer is

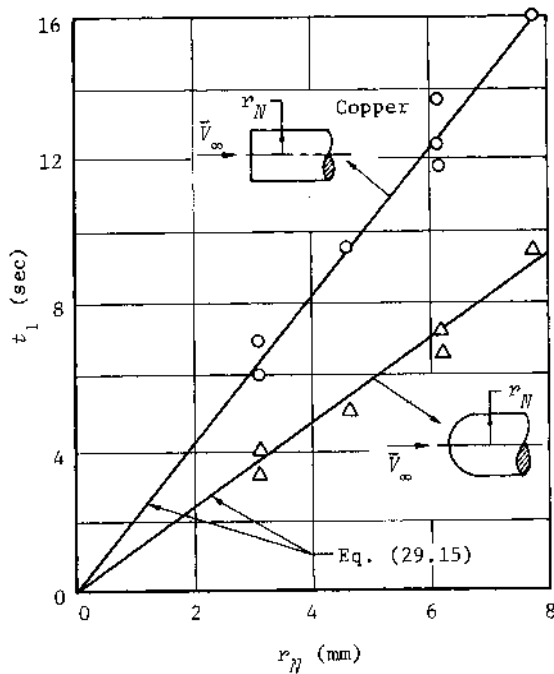


Fig. 292--Time to begin fusion as a function of the type of bluntness

$$q_0 = St_0 \rho_\delta V_\delta (i_r - i_w).$$

Combining this expression with Eq. (29.17), we obtain for the ratio of the Stanton numbers

$$\frac{St}{St_0} = m \frac{L}{q_0} + \frac{q_r}{q_0} = \frac{m}{\rho_\delta V_\delta St_0 A} + \frac{q_r}{q_0}, \quad (29.19)$$

in which the parameter $A = (i_r - i_w)/L$.

Since q_0/m represents the effective heat of ablation, Eq. (29.19) can be written as

$$\frac{St}{St_0} = \frac{L}{q} + \frac{q_r}{q_0}. \quad (29.19a)$$

The magnitude of this ratio depends on the Reynolds number and Mach number, on the form of ablation, on the properties of the material, as well as on the type of boundary layer, i.e., on whether it is laminar or turbulent. In the case of vaporization, for example, the Stanton number ratio is determined by the function ψ , the relation for which is given in Eq. (29.2).

The graph in Fig. 293 gives an idea of the character of the variation in the heat transfer parameter. The curve determines the relation

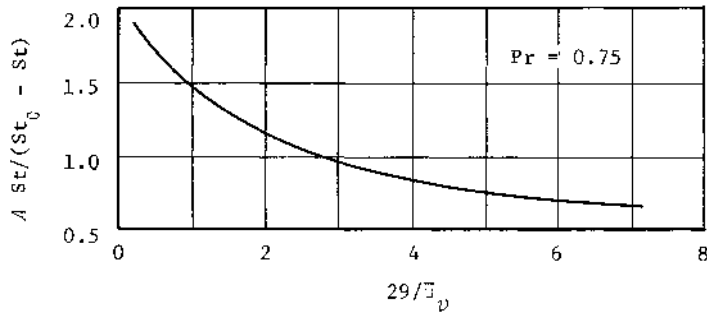


Fig. 293--Laminar heat transfer parameter
with vaporization

for $A_{St}/(St_0 - St)$ calculated from Eq. (29.19) as a function of the ratio of the molecular weights of the air and the vapor. This curve is approximated by the equation

$$\frac{A_{St}}{St_0 - St} = \frac{3.84}{(2 + 29/m_v)^{0.84}}. \quad (29.20)$$

The ratio of molecular weights has a strong influence on the heat transfer. It is possible to decrease the heat flux considerably by reducing the molecular weight of the vapor, thus causing an increase in the ratio $29/m_v$.

MASS LOSS

If the effective heat of ablation is known, the rate of mass loss per unit area is given by the equation

$$m = \frac{q_0}{q^*} = \frac{q_0}{(q^*)^\alpha} \left(1 - \frac{q_r}{q_0}\right) \text{ kgf/m}^2 \text{ sec.} \quad (29.21)$$

§ 30. CALCULATION OF THE HEAT OF ABLATIONTHE SYSTEM OF EQUATIONS

THE DETERMINATION OF THE HEAT of ablation consists of the study of the motion of a two-phase fluid over a body, i.e., a fluid having liquid and gaseous phases. If it is assumed that the motion of the liquid layer is independent of the gaseous layer, it is possible to study the liquid boundary layer separately, provided that the heat flow and friction at the liquid-gas interface are given.⁽³⁾

The motion of the molten layer is assumed to be steady in a coordinate system located on the liquid-gas interface. Therefore, in a study of this motion, it is possible to use the steady state boundary layer equations in the same form as for an incompressible fluid, with the difference that the viscosity in these equations must be considered a variable depending on the temperature.

The basic system of equations for the laminar layer (the liquid layer is assumed to be laminar) includes the equations of continuity, energy, and motion, Eqs. (3.19a), (3.43), and (3.33), respectively. In the last two equations, it is assumed that the thermal conductivity, the density, and the specific heat are constant, and that the coordinate r is constant and equal to its value for an unmelted surface. The last approximation is possible because the liquid layer is thin.

THE ABLATION RATE

The ablation rate will be considered only in a region close to the stagnation point, since this region experiences the strongest heating, and the problem of heat shielding is of special importance there. We can integrate the continuity equation, Eq. (3.19a), across the thickness of the liquid layer (assuming an infinitely thick liquid layer) to give

$$V_{yi} - V_{yw} = -\frac{1}{r} \int_{-\infty}^0 \frac{\partial(rV_x)}{\partial x} dy, \quad (30.1)$$

where V_{yi} is the normal velocity component of the liquid at the liquid-gas interface and represents the rate of vaporization, and V_{yw} is the normal velocity component of the molten material, i.e., the ablation rate. The latter velocity is assumed to be constant across the thickness of the liquid layer, since the thickness itself is very small.

The process of steady ablation can be represented in such a way that the surface of the melting and vaporizing material is motionless, but the solid body is moving away with the velocity of ablation V_{yw} . This velocity determines the total mass loss rate $m = \rho V_{yw}$, and the velocity V_{yi} determines the rate of mass loss by vaporization, equal to $m_v = \rho V_{yi}$. The velocity ratio $V_{yi}/V_{yw} = \bar{m} = m_v/m$ represents the degree of vaporization.

To determine the ablation rate from Eq. (30.1), it is necessary to find the tangential velocity component V_x of the liquid layer from the equation of motion, Eq. (3.33). Taking into account that the velocities are small due to the high viscosity of the liquid, we can neglect the inertial terms in this equation, and, assuming that $\tau = \mu \partial V_x / \partial y$, we can write Eq. (3.33) in the form

$$\frac{\partial}{\partial y} \left(\mu \frac{\partial V_x}{\partial y} \right) - \frac{\partial p}{\partial x} = 0.$$

If this equation is integrated twice with respect to y , with limits from 0 to y and from $-\infty$ to y , the tangential velocity component is

$$V_x = \left(\mu \frac{\partial V_x}{\partial y} \right)_i \int_{-\infty}^y \frac{dy}{\mu} + \frac{\partial p}{\partial x} \int_{-\infty}^y \frac{y}{\mu} dy, \quad (30.2)$$

where

$$\left(\mu \frac{\partial V_x}{\partial y} \right)_i = \tau_i$$

represents the shear stress at the liquid-gas interface.

The viscosity ν is a strong function of the temperature of the liquid layer and varies, therefore, across its thickness. To find the connection between ν and the coordinate y of an arbitrary point in the layer, it is first necessary to establish the temperature distribution across the thickness of the material. The energy equation, Eq. (3.43), can be simplified for stagnation conditions, because the longitudinal temperature gradient can be assumed to be zero, i.e., $\partial T / \partial x = 0$. Assuming that the ablation velocity V_{yw} is constant and equal to V_{yw} across the thickness of the layer, neglecting the variation in r , and assuming that λ , ρ , and c_p are also constant, we obtain the equation

$$V_{yw} \frac{\partial T}{\partial y} = \frac{\lambda_L}{\rho L c_p L} \frac{\partial^2 T}{\partial y^2}.$$

Integrating this equation twice with respect to y with limits from 0 to y and from $-\infty$ to y , we obtain the relation for the temperature of the liquid layer:

$$T(y) = \left(\frac{\partial T}{\partial y} \right)_i \delta_\pi \exp \left(\frac{y}{\delta_\pi} \right).$$

Here $(\partial T / \partial y)_i$ is the temperature gradient at the liquid-gas interface and

$$\delta_\pi = \frac{\lambda_L}{\rho L V_{yw} c_p L}$$

is the thickness of the so-called superheated layer (see Fig. 291); the parameters of the liquid material are designated by the subscript L . Studies have shown that the product $(\partial T / \partial y)_i \delta_\pi$ is approximately equal to the temperature T_i at the interface. Therefore,

$$T(y) = T_i \exp \left(\frac{y}{\delta_\pi} \right). \quad (30.3)$$

The variation of viscosity as a function of temperature is usually established experimentally. For example, for glassy materials, the viscosity varies with the temperature according to the exponential relation

$$\nu = \exp \left(\frac{a}{T} - b \right), \quad (30.4)$$

in which a and b are constants. Equation (30.4) can be approximately represented in a power form:

$$\frac{\nu}{\nu_i} = \left(\frac{T}{T_i} \right)^{-n}, \quad (30.4a)$$

where $n = a/T_i$. Introducing Eq. (30.4a) into Eq. (30.3), we obtain the expression relating the viscosity to the coordinate y :

$$\nu = \nu_i \exp \left(\frac{-y}{\delta_L} \right), \quad (30.5)$$

in which $\delta_L = \delta_\pi/n$ is the thickness of the liquid layer. Thus, the viscosity at the inner edge of the liquid layer, where $y = -\delta_L$, is increased by the factor e .

Substituting Eq. (30.5) for ν under the integral of Eq. (30.2), we can find the relation for the velocity V_x as a function of y . This relation, in turn, enables us to compute the integral in Eq. (30.1). As a result, we obtain the relation for the rate of ablation:

$$V_{yw} = V_{yi} + \frac{2\delta_L^2}{\nu_{Li}} \left[\left(\frac{\partial \tau}{\partial x} \right)_i - 2\delta_L \frac{\partial^2 p}{\partial x^2} \right], \quad (30.6)$$

which is the basic equation in the theory of the motion of a liquid layer. In this equation, the derivative $(\partial \tau / \partial x)_i = \tau'_i$ is a function of the vapor injection into the gaseous boundary layer in the general case, and $\partial^2 p / \partial x^2 = p''$ is, in agreement with Newtonian theory, constant and equal to $-2p_0'/R_N^2$.

ABLATION BY FUSION ALONE (NO VAPORIZATION)

In the case of fusion alone, it can be assumed that $V_{yi} = 0$ in Eq. (30.6), because vapor injection into the gas layer does not occur. Therefore, the liquid film has practically no influence on the gaseous boundary layer, and the ordinary boundary layer relation can be used to calculate the shear stress gradient τ'_i .

If it is assumed that the local skin friction coefficient c_{fx} is given by Reynolds analogy, the friction is

$$\tau_i = \sigma_{fx} \frac{\rho_\delta V_\delta^2}{2} = St \rho_\delta V_\delta^2 \text{Pr}^{\frac{2}{3}} = \frac{q_0 x}{i_0 - i_i} \frac{dV_\delta}{dx} \text{Pr}^{\frac{2}{3}}. \quad (30.7)$$

In this equation, the heating rate q_0 and the longitudinal velocity gradient dV_δ/dx at the stagnation point are determined from Eqs. (27.16) and (20.27a), respectively. The quantity $i_0 - i_i$ is used in Eq. (30.7) instead of the difference $i_r - i_i$ because it can be assumed that $i_r \approx i_0$ at high velocities.

Using these relations, we can rewrite Eq. (30.6) as

$$4 \frac{\rho_L u}{\rho_0 \mu_{Li}} \left(\frac{c_p \lambda_L}{n c_p L^\lambda} \right)^2 \left[\frac{(q^*)^0}{i_0 - i_i} \right]^3 \left\{ 1 + \frac{4}{\text{Pr}^{\frac{1}{3}} n c_p L^\lambda} \left[\frac{(q^*)^0}{i_0 - i_i} \right] \right\} = 1, \quad (30.8)$$

where the parameters without the subscript L correspond to conditions for the gas at the stagnation point.

Using Eq. (30.4) for the viscosity, we can determine the effective heat of ablation $(q^*)^0$ from Eq. (30.8) and compute the rate of mass loss from Eq. (29.21). The temperature of the interface T_i can be found from Eq. (29.13) if $(q^*)^0$ is replaced by q^* , as given by Eq. (29.7).

It is also necessary to know the physical and thermodynamic characteristics of the material for the calculations. One of the materials used for protective coatings, for example, is pyrex. Its composition is 81 percent SiO_2 ; 12 percent B_2O_3 ; and small amounts of aluminum (2 percent), sodium (4 percent), and potassium (1 percent). For liquid pyrex, the specific heat is $c_p = 0.25$ to $0.29 \text{ kcal/kgf deg}$, the thermal conductivity coefficient is $\lambda_L = 7.0 \cdot 10^{-4}$ to $9.7 \cdot 10^{-4} \text{ kcal/m sec deg}$, and the specific weight is $\rho_L = 2100$ to 2250 kgf/m^3 . The coefficient of dynamic viscosity μ_{Li} is determined from Eq. (30.4) for $b = 17$, $a = 38,000$, and a temperature equal to T_i ; the viscosity has the dimensions of g/cm sec . In addition to Eq. (30.4), another relation can be used in the calculation of the viscosity of glass:

$$\mu_{Li} = 0.017 \exp \left[\frac{4230}{T_i} \right]^{2.064} \text{ kgf sec/m}^2, \quad (30.9)$$

where T_i is in $^{\circ}\text{K}$. Having the physical and thermodynamic characteristics

of the material, we can determine the effective heat of ablation from Eq. (30.8).

An analysis of this equation shows that, in order of magnitude, the heat of ablation is

$$(q^*)^o \sim \frac{\frac{1}{2} \frac{L i}{\lambda}}{\frac{1}{2} \frac{L}{L}}$$

It is evident that the heat of ablation will be greater, the higher the viscosity and the less the thermal conductivity of the protective coating. However, the stagnation enthalpy of the flow, i_0 , is the principal factor.

Using Eq. (30.8) for the heat of ablation of pyrex at the stagnation point, we can obtain the following simple equation:⁽¹⁾

$$(q^*)^o = 178 \left(\frac{\rho_{\infty H}}{\rho_{\infty SL}} \right)^{1/(3+n)} \left(\frac{i_0}{RT_{\infty SL}} \right)^{3.64/(3+n)} \text{ kcal/kgf}, \quad (30.10)$$

where $RT_{\infty SL} = 18.8$ kcal/kgf, and the value of n can be assumed to be equal to 10 in approximate calculations for very high velocities.

Besides glass, metals also ablate by melting. Experimental data obtained for steel and aluminum give an estimate of the magnitude of the heat of ablation. Those interested in these data should consult the specialized literature.

SIMULTANEOUS FUSION AND VAPORIZATION

The expression for the effective heat of ablation in the case of melting and vaporization can be obtained with Eq. (30.6), which contains both the rate of vaporization V_{yi} and the rate of ablation V_{yw} . We can eliminate the velocity V_{yi} by using Eq. (30.1) and then replace the ablation rate V_{yw} by

$$V_{yw} = \frac{q_0}{\rho_L (q^*)^o}$$

We obtain the gradient of the shear stress by differentiating the relation

$\tau_i = \tau_0 \psi$ with respect to x . The latter expression results from the fact that

$$\frac{q_i}{q_0} = \frac{\tau_i}{\tau_0} = \psi.$$

From this relation, the effective heat of ablation can be determined:

$$4 \frac{p_L^4}{c'_C \mu_{L0}} \left(\frac{c_p \lambda_L}{n c_{pL} \lambda} \right)^2 \left[\frac{(q^*)^0}{i_0 - i_i} \right]^3 \left\{ \psi + \frac{4}{Pr^{\frac{1}{3}}} \frac{c_p \lambda_L}{n c_{pL} \lambda} \left[\frac{(q^*)^0}{i_0 - i_i} \right] \right\} \frac{\mu_{L0}}{\mu_{Li}}$$

$$+ \frac{(q^*)^0 - c_{pL} T_i}{i_v + B(i_0 - i_i)} = 1. \quad (30.11)$$

The parameter ψ is determined from Eq. (29.2), in which the mass loss rate is, in turn, found from Eq. (29.1). The ratio μ_{L0}/μ_{Li} is introduced into Eq. (30.11), in which μ_{L0} is the viscosity corresponding to the temperature at which the vaporization pressure of the material is equal to the stagnation pressure p'_0 , and μ_{Li} is the viscosity of the material at a vaporization pressure of p_{vi} . Studies show that this ratio is a function of the vapor pressure ratio according to the equation

$$\frac{\mu_{L0}}{\mu_{Li}} = \left(\frac{p'_0}{p_{vi}} \right)^{-\alpha}, \quad (30.12)$$

in which α is a constant that can be determined by experiment. For example, for silicon gas, $\alpha = 0.825$. The vapor pressure p_{vi} is related to the concentration c_{vi} of the injected vapor by

$$\frac{1}{c_{vi}} = 1 + \frac{29}{J_v} \left(\frac{p'_0}{p_{vi}} - 1 \right). \quad (30.13)$$

On the other hand, the concentration depends on the vaporization rate, as given by the equation

$$\sigma_{L Vi}^V = \frac{\psi q_C}{i_0 - i_i} \frac{c_{vi}}{1 - c_{vi}}. \quad (30.14)$$

Eliminating the concentrations from the last two expressions and substituting y_i from Eq. (30.6), we find for the vapor pressure

$$\frac{p'_0}{p_{vi}} = 1 + \frac{\bar{\nu}_v}{29} \frac{(q^*)^0}{(q^*)^0 - c_{pL} T_i} \left[\frac{i_v}{i_0 - i_i} + \beta \frac{c_{pL} T_i}{(q^*)^0} \right], \quad (30.15)$$

where β is given by Eq. (29.3). In the case of very strong vaporization, $c_{pL} T_i \ll (q^*)^0$, and Eq. (30.15) reduces to

$$\frac{p'_0}{p_{vi}} = 1 + \frac{\bar{\nu}_v i_v}{29(i_0 - i_i)}. \quad (30.16)$$

For approximate computations of the vapor pressure, it is also possible to use an empirical relation obtained for gaseous silica:⁽³⁾

$$p_{vi} = \exp \left(-\frac{46,000}{T_i} + 14.5 \right) \text{ kgf/cm}^2. \quad (30.17)$$

It is also useful to give the equation for the vapor pressure of pure gaseous quartz:[†]

$$p_{vi} = \exp \left(\frac{130,000}{T_i - 273} + 18.48 \right) \text{ kgf/cm}^2. \quad (30.18)$$

The viscosity is determined approximately from the vapor pressure:

$$\mu_{Li} = \frac{7 \cdot 10^{-3}}{(p_{vi})^{0.825}} \text{ g/cm sec.} \quad (30.19)$$

Thus, it is possible to determine all the necessary parameters and compute the effective heat of ablation from Eq. (30.11).

The calculations can be simplified by assuming that the temperature of the interface T_i is equal to the temperature of fusion T_f , a value that is known and constant. For example, the fusion temperature

[†]Editor's note: This expression is incorrect, but the original source cannot be located. With respect to Eq. (30.17), the Russian text reads silicon, but the basic reference states silica.

of glass is approximately equal to 1700°K, and the enthalpy is calculated directly from

$$c_{pL}^T i = c_{pL}^T f$$

The energy of vaporization is usually determined by experiment. For approximate calculations of the ablation of vitreous materials, it is possible to use, for example, the value $i_v = 2470$ kcal/kgf obtained for silicon. For pure quartz, the heat of vaporization is $i_v = 3000$ kcal/kgf.

In practical calculations, it is convenient to use an experimentally obtained relation for the effective heat of ablation of different materials. For example, data have been obtained for fiber glass, consisting of 30 percent plastic and 70 percent glass. From these data, for conditions at the stagnation point in laminar flow, the effective heat of ablation is⁽¹⁾

$$(q^*)^o = 125 + 2.7 \frac{i_0}{RT_{\infty H}} + 178 \left(\frac{\rho_{\infty H}}{\rho_{\infty SL}} \right)^{1/13} \left(\frac{i_0}{RT_{\infty H}} \right)^{7/25} \text{ kcal/kgf.} \quad (30.20)$$

Along with this equation, a more general relation can be used:

$$(q^*)^o = (q^*)_{\bar{m}=1}^o - (1 - \bar{m}) \tilde{q} \text{ kcal/kgf,} \quad (30.21)$$

which indicates a linear variation of the effective heat of ablation with the vaporization coefficient. The function \tilde{q} in this relation is given by

$$\tilde{q} = 0.554(7430 + 5.38 \cdot 10^{-5} V_{\infty}^2) \text{ kcal/kgf.} \quad (30.22)$$

The quantity $(q^*)_{\bar{m}=1}^o$ represents the effective heat of sublimation and can be determined by the equation

$$(q^*)_{\bar{m}=1}^o = 0.554(8580 + 5.38 \cdot 10^{-5} V_{\infty}^2) \text{ kcal/kgf.} \quad (30.23)$$

The velocity in Eqs. (30.22) and (30.23) is in meters per second. The case of sublimation to which Eq. (30.23) corresponds is unrealistic

for refractory and noncombustible materials like quartz; i.e., it is practically impossible to obtain the conditions for which $\bar{m} = 1$. For an estimate of the process that occurs, a series of values of $\bar{m} \leq 1$ can be chosen and the ablation rate and mass loss determined at various points of the trajectory. For example, values of $\bar{m} = 1$ and 0.25 can be assumed.

A special feature of quartz as a refractory material is the high surface temperature, approximately 2200° to 2300°K . Therefore, the correction for radiation in the computation of the effective heat will be more essential here. The radiative flux increases, making the material less liquid. Then, according to Eq. (29.7), the effective enthalpy reaches so great a value that the mass loss due to ablation will be negligibly small. In this case, the surface undergoes intense cooling by radiation, and the heat transfer will be close to that for radiative equilibrium. Under these conditions, the material practically behaves as a heat sink.

The phenomenon of total radiative equilibrium can occur for smooth variations of a small heat input (e.g., for a gradually descending satellite) when it is possible to establish a balance between the radiation and the heat input. For this limiting case, $q^* \rightarrow 0$, and the mass loss approaches zero. Thus, under conditions of radiation equilibrium characteristic of gliding vehicles, the material plays the role of a heat-insulating covering.

The noses of rockets are subject to a considerably higher heating rate for short periods of time, and the temperatures do not reach their equilibrium values; thus, the coating provides more protection as an ablating material than as ordinary thermal insulation.

In the special cases considered below, Eq. (30.11) gives comparatively simple results. Let us assume that for certain flight conditions

$$(i_v - i_i) \gg c_{pL} T_i, \quad i_v \gg c_{pL} T_i,$$

and, therefore, $(q^*)^0 \gg c_{pL} T_i$ so that the vaporization coefficient will also be considerably less than unity. The first term in Eq. (30.11), which contains the major effects of viscosity, will be greater than

the second term when the viscosity is moderate and when the effects of vaporization are large. Consequently, it is possible to neglect the second term, and Eq. (30.11) reduces to

$$\tilde{q}^3(A + B\tilde{q}) = \rho'_0 u L_0, \quad (30.24)$$

where $\tilde{q} = (q^*)^0 / (i_0 - i_i)$, and A and B are coefficients that can be derived from Eq. (30.11). For the assumptions stated above, A and B are weak functions of the temperature T_i .

The second limiting case is that of small viscosity and negligible vaporization. Hence,

$$[(q^*)^0 - c_{pL} T_i] \ll c_{pL} T_i.$$

Under these conditions, the second term of Eq. (30.11), which indicates the influence of vaporization, is negligibly small. It is apparent that, without the second term, the simplified equation is similar to Eq. (30.8) for determining the effective heat of ablation for fusion.

THE CASE OF VAPORIZATION ALONE (OR SUBLIMATION)

Another limiting case results from a very large viscosity. The first term in Eq. (30.11) will be small and can be neglected, and the equation transforms into Eq. (29.12) with $\bar{m} = 1$. This corresponds to that process of ablation in which the effective heat of ablation is maximum and independent of viscosity.

Experimental data are available for a number of materials from which one can evaluate certain characteristics and estimate the effective heat of ablation for sublimation. For example, data are known for polymer materials such as teflon $(C_2F_4)_n$. This polymer is subject to pyrolysis under the effect of heat, as a result of which the solid is vaporized into a monomer, C_2F_2 . The basic physical and thermodynamic parameters for teflon are the following. The ablation temperature for laminar heating is $T_i = 445^\circ K$, the sublimation enthalpy is $i_v = 416$ kcal/kgf, the molecular weight of the vapor is $\bar{v} = 100$, the heat of combustion of the vapor in oxygen is $i_c = 5550$ kcal/kgf, and the specific

heat of the material is $c_p = 0.25 \text{ kcal/kgf deg}$. For these data, Eq. (29.6) gives

$$(q^*)^o = 527 + 0.5i_0 \quad \text{kcal/kgf.} \quad (30.25)$$

Research shows that the ablation of teflon is accompanied by the burning of part of the vapor in the boundary layer, as a result of which the C_2F_2 is transformed into the compound COF_2 . This decreases the effective heat of ablation. Taking into account the effect of burning by using Eq. (29.10), we obtain

$$(q^*)^o = \frac{527i_0}{i_0 + 1165} + 0.5i_0. \quad (30.26)$$

A comparison of Eqs. (30.25) and (30.26) shows that the influence of burning on the effective heat of ablation is small for values of i_0 of the order of 1500 kcal/kgf and higher. In addition, radiation has an influence on the heat of ablation. However, the equations presented do not account for this effect because radiative cooling is negligibly small at the ablation temperature indicated above.

It should be added that Eqs. (30.25) and (30.26) were obtained in wind tunnels where the flow conditions corresponded to altitudes of 80 to 90 km. The effects of altitude can be considerable, especially at very high flight velocities and for significant changes in altitude. The effective heat of ablation increases with an increase in altitude. For example, as is evident from Fig. 294, for an enthalpy difference of $i_0 - i_w = 4420 \text{ kcal/kgf}$, an altitude change from 3 to 75 km causes an increase in the effective heat of ablation of teflon of approximately 30 percent.

For plastics consisting of a mixture of phenolic resin and nylon, the equation for the effective heat of ablation, analogous to the corresponding equation for teflon, has the form

$$(q^*)^o = 832 + 0.5i_0 \quad \text{kcal/kgf.} \quad (30.27)$$

The special feature of this plastic is that the carbon residue that

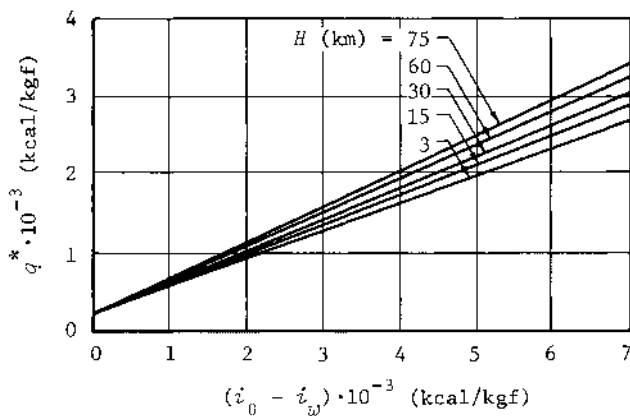


Fig. 294--The effective heat of ablation of teflon

remains after its vaporization is superheated and consequently can radiate intensely.

EVALUATION OF THE EFFECTIVENESS OF THE COATING MATERIAL

It is evident from Eq. (29.21) that the heat of ablation must be large to decrease the mass loss. However, for effective heat protective coatings, it is not enough that the heat of ablation be high. It is also necessary that the material absorb as little heat as possible from thermal conduction. In other words, it is necessary that the ratio of the heat conducted to the interior,

$$q_c = g \rho c_p T_i \delta_{\pi} = \lambda \frac{T_i}{V_{yw}},$$

to the total energy $Q = q_0 t$, i.e., the quantity

$$\frac{q_c}{Q} = \frac{\lambda T_i}{q_0 t V_{yw}} = \frac{\lambda p T_i q^*}{q_0^2 t} \quad (30.28)$$

be significantly less than unity. Thus, in addition to the requirement for a large value of q^* , it is necessary that the product $\lambda T_i q^*$ be small. For this reason, the material must have as small a coefficient of thermal

conductivity as possible. The required value of the coefficient of thermal conductivity can be estimated if it is assumed that the ratio q_c/q must be less than unity.

AN EXAMPLE OF THE CALCULATION OF ABLATION

As an illustration, let us calculate the mass loss from the nose section of a vehicle for the conditions of the example presented with Table 19 on page 693 ($M_\infty = 15$, $H = 30$ km). The stagnation enthalpy is given in the table as $i_0 = 2586$ kcal/kgf. For convenience, we shall consider a flat-face surface and assume the heating rate per unit area over the entire flat nose to be equal to that at the stagnation point. In the example, it was shown that at $R_N \approx 0.24$ m, the heating rate $q_0 = 560$ kcal/m² sec. In addition, it is necessary to know the duration of heating, which will be assumed to be 100 sec. The results of the calculation according to the foreign literature are presented in Table 20. The materials were chosen in order to present three different types of local ablation: fusion (pyrex glass), simultaneous fusion and vaporization (fiber glass and quartz), and sublimation (teflon).

Table 20
EXAMPLE CALCULATION OF MASS LOSS

Parameter	Material			
	Pyrex	Teflon	Fiber glass	Quartz
	Equation for $(q^*)^0$			
	(30.10)	(30.26)	(30.27)	(30.21)
Important results				
$(q^*)^0$ kcal/kgf	510	1820	1007	939
T_α °K (given) kcal/m ² sec	1300	445	2200	2200
$q_{rad} = \epsilon c T_\alpha^4$ (assuming $\epsilon = 1$)	39.2	0.54	323	323
q_{rad}/q_0	0.07	0.001	0.577	0.577
q^* kcal/kgf (Eq. (29.7))	548	1820	2376	2214
$m = 560/q^*$ kgf/m ² sec (Eq. (29.21))	1.02	0.307	0.236	0.253
Mass loss (kgf) $(\pi R_N^2 t)m = 19.6m$	20	6.02	4.63	4.96

In practice, this type of analysis of coating materials should take into account the variation with time of the heat transfer to the surface. If the variation is rapid and the ablation process is assumed to be steady then, due to the small coefficient of thermal conductivity, the rate of penetration of heat to the interior of the refractory material will be small compared with the rate of ablation. Thus, interior insulation of the ablating material may not be important. In the other case, when heating occurs over a long period of time and ablation is less important, an additional amount of protective refractory material may be required as insulation.

In the final choice of material, attention must be paid to its deformation, the depth of disintegration of the structure of the surface layer, the resistivity to thermal loads, etc.

If necessary, we can extend the calculation to the case of a blunt nose of arbitrary shape by determining the average heating rate from Eq. (29.16). We can then determine the mass loss by calculating the ablation of the material from the surface of a flat face with a heat flow per unit area equal to this average value.

It is evident from Table 20 that the mass loss due to ablation is not identical for the different materials; it is the least for fiber glass and quartz. However, to reach a final conclusion concerning the effectiveness of the coatings, it is necessary to compute, in addition, the weight of the heat-insulating layer and then determine the total amount of the shielding material. The heat-insulating layer is analyzed by the theory of thermal conductivity, with given conditions of the assumed temperature at the inside of the insulation and the temperature of the outer surface, T_i . The mass of fiber glass or quartz required for insulation will be larger, as a result of their high external temperatures, than of teflon or pyrex. Therefore, the total weight of the heat protection material will also be larger, and pyrex and teflon are preferable.

Chapter X

AERODYNAMICS OF RAREFIED GASES

Editor's Introduction

THIS CHAPTER PRESENTS a short summary of rarefied gas dynamics and application of the results to bodies of revolution. In general the material in the chapter is disappointing, and the interested reader must refer to other sources to obtain a basic understanding of the theory of rarefied gas dynamics or to find summaries of the plentiful analytical and experimental results for aerodynamic forces.

The introductory material in Section 31 contains a discussion of the flow regimes in rarefied gas flow, but little attention is given to the large and important region between slip flow and free molecule flow called the intermediate or transition region. A good summary of theoretical work on the transition regime is given by Patterson in his *Wright Brothers Lecture* (AIAA J., April 1965).

There is very little discussion in Section 31 of the importance of interactions between the molecules and the surface as discussed by Schaaf and by Schamberg (RAND R-339, 1959), among many others. Excellent summaries of the magnitude of the thermal accommodation coefficient with various surface conditions have been published by Hartnett (*Rarefied Gas Dynamics*, 1961) and by Wachman (ARS J., January 1962). A survey of current developments in the study of gas-surface interactions is presented by Hurlbut (*Rarefied Gas Dynamics*, 1967); the volume also contains many papers dealing with specific results. Patterson's *Wright Brothers Lecture* (*op. cit.*) also contains a good summary of the effects of surface interaction.

Section 32 on free molecule flow is based largely on material from Patterson's book.⁽²⁾ The only explicit formula given for the force coefficients on a specific body shape is that for the sharp cone in Eqs. (32.42) through (32.44). Formulas for the lift and drag of other shapes are given by Ashley (J. Aero. Sci., February 1949) and by Schaaf and Chambre (*Fundamentals of Gas Dynamics*, 1958).

Many theoretical and experimental results have been published in recent years on the gas dynamics of the slip flow and transition regimes; these supplement the discussion in Section 33. A good source for these results, as well as for other recent advances in the study of rarefied gas flow, is the series of volumes titled *Rarefied Gas Dynamics*, published biannually by the Academic Press, which represent the published proceedings of International Symposia on Rarefied Gas Dynamics initiated

in 1960. The proceedings of the Sixth Symposium, held in 1968, appear as Rarefied Gas Dynamics, Supplement 5, published in 1969.

§ 31. THE LIMITS OF APPLICABILITY OF CONTINUUM FLOW THEORY

THE EXPERIMENTAL DATA for flow around bodies in a rarefied gas differ considerably from the values of the force and moment characteristics (as well as the friction and heat transfer parameters) when these values are calculated from the relations presented for a continuous medium. The mechanics of rarefied gases must be studied by the kinetic theory of gases, accounting for the fact that the fluid actually consists of discrete molecules. The average distance traveled between collisions of molecules is called the mean free path, and for a rarefied gas this distance is comparable to a significant body dimension.

THE MEAN FREE PATH OF MOLECULES

First, let us examine the applicability of the theoretical relations based on the assumption of a continuum. It should be noted that the limits of applicability are of a conditional nature since, for example, it is impossible to indicate an atmospheric altitude above which only molecular theory must be used. Hence, all the relations pertaining to the limits of applicability are in the form of inequalities.

To establish these limits, the mean free path of the molecules must be determined. It is clear from physical considerations that the smaller the mean free path, the closer the medium is to a continuum. The flow of a dense medium is characterized by a large number of collisions between molecules, which implies that the time of establishment of equilibrium in the energy levels of the colliding molecules (the relaxation time) will be very short.

Air in the troposphere (0 to 16 km) and stratosphere (16 to 64 km) and probably in the lower part of the ionosphere (64 to 100 km) can be assumed to be a continuous medium in the sense indicated. The concept

of a continuous (or dense) medium represents a limiting case. Another limiting case originates with ascent to the upper layer of the ionosphere (to 640 km) and to the exosphere (above 640 km). Because the air in these layers is highly rarefied, collisions between the molecules are not important, and the air can be considered as a medium consisting of independent particles. When disturbances occur, the relaxation time is long, because for a period of time the particles do not encounter other molecules in their path.

The methods of statistical mechanics establish a certain mean distance traveled by a molecule between collisions. The distance is called the mean free path and its length is

$$l = \bar{c}t, \quad (31.1)$$

where \bar{c} is the average velocity of the random motion of the molecules and t is the time between two molecular collisions. In turn, this time is determined from the expression $t = 1/n$, in which n is the number of collisions in a unit time, given by $n = NA\bar{c}$ (where N is the number of molecules per unit volume and A is the cross-sectional area of a molecule). Thus,

$$l = \frac{1}{NA}. \quad (31.1a)$$

For example, for air under normal conditions, $N = 2.69 \cdot 10^{19} \text{ cm}^{-3}$, $A = 10^{-15} \text{ cm}^2$, and the length of the mean free path is $l = 4 \cdot 10^{-5} \text{ cm}$.

It follows from Eq. (31.1a) that the mean free path increases with a decrease in density. In addition, temperature has an influence on the mean free path; however, the temperature relation is more complex and is caused by its influence on both of the parameters N and A .

The influence of density on the mean free path is paramount. Therefore, this length increases with ascent in altitude (see Appendix A). At altitudes greater than 150 km the mean free path can be significantly larger than the dimensions of an aircraft.

Along with Eq. (31.1a), the following relation has been established by the kinetic theory of gases:

$$l = 1.225 \frac{v\sqrt{\gamma}}{\alpha}, \quad (31.2)$$

where γ is the adiabatic index, a is the speed of sound, and ν is the kinematic viscosity coefficient. This relation makes it possible to estimate the mean free path.

THE FLOW REGIONS OF A GAS

The characteristic parameter for determining the rarefaction of gas and establishing the limits of applicability of continuum theory is the mean free path. To estimate the degree of rarefaction, this length is compared with some characteristic linear dimension of the body.

Let us assume that the gas is located between two plates separated from one another by a small distance δ , with one of the plates moving parallel to the other at a velocity V . In this case, the characteristic parameter indicating the degree of rarefaction can be written as

$$\frac{l}{\delta} = 1.225 \frac{\nu \sqrt{\gamma}}{V \delta} \frac{V}{a} = 1.225 \sqrt{\gamma} \frac{M}{Re}. \quad (31.3)$$

The parameter l/δ is called the Knudsen number and is denoted by Kn . If $Kn \leq 0.01$, the gas can be considered dense. The disturbances from collisions with the wall are transmitted at the speed of sound to all the molecules due to the relative smallness of the mean free path, and continuum theory can be used. If the mean free path of the molecules is larger than the distance between the walls, such that the Knudsen number is $Kn \geq 10$, the gas must be considered highly rarefied and continuum theory is inapplicable.

It should be kept in mind that, in the latter case, the usual concept of the Reynolds number as a parameter reflecting the ratio of the inertial forces to the viscous forces has no meaning, since the collision of the particles is unimportant and, therefore, viscosity does not develop. Thus, we must consider the impacts of individual particles on the body instead of a continuous flow in determining the effective forces and heat rates. The two cases mentioned represent limits to the characteristic regions of flow. The first of these is the region of continuum flow, the second the region of free molecule flow.

It is commonly assumed that, despite the strong rarefaction and the negligibly small number of collisions per unit volume in free molecule

flow, the number of molecules per unit volume is sufficient to define the macroscopic properties of the gas. For example, the mean free path of the molecules is 3 m at an altitude of approximately 155 km, which indicates high rarefaction of the air. At the same time, the number of molecules per cubic centimeter remains rather large, approximately $1.5 \cdot 10^{17}$. For such a rarefied medium, the pressure and mass density can be calculated as an average for a given volume, and the flow characteristics are determined on the basis of the Maxwellian distribution of molecular velocities.

The intermediate regime ($1 \leq Kn \leq 10$) and the slip flow regime ($0.1 \leq Kn \leq 1$) are located between the two regimes of continuum and free molecule flows. The intermediate regime is characterized by the fact that the numbers of collisions of the molecules with the wall and with each other are of the same magnitude. Conditions corresponding to this regime occur in flight at altitudes of approximately 100 km. In the slip flow regime, occurring at altitudes somewhat less than 100 km, the collisions between molecules play a more important role. But despite the fact that the mean free path is small compared with the linear dimension δ , it cannot be neglected.

The difference between the various flow regimes is evident from the different velocity profiles between the parallel plates. In continuum flow, after collision with the moving plate, the gas particles acquire the velocity of the plate and the corresponding momentum. The momentum given up to the adjacent particles decreases due to friction, and as a result the velocity also decreases across the thickness δ , reaching the surface of the motionless plate with a zero value. The velocity profile that occurs will be similar to that in the boundary layer on the surface of a body in continuum flow.

In free molecule flow, the particles colliding with the wall do not change the momentum across the thickness of the layer because they do not collide with other molecules after rebounding from the surface. As a result, a velocity profile does not develop, and the gas between the plates is completely undisturbed by the motion of one plate relative to the other. Thus, it is clear that in free molecule flow around any body, the boundary layer concept loses its meaning, since the flow

on the surface has the same velocity as has the flow at some distance from it.

The velocity profile in slip flow occupies an intermediate position. In this case, the moving plate, just as in continuum flow, transmits momentum to the particles. However, after collision the molecule of gas does not acquire the velocity of the plate but, as it were, slips relative to it with a certain velocity v , so that the velocity of the particles relative to the moving plate will be the difference $V - v$. Hence, this type of flow is commonly called "slip flow"; the gas does not "adhere" to the surface of the body but acquires a velocity different from zero but less than that at the outer edge of the boundary layer.

Thus, a velocity discontinuity exists between the gas and the wall, and a velocity gradient will exist near the wall. The latter fact indicates that a boundary layer still exists in a less rarefied gas moving with slip. For this reason, the motion near the surface does not conform to the Maxwellian equilibrium distribution, and the general equations for a viscous, heat conducting, compressible gas must be used. However, we need to revise these equations, taking into account the more general boundary conditions that provide for a possible discontinuity of velocity, temperature, and pressure at the surface.

The boundaries of the flow regimes in question, in agreement with Eq. (31.3), are determined by the relation between the local Reynolds and Mach numbers. If the distance between the plates is the same as the boundary layer thickness in laminar flow, it is possible to convert from $Re = V\delta/v$ to the parameter $Re_L = Re(L/\delta)$. After substituting the ratio δ/L from Eq. (5.2) into Eq. (31.3), we obtain the relation for the Knudsen parameter:

$$Kn = \frac{\delta}{L} = 0.21 \sqrt{\frac{M}{Re_L}}. \quad (31.4)$$

Equations (31.3) and (31.4) are represented graphically in Fig. 295 for the different flow regimes,⁽¹⁾ where the curves have been calculated without considering the effect on the mean free path of possible physical-chemical changes in the air, particularly without the influence of dissociation of the air. Dissociation is accompanied by an increase in the number of particles, decreasing their mean free path.

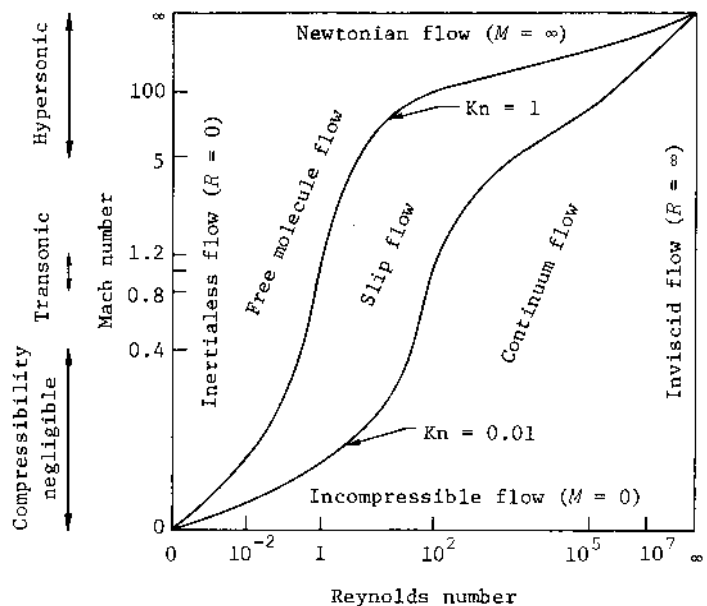


Fig. 295--Gas flow regimes

The curves in Fig. 295 pertain to the flow of an undisturbed gas. However, research shows that it is possible to use the curves for estimating the flow regime near the body if they are based on the local values of M and Re . Furthermore, it can be shown that, far from the nose of a body where the influence of the bow shock is small because of expansion of the flow, regions of slip and free molecule flow can arise even for flight at low altitudes. On the other hand, the compression behind the shock wave near the nose can lead to a region of continuum flow even in those cases when the flight is performed at high altitudes. This can be seen by calculating the Knudsen number from Eq. (31.4) using the local gas parameters.

The characteristic dimension δ must be selected in order to determine the Knudsen number. Since the estimate of the required flow regime is of an approximate nature, the boundary layer thickness can often be selected as the value of δ and can be calculated from the equations for continuum flow.

§ 32. FREE MOLECULE FLOWMECHANISM OF INTERACTION OF MOLECULES WITH THE WALL

A SERIES OF HYPOTHETICAL SCHEMES have been advanced because of the lack of research on the mechanism of the interaction of gas particles with the surface in free molecule flow.

Specular Reflection

Specular molecular reflection can occur when the surface is very smooth and inclined at a small angle of attack. Particles approaching the wall are reflected after impact at an angle equal to the angle of attack (Fig. 296b). Thus, the molecules behave like perfectly elastic spheres. The absolute values of the velocity components do not change, and the tangential component to the surface retains its sign, whereas the normal component reverses its sign. The friction force is absent

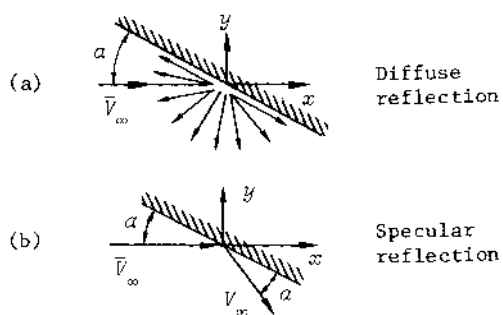


Fig. 296--Types of interaction of molecules with the wall

in the usual sense, and the heat transfer is zero. Therefore, the motion near the wall is isentropic and the temperature of the flow is independent of the thermal state of the surface.

Research has shown that even a carefully polished surface is not sufficiently smooth to achieve the mechanism of specular reflection. In practice, only an insignificant part of the molecules, of the order of several percent, interacts with the wall in this way.

Diffuse Reflection

A large fraction of the molecules interact with the wall by diffuse reflection (Fig. 296a). The gas molecules transfer all their kinetic energy to the body at the collision, diffuse into the wall and, after a lapse of time, are reflected from it in an arbitrary direction at some velocity. While the molecules are in contact with the wall, their temperature approaches that of the wall. The reflected particles do not necessarily have exactly the same temperature as the surface, but in the general case their temperature is different from that of the incident gas. Henceforth, we shall assume that the molecular motion of the incident and reflected molecules conforms to the Maxwellian law of velocity distribution, since the collisions of the impacting and reflecting molecules do not cause important deviations from this law.

FORCES ON THE WALL AND ENERGY TRANSFER FOR TRANSLATIONAL MOTION

IN FREE MOLECULE FLOW

Mass Transfer

Let us consider some of the characteristics of free molecule flow around a body.⁽²⁾ It will be assumed that the molecules, rebounding diffusely, obey the Maxwellian law of velocity distribution and the temperature of the reflected particles equals some value T_r that differs, in the general case, from the surface temperature T_w and the initial gas temperature T_i .

First, we will develop the expression for mass transfer. The velocity components of a molecule can be written as

$$u = \bar{u} + U, \quad v = \bar{v} + V, \quad w = \bar{w} + W.$$

The first terms in these expressions are the components of the velocity \bar{V}_∞ of the gas with respect to the surface. The velocity \bar{V}_∞ is the velocity of the mass (or ordered) motion and is determined from the following expression:

$$\bar{V}_\infty^2 = \bar{u}^2 + \bar{v}^2 + \bar{w}^2.$$

The second terms are the velocity components from the thermal motion, where

$$\sigma^2 = U^2 + V^2 + W^2.$$

Let us assume that the y -axis, which corresponds to the component v , is directed normal to the surface at a given point.

We are interested in the transfer of molecules to the surface of the body, which depends on the number of incident molecules. The number of incident molecules per unit volume having velocity components in the intervals

$$u, u + du, \quad v, v + dv, \quad w, w + dw$$

is given by the product $n_i f du dv dw$, in which n_i is the number of incident molecules per unit volume, and f is the Maxwellian distribution function. In kinetic theory, the distribution function is determined by the exponential relation

$$f = \frac{1}{(\pi c_m^2)^{\frac{3}{2}}} e^{-c^2/c_m^2}, \quad (32.1)$$

where c_m is related to the average speed of the random motion \bar{c} by the equation

$$c_m = \sqrt{\pi \bar{c}^2 / 4}$$

and is called the most probable speed of the molecules. The average speed is

$$\bar{c} = 2 \sqrt{2RT/n}.$$

The number of these incident molecules per unit volume colliding

with a unit area of surface in one second is

$$n_i v f du dv dw,$$

which is the number of molecules that reach the surface and are located in a volume with a unit area for the base and with a height equal to the vertical velocity component v :

We can obtain the total number of molecules N_i colliding with a unit surface area in one second by integrating over all possible values of u , v , and w ; i.e.,

$$N_i = \frac{n_i}{(\pi c_{mi}^2)^{3/2}} \int_{-\infty}^{\infty} e^{-H_1^2/2} du \int_0^{\infty} ve^{-H_2^2/2} dv \int_{-\infty}^{\infty} e^{-H_3^2/2} dw, \quad (32.2)$$

where

$$\frac{H_1}{\sqrt{2}} = \frac{U}{c_{mi}}, \quad \frac{H_2}{\sqrt{2}} = \frac{V}{c_{mi}}, \quad \frac{H_3}{\sqrt{2}} = \frac{W}{c_{mi}}.$$

Since $du = dU$ and $dw = dW$, the first and third integrals in Eq. (32.2) will be identical and equal to $\sqrt{\pi c_{mi}^2}$. The second integral can be written in the form

$$\int_{-\tilde{v}}^{\infty} (\tilde{v} + V) e^{-H_2^2/2} dV = \frac{c_{mi}^2}{2} \left[e^{-\tilde{x}^2} + \tilde{x} \sqrt{\pi} (1 + \operatorname{erf} \tilde{x}) \right], \quad (32.3)$$

where the probability integral is

$$\operatorname{erf} \tilde{x} = \frac{2}{\sqrt{\pi}} \int_0^{\tilde{x}} e^{-\tilde{x}^2} d\tilde{x}, \quad (32.4)$$

and $\tilde{x} = \tilde{v}/c_{mi}$. As is evident, \tilde{x} represents the ratio between the mass velocity component normal to the surface and the most probable velocity of the incident molecules.

The total number of molecules N_i is given by

$$N_i = n_i \sqrt{RT_i/2\pi} \left[e^{-\bar{x}^2} \pm \bar{x} \sqrt{\pi} (1 \pm \operatorname{erf} \bar{x}) \right]. \quad (32.5)$$

It should be noted that

$$c_{mi}^2 = \frac{\pi}{4} \bar{c}_i^2 = 2RT_i$$

and that the product RT_i in Eq. (32.5) is related to the velocity of sound by

$$a_i = \sqrt{\gamma RT_i}.$$

If c_{mi} is replaced by the velocity of sound in the dimensionless parameter \bar{x} , the latter can be written in the form

$$\bar{x} = \sqrt{\gamma/2} \frac{\bar{v}}{a_i}.$$

In addition, taking into account that δ is the angle between the direction of the vector \bar{V}_∞ and the tangent to the surface at a given point, we can write the relation for \bar{x} as

$$\bar{x} = \sqrt{\gamma/2} \frac{v_\infty}{a_i} \sin \delta = \bar{x}_\infty \sin \delta,$$

$$\bar{x}_\infty = \sqrt{\gamma/2} \frac{v_\infty}{a_i} = \sqrt{\gamma/2} M_\infty.$$

Since the area in question is located on the forward part of the body where $\delta > 0$ (Fig. 297), the upper (plus) sign must be selected in Eq. (32.5). If the area is located on the afterbody where $\delta < 0$, the relation for N_i is obtained by changing the limits of integration for v from $0 \leq v \leq \infty$ to $-\infty \leq v \leq 0$. In this case, we determine the number of molecules N_i by selecting the lower (minus) signs in Eq. (32.5).

Now let us consider the transfer of the reflected molecules. Since diffuse reflection obeys the Maxwellian distribution, it is possible to use Eq. (32.5), but it is assumed that $\bar{x} = 0$, since the particles lose

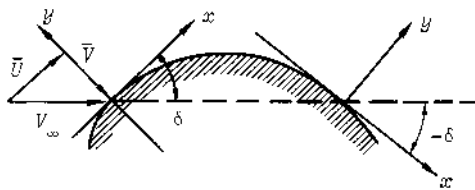


Fig. 297--Flow over a curved surface

all of their mass velocity on collision. On the basis that the reflected particles have a different temperature T_p , we obtain for their number

$$N_p = n_p \sqrt{RT_p/2\pi}, \quad (32.6)$$

where n_p is the number of reflected molecules per unit volume. If it is assumed that the total number of incident particles is equal to the number of reflected particles, i.e., $N_i = N_p$, we can find the relation between the concentrations n_p and n_i by equating the right sides of Eqs. (32.5) and (32.6).

Equation (32.5) can be simplified at sufficiently high velocities. For $\bar{x} \geq 2$, the quantity $\exp(-\bar{x}^2)$ differs little from zero, and the probability integral $\text{erf } \bar{x}$ differs little from unity. For example, for $\bar{x} = 2$, the value of $\exp(-\bar{x}^2)$ is 0.018 and $\text{erf } \bar{x} = 0.995$. For $\bar{x} \geq 2$, we get

$$M_\infty \geq \sqrt{2/\gamma} \frac{\bar{x}}{\sin \delta}.$$

For $\sin \delta = 0.2$ and $\gamma = 1.4$, the Mach number must be greater than 12. For $\delta = 90^\circ$, the smallest possible Mach number is reduced to 2.4. Thus, in the case of large velocities, Eq. (32.5) can be written in the form

$$(N_i)_f = \bar{x} n_i \sqrt{2RT_i}. \quad (32.7)$$

The subscript f indicates that the forward side of a curved surface ($\delta > 0$) is under consideration. If, however, the back side of the surface ($\delta < 0$) is considered, it is apparent that Eq. (32.5) results in $(N_i)_b = 0$ for the stated assumptions. This is because the molecules do not reach the rear surface of a body with a high flight velocity.

Pressure

The pressure is determined from the total loss of momentum normal to the surface by the molecules colliding with the wall. The pressure due to one molecule is mv , and the pressure of a group of molecules colliding in unit time with unit surface area is

$$m v^2 \int du \int dv \int dw.$$

Therefore, the pressure due to all of the molecules impacting on the forward surface is

$$p_i = \frac{\rho_i}{(\pi c_{mi}^2)^{3/2}} \int_{-\infty}^{\infty} e^{-H_1^2/2} du \int_0^{\infty} v^2 e^{-H_2^2/2} dv \int_{-\infty}^{\infty} e^{-H_3^2/2} dw, \quad (32.8)$$

where the density is $\rho_i = m n_i$.

If the pressure on the rear surface is determined, for which $\delta < 0$, the limits on v in the second integral of Eq. (32.8) must be changed to correspond to the interval $-\infty \leq v \leq 0$. Carrying out an integration similar to that for the mass transfer equation, we obtain the following expression for the pressure coefficient:

$$C_{pi} = \frac{2p_i}{\rho_i v_{\infty}^2} = \sin^2 \delta \left[\frac{1}{\bar{x} \sqrt{\pi}} e^{-\bar{x}^2} \pm \left(1 + \frac{1}{2\bar{x}^2} \right) (1 \pm \operatorname{erf} \bar{x}) \right], \quad (32.9)$$

in which the upper sign (plus) determines the pressure on the forward surface and the lower sign (minus) on the rear surface.

In addition to the incident particles, the reflected particles create a pressure equal to the sum of the momentum (normal to the surface) of the molecules leaving the wall. Since the reflected particles obey Maxwell's law, we can use Eq. (32.8) by substituting $\delta = 0$ and converting to parameters with the subscript r . Then, we get

$$p_r = \frac{\rho_r}{(\pi c_{mr}^2)^{3/2}} \int_{-\infty}^{\infty} e^{-H_1^2/2} du \int_{-\infty}^0 v^2 e^{-H_2^2/2} dv \int_{-\infty}^{\infty} e^{-H_3^2/2} dw,$$

which gives, after integrating,

$$p_r = \frac{1}{2} \rho_r R T_r. \quad (32.10)$$

Since the density of the reflected particles is $\rho_r = n m_r$, and their concentration n_r is determined from the condition $N_r = N_i$, the expression for the pressure coefficient due to the reflected molecules is

$$C_{pr} = \frac{2p_r}{\rho_i V_\infty^2} = \frac{\sin^2 \delta}{2\bar{x}^2} \sqrt{T_r/T_i} \left[e^{-\bar{x}^2} \pm \bar{x} \sqrt{\pi} (1 \pm \operatorname{erf} \bar{x}) \right], \quad (32.11)$$

in which, as before, the upper sign (plus) relates to the forward surface and the lower (minus) to the rear surface.

Therefore, the total value of the pressure coefficient is

$$\begin{aligned} C_p &= \frac{2(p_i + p_r)}{\rho_i V_\infty^2} = \sin^2 \delta \left[\frac{1}{\bar{x}} \left(\frac{1}{\sqrt{r}} + \frac{1}{2\bar{x}} \sqrt{T_r/T_i} \right) e^{-\bar{x}^2} \right. \\ &\quad \left. \pm \left(1 + \frac{1}{2\bar{x}^2} + \frac{\sqrt{\pi}}{2\bar{x}} \sqrt{T_r/T_i} \right) (1 \pm \operatorname{erf} \bar{x}) \right]. \end{aligned} \quad (32.12)$$

As is evident from this expression, the total value of the pressure coefficient depends on the orientation of the surface relative to the velocity vector \bar{V}_∞ (i.e., on the angle δ), on M_∞ , and on the temperature ratio T_r/T_i . It can be seen from Eq. (32.12) that the pressure on a motionless surface is

$$p = p_i + p_r = \frac{R}{2} (\rho_i T_i + \rho_r T_r). \quad (32.13)$$

If it is assumed that the temperature does not change in the reflection process, the pressure on the surface of a stationary body is determined by the equation of state $p = \rho_i R T_i$.

At high velocities, for which $\bar{x} \geq 2$, Eqs. (32.9) and (32.11) can be simplified. For the incident particles, the simplified relations will be

$$(C_{pi})_f = 2 \sin^2 \delta \left(1 + \frac{1}{2\bar{x}^2} \right), \quad (C_{pi})_b = 0. \quad (32.14)$$

The corresponding equations for the reflected particles are

$$(c_{pr})_f = \frac{\sin^2 \delta}{\bar{x}} \sqrt{\pi T_r/T_i}, \quad (c_{pr})_b = 0. \quad (32.15)$$

With Eqs. (32.14) and (32.15), the total values of the pressure coefficients are

$$c_{pf} = 2 \sin^2 \delta \left(1 + \frac{1}{2\bar{x}^2} + \frac{\sqrt{\pi}}{2\bar{x}} \sqrt{T_r/T_i} \right), \quad c_{pb} = 0. \quad (32.16)$$

Friction

A shear stress occurs because the tangential component of momentum is totally lost on molecular impact. This loss is $m u$ for one molecule and for a number of molecules (per unit area per unit time) is

$$n_i m f u v du dv dw.$$

Therefore, the friction caused by the incidence of all the molecules on the forward surface is

$$\tau_i = \frac{\rho_i}{(\pi c_{mi}^2)^{3/2}} \int_{-\infty}^{\infty} ue^{-H_1^2/2} du \int_0^{\infty} ve^{-H_2^2/2} dv \int_{-\infty}^{\infty} w e^{-H_3^2/2} dw. \quad (32.17)$$

The friction on the rear surface is determined from the same expression with the substitution of $-\infty$ and 0 for the limits in the second integral. Noting that $u = V_\infty \cos \delta$ (see Fig. 297), we find the following equation for the friction coefficient:

$$\sigma_f = \frac{2\tau_i}{\rho_i V_\infty^2} = \sin \delta \cos \delta \left[\frac{1}{\bar{x} \sqrt{\pi}} e^{-\bar{x}^2} \pm (1 \pm \text{erf } \bar{x}) \right]. \quad (32.18)$$

The reflected molecules do not contribute to the shear stress since all directions of motion are equally probable, and $\tau_p = 0$.

For an uninclined surface ($\delta = 0$), \bar{x} can be replaced by $\bar{x}_\infty \sin \delta$ and the friction coefficient is represented in a simpler form:

$$c_f = \frac{1}{\bar{x} \sqrt{\pi}} = \sqrt{2/Y^*} \frac{1}{M_\infty}. \quad (32.19)$$

The equations are also simplified for $\bar{x} \geq 2$. For conditions on the forward and rear surfaces, respectively, they have the following form:

$$(c_f)_f = 2 \sin \delta \cos \delta, \quad (c_f)_b = 0. \quad (32.20)$$

The Transfer of Kinetic Energy

We have seen that it is necessary to know the temperature ratio T_r/T_i to determine the normal pressure. The computation of this ratio, in turn, is related to the calculation of the energy of translational motion of the molecules on impact and reflection. On impact, each of the molecules transmits to the surface an energy equal to

$$\frac{1}{2} m c^2 = \frac{1}{2} m(U^2 + V^2 + W^2).$$

The energy supplied by a number of incident molecules arriving on a unit area in a unit time is determined by

$$\frac{1}{2} m n_i c^2 f v \, du \, dv \, dw.$$

As a result of integrating this expression within the same limits as before, we obtain the total amount of energy transmitted on impact:

$$E_i = \frac{1}{2} m N_i \left[V_\infty^2 + R T_i \left(4 \pm \frac{1}{\varphi \pm 1} \right) \right], \quad (32.21)$$

where N_i is determined from Eq. (32.5) and the function φ from

$$\varphi = \frac{e^{-\bar{x}^2}}{\bar{x} \sqrt{\pi} (1 \pm \text{erf } \bar{x})}. \quad (32.22)$$

The reflected particles remove from a unit surface an element of energy equal to

$$\frac{1}{2} m_p c^2 f v \, dv \, dy \, dz.$$

The total energy removed is obtained by integration:

$$E_r = \sqrt{2/\pi} \rho_p (RT_p)^{\frac{3}{2}}. \quad (32.23)$$

The density is given by $\rho_p = m_p$, and the concentration of the reflected particles can be replaced by n_i with $N_p = N_i$. Carrying out the required integration, we obtain the following relation for the kinetic energy removed as a result of reflection from the forward (plus sign) or from the rear (minus sign) surfaces:

$$E_r = 2mN_i RT_p = \sqrt{2/\pi} \rho_i RT_p \sqrt{RT_i} \left[e^{-\bar{x}^2} \pm \bar{x} \sqrt{\pi} (1 + \operatorname{erf} \bar{x}) \right]. \quad (32.23a)$$

The net kinetic energy transferred by the molecules is equal to the difference between the incoming and outgoing energies, i.e.,

$$E = E_i - E_r.$$

At high velocities ($\bar{x} \geq 2$), the determination of the energy of the translational motion is simplified. From Eq. (32.22), it can be assumed that φ_f and φ_b are approximately zero for the forward and rear surfaces. If the necessary simplifications in Eq. (32.21) are made, the energy of the impacting particles is

$$(E_i)_f = \frac{1}{2} \bar{x} \rho_i \sqrt{2RT_i} (V_\infty^2 + 5RT_i), \quad (32.24)$$

$$(E_i)_b = 0.$$

The corresponding equation for the energy of the reflected particles, Eq. (32.23a), can be written as

$$(E_r)_f = 2 \sqrt{2} \rho_i RT_p \sqrt{RT_i} \bar{x}, \quad (E_r)_b = 0. \quad (32.25)$$

HEAT TRANSFER IN FREE MOLECULE FLOWAccommodation

It is assumed in Eq. (32.25) that the temperature of the reflected particles differs from the wall temperature and that the energy of the molecules, due to the short time of contact, is not the same as the average energy corresponding to the temperature of the surface. This average energy is

$$E_w = 2mN_i RT_w = \sqrt{2/\pi} \rho_i RT_w \sqrt{RT_i} \left[e^{-\bar{x}^2} \pm \bar{x} \sqrt{\pi} (1 \pm \operatorname{erf} \bar{x}) \right]. \quad (32.26)$$

This type of reflection is the most general and is characterized by the absence of total adjustment, or what is called total accommodation, between the solid surface and the molecules. In the general case, the accommodation coefficient η differs from unity, where η is defined as

$$\eta = \frac{E_i - E_r}{E_i - E_w}. \quad (32.27)$$

The presence of the energy discontinuity appears as an abrupt change in temperature, i.e., the difference between T_r and T_w .

The accommodation coefficient plays an important role in the calculation of heat transfer, and it is of great practical value to establish quantitative estimates for this coefficient. At present, this can only be done experimentally, although there are few reliable measurements. Observations show that the nature of the change in the accommodation coefficient is extremely complex. For example, it has been established that η increases with increases in the molecular weight and the surface temperature. In addition, it can be assumed that the accommodation coefficient varies with the velocity of the body, the incidence angle of the surface, the properties of the material, the surface state, etc. In preliminary calculations, it can be assumed that $\eta = 1$, which implies that the temperature of the reflected molecules succeeds in reaching the wall temperature. In this case, the molecules totally adapt, as it were, to the wall conditions.

The Temperature of the Reflected Molecules and the Heat Transfer

Since the pressure depends on the value of T_p , so do the aerodynamic forces developed in free molecule flow. To determine this temperature, it is necessary to use the equation for the balance of energy between the body and the gas. The translational energy transported to a unit area of the surface by the incoming molecules is E_i . The corresponding energy of the reflected molecules is

$$E_r = (1 - \eta)E_i + \eta E_w = (1 - \eta)E_i + 2\eta m N_i R T_w. \quad (32.28)$$

If the heat due to external radiation, q_{rad} , is taken into account (e.g., that supplied by solar radiation), the incident energy will be equal to the sum, $E_i + q_{rad}$. Assuming that the outflow of energy is equal to the heat transported by the reflected molecules plus that radiated from the surface, and including cooling or heating from the interior (corresponding to plus or minus q_c), the heat balance equation for steady heat transfer per unit area is

$$\eta E_i + q_{rad} = 2\eta m N_i R T_w + \epsilon \sigma T_w^4 \pm q_c. \quad (32.29)$$

The wall temperature is obtained from Eq. (32.29) for given values of ϵ , q_{rad} , q_c , and T_i by the substitution of Eq. (32.21) for N_i and Eq. (32.5) for N_i . The temperature of the reflected molecules can be found from Eq. (32.28) in the form

$$\frac{T_p}{T_i} = \frac{T_w}{T_i} \left[\frac{(1 - \eta)E_i}{2m N_i R T_w} + \eta \right]. \quad (32.30)$$

Of special interest is the case of adiabatic conditions at the surface. If there is no radiation to or from the surface and no internal heat exchange, the wall is heated only by the transport of translational energy to and from the surface. In this case, Eq. (32.29) is reduced to

$$E_i = 2m N_i R T_w = E_w, \quad (32.31)$$

which corresponds to the condition that the net heat flow is zero. It is evident from Eq. (32.30) that the temperature of the reflected molecules is equal to the wall temperature. Thus, the temperature of an insulated surface is determined from

$$\frac{T_w}{T_i} = \frac{T_r}{T_i} = \frac{1}{4RT_i} \left[V_\infty^2 + RT_i \left(4 \pm \frac{1}{\varphi \pm 1} \right) \right]. \quad (32.32)$$

This equation can be simplified if RT_i is replaced by a_i^2/γ :

$$\frac{T_w}{T_i} = \frac{T_r}{T_i} = 1 + \frac{\gamma M_\infty^2}{4} \pm \frac{1}{4(\varphi \pm 1)}. \quad (32.32a)$$

It is evident from these equations that the wall temperature for adiabatic conditions is somewhat analogous to the stagnation temperature in continuous flow.

Flight conditions at high altitudes can be related to the maintenance of some constant wall temperature. In this case, the wall temperature is given and the temperature of the reflected particles can be determined from Eq. (32.30), which temperature is then used for the pressure calculation.

In addition, the heat transfer to each point can be calculated. It is equal (in corresponding thermal units) to the net flow of energy due to the translational motion of the molecules:

$$q = E = E_i - E_r.$$

The local heat transfer is not constant and, for given flight conditions, varies with the slope of the local surface relative to the incident velocity vector, being largest at the stagnation point. Experimental research has shown that the local heating rate at the stagnation point can be determined by the approximate equation

$$q = 7.35 \cdot 10^7 \eta \frac{\rho_{\infty H}}{\rho_{\infty SL}} \left(\frac{V_\infty}{V_c} \right)^3 \text{ kcal/m}^2 \text{ sec.} \quad (32.33)$$

Using this equation in the heat balance equation for steady heat transfer, we obtain the temperature at the stagnation point:

$$T_w = \left(\frac{q + q_{rad} \pm q_c}{\varepsilon \sigma} \right)^{\frac{1}{4}}. \quad (32.34)$$

If the wall is insulated on the inside ($q_c = 0$) and solar radiation is disregarded ($q_{rad} = 0$), the equilibrium wall temperature is given by

$$T_w = 4.83 \cdot 10^4 \left(\frac{\eta}{\varepsilon} \right)^{\frac{1}{4}} \left(\frac{\rho_{\infty H}}{\rho_{\infty SL}} \right)^{\frac{1}{4}} \left(\frac{V_{\infty}}{V_c} \right)^{\frac{3}{4}}. \quad (32.35)$$

For example, if it is assumed that the density ratio $\rho_{\infty H}/\rho_{\infty SL} = 10^{-8}$ ($H = 150$ km), that the accommodation coefficient $\eta = 1$, that the surface emissivity $\varepsilon = 1$, and that the body is moving with orbital velocity ($V_{\infty} = V_c$), the equilibrium temperature at the stagnation point is $T_w = 483^\circ K$.

In the case of very high velocities and a cooled surface, a simple equation can be derived to estimate the heat flow:

$$q = (E_i)_f - (E_r)_f, \quad (32.36)$$

where the values for energy on the right side are determined from Eqs. (32.24) and (32.25), respectively. Since $\alpha_i = \alpha_{\infty} = \sqrt{\gamma R T_i} \ll V_{\infty}$, the term $5RT_i$ in Eq. (32.24) can be neglected. In addition, the second term in Eq. (32.36) can be neglected in comparison with the first term, because the energy carried away by the reflected particles is very small due to the cooling of the surface.

After making these simplifications, we obtain

$$\begin{aligned} q &= \frac{1}{2} \rho_i V_{\infty}^3 \sin \delta \quad \text{kgf m/m}^2 \text{ sec} \\ &= 1.17 \cdot 10^{-3} \rho_i V_{\infty}^3 \sin \delta \quad \text{kcal/m}^2 \text{ sec}, \end{aligned} \quad (32.37)$$

where ρ_i is in units of $\text{kgf sec}^2/\text{m}^4$, and V_{∞} is in m/sec .

CALCULATION OF THE AERODYNAMIC FORCESThe General Expression for the Drag Force

As a result of collisions with a local unit area on the forward side of a body ($\delta > 0$), the axial force due to the normal pressure and friction is

$$\begin{aligned} (F_i)_f &= p_i \sin \delta + \tau_i \cos \delta \\ &= \frac{\rho_i V_\infty^2}{2} \sin \delta \left[\frac{e^{-\bar{x}^2}}{\bar{x} \sqrt{\pi}} + \left(1 + \frac{\sin^2 \delta}{2\bar{x}^2} \right) (1 + \operatorname{erf} \bar{x}) \right]. \end{aligned} \quad (32.38)$$

The relation for the forces on the rear side results from choosing the lower signs in Eqs. (32.9) and (32.18):

$$(F_i)_b = \frac{\rho_i V_\infty^2}{2} \sin \delta \left[\frac{e^{-\bar{x}^2}}{\bar{x} \sqrt{\pi}} - \left(1 + \frac{\sin^2 \delta}{2\bar{x}^2} \right) (1 - \operatorname{erf} \bar{x}) \right]. \quad (32.39)$$

The reflected particles create an additional force. Rebounding from the forward surface, they act on it with a force expressed as

$$(F_r)_f = p_r \sin \delta = \frac{\rho_i V_\infty^2}{2} \frac{\sin^3 \delta}{2\bar{x}^2} \sqrt{T_r/T_i} \left[e^{-\bar{x}^2} + \bar{x} \sqrt{\pi} (1 + \operatorname{erf} \bar{x}) \right]. \quad (32.40)$$

The corresponding expression for the forces caused by the action of the reflected molecules on the rear surface is

$$(F_r)_b = \frac{\rho_i V_\infty^2}{2} \frac{\sin^3 \delta}{2\bar{x}^2} \sqrt{T_r/T_i} \left[e^{-\bar{x}^2} - \bar{x} \sqrt{\pi} (1 - \operatorname{erf} \bar{x}) \right]. \quad (32.41)$$

For cases where $\bar{x} \geq 2$, these equations can be simplified as before. Instead of Eqs. (32.38) and (32.39), we have the corresponding relations

$$(F_i)_f = \rho_i V_\infty^2 \sin \delta \left(1 + \frac{\sin^2 \delta}{2\bar{x}^2} \right), \quad (32.38a)$$

$$(F_i)_b = 0, \quad (32.39a)$$

and, instead of Eqs. (32.40) and (32.41), we have

$$(F_r)_f = \frac{\rho_i V_\infty^2}{2} \frac{\sin^3 \delta}{\bar{x}} \sqrt{\pi T_r / T_i}, \quad (32.40a)$$

$$(F_r)_b = 0. \quad (32.41a)$$

Pointed Cones

The elementary area of a cone is $2\pi r dr$. Therefore, in symmetric flow the drag acting on this area is

$$[(F_i)_f + (F_r)_f] \frac{2\pi r}{\sin \delta} dr.$$

Integrating from 0 to r_{mid} , we obtain the nose drag coefficient:

$$C_{Dp} = \left(\frac{1}{\sqrt{\pi}} + \frac{\sin \delta}{2\bar{x}_\infty} e \sqrt{T_r / T_i} \right) \frac{e^{-\bar{x}^2}}{\bar{x}} + \left(1 + \frac{1}{2\bar{x}_\infty^2} + \frac{\sin \delta}{2\bar{x}_\infty} e \sqrt{\pi T_r / T_i} \right) (1 + \operatorname{erf} \bar{x}). \quad (32.42)$$

The interaction of the molecules with the base area results in an accelerating force rather than in a drag force. The magnitude of the accelerating force is

$$[(F_i)_b + (F_r)_b] \pi r_{\text{mid}}^2.$$

The accelerating force coefficient is

$$C_{DB} = \left(\frac{1}{\sqrt{\pi}} + \frac{1}{2\bar{x}_\infty} \sqrt{T_r / T_i} \right) \frac{e^{-\bar{x}_\infty^2}}{\bar{x}_\infty} - \left(1 + \frac{1}{2\bar{x}_\infty^2} + \frac{1}{2\bar{x}_\infty} \sqrt{\pi T_r / T_i} \right) (1 - \operatorname{erf} \bar{x}_\infty). \quad (32.43)$$

Therefore, the total drag coefficient acting on a cone is given by the difference

$$C_D = C_{Dp} - C_{DB}. \quad (32.44)$$

As an example, let us calculate C_D for the flight conditions for

which the wall temperature was determined to be $T_w = 483^\circ\text{K}$. The speed of sound at an altitude of 150 km is approximately 400 m/sec and $M_i = 7900/400 = 19.7$; therefore, $\bar{x}_\infty = 19.7 \sqrt{1.4/2} = 16.5$. If a cone angle of 60° is assumed, $\bar{x} = 16.5 \cdot 0.866 = 14.3$. The values of the probability integrals can be found from standard mathematical tables, but they differ so little from unity that it can be assumed that $\text{erf } \bar{x} \approx \text{erf } \bar{x}_\infty \approx 1$ and that the exponentials $e^{-\bar{x}^2}$ and $e^{-\bar{x}_\infty^2}$ are equal to zero.

As a result, the base force coefficient is equal to zero and the nose drag coefficient is approximately equal to 2, so that the total drag coefficient of the cone is

$$C_D = 2. \quad (32.45)$$

It is apparent that this result will apply for very high velocities, corresponding to large values of \bar{x} and \bar{x}_∞ . Actually, for $\bar{x} \gg 1$, Eqs. (32.42) and (32.43) indicate that $C_{DB} \approx 0$ and $C_{Dp} \approx 2$. For small velocities for which \bar{x} is small, the value of C_D increases due to the influence of the reflected molecules, as is evident from Fig. 298.

It is noteworthy that the value $C_D = 2$ corresponds to the results of Newtonian theory, where the drag is determined by the total momentum loss of the particles corresponding to the largest cross-sectional area

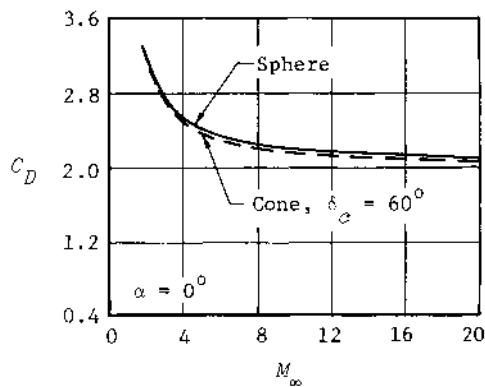


Fig. 298--Drag coefficient of a sphere and a cone in free molecule flow

of the body; at zero angle of attack, the drag force is $\rho_\infty V_\infty^2 \pi r_{\text{mid}}^2$, and the drag coefficient is $C_D = 2$. The same formula applies to a body at an angle of attack. The force must be computed as the product of the coefficient $C_D = 2$, the dynamic pressure, and the projection of the body on a plane normal to the direction of the velocity vector \bar{V}_∞ .

It is evident that the impact theory discussed above differs in principle from the Newtonian theory of § 18. According to Newtonian theory, the particles are deflected at the incident angle and continue their motion along the wall. The normal component is absorbed and the tangential component remains unvaried. According to impact theory, both components are absorbed and therefore a tangential stress must exist along with the normal pressure.

It can be seen in Fig. 298 that the results of the exact calculation for $M_\infty > 4$ differ little from the value of 2 found from Newtonian theory. Therefore, calculations can be made according to the diffuse reflection theory for comparatively small Mach numbers, and from Newtonian theory for large Mach numbers.

Arbitrary Body Shapes

In the example of the pointed cone, we indicated the possibility of calculating the drag at very large velocities on the basis of the simplified conclusions of the theory of diffuse reflection. This result can be used to calculate free molecule flow around bodies of arbitrary shape and to compute the axial and normal components of the total force and the pitching moment. We can base these calculations on computed values of the local coefficients of normal pressure and friction derived from the theory of free molecule flow, neglecting the influence of diffuse reflection and also excluding all effects in the shadow zone. For example, the equation for the pressure coefficient can be obtained from Eq. (32.16), in which the second and third terms in the parentheses are neglected:

$$C_p \approx 2 \sin^2 \delta. \quad (32.46)$$

Equations (32.20) can be used for the local skin friction coefficient. Equations (1.6) and (1.9a) give the axial force coefficients due to normal

pressure and shear stress, respectively. Their sum is the total axial force coefficient for a given axisymmetric body.

Let us consider a sphere, for example. The axial force coefficient (or drag coefficient) is

$$C_D = 4 \int_0^{\pi/2} \sin^3 \delta \cos \delta d\delta + 4 \int_0^{\pi/2} \sin \delta \cos^3 \delta d\delta = 2,$$

which is the same result as for a cone. It is evident in Fig. 298 that, as for a cone, the value of $C_D = 2$ at high Mach numbers practically coincides with that obtained from the exact computation. A flat face has exactly the same drag coefficient ($C_D = 2$), as follows from Eqs. (32.46) and (32.20).

If the flat face or hemisphere is followed by a cylinder with length l_{cyl} , the equation for the drag coefficient of the combined body is obtained from Eqs. (32.45) and (32.19) and has the form

$$C_D = 2 \left(1 + \frac{2 \sqrt{2/\gamma\pi}}{M_\infty} \frac{l_{cyl}}{d_N} \right). \quad (32.47)$$

It is apparent that the drag is a linear function of the cylinder length.

Asymmetric Flow

The expressions obtained above for the local pressure and friction coefficients can be used as a basis for the calculation of the axial force, normal force, and moment coefficients at angle of attack. It should be noted that the angle δ must be replaced by θ_c , which is the angle between the direction of the flow velocity and the local area and is computed from Eq. (7.1) or Eq. (7.14a). Once the distributions of the local pressure and friction coefficients are known, the aerodynamic coefficients can be calculated from the general expressions presented in § 1. The results of this type of calculation are presented in Fig. 299 for a cylinder with a truncated nose cone, with $M_\infty = 7$ and the temperature ratio $T_r/T_i = 0.18$. The moment coefficient in the figure is calculated with respect to a center of gravity located at a distance of one cylinder diameter from the large end of the cone. It

is necessary to know the atmospheric density to calculate the actual forces and moment from the coefficients. The density up to 700 km can be determined from Appendix A.

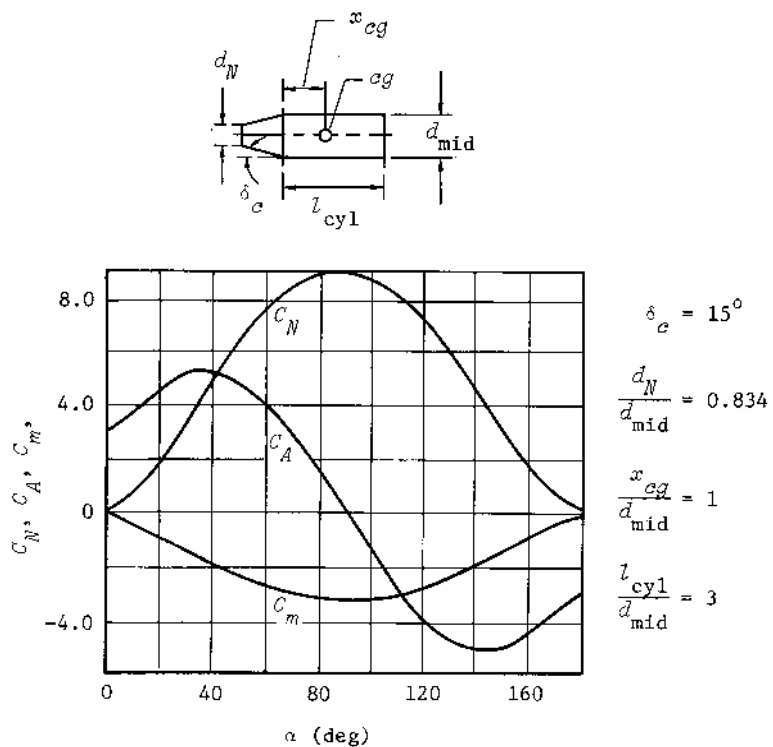


Fig. 299--Aerodynamic coefficients for a truncated cone-cylinder in free molecule flow

S 33. FRICTION AND HEAT TRANSFER IN SLIP FLOW

SHEAR STRESS DUE TO FRICTION

The Slip Velocity and the Slip Coefficient

AS ALREADY INDICATED, a special feature of slip flow is the development of a velocity discontinuity at the surface of the body. The fluid does not adhere to the wall but slips along it with a relative velocity v . Because of slip, the difference between the gas velocity at the outer edge of the boundary layer and at the wall is $V_\delta \sim v$, and the deceleration will be less than that of a nonslipping denser flow. Therefore, the friction is decreased and, according to Newton's law, can be written approximately in the form

$$\tau = \mu \frac{V_\delta - v}{\delta}.$$

We can estimate the slip velocity v by relating the shear force to the change in momentum for the random transfer of molecules with velocity \bar{c} across the boundary layer. If the mass of molecules that cross a unit area is $m = k\rho\bar{c}$ (k is a proportionality factor), the change in momentum of the gas across a small layer is $m \Delta v$ and is equal to the shear stress between two adjacent layers:

$$\tau = k\rho\bar{c} \Delta v. \quad (33.1)$$

At the wall, where $\Delta v = v$, Eq. (33.1) can be written as

$$\tau = k\rho\bar{c}v.$$

Equating this relation to the original expression for τ , we obtain

$$k\rho\bar{v} = \mu \frac{V_\delta - v}{\xi}. \quad (33.2)$$

To eliminate the viscosity from this equation, we can make use of Newton's relation, $\tau = \mu(\Delta v/\Delta y)$, in which Δy is the distance between the layers. This gives the force that causes the deceleration of one layer with respect to the other. Physically, the deceleration is explained by the change in momentum of the molecules that are moving up and down with the velocity of the thermal motion \bar{v} . In turn, this change occurs due to the collision of molecules over the mean free path l . Therefore, $\tau = \mu(\Delta v/l)$, and we obtain a relation for μ from Eq. (33.1):

$$\mu = k\rho\bar{v}l. \quad (33.3)$$

If μ is eliminated from Eq. (33.2) with the help of Eq. (33.3) and the ratio V_δ/δ is replaced by the derivative $\partial V_x/\partial y$, the equation for the slip velocity becomes

$$v = \xi \frac{\partial V_x}{\partial y}, \quad (33.4)$$

in which the factor ξ is called the slip coefficient and is given by

$$\xi = \frac{l}{1 + l/\delta}.$$

For slip flow, $l/\delta \ll 1$, so that $\xi = l$ approximately, and the slip coefficient is equal to the mean free path of the molecules.

Friction on a Plate and a Cone

The method of solving the problem of determining the viscous slip flow parameters can be illustrated by the example of a flat plate.⁽²⁾ The results of this example must be considered approximate, and are useful for quick estimates of the possible effects of slip in the study of bodies of revolution. For convenience, let us consider an unsteady, viscous, compressible, slip flow over a flat plate, which will be converted to steady flow. We shall not dwell in detail on the mathematical methods of solving the equations but shall present only the final results.

Since an infinitely long plate is considered, all the derivatives with respect to x will be zero, and the equations of continuity and momentum for unsteady flow become

$$\frac{\partial \rho}{\partial t} + \frac{\partial}{\partial y} (\rho V_y) = 0, \quad (33.5)$$

$$\frac{\partial V_x}{\partial t} + V_y \frac{\partial V_x}{\partial y} = \frac{1}{\rho} \frac{\partial}{\partial y} \left(\mu \frac{\partial V_x}{\partial y} \right). \quad (33.6)$$

Let us introduce the dimensionless variables

$$\bar{V}_x = \frac{V_x}{V_\delta}, \quad \bar{V}_y = \frac{V_y}{V_\delta}, \quad \bar{\rho} = \frac{\rho}{\rho_\delta}, \quad \bar{\mu} = \frac{\mu}{\mu_\delta}, \quad \bar{y} = \frac{y}{l}, \quad \bar{t} = \frac{t}{t_\delta},$$

where t_δ is a characteristic time equal, for example, to l/V_δ . Equations (33.5) and (33.6) can now be written as

$$\frac{\partial \bar{\rho}}{\partial \bar{t}} + \frac{\partial (\bar{\rho} \bar{V}_y)}{\partial \bar{y}} = 0, \quad (33.5a)$$

$$\frac{\partial \bar{V}_x}{\partial \bar{t}} + \bar{V}_y \frac{\partial \bar{V}_x}{\partial \bar{y}} = \frac{1}{\bar{\rho} \text{Re}_\delta} \frac{\partial}{\partial \bar{y}} \left(\bar{\mu} \frac{\partial \bar{V}_x}{\partial \bar{y}} \right). \quad (33.6a)$$

The Reynolds number in Eq. (33.6a) is based on the mean free path:

$$\text{Re}_\delta = \frac{\rho_\delta V_\delta l}{\mu_\delta}.$$

Let us introduce the function $\psi(\bar{t}, \bar{y})$, which is related to the dimensionless gasdynamic parameters by

$$\frac{\partial \psi}{\partial \bar{y}} = \bar{\rho}, \quad \frac{\partial \psi}{\partial \bar{t}} = -\bar{\rho} \bar{V}_y. \quad (33.7)$$

If Eq. (33.7) is introduced into Eq. (33.5a), it becomes clear that the

continuity equation is satisfied identically, which demonstrates that the function defined by Eq. (33.7) actually exists. Using ψ and the operators

$$\left(\frac{\partial}{\partial \bar{t}}\right)_{\bar{y}} = \frac{\partial}{\partial \bar{t}} - \bar{\rho} \bar{\gamma}_y \frac{\partial}{\partial \psi}, \quad \left(\frac{\partial}{\partial \bar{y}}\right)_{\bar{t}} = \bar{\rho} \frac{\partial}{\partial \psi}, \quad (33.8)$$

we can convert the equation of motion, Eq. (33.6a) to the form

$$\frac{\partial \bar{V}_x}{\partial \bar{t}} = \frac{\sigma}{Re_l} \frac{\partial^2 \bar{V}_x}{\partial \psi^2}, \quad (33.9)$$

where $\sigma = \bar{\rho} \bar{\mu}$ is assumed to be constant.

Equation (33.9) is solved for the following conditions. At the initial moment of time $\bar{t} = 0$, the flow over the plate is everywhere uniform and $\bar{V}_x = 1$ for $\psi > 0$. For $t \geq 0$ ($\bar{t} \geq 0$), a slip velocity occurs at the surface:

$$(\bar{V}_x)_w = \frac{v}{V_\delta} = \left(\frac{\partial \bar{V}_x}{\partial \bar{y}} \right)_w.$$

At great distances from the plate, for which $\psi \rightarrow \infty$, the velocity tends toward its value for undisturbed flow, i.e., $\bar{V}_x \rightarrow 1$.

Equation (33.9) is similar to the equation for heat conduction in a solid body, and the solution for the conditions indicated can be obtained with the help of Laplace transforms (see § 16). This solution gives the velocity as a function of t and y . At the wall, the dimensionless slip velocity is

$$(\bar{V}_x)_w = \frac{v}{V_\delta} = \exp(-x^2) \operatorname{erfc} x, \quad (33.10)$$

where the new parameter is

$$x = \sqrt{\sigma \bar{t} / Re_l},$$

and $\operatorname{erfc} x$ is the so-called complementary probability integral, given by

$$\operatorname{erfc} x = 1 - \operatorname{erf} x = \frac{2}{\sqrt{\pi}} \int_x^{\infty} e^{-y^2} dy. \quad (33.11)$$

The local skin friction coefficient on the surface of the plate is determined from

$$c_{fx} = \frac{2 \tau_w}{\rho_0 V_\infty^2} = \frac{2 \sigma}{\operatorname{Re}_l} \exp(-x^2) \operatorname{erfc} x. \quad (33.12)$$

To convert this result to steady flow, it is first necessary to examine the solutions for steady and unsteady flows without slip, i.e., with zero velocity at the wall. The solutions for these cases are

$$c_{fx} = 0.664 \left(\frac{\sigma}{\operatorname{Re}_l} \bar{x} \right)^{\frac{1}{2}}, \quad c_{fx} = 1.13 \left(\frac{\sigma}{\operatorname{Re}_l} \bar{t} \right)^{\frac{1}{2}}, \quad (33.13)$$

where $\bar{x} = x/l$. An interesting feature of the solution of the steady and unsteady problems is observed in these expressions, since it is possible to transfer from one solution to the other by assuming that $\bar{t} = 2.89\bar{x}$. This feature can also be used in the study of slip flow. In particular, we can find the local friction coefficient in steady flow from Eq. (33.12) by making this substitution and assuming that $\sigma = 1$,

$$c_{fx} = \frac{2}{\operatorname{Re}_l} e^{\bar{x}} \operatorname{erfc} \bar{x}^{\frac{1}{2}}, \quad (33.14)$$

where[†]

$$\bar{x} = \frac{2.89\bar{x}}{\operatorname{Re}_l}.$$

It must be kept in mind that in converting from the unsteady to the steady solution in the case of slip, based on the available analogy for continuous flow, it is necessary to assume a small difference in these

[†]Editor's note: There is some confusion in the original text regarding the presence of a square root in the definitions of x and \bar{x} . Equation (33.14) and all later relations have been made consistent with the definition of \bar{x} appearing here.

flows, i.e., small slip velocities. For these conditions, \bar{x} will be large, and Eq. (33.10) for the slip velocity can be approximated by

$$(\bar{V}_x)_w = \frac{0.56}{\bar{x}^{\frac{1}{2}}}. \quad (33.15)$$

Large values of \bar{x} correspond to large values of \bar{z} , since the mean free path l is small compared with the length x .

Equation (33.14) can also be expanded for large values of \bar{x} , resulting in the following expression for the local friction coefficient:

$$c_{fx} = \frac{0.664}{\sqrt{Re_\delta}} \left(1 - \frac{1}{2} \frac{1}{\bar{x}} + \frac{3}{4} \frac{1}{\bar{x}^2} - \dots \right), \quad (33.16)$$

where $Re_\delta = V_\delta \rho_\delta x / \mu_\delta$. It follows from Eq. (33.16) that slip decreases the friction coefficient.

Equation (33.14) can also be transformed by using the relation $\mu_\delta = k \nu_\delta \bar{z} l$ and assuming that $k = 0.5$ for air. Then the Reynolds number Re_l in this equation can be replaced by $Re_l = 1.46 M_\delta$. As a result we obtain

$$M_\delta c_{fx} = 1.37 e^{\bar{x}} \operatorname{erfc} \frac{1}{\bar{x}^{\frac{1}{2}}}, \quad (33.17)$$

where \bar{x} is now defined as

$$\bar{x} = \frac{1.98 \bar{z}}{M_\delta}.$$

Thus, \bar{x} is the similarity parameter for the function $M_\delta c_{fx}$, which determines the friction in slip flow. Near the leading edge where x is small, \bar{x} is also small. Therefore, the greatest influence of slip on the flow can be expected in this region.

The Knudsen number, defined as $Kn = l/\delta$, can be used instead of \bar{x} for the analysis of slip flow. The curve presented in Fig. 300 shows the variation in the theoretical values of the ratio of skin friction coefficients c_f/c_{fo} (where c_{fo} is the friction coefficient in continuum flow) as a function of Knudsen number. These results, which were obtained by assuming a cubic variation of velocity in the boundary layer,

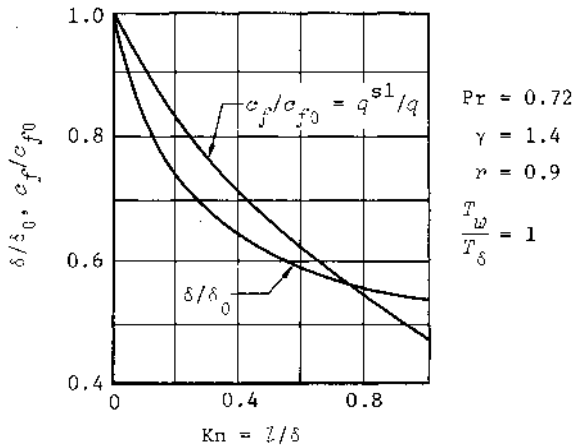


Fig. 300--Slip effects on friction and heat transfer on a flat plate

indicate that slip can considerably decrease the friction coefficient. In the same figure, a theoretical curve is shown illustrating that slip also decreases the boundary layer thickness even more significantly than the friction coefficient.

Equation (33.17) can be used to estimate the limits on \bar{x} for the slip regime, but, unfortunately, these estimates can be given only very tentatively at the present time. Observations show that for $\bar{x}/M_\delta > 10$, slip flow changes into continuum flow, and for $\bar{x}/M_\delta < 0.1$, it changes into free molecule flow. Then the expected range of variation in \bar{x}/M_δ for the slip flow regime will be $0.1 < \bar{x}/M_\delta < 10$, corresponding to $0.2 < \bar{x} < 20$. Therefore, Eq. (33.17) should give better results for large values of \bar{x} , because it is based on the condition that the slip flow differs little from the flow in the continuum regime.

With these limits in mind, Eq. (33.17) can be used for estimating slip flow around a cone. Assuming that we also use the conversion coefficient $\sqrt{3}$ (for converting from a flat plate to a cone in laminar continuum flow) for slip flow close to continuum, we obtain for a cone

$$M_\delta c_{fx} = 2.37 e^{\bar{x}} \operatorname{erfc} \frac{\bar{x}^{\frac{1}{2}}}{\sqrt{3}}. \quad (33.18)$$

The range of variation of \bar{x} for actual calculations will be the same as that for a plate, i.e., $0.2 < \bar{x} < 20$.

The skin friction coefficient on a cone surface in viscous continuum flow without slip can be calculated from a convenient equation for c_{fx} as a function of \bar{x} . Assuming, in the first expression of Eq. (33.13), that $\sigma = 1$ and using the relation $Re_l = 1.46M_\delta$, we find for a cone

$$M_\delta c_{fx} = \frac{1.34}{\bar{x}^2}, \quad (33.19)$$

which is applicable for values of $\bar{x} > 20$.

Finally, if we consider the other limiting case of free molecule flow around a cone or any other inclined surface, we can determine the magnitude of $M_\delta c_{fx}$ from Eq. (32.20) in the form

$$M_\delta c_{fx} = 2M_\delta \sin \delta \cos \delta. \quad (33.20)$$

This expression is applicable only for $\bar{x} < 0.2$ (or for $\bar{x}/M_\delta < 0.1$), for which it is evident that the product $M_\delta c_{fx}$ remains constant if M_δ does not change.

Equations (33.18) to (33.20) enable us to calculate a curve for the variation in the function $M_\delta c_{fx}$ with \bar{x} for all three flow regimes. The elements of the curves between the continuum and slip flow regimes and between slip flow and free molecule flow can be constructed by fairing the separate curves. A rough estimate of the friction coefficient can be obtained in the following manner. Instead of Eq. (33.18), computations can be made with only Eqs. (33.19) and (33.20), and in the slip region, $0.2 < \bar{x} < 20$, the straight line of Eq. (33.20) and the curve of Eq. (33.19) can be joined by a smooth line.

In determining the parameter \bar{x} , we must know the mean free path of the molecules. For a cooled surface, this can be calculated from the inviscid flow parameters around a cone in Eq. (31.2):

$$\ell = 1.225 \sqrt{\gamma_\delta} \frac{\mu_\delta}{c_\delta a_\delta}, \quad (33.21)$$

in which μ_δ , c_δ , and a_δ are the viscosity, density, and velocity of

sound at the outer edge of the boundary layer, respectively, and γ_s is the adiabatic exponent.

HEAT TRANSFER

Slip flow with a velocity discontinuity is also accompanied by a discontinuity between the gas temperature and the surface temperature. The heating rate with slip is related to that for continuum flow by

$$q^{sl} = q \left(1 - \frac{1.89}{\bar{x}} + \frac{10.7}{\bar{x}^2} - \dots \right), \quad (33.22)$$

which is obtained for low velocity flow with small slip. Equation (33.22) can be used to estimate the decrease in heat transfer when \bar{x} is sufficiently large. The Reynolds analogy can also be used for estimates in engineering calculations of heat transfer including slip (Fig. 300):[†]

$$\frac{q^{sl}}{q} \approx \frac{c_f}{c_{fc}}. \quad (33.23)$$

To simplify the calculations for arbitrary values of \bar{x} , estimates of the magnitude of the heat transfer in slip flow can be obtained by sketching a smooth transition between the curve for heat transfer in continuum flow and that for free molecule flow. An approximate construction of this type for heat transfer at the stagnation point is shown in Fig. 301. The curve for continuum flow was obtained for a cooled surface; i.e., it was assumed that $i_w = 0$ in Eq. (27.16), since the wall enthalpy introduces only a small correction. The results for free molecule flow in Fig. 301 were found from Eq. (32.33), in which the accommodation coefficient η was assumed to be unity. A similar method can be applied to an arbitrary point on the surface.

Although this method is very convenient for preliminary estimates, it must be kept in mind that it gives values of shear stress and heat transfer somewhat less than the real values. For confirmation, let us

[†]Editor's note: Comparison of Eqs. (33.16) and (33.22) shows that this is a poor approximation.

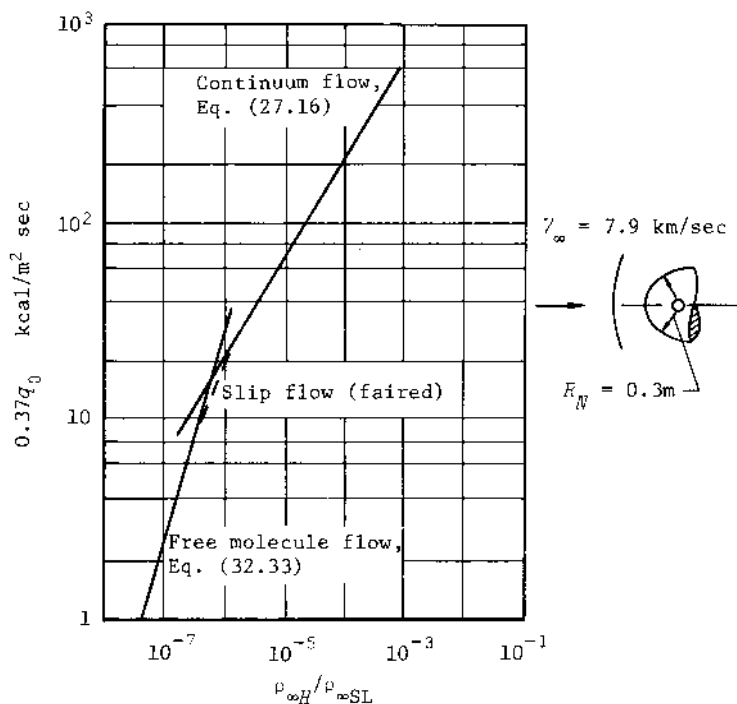


Fig. 301--Heat transfer at the stagnation point of a cooled surface as a function of atmospheric density

examine some theoretical results for viscous flow in the vicinity of the stagnation point at small Reynolds numbers.

VISCOUS RAREFIED FLOW AROUND A BLUNT NOSE

An essential question in research on flow around blunt bodies at high altitudes involves the estimate of the flow regime of a rarefied gas. It was mentioned above that a general criterion for such an estimate is provided by the Knudsen number $Kn = l/\delta$, which depends on a characteristic length δ . It must be emphasized that the choice of the characteristic length is related to the phenomenon being studied; a particular characteristic dimension δ corresponds to each phenomenon. For example, the length of the plate x was chosen as the dimension in the study of flow over a flat plate. In the study of flow around a

blunt nose, it is usual to choose the thickness of the shock layer s_o as the characteristic length. Therefore, in an estimate of the limits of applicability of continuum flow theory, it is necessary to assume that the local mean free path must be small compared with the quantity s_o ; i.e., the condition $l/s_o \ll 1$ must be fulfilled.

According to the theory of supersonic flow, the dimensionless thickness s_o/R_N is of the order of the density ratio across a normal shock wave, i.e., $s_o/R_N \sim \bar{\rho} = \rho_{\infty H}/\rho_2$. Thus, the condition for continuum flow is written in the form $l/R_N \ll \bar{\rho}$. If the Reynolds number

$$Re_{\infty} = \frac{V_{\infty} C_{\infty H} R_N}{\mu_{\infty H}}$$

is introduced, and the local value of the mean free path is replaced by its free stream value, we can write

$$\frac{l}{R_N} \sim \frac{l_{\infty H}}{R_N} = \frac{M_{\infty}}{Re_{\infty}}.$$

Therefore, the condition indicated above will take the form

$$\frac{M_{\infty}}{Re_{\infty}} \ll \bar{\rho}. \quad (33.24)$$

For example, at Mach numbers from 10 to 20, the density ratio lies between 0.1 and 0.07. Thus, it follows that continuum flow will be maintained for $Re_{\infty} > 1000$. If this condition is fulfilled, the continuum flow regime between the body and the shock will be divided into a thin boundary layer and an inviscid zone adjacent to the shock.

As the Reynolds number decreases, the boundary layer will grow thicker, until the shock layer consists of a completely viscous continuous medium. The process of shock transition with time still can be considered to be instantaneous and, therefore, the shock thickness can be considered as infinitesimal. Approximate estimates show that the shock layer must be considered completely viscous when

$$\frac{M_\infty}{Re_\infty} \ll \beta^{\frac{1}{2}}. \quad (33.25)$$

It is evident that the Reynolds number, approximately 100, is less by an order of magnitude than in the previous case.

As the rarefaction increases, viscosity and thermal conductivity have continually more influence on the formation of the shock wave, which gradually "erodes" and increases in thickness. This regime, sometimes called the merged layer regime, is limited by the condition

$$\frac{M_\infty}{Re_\infty} < 1. \quad (33.26)$$

For example, at $M_\infty = 20$, the Reynolds number should be in the range $20 < Re_\infty < 100$. In this regime, the shock wave is not thin and the flow behind it differs somewhat from continuum flow; moreover, the flow on the surface is accompanied by the beginning of slip.

As the degree of rarefaction increases further, the flow deviates increasingly from continuum flow, and slip becomes the deciding factor in the formation of flow behind the shock wave, the thickness of which can be very large. For

$$\frac{M_\infty}{Re_\infty} > 1, \quad (33.27)$$

the flow is called transitional flow. It is characterized by a large mean free path (by a large value of the Knudsen number $Kn = l/s_0$), but not large enough for free molecule flow to be assumed.

For free molecule flow, the parameter M_∞/Re_∞ must be larger by an order of magnitude, i.e.,

$$\frac{M_\infty}{Re_\infty} \gg 1. \quad (33.28)$$

For example, for $M_\infty = 20$, the Reynolds number must satisfy the inequality $Re_\infty \ll 20$.

At the present time, the problems of continuum and free molecule

flows around blunt noses have received the most attention. The results for the intermediate regimes are less complete. In a number of cases, they are of a qualitative nature and can be used only for rough estimates. This is because of lack of study of the process of transition from continuum to free molecule flow.

In this intermediate regime, a rigorous formulation of the flow of the rarefied gas is required, and, in general, the treatment of the problem depends on the use of the kinetic theory of gases. The derivation by such means of the aerodynamic characteristics (e.g., friction and heat transfer) is extremely complicated and in many cases is as yet an unsolved problem. In this connection, attempts have been made to obtain these characteristics from the most general equations of gas dynamics developed for continuum flow conditions, such as the Navier-Stokes relations. For finding approximate solutions, it is assumed that these equations represent satisfactorily the flow in both the viscous layer and the merged layer between the shock wave and the body. Thus, instead of Prandtl's equations, which are themselves simplified Navier-Stokes equations suitable for the study of the thin viscous boundary layer, the Navier-Stokes equations in their full form are used in the intermediate regime, since the effects of viscosity are important throughout the region of flow. The solution must satisfy the given conditions at the outer edge of the layer. For a viscous layer, the conditions are determined by the flow parameters behind the shock wave and for the merged layer by the unperturbed flow parameters, since the shock wave is so "smeared" that its thickness can be considered to be infinitely large analytically. It is understood that the solutions must also satisfy the boundary conditions on the body surface.

As a result of the solution of the viscous layer problem, the parameters in this layer can be completely determined, including those at the surface of the body near the stagnation point, and the distance to the shock wave can be calculated. The standoff distance and the friction and heat transfer rate at the stagnation point are represented graphically in Figs. 302 to 304. The calculations were made for $\delta = 0.1$ and for a strongly cooled surface, so that the enthalpy at the wall would not be of importance. The Reynolds number based on the nose radius was

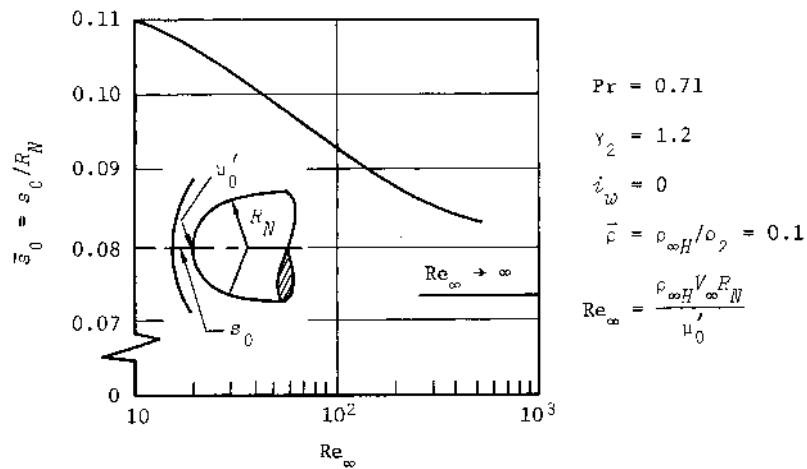


Fig. 302--Shock standoff distance
for small Reynolds number

- 1 — Free molecule flow
- 2 — Viscous layer (infinitesimal shock thickness)
- 3 — Incipient merged layer (thick shock)
- 4 — Boundary layer theory

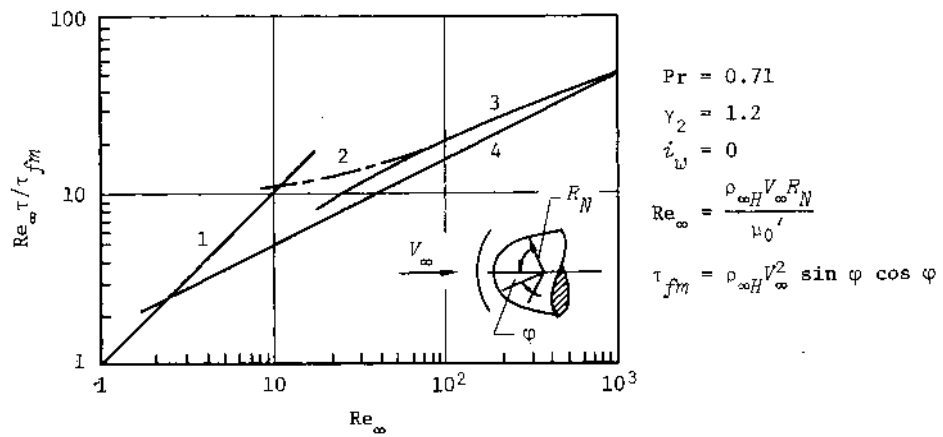


Fig. 303--Shear stress on a cooled sphere

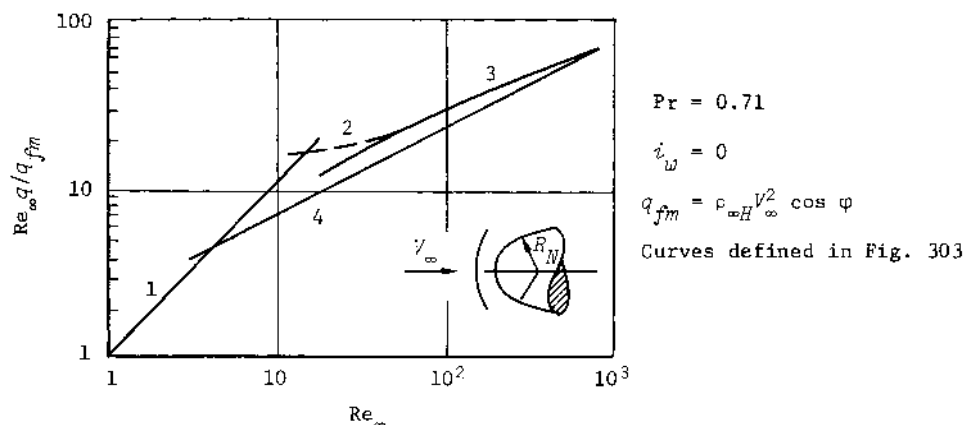


Fig. 304--Stagnation point heat transfer on an insulated sphere

assumed to be the independent variable in the calculations, and the viscosity coefficient μ'_0 was based on stagnation conditions. The upper limit for the Reynolds number was chosen as 1000, which corresponds to the usual boundary layer, and the lower limit was chosen as 10, at which the existence of a viscous layer is doubtful and it is normal to assume a merged layer.

It is evident from Fig. 302 that the distance to the shock wave is a function of Reynolds number. Included in this functional relation is the effect of viscosity on the formation of the shock wave in front of a blunt nose in rarefied gas flow. Therefore, the greater the degree of rarefaction and the less the Reynolds number, the greater in magnitude is the displacement of the shock wave from the body compared with its value for continuum (inviscid) flow (in Fig. 302 this value is indicated for $Re_\infty \rightarrow \infty$).

The results obtained for friction and heat transfer at the stagnation point (Figs. 303 and 304) indicate that a decrease in Reynolds number leads to some increase in friction and heat transfer compared with continuum (inviscid) flow in the shock layer, i.e., the results of ordinary boundary layer theory. This is caused by the additional effect of viscous stresses.

The model of the viscous layer for which these results were obtained becomes unsuitable at small Reynolds numbers, and at $Re_\infty < 100$ it is necessary to transfer to a model of a merged layer.

To obtain a solution for the merged layer using the Navier-Stokes equations, it is helpful to examine the initial stage of development of a merged layer, which corresponds to Reynolds numbers from 100 down to 20 or 30. The properties of this layer are still specified by continuum flow. The shock wave has an inner boundary with a radius of curvature R_{so} on the axis, but the leading edge of the shock is smeared out. The undisturbed flow parameters are the boundary conditions, together with the additional condition that at infinity the gradients of the flow parameters are zero. Thus, it is impossible to examine the shock wave on the basis of the ordinary equations corresponding to an infinitely thin shock. The boundary conditions for the formation of a diffuse shock wave are obtained from the conservation equations; the latter are derived in integral form taking into account the shock thickness, which depends on the viscosity and thermal conductivity.

The calculations carried out by this method (see Figs. 303 and 304) enable us to refine the results obtained for the viscous layer regime. The friction and heat transfer parameters are less than those given by the viscous layer analysis for Reynolds numbers less than about 100 because of an increase in the degree of rarefaction, as a result of which the flow becomes closer in character to free molecular flow.

The merged layer theory has been used to determine the effects of changes in Reynolds number on the density and pressure behind the shock wave. It was shown that, contrary to the usual picture of flow, the parameters behind a normal shock depend on the conditions at the surface of the body, particularly on whether the wall is cooled or insulated. For example, as the Reynolds number decreases the density increases for a cooled surface and decreases for an insulated surface, but the pressure is reduced in both cases. (Fig. 305).

The graph in Fig. 306 is an illustration of the effect of small Reynolds numbers on the heat transfer at the stagnation point. The ordinate is the ratio of the heating rate q_w (including real gas effects behind the shock wave) to the heating rate q_0 from ordinary boundary

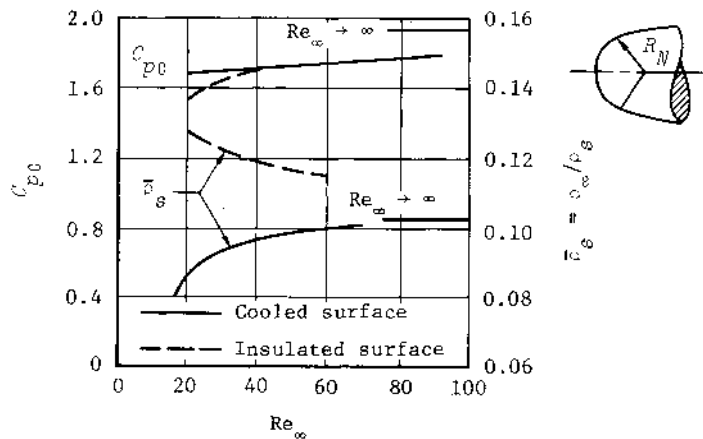


Fig. 305--Pressure and density near the stagnation point of cooled and insulated surfaces at low Reynolds numbers

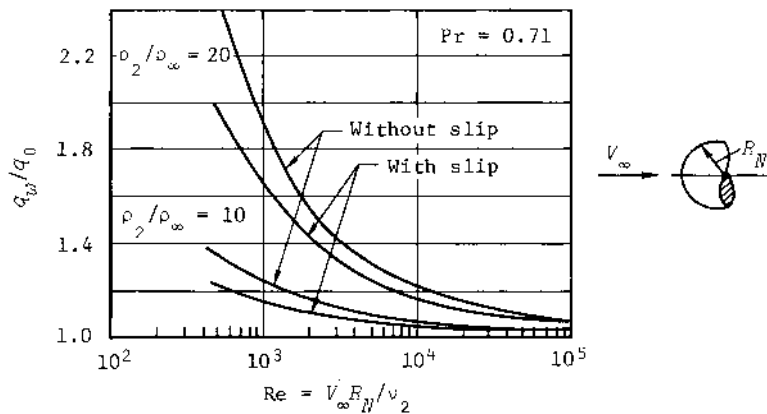


Fig. 306--Effects of vorticity and slip on heat transfer at the stagnation point for low Reynolds numbers

layer theory. The influence of vorticity caused by the curved shape of the shock wave is especially large at small Reynolds numbers. It leads to a considerable increase in heat transfer, because the boundary layer thickness includes almost the entire region between the body and the

shock. Since the vorticity increases with an increase in the strength of the shock wave, its influence will be stronger at high velocities and, accordingly, at large values of the density ratio ρ_2/ρ_∞ .

Slip flow is observed on the surface at small Reynolds numbers. Therefore, the heat transfer is reduced somewhat, compensating in some measure for the influence of vorticity. This is evident from Fig. 306, where theoretical results are presented for density ratios of 20 and 10. The curve q_w/q_0 for the lower density ratio is approximated satisfactorily by the equation

$$\frac{q_w}{q_0} = 1 + \frac{14.8}{Re^{0.5}} \left(1 - \frac{0.98}{Re^{0.17}} \right), \quad (33.29)$$

in which Re is computed from the velocity V_∞ , the radius of the spherical nose R_N , and the kinematic viscosity ν_2 behind the shock, i.e., $Re = V_\infty R_N / \nu_2$. If the right side of Eq. (33.29) is expanded, the second term represents the increase in heat transfer due to the effect of vorticity, and the third term indicates the decrease in heat transfer caused by the slip effect.

Chapter XI

SIMILARITY LAWS AND AERODYNAMIC CHARACTERISTICS AT TRANSONIC VELOCITIES

Editor's Introduction

THE DEVELOPMENT OF THE SMALL DISTURBANCE THEORY and the similarity laws for transonic flow in Section 34 follows the original analysis of von Kármán.⁽¹⁾ Reference is also made in the text to the work of Spreiter and Alksne,⁽²⁾ and the reader is referred to their report for additional details on the application of transonic flow theory to slender bodies of revolution. Several books on the theory of transonic flow have appeared in the last ten years, and these are excellent sources for those interested in the basic theory. They include Guderley (The Theory of Transonic Flow, 1962), Oswatitsch (editor, Symposium Transsonicum, 1964), and Ferrari and Tricomi (Transonic Aerodynamics, 1968). Unfortunately, the texts by Guderley and by Ferrari and Tricomi contain only a few pages on axisymmetric transonic flow; the book by Oswatitsch is a collection of papers presented at a 1962 symposium, and the major portion of the section related to axisymmetric flow is a paper by Spreiter summarizing the results of Ref. 2.

The first half of Section 35 consists of a qualitative discussion of the gross characteristics of transonic flow over bodies of revolution, based largely on German wartime experimental data. Very little has been done in recent years in the way of experiments on the drag-rise Mach number for axisymmetric bodies. A comprehensive collection of free-flight data on bodies of revolution (at both transonic and supersonic speeds) has been published by Stoney (NASA TR R-100, 1961), but the details of the drag-rise region are not easily identified.

The pressure distribution on a flat-nosed cylinder at transonic speeds (Fig. 317) has been carefully measured and analyzed by Stanbrook (Aeronautical Research Council R&M 3425, 1966). In connection with this, Graff (Union Carbide Research Institute TR C-24, October 1964) has obtained an analytical expression for the velocity distribution in compressible flow over a flat face, using the Rayleigh-Janzen method. This result is useful in calculating the pressure distribution and pressure drag of blunt-nosed bodies at high subsonic speeds.

The drag of a pointed cone at Mach numbers near that for shock detachment is discussed on pages 858-860. South (NASA TN D-4563, May 1968) has successfully applied the Belotserkovskii integral method to the calculation of the flow about pointed cones with detached shock waves. The

limits of applicability of the method to this problem have not been completely defined, but it appears that there is a minimum Mach number for a given body shape below which solutions do not exist.

Equation (35.7) for the pressure drag coefficient of sharp-nosed bodies at Mach numbers near unity was obtained from a paper by the editor.⁽⁹⁾ The application of this equation to cones and ogive noses is illustrated in the figures given in the Introduction to Chapter III.

§ 34. THE TRANSONIC SIMILARITY LAWSTHE EQUATIONS OF SYMMETRIC FLOWGeneral Observations

THUS FAR, THE AERODYNAMICS of bodies of revolution have been investigated under conditions of supersonic velocities considerably larger than the velocity of sound. The study of some of the aerodynamic problems at low supersonic speed around slender pointed bodies was carried out using the linear equations of motion of a gas. However, these equations are inapplicable in the case of transonic (near sonic) velocities of flow around a body of revolution, even if it is slender. In the linearized equations, the difference between the squares of the local velocities, $a^2 - V_x^2$, was replaced by the corresponding free-stream quantity $a_\infty^2 - V_\infty^2$. Since $a^2 - V_x^2$ is equal to $a_\infty^2 - V_\infty^2 - (\gamma + 1)V_\infty V'_x$ when expanded, the approximation is acceptable when the term $(\gamma + 1)V_\infty V'_x$ is small compared with the difference $a_\infty^2 - V_\infty^2$. Under transonic flow conditions when the flow velocity is close to sonic, $(\gamma + 1)V_\infty V'_x$ is of the same order of magnitude as $a_\infty^2 - V_\infty^2$, and linearization of the equation is impossible. However, the basic equations can be simplified somewhat, although not linearized; the simplified equations considerably facilitate the study of transonic symmetric flow.⁽¹⁾

The Equation for the Velocity Potential

The equation for the velocity potential can be derived from Eq. (3.22) for steady symmetric motion. A perturbation potential ϕ is defined by

$$\frac{\partial \phi}{\partial x} = V_x - a^*, \quad \frac{\partial \phi}{\partial r} = V_r, \quad (34.1)$$

where φ corresponds to the flow around a slender body of revolution when the local velocity differs little from the critical velocity a^* ; therefore, $\partial\varphi/\partial x$ is very small. The potential φ must satisfy the conditions at infinity:

$$\left(\frac{\partial\varphi}{\partial x}\right)_\infty = V_\infty - a^*, \quad \left(\frac{\partial\varphi}{\partial r}\right)_\infty = 0. \quad (34.2)$$

After the introduction of φ into Eq. (3.22), the equation takes the form

$$\left(1 - \frac{V_x^2}{a^2}\right)\varphi_{xx} + \left(1 - \frac{V_r^2}{a^2}\right)\varphi_{rr} - \frac{2V_x V_r}{a^2} \varphi_{rx} + \frac{V_r}{r} = 0. \quad (34.3)$$

If V_r^2 is neglected in comparison with V_x^2 , the expression for the velocity of sound can be written as

$$a^2 = \frac{\gamma + 1}{2} a^{*2} - \frac{\gamma - 1}{2} V_x^2. \quad (34.4)$$

Since the flow velocity around the body is close to the speed of sound, we can obtain the following relations from Eqs. (34.1) and (34.4) by neglecting terms containing $(\varphi_x/a)^2$:

$$\frac{V_x^2}{a^2} = 1 + \frac{\gamma + 1}{a^*} \frac{\partial\varphi}{\partial x}, \quad (34.5)$$

$$\frac{V_r^2}{a^2} = \frac{\varphi_r^2}{a^{*2}}, \quad (34.6)$$

$$\frac{V_x V_r}{a^2} = \frac{\varphi_r}{a^*}. \quad (34.7)$$

Introducing Eqs. (34.5) through (34.7) into Eq. (34.3) and neglecting higher-order terms, the differential equation for steady transonic flow becomes

$$\frac{\gamma + 1}{a^*} \varphi_x \varphi_{xx} + \frac{2}{a^*} \varphi_r \varphi_{rx} = \varphi_{rr} + \frac{\varphi_r}{r}. \quad (34.8)$$

This equation is nonlinear with respect to φ ; it is more complicated than the linearized equation but is simpler than the general equation (Eq. (3.20)) for the velocity potential.

THE LAW OF FLOW SIMILARITY

The Affine Transformation

The similarity law for transonic flow around bodies of revolution with different fineness ratios but with similar thickness distributions (e.g., conical and parabolic bodies) is obtained by combining the boundary conditions, Eq. (34.2), with Eq. (34.8). The condition of continuous flow at the surface of the body must be satisfied:

$$\frac{dr}{dx} = \frac{V_r}{V_x} \approx \frac{\varphi_r^*}{\alpha^*}. \quad (34.9)$$

The derivative dr/dx can be written in the form $dr/dx = s(x/l)/\lambda_l^*$, where $\lambda_l^* = l/d_{mid}$ is the fineness ratio of the body, and $s(x/l)$ is a function representing the slope of the body profile. Then, from Eq. (34.9), we obtain

$$\varphi_r^* = \frac{\alpha^*}{\lambda_l^*} s\left(\frac{x}{l}\right). \quad (34.10)$$

Equation (34.10) shows that the magnitude of the potential on the body surface is of the order of $\varphi \sim r \alpha^*/\lambda_l^*$ since $s(x/l) \sim 1$. Introducing the affine variables ξ and η , which are related to the coordinates x and r by

$$x = l\xi, \quad r = \frac{l\lambda_l^*}{\sqrt{\Gamma}} \eta,$$

we can write an expression for φ :

$$\varphi = l\alpha^* \frac{1 - M_\infty^*}{\Gamma} F(\xi, \eta), \quad (34.11)$$

where $\Gamma = (\gamma + 1)/2$ and $M_\infty^* = V_\infty/a_\infty$ is the free-stream Mach number. The coefficient $1 - M_\infty^*$ has been introduced into Eq. (34.11) to satisfy the boundary conditions at infinity, and $F(\xi, \eta)$ is the unknown function to be determined.

Equation (34.8), converted to these variables, has the form

$$\frac{2\lambda_l^2}{\Gamma} (1 - M_\infty) \frac{\partial F}{\partial \xi} \frac{\partial^2 F}{\partial \xi^2} + \frac{2}{\Gamma} (1 - M_\infty) \frac{\partial F}{\partial \eta} \frac{\partial^2 F}{\partial \eta \partial \xi} = \frac{\partial^2 F}{\partial \eta^2} + \frac{1}{\eta} \frac{\partial F}{\partial \eta}. \quad (34.12)$$

The second term on the left can be neglected because it is less than the first term by at least a factor λ_l^2 . Introducing the designation

$$K = \frac{1 - M_\infty}{\Gamma} \lambda_l^2, \quad (34.13)$$

Eq. (34.12) is simplified to

$$2K \frac{\partial F}{\partial \xi} \frac{\partial^2 F}{\partial \xi^2} = \frac{\partial^2 F}{\partial \eta^2} + \frac{1}{\eta} \frac{\partial F}{\partial \eta}. \quad (34.14)$$

Replacing $F(\xi, \eta)$ by a function $f(\xi, \eta)$, where

$$F(\xi, \eta) = \frac{1}{K} f(\xi, \eta), \quad (34.15)$$

we obtain

$$2 \frac{\partial f}{\partial \xi} \frac{\partial^2 f}{\partial \xi^2} = \frac{\partial^2 f}{\partial \eta^2} + \frac{1}{\eta} \frac{\partial f}{\partial \eta}. \quad (34.16)$$

The boundary conditions that the solution of Eq. (34.16) must satisfy are written in the following manner. The conditions at infinity are

$$\left(\frac{\partial \varphi}{\partial x} \right)_\infty = \frac{\alpha^*(M_\infty - 1)}{\Gamma}, \quad \left(\frac{\partial \varphi}{\partial r} \right)_\infty = 0.$$

If φ is replaced by $f(\xi, \eta)$, these become

$$\left(\frac{\partial f}{\partial \xi} \right)_\infty = -K, \quad \left(\frac{\partial f}{\partial \eta} \right)_\infty = 0. \quad (34.17)$$

The condition at the surface of the body is obtained from Eq. (34.9) as

$$2\eta \frac{\partial f}{\partial \eta} = t(\xi), \quad (34.18)$$

where $t(\xi) = t(x/l)$ depends on the geometric shape of the body.

Obviously, for identical values of K , Eq. (34.16) with the boundary conditions of Eqs. (34.17) and (34.18) will give a unique solution that describes a whole class of flows around bodies of revolution with large fineness ratios and with an identical law of thickness distribution; the parameter K represents the similarity parameter for flows at transonic velocity.

The Pressure and Drag Coefficients

The general equation for the pressure coefficient can be found from Eq. (3.58),

$$p = p_0 \left(1 - \frac{\gamma^2 + V_x^2}{V_{\max}^2} \right)^{\gamma/(\gamma-1)},$$

by replacing V_x^2 by the approximate expression $V_x^2 = V_\infty^2 + 2V_\infty(\varphi_x - \varphi_{x\infty})$, which can be derived from Eqs. (34.1) and (34.2). Noting that

$$V_{\max}^2 = \left(M_\infty^2 + \frac{2}{\gamma-1} \right) a_\infty^2,$$

and

$$p_0 = p_\infty \left(1 + \frac{\gamma-1}{2} M_\infty^2 \right)^{\gamma/(\gamma-1)},$$

we can write the expression for the static pressure as

$$p = p_\infty \left[1 - \frac{\gamma-1}{2} \frac{2V_\infty(\varphi_x - \varphi_{x\infty}) + \varphi_r^2}{a_\infty^2} \right]^{\gamma/(\gamma-1)}.$$

Expanding in a series and retaining only two terms in the expansion,

we get

$$p - p_{\infty} = - \frac{\gamma p_{\infty}}{2 \alpha_{\infty}^2} [2V_{\infty}(\varphi_x - \varphi_{x\infty}) + \varphi_p^2] = -p_{\infty}(\varphi_x - \varphi_{x\infty})V_{\infty} - \frac{1}{2} p_{\infty} \varphi_p^2.$$

Hence the pressure coefficient is

$$C_p = - \frac{2(\varphi_x - \varphi_{x\infty})}{V_{\infty}} - \frac{\varphi_p^2}{V_{\infty}^2} = - \frac{2(V_x - V_{\infty})}{V_{\infty}} - \frac{V_p^2}{V_{\infty}^2}. \quad (34.19)$$

The axial velocity component is obtained from Eqs. (34.1), (34.11), and (34.15):

$$V_x = a^* \left(1 + \frac{1 - M_{\infty}}{\Gamma K} \frac{\partial f}{\partial \xi} \right). \quad (34.20)$$

Using Eqs. (34.10) and (34.20) and the approximate relation

$$1 - \frac{V_{\infty}}{a^*} = \frac{1 - \lambda_{\infty}}{\Gamma},$$

Eq. (34.19) can be written in the form

$$C_p = \frac{1}{\lambda_l^2} P(K, \xi), \quad (34.21)$$

where the function is

$$P(K, \xi) = -2K \left(1 + \frac{1}{K} \frac{\partial f}{\partial \xi} \right) - s^2(\xi). \quad (34.22)$$

For a given point with the dimensionless coordinate ξ , $P(K, \xi)$ varies only with the similarity parameter K .

The general expression for the pressure drag coefficient can be found by substituting C_p into Eq. (1.6) to obtain

$$C_{Dp} = \frac{1}{\lambda_l^2} D(K), \quad (34.23)$$

where $D(K)$ is determined from the expression

$$D(K) = 4 \int_0^1 \lambda_l P(K, \tilde{x}) \bar{r} \tan \delta d\tilde{x}. \quad (34.24)$$

The relations for C_p and C_{Dp} indicate that, for identical values of K , the transonic flows around affine-similar bodies of revolution are similar in the sense that the quantities $\lambda_l^2 C_p$ and $\lambda_l^2 C_{Dp}$ remain identical. Thus, K is the basic parameter characterizing the flow in the study of transonic flow, and the law of similarity of flows in terms of K can be used as the basis for experimental and theoretical studies of aerodynamic characteristics.

A relation differing somewhat from Eq. (34.13) can be used for K :

$$K = \frac{(M_\infty^2 - 1)\lambda_l^2}{(\gamma + 1)M_\infty^2}, \quad (34.25)$$

which represents the similarity more exactly.⁽²⁾ The more detailed study in Ref. (2) leads to the conclusion that the similarity laws are more complicated than those given by Eqs. (34.21) and (34.23); that is,

$$C_p = \frac{B(K, \xi)}{\lambda_l^2} + E(M_\infty, \lambda_l, \gamma, \xi), \quad (34.26)$$

$$C_{Dp} = \frac{C(K)}{\lambda_l^2} + G(M_\infty, \lambda_l, \gamma), \quad (34.27)$$

where B , C , E , and G are certain functions depending on the variables indicated in Eqs. (34.26) and (34.27). According to these equations, the similarity pertains not to the functions $\lambda_l^2 C_p$ and $\lambda_l^2 C_{Dp}$ but to the parameters $\lambda_l^2(C_p - E)$ and $\lambda_l^2(C_{Dp} - G)$, respectively.

The Slender Pointed Body with a Curved Profile

Research has shown that for families of affine-similar slender pointed bodies of revolution the second term in Eq. (34.26) has the form^(2,3)

$$E = -\frac{1}{\pi} S''(x) \log \left(\frac{M_\infty}{\lambda_l^2} \sqrt{\gamma + 1} \right). \quad (34.28)$$

Equations (34.28) and (34.26) can be used to generalize experimental data for a given Mach number and for a specific model of a given fineness ratio. An experimental pressure distribution is shown in Fig. 307.

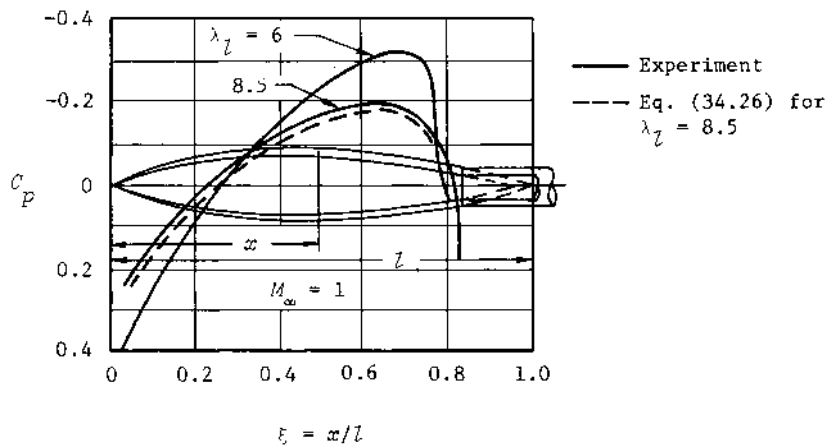


Fig. 307--Application of the similarity law to the calculation of the pressure distribution over a slender body at sonic speed

for $M_\infty = 1$ around a parabolic body of revolution with a fineness ratio $\lambda_l = 6$. The values of $B(\xi)$ were calculated as a function of ξ from these experimental values and Eq. (34.26), and then the pressure coefficients were computed at the corresponding points of a more slender body of revolution with a fineness ratio of 8.5. The results agreed well with experimental data for the more slender body.

Introducing Eq. (34.26) for C_p into Eq. (1.6), we obtain the following similarity law for the drag coefficient:

$$C_{Dp} = \frac{4}{\pi} \frac{C(K)}{\lambda_l^2} - \frac{1}{2\pi} \frac{[S'(l)]^2}{S_{mid}} \log \left[\frac{M_\infty}{\lambda_l^2} \sqrt{\gamma + 1} \right], \quad (34.29)$$

from which the function G in Eq. (34.27) can be found.

The similarity law of Eq. (34.29) is simplified if the base of the body lies at the maximum cross section or if the afterbody is pointed;

in both cases, the derivative of the cross-sectional area $S'(x_j) = 0$. The relations presented for the similarity law are applicable in the vicinity of $M_\infty = 1$, and the results of calculations agree well with the data obtained for sonic or slightly supersonic flows.

The Slender Pointed Cone with a Cylindrical Afterbody

The peculiarity of transonic or sonic flow around a conical body is that sonic velocity is always obtained at the shoulder. Therefore, the pressure at this point can be calculated beforehand. The flow parameters at the other points of the cone can be found either experimentally or by solving Eq. (34.16). This solution leads to the following relation for the pressure coefficient at $M_\infty = 1$:⁽²⁾

$$\frac{C_p}{\delta_c^2} = -2 \log (\delta_c \xi) + \log A - B, \quad (34.30)$$

in which

$$A = \frac{8.96\xi(1-\xi)}{(\gamma+1)\delta_c^2}, \quad B = \frac{1}{2} \frac{1+\xi}{1-\xi} \quad \text{for } 0 < \xi \leq \frac{1}{3}$$

(34.31)

$$A = \frac{\delta_c^2}{(\gamma+1)\delta_c^2} + \frac{2.24(1-\xi^2)}{(\gamma+1)\delta_c^2}, \quad B = 1 \quad \text{for } \frac{1}{3} < \xi \leq 1.$$

The curve calculated from Eq. (34.30) is presented in Fig. 308 for a cone with $\delta_c = 7^\circ$. These results agree well with experiment.

A similarity law analogous to Eq. (34.30) can be obtained for $M_\infty \neq 1$ by combining Eqs. (34.26) and (34.28). Since $S(x) = \pi x^2 \delta_c^2$, $S''(x) = 2\pi \delta_c^2$, and $\lambda_l = \frac{1}{2}\delta_c$ for a cone, Eq. (34.26) can be written as

$$C_p = 4\delta_c^2 B(K, \xi) - 2\delta_c^2 \log (4\delta_c^2 M_\infty \sqrt{\gamma+1}). \quad (34.32)$$

The expression for the drag coefficient corresponding to Eq. (34.29) is written in the form

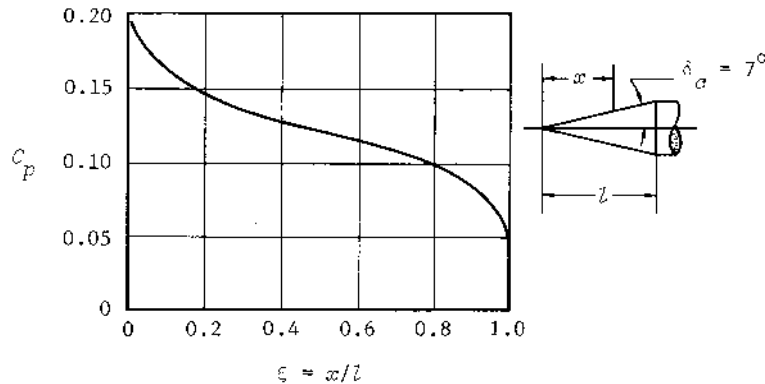


Fig. 308--The pressure distribution on a cone-cylinder at $M_\infty = 1$

$$C_{Dp} = \frac{8\delta_c^2}{\pi} C(K) - 2\delta_c^2 \log (4\delta_c^2 M_\infty \sqrt{\gamma + 1}). \quad (34.33)^+$$

For $M_\infty = 1$, Eqs. (34.32) and (34.33) are simplified since in this case $K = 0$. For example, the expression for the drag coefficient is

$$(C_{Dp})_{M_\infty=1} = -\delta_c^2 (1.09 + 4 \log \delta_c). \quad (34.34)$$

In the case of a Mach number differing from unity, we can use a specific relation for a slender cone instead of the general Eq. (34.33):

[†]Editor's note: Spreiter and Alksne⁽²⁾ give explicit expressions for C_p and C_{Dp} for $M_\infty \neq 1$ that can be written in the same format as Eq. (34.30); the expression for A is modified from that in Eq. (34.31) by replacing $(\gamma + 1)$ with $(\gamma + 1)M_\infty^2$. The equations are

$$C_p/\delta_c^2 = 8K - 2 \log (\delta_c \xi) + \log A - B, \quad (34.32a)$$

$$C_{Dp}/\delta_c^2 = 8K - \frac{1}{2} + \log [1.33/(\gamma + 1)M_\infty^2 \delta_c^4], \quad (34.33a)$$

where K is defined in Eq. (34.25). Equation (34.33a) leads directly to the later equations for C_{Dp} (Eqs. (34.34) and (34.35)).

$$C_{Dp} = -\frac{\delta_c^2}{\sigma} (1.09 - 8K + 4 \log \delta_c). \quad (34.35)$$

It follows from this equation that for a slender conical body the quantity $(C_{Dp}/\delta_c^2) + 4 \log \delta_c$ depends only on the similarity parameter K . The application of Eq. (34.35) is limited to values of K that satisfy the inequality

$$K \approx \frac{M_\infty^2 - 1}{4(\gamma + 1)M_\infty^2 \delta_c^2} \ll 1. \quad (34.36)$$

This condition corresponds to a weak shock wave located a rather large distance from the body. The distance of the shock from the apex (Fig. 309) is determined by

$$0.125 \log \left(\frac{l_N}{x_s} + 1 \right) - \left(1 + \frac{x_s}{l_N} \right) = K. \quad (34.37)$$

This equation serves as another illustration of the similarity law with respect to the parameter K .[†]

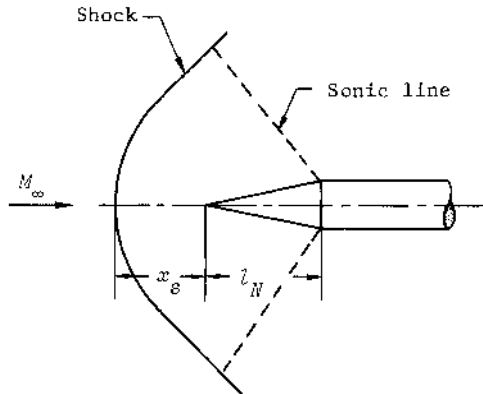


Fig. 309--The detached shock wave for M_∞ slightly greater than one

[†]Editor's note: This equation is clearly incorrect, but the reference is unknown.

§ 35. SOME DATA ON TRANSONIC FLOW AROUND BODIES OF REVOLUTIONTHE PHENOMENON OF SHOCK STALLThe Shock Wave on the Body at Subsonic Speeds

ON THE BASIS OF EXPERIMENTAL DATA, it is possible to explain a number of physical phenomena related to shock stall, among which is the formation of a shock wave at subsonic flight velocities. Schlieren photographs of a body of revolution are shown in Fig. 310. Analysis of the photographs shows that at $M_\infty = 0.67$ the local velocity does not exceed sonic velocity (see Fig. 310a) at any point on the body. The drag at this velocity is due only to skin friction and is very small.

The flow at a somewhat larger Mach number, $M_\infty = 0.78$, is shown in Fig. 310b, and it is evident that the velocity is sonic not far from the nose section of the body and then exceeds the velocity of sound somewhat downstream. As a result, a local supersonic zone occurs on the surface of the body. Behind this zone, at approximately half the length of the body, the velocity is decreased by a shock wave and the flow again becomes subsonic. A series of normal shocks is evident in the schlieren photograph, but their strength is small and the velocity is almost unchanged. A sharp change in velocity occurs when the strength of the shock wave increases. A similar phenomenon is observed more clearly in the case of flow around the body at $M_\infty = 0.89$ (Fig. 310c). In this case, the shaded streak in the schlieren represents a strong shock wave.

With the occurrence of shock waves, the kinetic energy of the flow is dissipated by the formation of the shocks, resulting in a considerable increase in drag. In Fig. 310, the relative magnitude of the wave drag coefficient is shown by the light vertical lines on the right, and it is evident that the wave drag coefficient increases sharply with an increase

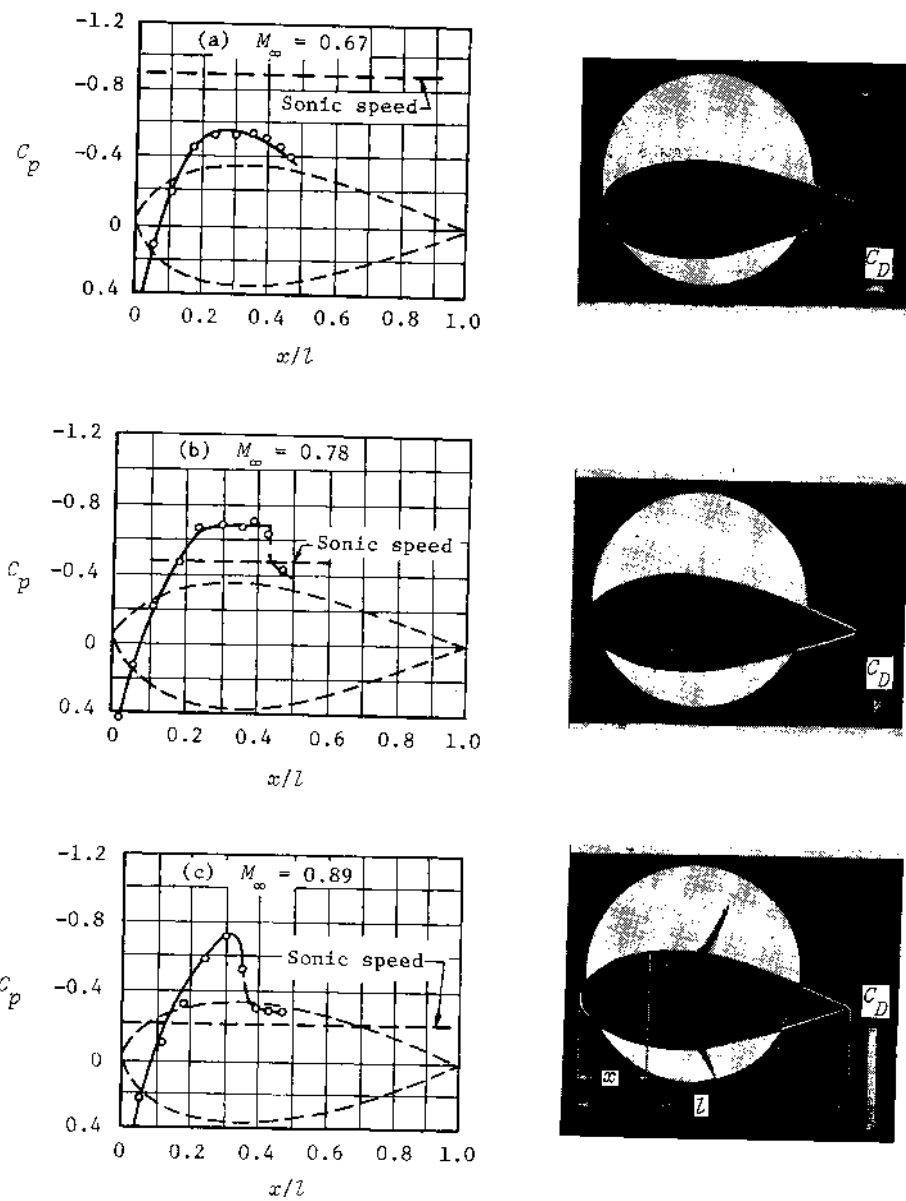


Fig. 310—Schlieren photographs and pressure distributions on bodies of revolution at high subsonic speeds

in M_∞ . Thus, the drag coefficient at $M_\infty = 0.89$ is more than ten times greater than that at $M_\infty = 0.78$. The sharp increase in drag and the changes in the other aerodynamic characteristics at transonic speeds is connected with the general concept of shock stall.

The Effect of the Shape of the Body

Experimental research has shown that the phenomenon of shock stall depends essentially on the shape of the body of revolution. Data are presented in Fig. 311 indicating the effects of the shape of the nose, the fineness ratio, and the location of the maximum cross section of the body on the nose drag coefficient and the critical Mach number M_{cr} .

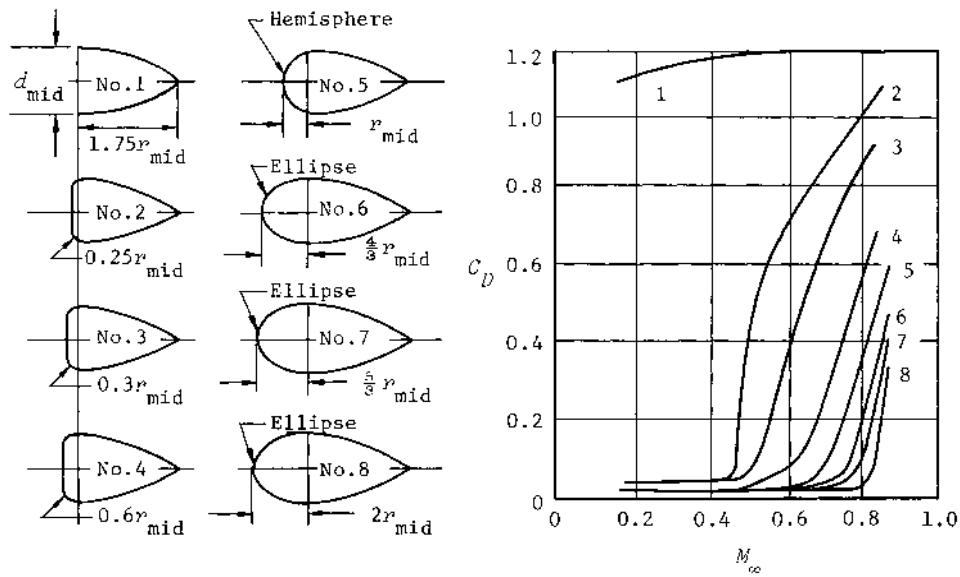


Fig. 311--Drag of different bodies of revolution at subsonic speeds

(the value of M_∞ at which the velocity becomes sonic at some point on the body). The absolute thickness of all bodies under investigation is the same. It is evident from the figure that an increase in the total fineness ratio of the body, in the nose fineness ratio, and in

the curvature of the nose all affect the drag rise and also the general level of the drag. Different local curvatures have an especially strong effect in reducing the drag level, as can be seen from the comparison of the curves for models 1 and 2.

Curves are presented in Fig. 312 for the minimum pressure coefficient in subsonic flow around models 5 to 8 of the bodies shown in Fig. 311. As the nose fineness ratio is increased, the flow needs to expand less and the shock stall is delayed to higher Mach numbers.

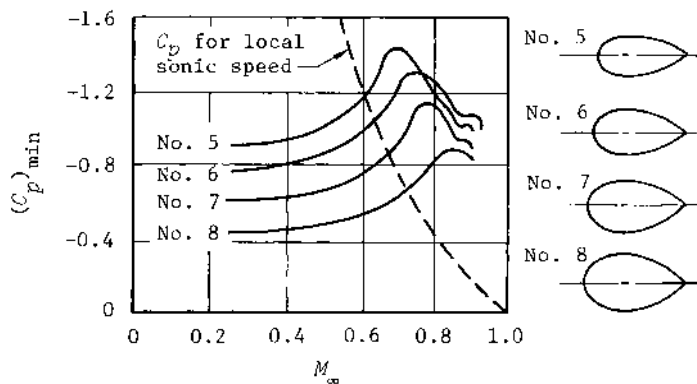


Fig. 312--Minimum pressure coefficients for subsonic flow over bodies of revolution

The critical Mach number for each model can be determined from Fig. 312 as the point of intersection of the curves of $(C_p)_{\min}$ with the curve corresponding to local sonic velocity (dashed curve). However, the critical Mach number does not correspond with the beginning of the sharp increase in drag (see Fig. 311), because only the necessary conditions for the development of the stall regime have been reached.

The rapid increase in drag begins at Mach numbers larger than critical, equal approximately to the values corresponding to the points of greatest expansion in the curves in Fig. 312. This indicates that a significant region of supersonic velocities must be developed on the surface of the body as a condition for the formation of strong shock waves and the rapid increase in drag associated with them.

The drag increases to some extent as the result of the interaction of the shock waves with the boundary layer. This interaction promotes the separation of the boundary layer from the surface of the body and necessitates a redistribution of pressure. Moreover, premature turbulence develops in the boundary layer, also increasing the drag of the body.

It is evident from the data presented that transonic flow around rather thick bodies is accompanied by the development of shock waves. This picture of transonic flow changes when slender bodies are considered. In this connection, let us examine some experimental results⁽⁴⁾ obtained on a model of a pointed body of revolution with a parabolic shape, having a nose fineness ratio of 3 (Fig. 313). The pressures at

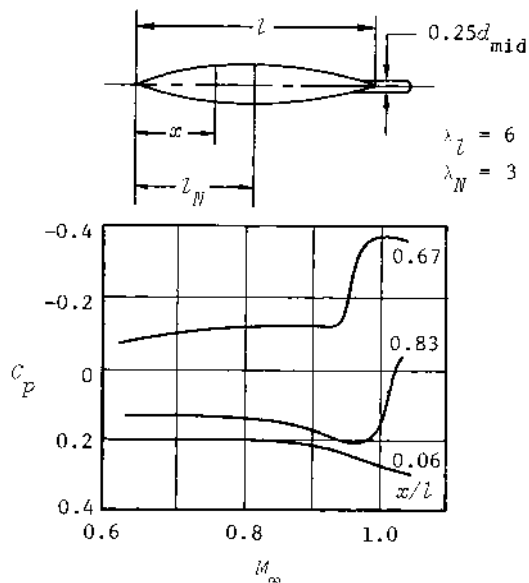


Fig. 313--Pressure coefficient at three stations on a pointed body at high subsonic and transonic speeds

three different stations of this model ($x/l = 0.06, 0.67, 0.83$) were measured in flight. As is apparent, the effects of compressibility are insignificant and can, in practice, be neglected up to $M_\infty = 0.90$.

Curves are presented in Fig. 314 for the pressure distribution along the body for different free-stream Mach numbers, from which it can be seen that the critical Mach number (M_{cr}) is equal to approximately 0.90. These data show that the velocity field changes character as it progresses back

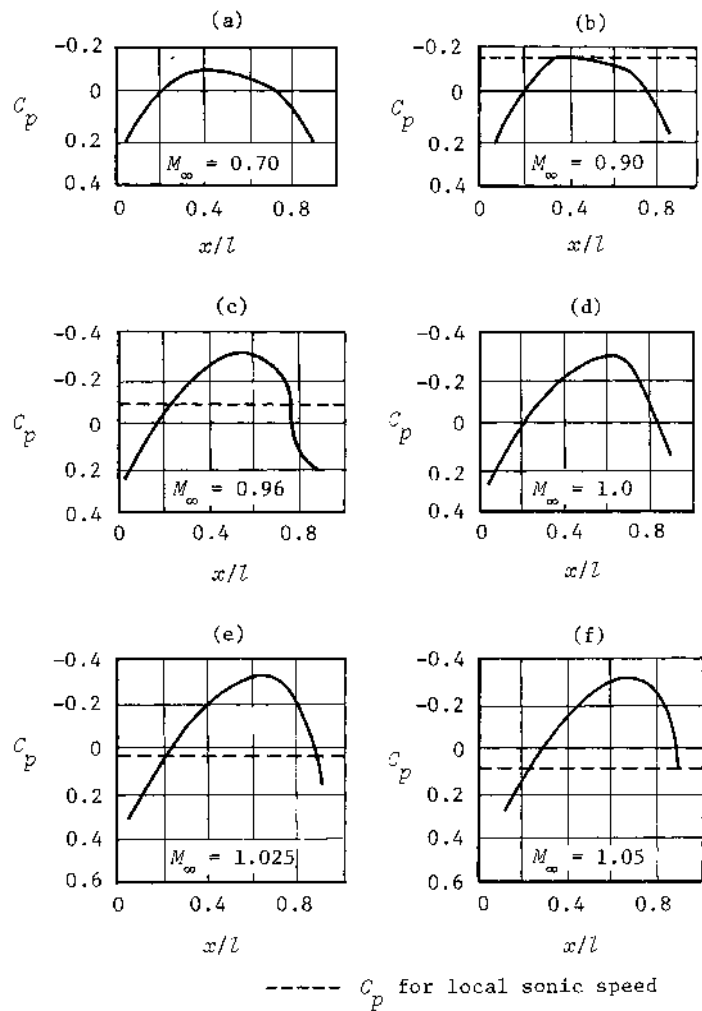


Fig. 314--Pressure distribution on a slender pointed body of revolution at high subsonic and transonic speeds

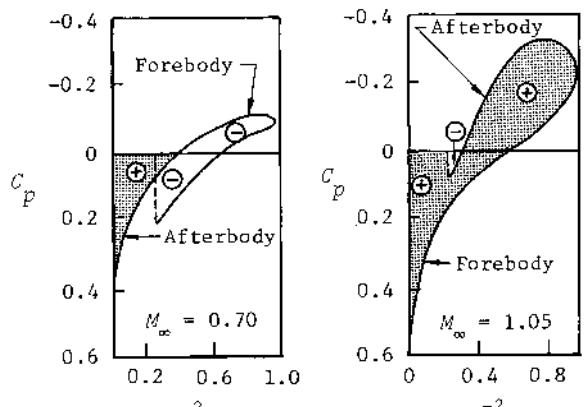
along the body, as indicated by the fact that the supersonic regions on the body become larger and the region of the negative pressure coefficient is shifted backward. From the physical point of view, an expanding supersonic flow is accompanied by a reduction in pressure, whereas an expanding subsonic flow is associated with a pressure increase. The increase in and the backward shift of the region of negative pressure coefficient leads to a rapid increase in the drag coefficient.

Even in the case of a significant supersonic region on the surface of the body, the transition from supersonic to subsonic flow at the rear, rapid though it is, is accomplished very smoothly. Obviously, it is accomplished through a system of very weak shocks and can, in practice, be considered an isentropic compression.

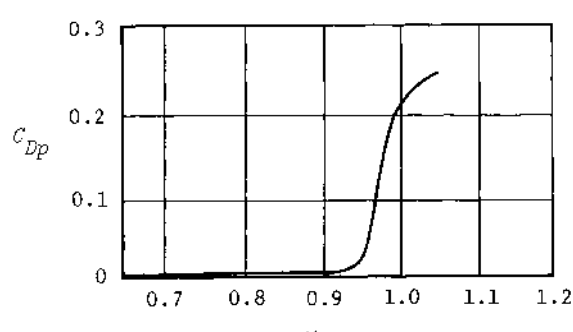
Using the pressure distributions in Fig. 314, we can compute by graphical integration the drag coefficient for different Mach numbers from Eq. (1.6). As an illustration of this method, Fig. 315 shows the variation in the pressure coefficient with \bar{r}^2 for $M_\infty = 0.70$ and 1.05 . The pressure drag coefficient can be determined by measuring the net area under the curves, taking into account the signs shown on the graph (measured in a counterclockwise direction around the contour of the body).

Figure 315b shows the variation of the pressure drag coefficient C_{Dp} with Mach number for the body under consideration. The drag coefficient is very small, less than 0.01, up to $M_\infty = 0.9$, because the pressure is distributed practically symmetrically fore and aft in subsonic flow (if the small asymmetry caused by the model support is neglected), and therefore the pressure drag is negligibly small. The almost symmetrical pressure distribution indicates that the boundary layer has little effect on the pressure distribution and that there is no noticeable flow separation. Additional research has shown a tendency toward separation of flow near the support due to a small compression from it. However, this separation does not have much influence on the pressure drag, since the cross section of the body at the aft end is small.

Beginning with a Mach number of 0.94, the drag coefficient increases sharply, reaching 0.21 at $M_\infty = 1$. This sharp increase is associated with the rapid backward shift of the region of negative pressure coefficients



(a)



(b)

*Fig. 315--Method of graphical integration
for the pressure drag coefficient*

as sonic speed is approached. Flow separation in the transonic regime does not occur in practice due to the smooth shape of the slender body, so that it is not necessary to consider the effects of separation on the drag.

After the free-stream Mach number reaches unity, a rather extended region of supersonic velocities is formed on the body surface, the backward shift of the point of minimum pressure slows down, and the overall

pressure level decreases. In the range of Mach numbers from 1 to 1.05, all these phenomena are accompanied by a more gradual increase in the pressure drag coefficient.

The Total Drag of Various Bodies of Revolution at Transonic Speeds

The transonic regime for slender bodies of revolution lies approximately within the range $M_\infty = 0.9$ to 1.3. Artillery shells were the first axisymmetric bodies for which the drag was studied at transonic speeds. The experimental data obtained for one of these projectiles, consisting of a cylindrical body with a nose cone, show that the drag coefficient increases rapidly beginning at $M_\infty = 0.9$ and reaches a maximum at approximately $M_\infty = 1.1$. The magnitude of the maximum drag coefficient is almost three times larger than that at subsonic velocities.

The experimental curve for C_D as a function of M_∞ for a bomb is presented in Fig. 316. (5) Due to the fact that the afterbody of the bomb is tapered, the drag in the subsonic regime is less than that for a body without a boattail. The shape of the nose section has an increasingly greater influence on the drag at transonic and supersonic speeds. The difference in the drag of the bomb and the shell is due to the different shape of their noses. The drag of the bomb is almost twice as large as that of the shell because its nose is less pointed.

The experimental data in Fig. 317 were obtained for a cylindrical

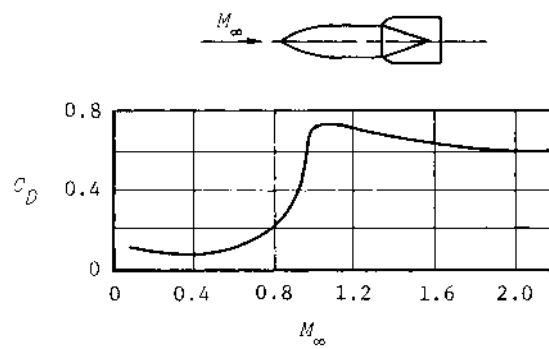


Fig. 316--Experimental drag curve for a bomb

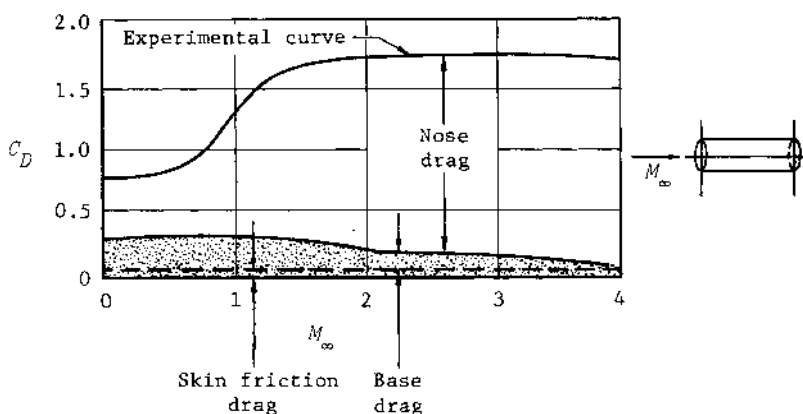


Fig. 317--Drag coefficient for a blunt cylinder

body with a blunt nose.⁽⁵⁾ The comparatively rapid increase in drag at $M_\infty = 1$ is in agreement with that predicted by Eq. (20.40).

The drag of a body with a rounded nose is considerably less, particularly a spherical body. An experimental curve for the drag of a sphere at transonic speeds is shown in Fig. 318, and it is evident that the sphere has about two-thirds the drag of a blunt cylinder at $M_\infty = 1$.

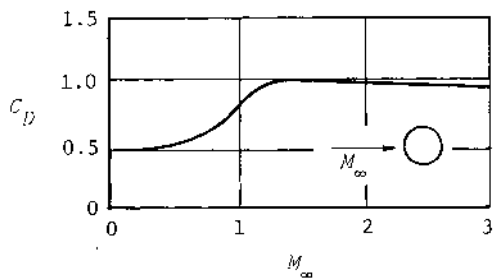


Fig. 318--Experimental drag curve for a sphere

The drag coefficient of the sphere reaches about twice its value at low speeds and then stays approximately constant at $C_D = 1$. The magnitude and character of the variation in drag at supersonic speeds differ from

that presented in Fig. 207 (page 570). The cause of the difference is that the curve in Fig. 318 represents the total drag, whereas that in Fig. 207 represents only the drag due to the pressure acting on the front hemisphere. In addition to pressure drag, the total drag consists also of the drag components caused by skin friction and by expansion over the rear of the body. The influence of these components causes a leveling out of the drag curve at supersonic speeds rather than the increased indicated in Fig. 207.

The following conclusions can be drawn from a summary of the data presented here and other experimental data:

1. The nose drag coefficient reaches a maximum value $C_{D\max}$ at a Mach number somewhat larger than unity and located in a range between $M_\infty = 1.1$ and 1.5.
2. The dominating influence on the magnitude of $C_{D\max}$ is the shape of the nose of the body.

In practice, we can be guided by these conclusions in estimating the maximum value of the nose drag coefficient. It is also possible to use curves based on experimental data, such as shown in Fig. 319, which give the relation between $C_{D\max}$ and the fineness ratio of the nose.⁽⁵⁾ This relation can be given by the following empirical equation:

$$C_{D\max} = \frac{0.8}{\lambda_N} + 0.01\lambda_N. \quad (35.1)$$

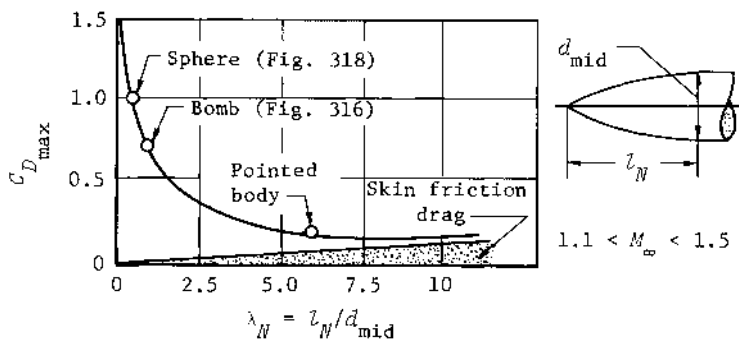


Fig. 319--Maximum drag coefficient of bodies of revolution as a function of nose fineness ratio

The second term on the right in Eq. (35.1) approximates the magnitude of the friction drag coefficient. The minimum value of $C_{D\max}$ according to Eq. (35.1) occurs at a nose fineness ratio of about 9, which corresponds to a very slender body. The friction drag for such a body represents a large proportion of the total drag.

The Normal Force Coefficient and Center of Pressure of Bodies of Revolution at Transonic Speeds

The normal force coefficient and the center of pressure in transonic flow are as difficult to treat in theoretical and experimental research as are the other aerodynamic characteristics. The difficulty in experimental research results chiefly from the instability of the flow in transonic wind tunnels. Only after the development and introduction into the technology of special tunnels with flow stability at Mach numbers of approximately 0.9 to 1.3 did it become possible to obtain reliable information on aerodynamic forces and their coefficients under transonic flow conditions. As a result, much of the aerodynamic data accumulated on bodies of revolution is obtained by means of flight tests. Some of these data relating to nose drag were presented above.

It has been established experimentally that, for slender bodies of revolution, the normal force coefficient at near sonic speeds can attain a maximum value exceeding that for subsonic speeds by 25 to 35 percent. The curve in Fig. 320 shows C_N/α as a function of M_∞ for a

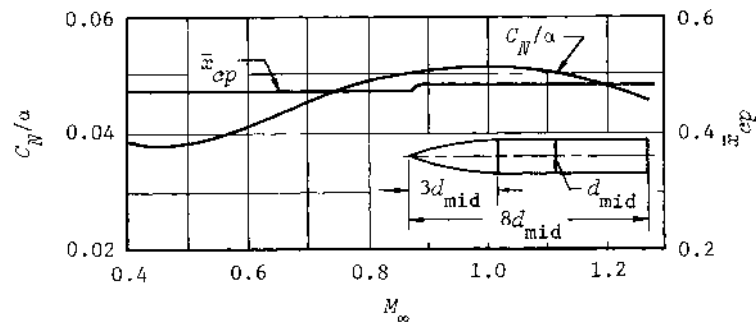


Fig. 320--Variation of C_N/α and the center-of-pressure coefficient at transonic speeds

typical body at angles of attack of 3° and less. The ratio C_N/α attains a maximum value at $M_\infty = 1.0$, where it is approximately 35 percent larger than C_N/α for $M_\infty = 0.4$. The pitching moment also increases with an increase in the normal force. As a result, the location of the center of pressure may not change in practice. This is evident in Fig. 320, where results are presented for the center-of-pressure coefficient of a cylindrical body with a parabolic nose. The variation in this coefficient is only 2 percent for the entire speed range shown.

A similar result is also observed in experimental studies of flow around cones. It is known that the center-of-pressure coefficient of a cone at supersonic speeds is approximately 0.667. Experiments at subsonic speeds show that, for example, for a cone with a semiaxial angle of 15°, the center-of-pressure coefficient is less by 4 percent, i.e., the center of pressure is closer to the tip. At transonic speeds, the center-of-pressure coefficient increases slightly, reaching about 0.65 at $M_\infty = 1.0$.

Experimental data indicate that the center of pressure of a cone shifts toward the base of the cone when a cylindrical afterbody is attached to the cone. This occurs both at subsonic and transonic speeds, with the amount of the shift depending on the length of the cylinder. The center of pressure of the cone moves aft because the cylindrical part of the body introduces additional disturbances into the flow, which in subsonic flow are propagated upstream on the surface of the body. The greatest influence of these disturbances is in the region at the base of the cone, causing an increase in pressure. Consequently, an additional normal pressure develops that leads to a displacement in the center of pressure. The longer the afterbody, the larger the disturbances, and the more the center of pressure is displaced.

For slender cones with cylindrical afterbodies whose length is about a half a diameter, the increase in the center-of-pressure coefficient is 5 to 7 percent in the Mach number range from 0.7 to 1.2. For a cylinder length of $0.75d_{mid}$, this increase reaches 7 to 13 percent, and \bar{x}_{cp} is close to its maximum value. The location of the center of pressure does not change appreciably for a further increase in the length of the cylinder because the perturbations from the lengthened section of

the cylinder do not reach the cone. To have some idea of the variation in the center-of-pressure coefficient of the entire body (consisting of a cone and a cylinder), it is necessary to take into account the normal force on the cylinder as well as that on the cone. The presence of a normal load on the cylinder leads to an additional backward shift in the center of pressure.

The center of pressure does not change noticeably for bodies with parabolic noses at transonic speeds.

FLOW IN THE NEAR-CRITICAL REGIME

The Velocity Field

Let us examine a few of the results of experimental research on flow around conical bodies. Some of these results are related to the case of a shock wave still attached to the apex but distorted from its conical shape, and some are related to the formation of a detached shock. These types of flow occur when the cone angle is close (or equal) to the critical value, and a subsonic region occurs between the shock and the cone surface.

In this connection, a question arises concerning the limit of applicability of the theory of conical flow to the calculation of the flow around a cone. Sketches from schlieren photographs of conical models in wind tunnels are presented in Fig. 321 for $M_{\infty} = 1.415$ and 1.328 .⁽⁶⁾ An analysis of these photographs shows that the shock wave is still

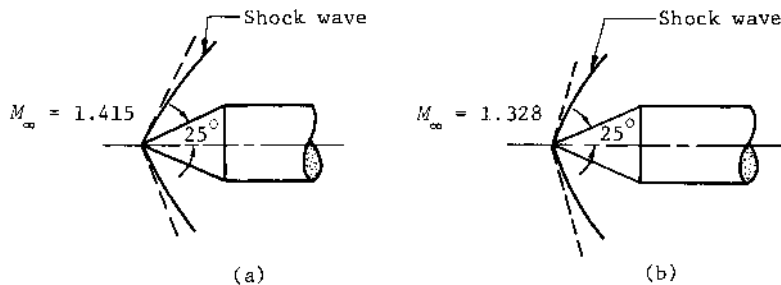


Fig. 321--Shock waves on a cone-cylinder for near-critical flow conditions

attached to the apex of the cone. In Fig. 321a, the shock is straight near the apex but is curved at some distance from it; in Fig. 321b, the shock wave at the lower Mach number is already curved at the apex. The curvature of the shock indicates that the flow is nonconical and that the junction of the cone with the cylinder influences the flow close to the apex of the cone, causing the development of a subsonic region extending from the shoulder to the apex. Figure 322 shows the location

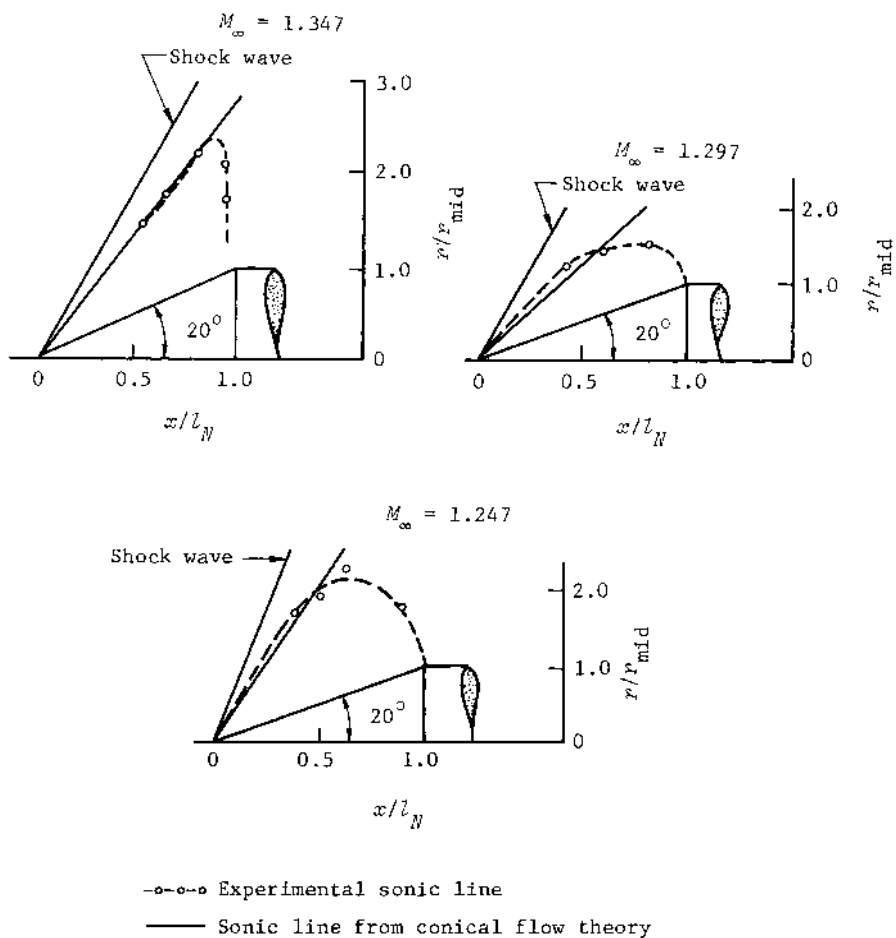


Fig. 322--Location of the sonic line for a cone-cylinder at near-critical flow conditions

of the sonic line separating the subsonic from the supersonic region. The sonic lines begin at the cone-cylinder junction and go in the direction of the apex, where they become straight. Their location in the region adjacent to the apex agrees well with the conical theory. In this connection, it can be assumed that the flow in the vicinity of the apex probably remains conical.

A more detailed study of the flow around a cone cylinder is possible with the help of an interferometer.^(6,7) Some of the results of these interferograms are presented in Fig. 323, where the velocity field between the surface of a 25° cone cylinder and a shock wave is shown for three decreasing Mach numbers, $M_\infty = 1.401, 1.273$, and 1.229 . The theoretical Mach number at which the flow on the surface becomes sonic for this body is 1.5, and the experiments show a significant subsonic region on the cone at $M_\infty = 1.401$ (Fig. 323a). Therefore, the sonic line originating at the shoulder becomes straight close to the apex (similar to the shock wave). The agreement between the pressures calculated according to exact theory and those measured on the cone surface near the apex confirms the assumption concerning the existence of local conical flow near the apex. The subsonic region increases with a decrease in Mach number, and the sonic line (as is evident in Fig. 323b) intersects the shock wave, which is already considerably curved at the apex. The influence of a further decrease in Mach number on the location of the sonic line can be seen in Fig. 323c.

It is possible to give some explanation of the flow processes observed using transonic shock polars and the apple curves shown in Fig. 324. In this figure, the magnitude of u (representing the difference between the velocity of the perturbed flow and the critical velocity a^*) is plotted on the abscissa and the radial velocity component is plotted on the ordinate. From these values, curves I to IV are constructed, the points of which specify the velocities on an intermediate conical surface, i.e., along the ray R . The geometric positions of the lower ends of curves I to IV on the shock polar also represent an apple curve. Every point C on the apple curve corresponds to a conical surface in the physical plane, and the coordinates of these points specify the velocity. The point S on the shock polar corresponds to the shock wave, and the coordinates of this point give the velocity directly behind the shock.

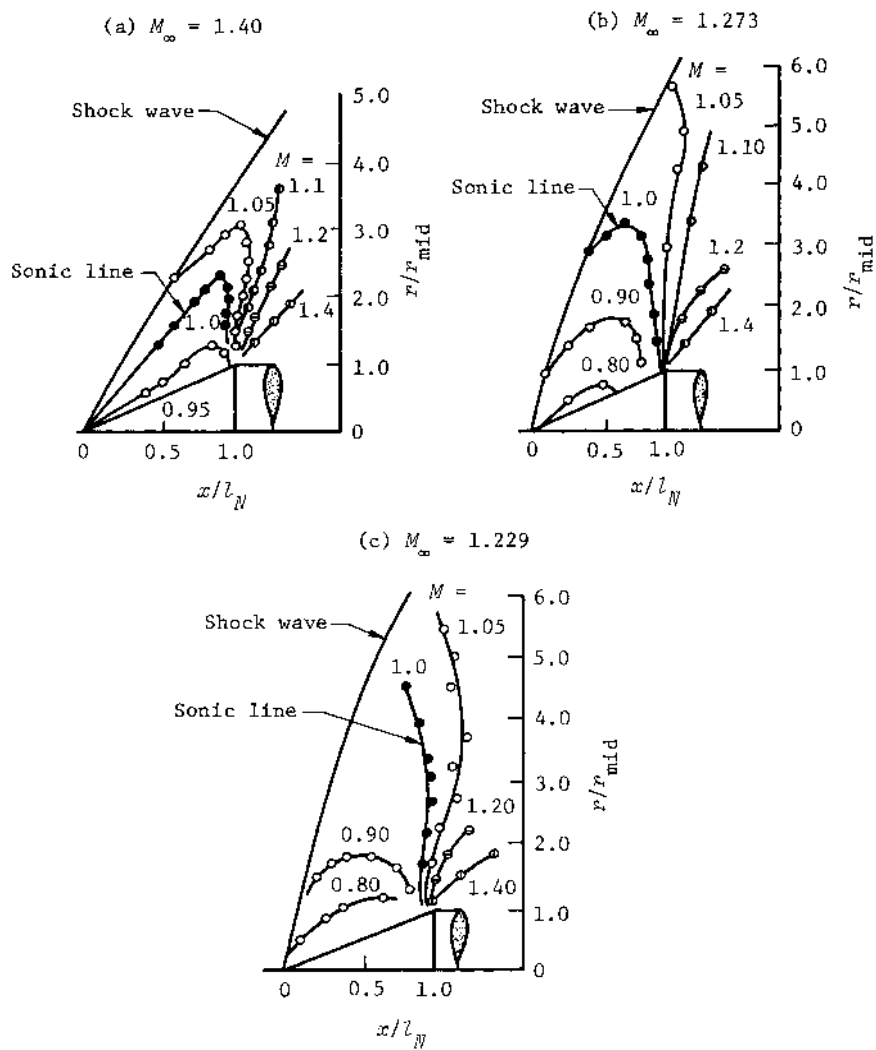


Fig. 323--Velocity field about a 25° cone-cylinder

It is apparent that the vertical axis corresponds to the sonic line in the physical plane, which is also called the sonic line in the hodograph line.

Curve I is located entirely to the right of the sonic line and corresponds to completely supersonic flow between the cone and the shock

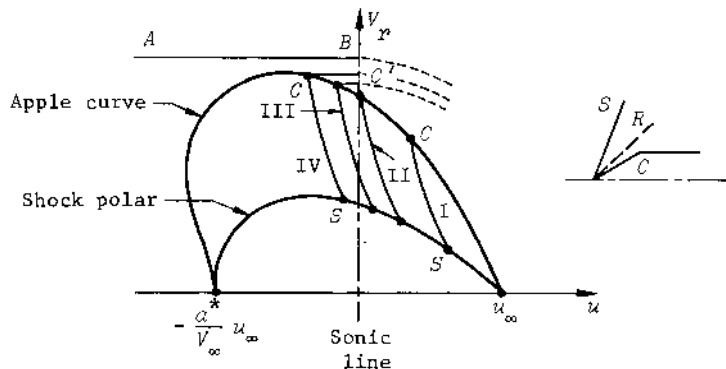


Fig. 324--Hodograph for near-critical flow over a cone

wave. For an increase in the cone angle and a fixed Mach number, curve I will be shifted to the left toward curve II. The terminal point of curve II lies on the sonic line, indicating that the velocity of sound has been attained. A subsonic region occurs near the surface as δ_σ continues to increase and it becomes impossible to maintain conical flow in the entire region between the shock wave and the body. As the cone angle is increased still more, corresponding to transition from curve II to curve III, the velocity at the shoulder remains sonic (point C') and the velocity near the apex (point C of curve III) is subsonic. In other words, the velocity does not remain constant along the conical surface, represented in Fig. 324 by the horizontal line CC' , but increases from subsonic near the apex to sonic at the junction line.

The sonic line that begins at the shoulder approaches the apex for specific values of δ_σ and M_∞ , as is evident from Fig. 323a. In Fig. 324, the point C on curve III corresponds to this sonic line.

Curve IV is developed for a further increase in the cone angle; it corresponds to a completely subsonic velocity and does not intersect the sonic line in the hodograph plane. Thus, the sonic line in the physical plane, as is evident from Fig. 323b, passes directly from the shoulder to the shock wave.

When the cone angle reaches supercritical values, the conical surface is no longer specified by a point on the apple curve (in Fig. 324,

this corresponds to the fact that the horizontal line AB does not intersect the apple curve). Therefore, the shock wave must have detached from the apex of the cone. Experimental data show that the shock wave detaches from the apex at values of δ_c somewhat larger than those specified by exact theory. For example, for $M_\infty = 2.45$ it was found experimentally that shock detachment occurred at $\delta_c = 46^\circ$, whereas this angle is $45^\circ 40'$ according to exact theory.

The Drag of a Cone

The experimental pressure distribution around various cones at $M_\infty = 2.45$ indicates that the conical flow corresponding to constant pressure on the cone is maintained as long as the speed of sound is not attained on its surface.⁽⁸⁾ This occurs at $\delta_c = 42^\circ 30'$ (Fig. 325). For cone angles exceeding this value, the structure of the flow in the region of the shoulder and the finite dimensions of the model have an

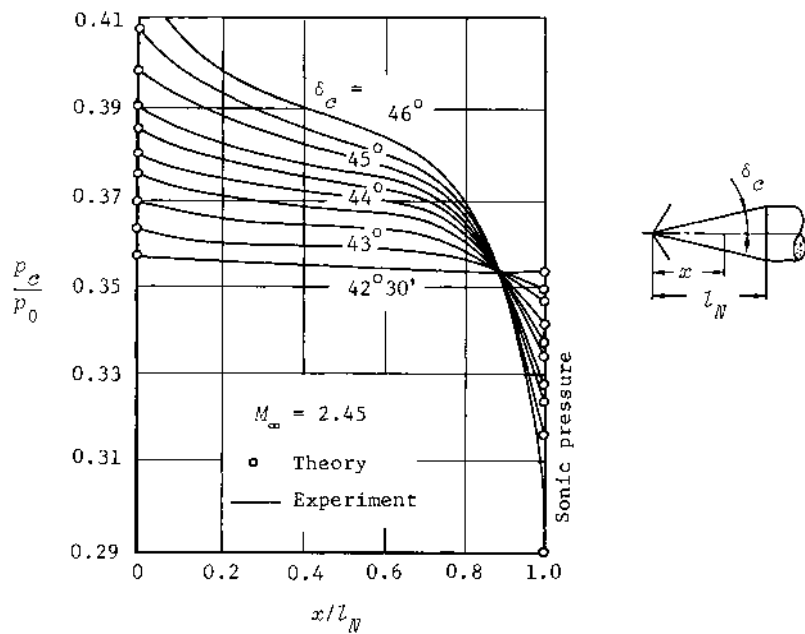


Fig. 325--Pressure ratio on a cone in near-critical flow

effect on the character of the flow. As a result, the pressure along the body varies, as is evident from Fig. 325. In this figure, the theoretical pressure ratios at the terminal points of all the curves are obtained on the basis of the following assumptions:

1. The pressure on the nose of the model is assumed equal to the pressure for an infinitely long cone; i.e., it is assumed that the expansion of the flow at the cone-cylinder junction does not change the pressure at the apex.
2. The pressure at the tip can be calculated from conical theory, provided the shock wave still has not detached from the apex of the cone.
3. The pressure at the shoulder of the body is determined by assuming that the speed of sound is attained at this point.

A comparison of the pressures calculated on the basis of these assumptions with the pressures obtained experimentally shows good agreement for all terminal points. It should be noted that the pressure at the cone-cylinder junction begins to decrease with a further increase in the cone angle because the strength of the shock wave is increasing. The pressure increases slightly on the surface of the cone forward of the corner as the cone angle approaches the value for shock detachment. The deviation from the conical character of the flow along the cone becomes increasingly greater with the increase in the subsonic region between the shock wave and the body surface.

Experimental research has also shown that the boundary layer on the model surface has almost no influence on the pressures on the cone but can play a decisive role in the formation of flow in the vicinity of the cone-cylinder junction, especially in those cases where the cone angle is less than critical and a favorable (negative) pressure gradient is absent. When the cone angle reaches the critical value or exceeds it (in the latter case, the shock wave detaches from the apex), the pressure at the corner is very close to the theoretical value corresponding to sonic velocity.

The variation of the pressure drag coefficient with cone angle at $M_\infty = 2.45$ is shown in Fig. 326. The coefficient C_{Dp} was calculated from the pressure distributions given in Fig. 325. It will be noted that C_{Dp} increases continuously as the cone angle passes through the value

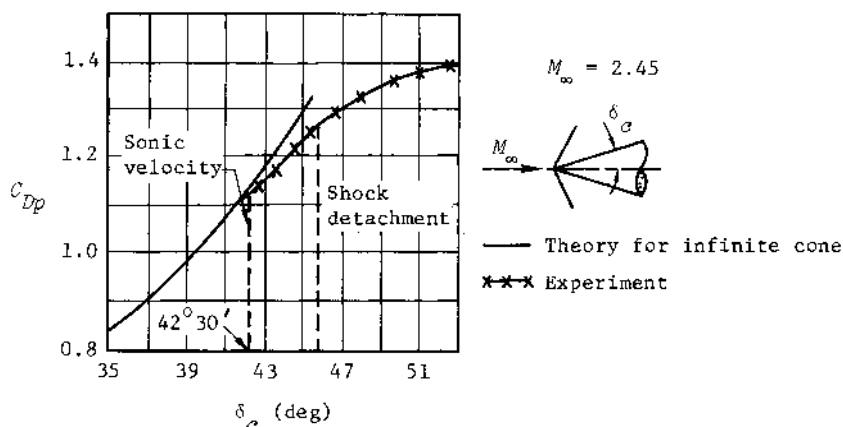


Fig. 326--Pressure drag coefficient on a cone at near-critical velocity

for shock detachment. There is no sudden change in drag as the shock detaches, but this angle corresponds more to a point of inflection in the drag curve. The region of high pressures developed at the apex of the cone is limited to so small a section of the body that it does not cause an abrupt increase in drag.

As soon as conical flow is destroyed, the drag of the body becomes somewhat less than the values calculated theoretically for an infinitely long cone. This is also confirmed by the experimental data presented in Fig. 327,⁽⁷⁾ which agree well with the theory of conical flow for supersonic Mach numbers. With a decrease in Mach number, conical theory becomes invalid when the local Mach number on the surface is equal to unity. A further decrease in Mach number leads to an increase in pressure in the vicinity of the cone apex, but the pressure remains sonic near the shoulder. Therefore, as already noted, the actual drag curve is lower than the drag values determined by conical theory. The nose drag for subsonic velocities (see Fig. 327) increases as the Mach number approaches one.

The slope of the drag curves at \$M_\infty = 1\$ can be obtained by a method based on the principle of stationarity of the local Mach number, formulated and tested first for two-dimensional flows. According to this principle, it is assumed that the derivative \$(\partial M / \partial M_\infty)_{M_\infty=1} = 0\$; i.e., the

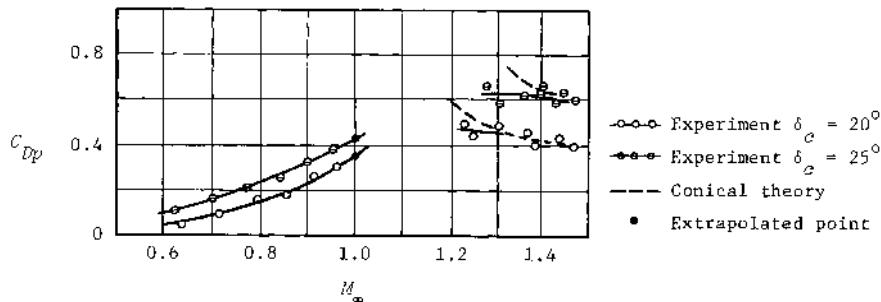


Fig. 327--Pressure drag coefficients of cone-cylinders

local Mach number M does not vary while the Mach number of the incident flow passes through unity. The constancy of the local Mach number for a cone was also tested experimentally.⁽⁷⁾ The results of this test are presented in Fig. 328, where the curves show the change in M with M_∞ . Each of the curves pertains to a specific station on the cone. The range of free-stream Mach numbers for which the distribution of the local Mach number is constant is comparatively narrow. For example,

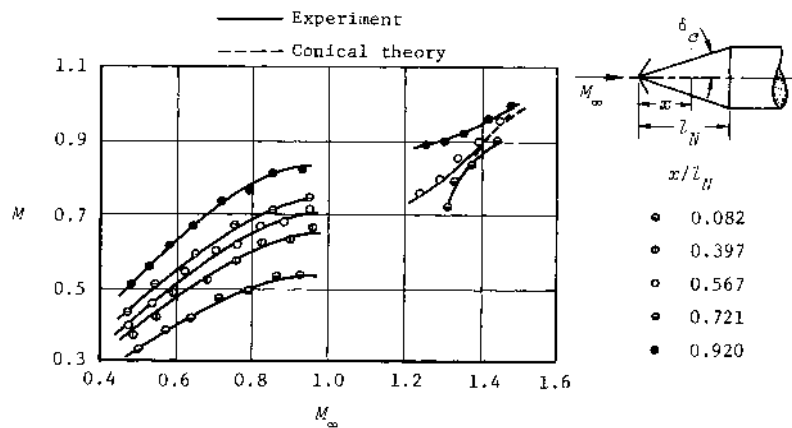


Fig. 328--Surface Mach number on a cone-cylinder

for a 25° cone, this range is specified by the values $M_\infty = 0.9$ to 1.1, and for $\delta_c = 7^\circ$ by $M_\infty = 0.99$ to 1.01.

Using the principle of stationarity of the local Mach number, we can obtain a relation for the drag of a cone at transonic speeds.⁽⁹⁾ If the distribution of local Mach numbers on the surface of a cone is assumed to be known, the corresponding velocities are found from

$$\frac{V^2}{V_\infty^2} = \left(\frac{M}{M_\infty} \right)^2 \frac{2 + (\gamma - 1)M_\infty^2}{2 + (\gamma - 1)M^2}, \quad (35.2)$$

and the pressure coefficients from the equation

$$C_p = \frac{2}{\gamma M_\infty^2} \left\{ \left[1 + \frac{\gamma - 1}{2} M_\infty^2 \left(1 - \frac{V^2}{V_\infty^2} \right) \right]^{\gamma/(\gamma-1)} - 1 \right\}. \quad (35.3)$$

If Eqs. (35.2) and (35.3) are substituted into Eq. (1.6) (with $\tan \delta dx$ replaced by $d\bar{r}$), the relation for the drag coefficient is

$$C_{DP} = \frac{2}{\gamma M_\infty^2} \left\{ \int_0^1 \left[\frac{2 + (\gamma - 1)M_\infty^2}{2 + (\gamma - 1)M^2} \right]^{\gamma/(\gamma-1)} d\bar{r}^2 - 1 \right\}. \quad (35.4)$$

Expanding the expression in the square brackets into a series in $(M_\infty^2 - 1)$ and neglecting terms of the second or higher power, we get

$$C_{DP} = \frac{2}{\gamma M_\infty^2} \left\{ \left[1 + \frac{\gamma}{\gamma + 1} (M_\infty^2 - 1) \right] \int_0^1 \left[\frac{\gamma + 1}{2 + (\gamma - 1)M^2} \right]^{\gamma/(\gamma-1)} d\bar{r}^2 - 1 \right\}. \quad (35.5)$$

Assuming $M_\infty = 1$ in this expression, the equation that determines the drag at sonic speed is obtained:

$$(C_{DP})_{M_\infty=1} = \frac{2}{\gamma} \left\{ \int_0^1 \left[\frac{\gamma + 1}{2 + (\gamma - 1)M^2} \right]^{\gamma/(\gamma-1)} d\bar{r}^2 - 1 \right\}. \quad (35.6)$$

According to the stationarity principle, the local Mach number M is

invariant with respect to M_∞ (close to unity), and the integral in Eq. (35.6) can be substituted for that in Eq. (35.5). We thus obtain

$$C_{Dp} = \frac{\gamma M_\infty^2 + 1}{(\gamma + 1) M_\infty^2} (C_{Dp})_{M_\infty=1} + \frac{2(M_\infty^2 - 1)}{(\gamma + 1) M_\infty^2}. \quad (35.7)$$

The experimental curve for $(C_{Dp})_{M_\infty=1}$ is presented in Fig. 329. Using this curve and Eq. (35.7), values of C_{Dp} can be calculated for other transonic velocities. It is evident in Fig. 329 that the drag coefficient at $M_\infty = 1$ depends strongly on the bluntness of the cone; the value corresponding to a cone half-angle of $\delta_c = 90^\circ$ actually represents the drag of a flat face at sonic speed.

Equation (35.7) can be written in a different form:

$$C_{Dp} = \left[1 - \frac{2}{\gamma + 1} m + f_1(\gamma)m^2 \right] (C_{Dp})_{M_\infty=1} + \frac{4}{\gamma + 1} m - f_2(\gamma)m^2, \quad (35.8)$$

in which $m = M_\infty - 1$ and $f_1(\gamma)$ and $f_2(\gamma)$ are functions of the ratio of specific heats. For $\gamma = 1.4$, $f_1(\gamma) = 125/72$ and $f_2(\gamma) = 65/36$. The equations presented for C_{Dp} can be used to find the slope of the drag

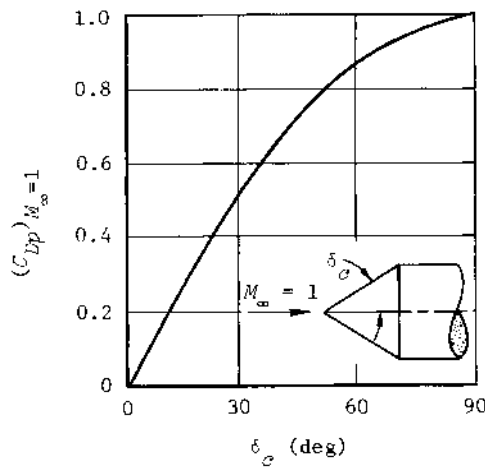


Fig. 329—Drag coefficients of cones at sonic velocity

curve at $M_\infty = 1$. Differentiating C_{Dp} with respect to M_∞ and substituting $M_\infty = 1$, we obtain

$$\left(\frac{\partial C_{Dp}}{\partial M_\infty}\right)_{M_\infty=1} = \frac{4}{\gamma + 1} \left[1 - \frac{1}{2} (C_{Dp})_{M_\infty=1} \right]. \quad (35.9)$$

It has been established experimentally that a rough estimate based on interpolation for $(C_{Dp})_{M_\infty=1}$ for a cone will give good results in Eq. (35.9) for determining the slope of the curve of C_{Dp} at $M_\infty = 1$. For example, for a cone with an angle $\delta_c = 20^\circ$, we find $C_{Dp} = 0.363$ at $M_\infty = 1$ from Fig. 327. The derivative from Eq. (35.9) is

$$\left(\frac{\partial C_{Dp}}{\partial M_\infty}\right)_{M_\infty=1} = \frac{4}{1.4 + 1} \left(1 - \frac{0.363}{2} \right) = 1.365,$$

which corresponds well to the correct value.

Experimental results are presented in Fig. 330 for the drag of a

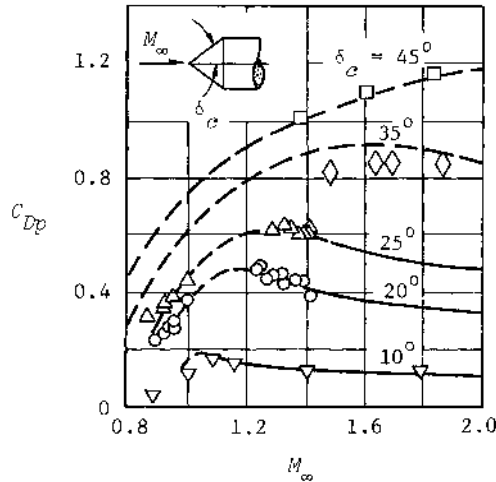


Fig. 330--Drag coefficients of cones
at transonic speeds

cone at transonic velocities. These data agree satisfactorily with the results of the calculation of the drag coefficient in the transonic regime and the slope of the curve at $M_\infty = 1$.

The Ogive Nose

Research shows that the principle of stationarity of the local Mach number can also be used for calculating the drag of ogive bodies at transonic speeds, so that Eqs. (35.7) and (35.8) can be used.⁽⁹⁾ The values of $(C_{Dp})_{M_\infty=1}$ in these equations can be determined from the graph in Fig. 331, which gives the drag at $M_\infty = 1$ for an ogive nose as a function

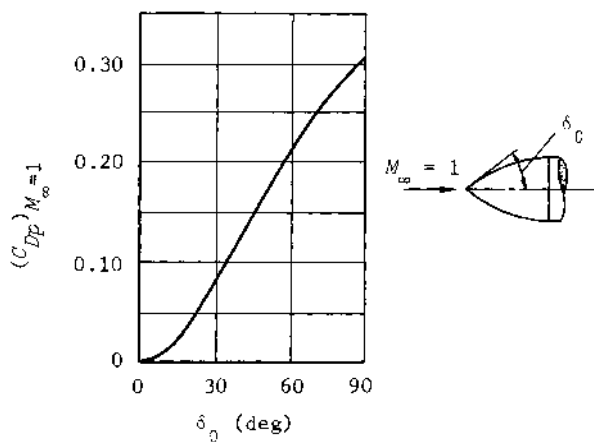


Fig. 331--Drag coefficients of ogive noses at sonic velocity

of the initial half-angle δ_0 . The point on the curve corresponding to $\delta_0 = 90^\circ$ is the pressure drag on a hemisphere.

From these values of $(C_{Dp})_{M_\infty=1}$, the slope of the drag curve at $M_\infty = 1$ can be calculated from Eq. (35.9), and the drag coefficient in the vicinity of this point from Eqs. (35.7) or (35.8). Comparison shows that the theoretical and experimental results agree satisfactorily. The general form of the drag curves for a series of ogive noses is shown in Fig. 332.

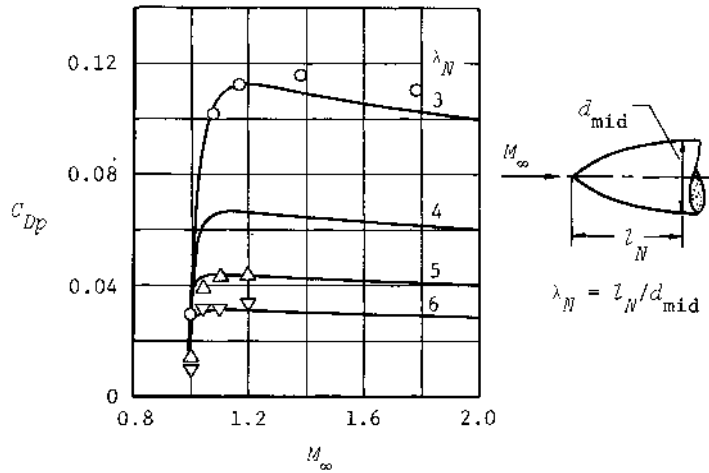


Fig. 332--Drag coefficients of ogive noses at transonic speeds

The Hemispherical Nose

The point on the curve of Fig. 331 corresponding to an angle of 90° determines the drag coefficient of a hemispherical nose at $M_\infty = 1$, as was indicated above. For a Mach number differing from but close to unity, i.e., corresponding to transonic speeds, the drag coefficient can be determined from the empirical equation⁽¹⁰⁾

$$C_{Dp} = 0.46 - \frac{1}{\pi} \operatorname{arc \tan} [1.61(1.20 - M_\infty)]. \quad (35.10)$$

This "arc tangent" law can also be used to calculate the pressure coefficient at the stagnation point of a sphere in a transonic flow:

$$C_{po} = 1.35 - \frac{1}{\pi} \operatorname{arc \tan} [1.96(1 - M_\infty)]. \quad (35.11)$$

It is evident from Fig. 333 that Eqs. (35.10) and (35.11) give satisfactory results not only in the transonic range of velocities but also for a wide range of Mach numbers from $M_\infty = 0$ to 7 or 8.

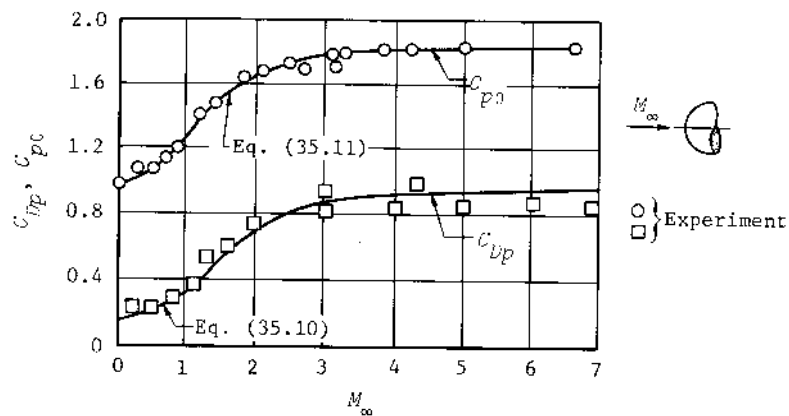


Fig. 333--Stagnation pressure coefficient
and pressure drag coefficient for a hemisphere

APPENDIXES

Appendix A

PARAMETERS OF AIR AT VARIOUS ALTITUDES
(Standard Atmosphere)

Altitude, H (km)	Pressure, P $\cdot 10^{-3}$ (dynes/cm ²)	Density, ρ (kg/m ³)	Speed of Sound, a (m/sec)	Average Particle Speed, Ē (m/sec)	Acceleration of Gravity, g (m/sec ²)	Kinematic Viscosity Coefficient, ν (m ² /sec)	Temperature, T (°K)	Thermal Conductivity Coefficient, λ (kcal/m sec °K)	Average Molecular Weight, \bar{w}_{avg}
Troposphere									
0	1013	1.225	340.3	458.9	9.807	$1.461 \cdot 10^{-3}$	288.2	$6.053 \cdot 10^{-6}$	28.97
2	$7950 \cdot 10^{-3}$	1.007	332.5	448.5	9.800	1.715	275.2	5.808	28.97
4	6166	$8.194 \cdot 10^{-3}$	324.6	437.8	9.794	2.028	262.2	5.559	28.97
6	4722	6.601	316.4	426.8	9.788	2.416	249.2	5.307	28.97
8	3565	5.258	308.1	415.5	9.782	2.905	236.2	5.052	28.97
10	2650	4.135	299.5	404.0	9.776	3.525	223.3	4.794	28.97
12	1940	3.119	295.1	398.0	9.770	4.558	216.7	4.662	28.97
Stratosphere									
14	1417	2.278	295.1	398.0	9.764	6.239	216.7	4.662	28.97
16	$1035 \cdot 10^{-3}$	1.665	295.1	398.0	9.758	$8.540 \cdot 10^{-5}$	216.7	4.662	28.97
18	$7565 \cdot 10^{-3}$	$1.216 \cdot 10^{-1}$	295.1	398.0	9.751	$1.169 \cdot 10^{-4}$	216.7	4.662	28.97
20	5529	$8.891 \cdot 10^{-2}$	295.1	398.0	9.745	1.599	216.7	4.662	28.97
22	4042	6.500	295.1	398.0	9.739	2.187	216.7	4.662	28.97
24	2955	4.752	295.1	398.0	9.733	2.992	216.7	4.662	28.97
Mesosphere									
28	1595	2.466	300.9	405.8	9.721	5.955	225.3	4.835	28.97
30	$1186 \cdot 10^{-2}$	1.786	304.8	411.1	9.715	$8.402 \cdot 10^{-4}$	231.2	4.953	28.97
32	$8880 \cdot 10^{-3}$	$1.304 \cdot 10^{-2}$	308.7	416.4	9.709	$1.175 \cdot 10^{-3}$	237.2	5.071	28.97
34	6701	$9.602 \cdot 10^{-3}$	312.6	421.6	9.703	1.628	243.1	5.188	28.97
36	5091	7.122	316.4	426.7	9.696	2.238	249.0	5.304	28.97
38	3894	5.321	320.2	431.7	9.690	3.053	255.0	5.420	28.97
40	2998	4.003	323.8	436.7	9.684	4.134	260.9	5.534	28.97
42	2322	3.031	327.5	441.6	9.678	5.558	266.8	5.648	28.97
44	1808	2.310	331.1	446.5	9.672	7.422	272.8	5.762	28.97
46	1416	1.770	334.6	451.3	9.666	$9.846 \cdot 10^{-3}$	278.7	5.874	28.97
48	$1115 \cdot 10^{-3}$	1.374	337.0	454.5	9.660	$1.283 \cdot 10^{-2}$	282.7	5.950	28.97
50	$8786 \cdot 10^{-4}$	$1.083 \cdot 10^{-3}$	337.0	454.5	9.654	1.628	282.7	5.950	28.97
52	6926	$8.536 \cdot 10^{-4}$	337.0	454.5	9.648	2.065	282.7	5.950	28.97
54	5459	6.787	335.6	452.6	9.642	2.580	280.2	5.903	28.97
56	4279	4.593	330.2	445.4	9.636	3.108	271.4	5.735	28.97
58	3327	4.416	324.8	438.0	9.630	3.766	262.5	5.565	28.97
60	$2566 \cdot 10^{-4}$	3.524	319.3	430.6	9.624	$4.592 \cdot 10^{-2}$	257.7	5.394	28.97
70	$6021 \cdot 10^{-5}$	$1.001 \cdot 10^{-4}$	290.2	391.4	9.594	$1.382 \cdot 10^{-1}$	209.6	4.519	28.97
80	$1008 \cdot 10^{-5}$	$2.120 \cdot 10^{-5}$	258.0	348.0	9.564	5.311	165.7	3.612	28.97

PARAMETERS OF AIR AT VARIOUS ALTITUDES--*continued*

Altitude, H (km)	Pressure, $P \cdot 10^{-3}$ (dynes/cm ²)	Density, ρ (kgm/m ³)	Speed of Sound, a (m/sec)	Average Particle Speed, \bar{c} (m/sec)	Acceleration of Gravity, g (m/sec ²)	Kinematic Viscosity Coefficient, ν (cm. ² /sec.)	Temperature, T (°K)	Thermal Conductivity Coefficient, λ (kcal/m sec °K)	Average Molecular Weight, \bar{u}_{avg}
Thermosphere									
90	$1353 \cdot 10^{-6}$	$2.846 \cdot 10^{-5}$	258.0	348.0	9.505	$3.957 \cdot 10^{-1}$	165.7	$3.612 \cdot 10^{-6}$	28.97
100	$2138 \cdot 10^{-7}$	$3.734 \cdot 10^{-7}$	--	381.8	9.505	--	199.0	--	28.90
120	$2044 \cdot 10^{-8}$	$1.480 \cdot 10^{-8}$	--	593.1	9.447	--	477.0	--	28.71
140	$7502 \cdot 10^{-9}$	$3.020 \cdot 10^{-9}$	--	795.3	9.389	--	849.9	--	28.45
160	$4018 \cdot 10^{-9}$	$1.123 \cdot 10^{-9}$	--	954.7	9.331	--	1207	--	28.04
180	$2305 \cdot 10^{-9}$	$6.015 \cdot 10^{-10}$	--	1030	9.274	--	1371	--	27.36
200	$1629 \cdot 10^{-9}$	$3.673 \cdot 10^{-10}$	--	1063	9.217	--	1404	--	26.32
300	$2565 \cdot 10^{-11}$	$4.757 \cdot 10^{-11}$	--	1172	9.942	--	1473	--	21.95
400	$5661 \cdot 10^{-11}$	$8.994 \cdot 10^{-12}$	--	1266	8.680	--	1480	--	19.56
500	$1586 \cdot 10^{-11}$	$2.212 \cdot 10^{-12}$	--	1351	8.428	--	1576	--	18.28
600	$5308 \cdot 10^{-12}$	$6.617 \cdot 10^{-13}$	--	1429	8.187	--	1691	--	17.52
700	$2037 \cdot 10^{-12}$	$2.302 \cdot 10^{-13}$	--	1501	7.957	--	1812	--	17.03

Appendix B

CONVERSION TABLE TO INTERNATIONAL UNIT SYSTEM (SI)

Quantity	Dimensional Units in Book	Units in SI System
Force	1 kgf	9.80665 N (newton)
	1 dyne	10^{-5} N
Pressure (stress)	1 kgf/cm ²	98066.5 N/m ²
	1 mm mercury	0.980665 bar 133.322 N/m ² $1.33322 \cdot 10^{-3}$ bar
Dynamic viscosity	1 kgf sec/m ²	9.80665 N sec/m ²
	1 poise	9.80665 kgm/m sec 0.1 N sec/m ²
Kinematic viscosity	m ² /sec	m ² /sec
Density	1 kgf sec ² /m ⁴ (mass)	9.80665 kgm/m ³
	1 kgf/m ³ (weight)	9.80665 N/m ³
Work, energy, heat	1 kgf m	9.80665 J (joule)
	1 hp hr [†]	$2.65 \cdot 10^6$ J
	1 kW hr	$3.6 \cdot 10^6$ J
	1 eV (electron-volt)	$1.60207 \cdot 10^{-16}$ J
	1 cal	4.1868 J
	1 erg	10^{-7} J
Power	1 hp [†]	735.499 W
	1 cal/sec	4.1868 W
	1 erg/sec	10^{-7} W

[†]Editor's note: This is metric horsepower, equal to 0.986 hp in British units.

REFERENCES

Chapter I

1. Predvoditelev, A. S., et al., *Tables of Thermodynamic Functions of Air for the Temperature Range 6000-12,000°K and Pressure Range 0.001-1000 Atm*, Infosearch Limited, London, 1958.
2. Ehricke, K. A., "Aero-Thermodynamics of Descending Orbital Vehicles," *Astronautica Acta*, Vol. 2, No. 1, 1956, pp. 1-19.
3. Predvoditelev, A. S., et al., *Tables of Thermodynamic Functions of Air for Temperatures of 12,000 to 20,000°K and Pressures of 0.001 to 1000 Atm*, Associated Technical Services, Inc., Glen Ridge, New Jersey, 1962.
4. Predvoditelev, A. S. (ed.), *Physical Gas Dynamics*, Pergamon Press, New York, 1961.
5. Kibardin, Iu. A., et al., *Atlas of Gasdynamic Functions for High Velocity and High Temperature Air Flow* (in Russian), Gosenergoizdat, Moscow, 1961.
6. Lighthill, M. J., "Dynamics of a Dissociating Gas: Part 1: Equilibrium Flow," *J. Fluid Mech.*, Vol. 2, Part 1, January 1957, pp. 1-32.
7. Gouillard, R., "On Catalytic Recombination Rates in Hypersonic Stagnation Heat Transfer," *Jet Propulsion*, Vol. 28, No. 11, November 1958, pp. 737-745.
8. Liepmann, H. W., and A. Roshko, *Elements of Gasdynamics*, John Wiley & Sons, Inc., New York, 1957.
9. Hilsenrath, J., et al., *Tables of Thermal Properties of Gases*, National Bureau of Standards, Circular 564, Washington, D. C., 1955.
10. Dorrance, W. H., "On the Approach to Chemical and Vibrational Equilibrium behind a Strong Normal Shock Wave," *J. Aero. Sci.*, Vol. 28, No. 1, January 1961, pp. 43-50.

11. Schlichting, H., *Boundary Layer Theory*, Pergamon Press, New York, 1955.
12. Luther, M. L., "Comments on 'Turbulent Boundary-Layer Characteristics...,'" *J. Aero. Sci.*, Vol. 19, No. 5, May 1952, p. 357.
13. Saelman, B., "An Additional Note on Equilibrium Skin Temperatures," *J. Aero. Sci.*, Vol. 27, No. 4, April 1960, p. 320.

Chapter II

1. Kopal, Z., *Tables of Supersonic Flow around Cones*, MIT Dept. of Electrical Engineering, Center of Analysis, Technical Report No. 1, Cambridge, Mass., 1947.
2. Neice, S. E., and D. M. Ehret, "Similarity Laws for Slender Bodies of Revolution in Hypersonic Flows," *J. Aero. Sci.*, Vol. 18, No. 8, August 1951, pp. 527-530.
3. Kuznetsov, S. I., *Graphs and Tables for the Flow of Dissociating Air over Wedges, Cones, and Convex Surfaces*, Moscow, Oborongiz, 1962.
4. Kopal, Z., *Tables of Supersonic Flow around Yawing Cones*, MIT Dept. of Electrical Engineering, Center of Analysis, Technical Report No. 3, Cambridge, Mass., 1947.
5. Kopal, Z., *Tables of Supersonic Flow around Cones of Large Yaw*, MIT Dept. of Electrical Engineering, Center of Analysis, Technical Report No. 5, Cambridge, Mass., 1949.
6. Young, G.B.W., and C. P. Siska, "Supersonic Flow around Cones at Large Yaw," *J. Aero. Sci.*, Vol. 19, No. 2, February 1952, pp. 111-119.
7. Gonor, A. L., "Location of Frontal Wave in Asymmetrical Flow of Gas at High Supersonic Speed over a Pointed Body," *ARS J.*, (Russian Supplement), Vol. 30, No. 9, September 1960, pp. 841-842.

Chapter III

1. Frankl, F. I., "Supersonic Flow with Axial Symmetry" (in Russian), *Izv. artil. akad.*, Vol. 1, No. 6, Leningrad, 1934.
2. Ferri, Antonio, *Elements of Aerodynamics of Supersonic Flows*, The Macmillan Co., New York, 1949.

3. Miles, E.R.C., *Semi-empirical Formulas for Ogives*, Applied Physics Laboratory, CM-505, Johns Hopkins University, Baltimore, Md., 1948.
4. Vallander, S. V., unpublished doctoral thesis, Leningrad University, 1949, as cited in G. G. Chernyi, *Introduction to Hypersonic Flow*, Academic Press, New York, 1961.
5. Neice, S. E., and D. M. Ehret, "Similarity Laws for Slender Bodies of Revolution in Hypersonic Flows," *J. Aero. Sci.*, Vol. 18, No. 8, August 1951, pp. 527-530.
6. Resler, E. L., Jr., "Characteristics and Sound Speed in Nonisentropic Gas Flows with Nonequilibrium Thermodynamic States," *J. Aero. Sci.*, Vol. 24, No. 11, November 1957, pp. 785-790.
7. Kuptsov, V. M., "Method of Characteristics for Equilibrium Axisymmetric Flow of a Real Gas" (in Russian), *AN SSSR. Izv. Otd. tekhn. nauk. mash. i mash.*, No. 2, 1960, pp. 138-140.
8. Eggers, A. J., Jr., R. C. Savin, and C. A. Syvertson, "The Generalized Shock-expansion Method and Its Application to Bodies Traveling at High Supersonic Air Speeds," *J. Aero. Sci.*, Vol. 22, No. 4, April 1955, pp. 231-238.

Chapter IV

1. Van Dyke, M. D., "First- and Second-order Theory of Supersonic Flow past Bodies of Revolution," *J. Aero. Sci.*, Vol. 18, No. 3, March 1951, pp. 161-178.
2. Broderick, J. B., "Supersonic Flow round Pointed Bodies of Revolution," *Quart. J. Mech. Appl. Math.*, Vol. 2, Part 1, March 1949, pp. 98-120.
3. Frankl, F. I., and E. A. Karpovich, *Gas Dynamics of Thin Bodies*, Interscience Publishers Inc., New York, 1953.
4. Hoerner, S. F., *Fluid-dynamic Drag*, published by the author, Midland Park, New Jersey, 1958.

Chapter V

1. Syvertson, C. A., and D. H. Dennis, *A Second-order Shock-expansion Method Applicable to Bodies of Revolution Near Zero Lift*, National Advisory Committee for Aeronautics, Report 1328, Washington, D.C., 1957.

2. Mello, J. F., "Investigation of Normal Force Distributions and Wake Vortex Characteristics of Bodies of Revolution at Supersonic Speeds," *J. Aero. Sci.*, Vol. 26, No. 3, March 1959, pp. 155-168.
3. Van Dyke, M. D., "First- and Second-order Theory of Supersonic Flow past Bodies of Revolution," *J. Aero. Sci.*, Vol. 18, No. 3, March 1951, pp. 161-178.
4. Dorrance, W. H., "Nonsteady Supersonic Flow about Pointed Bodies of Revolution," *J. Aero. Sci.*, Vol. 18, No. 8, August 1951, pp. 505-511.

Chapter VI

1. Lees, L., "Note on the Hypersonic Similarity Law for an Unyawed Cone," *J. Aero. Sci.*, Vol. 18, No. 10, October 1951, pp. 700-702.
2. Van Dyke, M. D., "Applications of Hypersonic Small-disturbance Theory," *J. Aero. Sci.*, Vol. 21, No. 3, March 1954, pp. 179-186.
3. Van Dyke, M. D., *A Study of Hypersonic Small-disturbance Theory*, National Advisory Committee for Aeronautics, Report 1194, Washington, D. C., 1954.
4. Grimminger, G., E. P. Williams, and G.B.W. Young, "Lift on Inclined Bodies of Revolution in Hypersonic Flow," *J. Aero. Sci.*, Vol. 17, No. 11, November 1950, pp. 675-690.
5. Large, E., "Nose Shape for Minimum Drag in Hypersonic Flow," *J. Aero. Sci.*, Vol. 29, No. 1, January 1962, pp. 98-99.

Chapter VII

1. Dorodnitsyn, A. A., "The Method of Integral Relations for the Numerical Solution of Partial Differential Equations" (in Russian), in *Trudy instituta tochnoi mekhaniki i vychislitelnoi tekhniki*, AN SSSR, 1958.
2. Belotserkovskii, O. M., "On the Calculation of Flow past Axisymmetric Bodies with Detached Shock Waves Using an Electronic Computing Machine," *J. Appl. Math. Mech.*, Vol. 24, No. 3, 1960, pp. 745-755.
3. Li, T.-Y., and R. E. Geiger, "Stagnation Point of a Blunt Body in

- Hypersonic Flow," *J. Aero. Sci.*, Vol. 24, No. 1, January 1957, pp. 25-32.
4. Oliver, R. E., "An Experimental Investigation of Flow about Simple Blunt Bodies at a Nominal Mach Number of 5.8," *J. Aero. Sci.*, Vol. 23, No. 2, February 1956, pp. 177-179.
 5. Serbin, H., "Supersonic Flow Around Blunt Bodies," *J. Aero. Sci.*, Vol. 25, No. 1, January 1958, pp. 58-59.
 6. Inouye, M., *Blunt Body Solutions for Spheres and Ellipsoids in Equilibrium Gas Mixtures*, National Aeronautics and Space Administration, Technical Note TN D-2780, Washington, D. C., May 1965.
 7. Hayes, W. D., and R. F. Probstein, *Hypersonic Flow Theory*, Academic Press, New York, 1959.
 8. Seiff, A., *Recent Information on Hypersonic Flow Fields in Gas Dynamics in Space Exploration*, National Aeronautics and Space Administration, SP-24, Washington, D. C., 1962.
 9. Holt, M., "Direct Calculation of Pressure Distribution on Blunt Hypersonic Nose Shapes with Sharp Corners," *J. Aero. Sci.*, Vol. 28, No. 11, November 1961, pp. 872-876.
 10. Chernyi, G. G., *Introduction to Hypersonic Flow*, R. F. Probstein (trans. and ed.), Academic Press, New York, 1961.
 11. Lees, L., and T. Kubota, "Inviscid Hypersonic Flow over Blunt-nosed Slender Bodies," *J. Aero. Sci.*, Vol. 24, No. 3, March 1957, pp. 195-202.
 12. Swigart, R. J., "Third-order Blast Wave Theory and Its Application to Hypersonic Flow past Blunt-nosed Cylinders," *J. Fluid Mech.*, Vol. 9, Part 4, December 1960, pp. 613-620.
 13. Bertram, M. H., "Tip-bluntness Effects on Cone Pressures at $M = 6.85$," *J. Aero. Sci.*, Vol. 23, No. 9, September 1956, pp. 898-900.
 14. O'Bryant, W. T., and R. M. Machell, "An Experimental Investigation of Flow over Blunt Nosed Cones at a Mach Number of 5.8," *J. Aero. Sci.*, Vol. 23, No. 11, November 1956, pp. 1054-1055.
 15. Chushkin, P. I., "Supersonic Flows around Blunted Bodies of Simple Shape," *J. Appl. Math. Mech.*, Vol. 24, No. 5, 1960, pp. 1397-1403.
 16. Cole, J. D., "Newtonian Flow Theory for Slender Bodies," *J. Aero. Sci.*, Vol. 24, No. 6, June 1957, pp. 448-455.
 17. Bloom, M. H., and M. H. Steiger, "Inviscid Flow with Nonequilibrium Molecular Dissociation for Pressure Distributions Encountered in Hypersonic Flight," *J. Aero. Sci.*, Vol. 27, No. 11, November 1960, pp. 821-835.

Chapter VIII

1. Moeckel, W. E., *Some Effects of Bluntness on Boundary-Layer Transition and Heat Transfer at Supersonic Speeds*, National Advisory Committee for Aeronautics, Report 1312, Washington, D.C., 1957.
2. Van Driest, E. R., and J. C. Boison, "Experiments on Boundary Layer Transition at Supersonic Speeds," *J. Aero. Sci.*, Vol. 24, No. 12, December 1957, pp. 885-899.
3. Lees, L., "Laminar Heat Transfer Over Blunt-nosed Bodies at Hypersonic Flight Speeds," *Jet Propulsion*, Vol. 26, No. 4, April 1956, pp. 259-269.
4. Fay, J. A., and F. R. Riddell, "Theory of Stagnation Point Heat Transfer in Dissociated Air," *J. Aero. Sci.*, Vol. 25, No. 2, February 1958, pp. 73-85.
5. Kemp, N. H., and F. R. Riddell, "Heat Transfer to Satellite Vehicles Re-entering the Atmosphere," *Jet Propulsion*, Vol. 27, No. 2, Part 1, February 1957, pp. 132-137.
6. Goulard, R., "On Catalytic Recombination Rates in Hypersonic Stagnation Heat Transfer," *Jet Propulsion*, Vol. 28, No. 11, November 1958, pp. 737-745.
7. Kemp, N. H., P. H. Rose, and R. W. Detra, "Laminar Heat Transfer around Blunt Bodies in Dissociated Air," *J. Aero. Sci.*, Vol. 26, No. 7, July 1959, pp. 421-430.
8. Detra, R. W., and H. Hidalgo, "Generalized Heat Transfer Formulas and Graphs for Nose Cone Re-entry into the Atmosphere," *ARS J.*, Vol. 31, No. 3, March 1961, pp. 318-321.
9. Rose, P. H., R. F. Probstein, and M. C. Adams, "Turbulent Heat Transfer Through a Highly Cooled, Partially Dissociated Boundary Layer," *J. Aero. Sci.*, Vol. 25, No. 12, December 1958, pp. 751-760.
10. Cresci, R. J., D. A. Mackenzie, and P. A. Libby, "An Investigation of Laminar, Transitional, and Turbulent Heat Transfer on Blunt-nosed Bodies in Hypersonic Flow," *J. Aero. Sci.*, Vol. 27, No. 6, June 1960, pp. 401-414.
11. Probstein, R. F., M. C. Adams, and P. H. Rose, "On Turbulent Heat Transfer Through a Highly Cooled Partially Dissociated Boundary Layer," *Jet Propulsion*, Vol. 28, No. 1, January 1958, pp. 56-58.

Chapter IX

1. Adams, M. C., "Recent Advances in Ablation," *ARS J.*, Vol. 29, No. 9, September 1959, pp. 625-632.
2. Hartnett, J. P., and E.R.G. Eckert, "Mass Transfer Cooling with Combustion in a Laminar Boundary Layer," *1958 Heat Transfer and Fluid Mechanics Institute*, June 1958, pp. 54-68.
3. Bethe, H. A., and M. C. Adams, "A Theory for the Ablation of Glassy Materials," *J. Aero. Sci.*, Vol. 26, No. 6, June 1959, pp. 321-328.

Chapter X

1. Warren, G.H.E., and A. D. Young, *Some Proposals Regarding the Definitions of Terms Relating to Various Flow Regimes of a Gas*, Ministry of Supply, Aeronautical Research Council Current Papers, C. P. No. 368, London, 1958.
2. Patterson, G. N., *Molecular Flow of Gases*, John Wiley & Sons, Inc., New York, 1956.

Chapter XI

1. von Kármán, T., "The Similarity Law of Transonic Flow," *J. of Math. and Physics*, Vol. 26, No. 3, October 1947, pp. 182-190.
2. Spreiter, J. R., and A. Y. Alksne, *Slender-Body Theory Based on Approximate Solution of the Transonic Flow Equation*, NASA Technical Report R-2, 1959.
3. Oswatitsch, K., and S. B. Berndt, *Aerodynamic Similarity at Axisymmetric Transonic Flow Around Slender Bodies*, KTH Stockholm Aeronautics Div., Technical Note 15, 1950.
4. Danforth, E.C.B., and J. F. Johnston, *Pressure Distribution Over a Sharp-Nose Body of Revolution at Transonic Speeds by the NACA Wing-Flow Method*, NACA RM L7K12, 1948.
5. Hoerner, S. F., *Aerodynamic Drag*, published by the author, 1951. (Note: Hoerner's revised and expanded edition, *Fluid-Dynamic Drag*, published in 1958, does not contain some of the figures used by Krasnov.)

6. Solomon, G. E., *Transonic Flow Past Cone Cylinders*, NACA Technical Note 3213, 1954.
7. Cole, J. D., G. E. Solomon, and W. W. Willmarth, "Transonic Flow Past Simple Bodies," *J. Aero. Sci.*, Vol. 20, No. 9, September 1953, pp. 627-634.
8. Johnston, G. W., "An Investigation of the Flow About Cones and Wedges at and Beyond the Critical Angle," *J. Aero. Sci.*, Vol. 20, No. 6, June 1953, pp. 378-382.
9. Morris, D. N., "A Summary of the Supersonic Pressure Drag of Bodies of Revolution," *J. Aero. Sci.*, Vol. 28, No. 7, July 1961, pp. 563-572.
10. Li, T., "Arc-Tangent Fits for Pressure and Pressure-Drag Coefficients of Axisymmetric Blunt Bodies at All Speeds," *J. Aero. Sci.*, Vol. 27, No. 4, April 1960, pp. 309-311.

BIBLIOGRAPHY FOR THE SECOND EDITION

1. Chernyi, G. G., *Techeniia gaza s bol'shoi sverkhvukovoi skorost'iu* [Gas Flows at High Supersonic Velocities], Fizmatgiz, 1959.
2. Arzhanikov, N. S., and V. N. Mal'tsev, *Aerodinamika* [Aerodynamics], Oborongiz, 1956.
3. Landau, L. D., and E. M. Lifshits, *Mekhanika sploshnykh sred* [Mechanics of Continuous Media], Gostekhizdat, 1954.
4. Ferri, A., *Aerodinamika sverkhvukovykh techenii* [Aerodynamics of Supersonic Flows], Gostekhizdat, 1953.
5. Zel'dovich, Ia. B., and Iu. P. Raizer, *Fizika udarnykh voln i vysokotemperaturnykh gidrodinamicheskikh iavlenii* [The Physics of Shock Waves and High-temperature Hydrodynamic Phenomena], Fizmatgiz, 1963.
6. Krasnov, N. F., *Aerodinamika* [Aerodynamics], Oborongiz, 1958.
7. Loitsianskii, L. G., *Mekhanika zhidkosti i gaza* [The Mechanics of Liquids and Gases], Gostekhizdat, 1950.
8. Kochin, N. E., I. A. Kibel', and N. V. Roze, *Teoreticheskaiia gidromekhanika* [Theoretical Hydromechanics], Parts 1 and 2, Gostekhizdat, 1948.
9. Vallander, S. V. (ed.), *Aerodinamika razreshennykh gazov; sb. statei* [Aerodynamics of Rarefied Gases; a collection of articles], Izd. Leningradskogo universiteta, 1963.
10. Rosliakov, G. S., and L. A. Chudov (eds.), *Chislennye metody v gazovoi dinamike; sb. statei* [Numerical Methods in Gas Dynamics; a collection of articles], Izd. Moskovskogo universiteta, 1963.
11. *Gazodinamika razreshennykh gazov; sb. statei* [Rarefied Gas Dynamics; a collection of articles], Inogiz, 1963.
12. Kuznetsov, S. I., *Diagrammy i tablitsy techeniiia dissotsiruiushchego vozdukhha okolo kлина, konusa i vypukloj poverkhnosti* [Diagrams and Tables of the Flow of Dissociating Air around a Wedge, a Cone, and a Convex Surface], Oborongiz, 1962.
13. Nielsen, J., *Aerodinamika upravliaemykh snariadov* [Missile Aerodynamics], Oborongiz, 1962.
14. Kibardin, Iu. A., S. I. Kuznetsov, A. N. Liubimov, and B. Ia. Shumiatskii, *Atlas gazodinamicheskikh funktsii pri bol'shikh skorostakh i vysokikh temperaturakh vozduzhnogo potoka* [Atlas of Gas Dynamic Functions for High-velocity and High-temperature Air Flow], Gosenergoizdat, 1961.

15. *Problemy vysokikh temperatur v aviatsionnykh konstruktsiakh; sb. statei* [High-temperature Problems in Airplane Construction; a collection of articles], Inogiz, 1961.
16. Drakin, I. I., *Aerodinamicheskii i luchistyi nagrev v polete* [Aero-dynamic and Radiative Heating in Flight], Oborongiz, 1961.
17. Predvoditelev, A. S., E. V. Stupochenko, V. P. Ionov, A. S. Pleshanov, I. B. Rozdestvenskii, and E. V. Samuilov, *Termodynamicheskie funktsii vozdukh dlia temperatur ot 1000 do 12000°K i davlenii ot 0,001 do 1000 at (grafiki funktsii)* [The Thermodynamic Functions of Air for Temperatures from 1000 to 12,000°K and Pressures from 0.001 to 1000 Atmospheres, (graphs of functions)], Izd. AN SSSR, 1960.
18. Liepmann, H. W., and A. Roshko, *Elementy gazovoи dinamiki*, [Elements of Gas Dynamics], Inogiz, 1960.
19. Patterson, G. N., *Molekularmoe techenie gazov*, [Molecular Flow of Cases], Fizmatgiz, 1960.
20. Guderley, K. G., *Teoriia okolosvukovykh techenii* [The Theory of Transonic Flow], 1960.
21. Koshkin, V. K. (ed.), *Osnovy teploperedachi v aviatsionnoi tekhnike* [The Bases of Heat Transfer in Aviation Technology], Oborongiz, 1960.
22. *Fizicheskaiia gazodynamika; sb. statei* [Physical Gas Dynamics; a collection of articles], Izd. AN SSSR, 1959.
23. *Problemy dvizheniya golomoi chasti raket dal'nego deistviia* [Problems of the Motion of the Nose Cone of Long Range Rockets], Inogiz, 1959.
24. *Nauchnye problemy iskusstvennykh sputnikov zemli* [Scientific Problems of Artificial Earth Satellites], Inogiz, 1959.
25. *Aerodinamika chastei samoleta pri bol'sikh skorostях* [Aerodynamic Components of Aircraft at High Speeds], Inogiz, 1959.
26. Dorodnitsyn, A. A., *Metod integral'nykh sootnoshenii dlia chislennogo resheniya differentsial'nykh uravnenii v chastnykh proizvodnykh* [The Method of Integral Relations for the Numerical Solution of Partial Differential Equations], Trudy Instituta tochnoi mekhaniki i vychislitel'noi tekhniki [Transactions of the Institute of Precision Mechanics and Computer Technology], AN SSSR, 1958.
27. Ostoslavskii, I. V., *Aerodinamika samoleta* [Aircraft Aerodynamics], Oborongiz, 1957.

28. Predvoditelev, A. S., E. V. Stupochenko, E. V. Samuilov, I. P. Stakhanov, A. S. Pleshanov, and I. B. Rozhdestvenskii, *Tablitsy termodinamicheskikh funktsii vozdukh (dlya temperatur ot 6000 do 12000°K i davlenii ot 0,001 do 1000 atmosfer)* [Tables of the Thermodynamic Functions of Air (for Temperatures from 6000 to 12,000°K and Pressures from 0.001 to 1000 Atmospheres)], Izd. AN SSSR, 1957.
29. Sedov, L. I., *Metody podobiia i razmernosti v mekhanike* [Methods of Similarity and Dimensionality in Mechanics], Gostekhizdat, 1957.
30. Kalikhman, L. E., *Turbulentnyi pogranichnyi sloi na krivolineinoi poverkhnosti, obtekaemoi gazom* [The Turbulent Boundary Layer on a Streamlined Curved Surface], Oborongiz, 1956.
31. Staniukovich, K. P., *Neustanovivushiesia dvizheniya sploshnoi sredy* [Unsteady Motion of a Continuous Medium], Gostekhizdat, 1955.
32. Sovremennoe sostoyanie aerodinamiki bol'sikh skorosteii [The Present State of High-Speed Aerodynamics], 2 vols., Inogiz, 1955-1956.
33. Hilton, W. F., *Aerodinamika bol'sikh skorosteii* [High-Speed Aerodynamics], Inogiz, 1955.
34. Sauer, R., *Techeniia sschimaemoi shidkosti* [Flow of Compressible Fluids], Inogiz, 1954.
35. Vukalovich, M. P., V. A. Kirillin, S. A. Remizov, V. S. Siletskii, and V. N. Timofeev, *Termodinamicheskie svoistva gazov* [The Thermodynamic Properties of Gases], Gostekhizdat, 1953.
36. Hoerner, Sigard F., *Aerodynamic Drag*, Dayton, Ohio, 1951.
37. *Gazovaia dinamika; sb. statei* [Gas Dynamics; a collection of articles], Inogiz, 1950.
38. Courant, R., and K. Friedrichs, *Sverkhzvukovoe techenie i udarnye volny* [Supersonic Flow and Shock Waves], Inogiz, 1950.
39. Frankl', F. I., and E. A. Karpovich, *Gazodinamika tonkikh tel* [The Gas Dynamics of Thin Bodies], Gostekhizdat, 1948.
40. Kopal, Z., *Tables of Supersonic Flow Around Cones of Large Yaw*, Technical Report 5, Massachusetts Institute of Technology, 1949.
41. Kopal, Z., *Tables of Supersonic Flow Around Yawing Cones*, Technical Report 3, Massachusetts Institute of Technology, 1947.
42. Kopal, Z., *Tables of Supersonic Flow Around Cones*, Technical Report 1, Massachusetts Institute of Technology, 1947.

43. *Izvestiia AN SSSR, Mekhanika i mashinostroenie* [Bulletin of the Academy of Sciences of the USSR, Mechanics and Mechanical Engineering], No. 4, 1959; Nos. 2, 3, 1960; No. 11, 1961.
44. *Prikladnaia matematika i mekhanika AN SSSR* [Journal of Applied Mathematics and Mechanics, Academy of Sciences of the USSR], Vol. 24, Nos. 3, 5, 1960; No. 6, 1961.
45. *Journal of the Aeronautical Sciences* [Journal of the Aerospace Sciences], No. 7, 1949; Nos. 11, 12, 1950; Nos. 2, 3, 8, 10, 1951; Nos. 2, 5, 10, 1952; No. 9, 1953; No. 3, 1954; Nos. 1, 2, 3, 4, 6, 1955; No. 2, 1956; Nos. 1, 3, 11, 1957; Nos. 1, 2, 8, 11, 12, 1958; Nos. 2, 3, 5, 6, 8, 9, 10, 1959; Nos. 2, 4, 5, 6, 10, 11, 1960; Nos. 1, 4, 5, 7, 10, 11, 12, 1961; Nos. 1, 2, 7, 11, 12, 1961; Nos. 1, 2, 4, 12, 1962.
46. *Jet Propulsion* [ARS Journal], No. 11, 1957; Nos. 11, 12, 1958; Nos. 2, 4, 6, 1960; Nos. 2, 3, 5, 7, 8, 11, 1961.
47. National Advisory Committee for Aeronautics (NACA), [TR] No. 835, 1946; No. 1194, 1947; [TN] Nos. 2726, 2744, 2579, 2811, 1952.
48. *Journal of Fluid Mechanics*, No. 1, 1957; No. 4, 1958.

INDEX

- Ablation, charring ablators, 751
definition, 753
effective heat of, 756-759
fusion time, 759-761
heat transfer, 760
mass loss, 763
rate of, 764-767
transpiration coefficient, 755
two-phase boundary layer, 753-754
vapor pressure, 770-771
Ablative materials, physical properties, 752, 774
Adiabatic exponent, definition, 30
Affine-similar bodies, 23
Angle of attack, definition, 4
Arbitrary body, Newtonian flow, axial force coefficient, 505-511
center-of-pressure coefficient, 531-532
normal force coefficient, 516, 519
pitching moment coefficient, 527
pressure distribution, hypersonic flow, 487-495
linearized flow, 345-359, 372, 407-414
Newtonian flow, 500-504, 640-641
supersonic flow, 263-268, 322-328
Axial force, definition, 4
Axial force coefficient, 6-9
Newtonian flow, 498-515
unsteady flow, 450
see also Pressure drag coefficient
- Base drag, 387-397
Base drag coefficient, definition, 7
Base pressure coefficient, 334, 388-397
definition, 7
free molecule flow, 803
Beveled flat nose, geometry of, 28-29
- laminar heat transfer, 718-719
pressure distribution, 580-581
pressure drag coefficient, 582
Blast wave theory, 586-600
piston analogy, 586-588, 597-600
Blunt cone, center-of-pressure coefficient, 624-626
laminar heat transfer, 720-724, 738-741
local Reynolds number, 670-671
normal force coefficient, 544
piston analogy, 597-611
pitching moment coefficient, 544
pressure distribution, 599-609
universal curve, 544, 606, 623
pressure drag coefficient, 602
609-611
shock wave shape, 599-604
similarity law, 603-606
surface Mach number, 666
Blunt curved bodies, piston analogy, 627-631
Blunt cylinder, piston analogy, 590-597
pressure distribution, 596
shock wave shape, 596
Blunt nose, at angle of attack, 621-626
degree of dissociation, 644-646, 655
equivalent radius, 579-580, 585
frozen flow, 646, 658
geometry of, 24
inviscid flow, 549-554
heat transfer, laminar, 683-727
turbulent, 727-737
method of integral relations, 550-554
nonequilibrium flow, 642-660
piston analogy, 586-588, 597-600
shock wave curvature, 543
stagnation point flow, 554-565
velocity gradient at stagnation point, 543
viscosity effects on external flow, 742-749

- Boattail, center-of-pressure coefficient, 439
- pressure distribution, hypersonic flow, 496
- linearized flow, 372
- pressure drag coefficient, hypersonic flow, 496
- linearized flow, 363-375
- Body coordinates, definition, 4.
- Boundary layer, displacement thickness, 8, 298-302, 678-679, 743-747
- effect of compressibility, 143-144
- effects on inviscid flow, 297-302
- effective enthalpy, 147, 150, 725, 736
- effective temperature, 145
- frozen flow, 701
- incompressible, 140
- laminar, blunt cone, 661
- equilibrium dissociation, 683-687
- heat transfer, 683-727
- nonequilibrium, 662
- momentum thickness, 81, 730-732
- quasi-equilibrium 707-708
- recovery temperature, 151
- thickness, 141
- laminar, 145
- turbulent, 146
- turbulent, heat transfer, 727-737
- velocity profile, 140
- Boundary layer transition, 670-676
- effect of blunting, 672
- effect of pressure gradient, 675
- effect of surface temperature, 673-674, 732-734
- Catalytic coefficient, definition, 703
- Catalytic parameter, definition, 705
- Catalytic recombination, 59-62, 700-710
- Center-of-pressure coefficient, arbitrary body, Newtonian flow, 531-532
- blunt cone, 624-626
- boattail, 439
- cone, Newtonian flow, 533
- supersonic flow, 232
- cone-cylinder, 403, 436, 438
- conical flare, 435
- definition, 14-15
- hypersonic flow, 534-535
- linearized flow, 430-439
- Newtonian flow, 531-533
- ogive-cylinder, 403
- ogive nose, linearized flow, 431
- Newtonian flow, 532
- parabolic nose, linearized flow, 431
- Newtonian flow, 532
- parabolic nose with cylinder, 438
- transonic flow, 851-853
- viscous crossflow, 439
- Cone, at angle of attack, 207-236
- axial force coefficient, Newtonian flow, 509
- supersonic flow, 230-231
- blunt, *see* Blunt cone
- center-of-pressure coefficient, Newtonian flow, 533
- supersonic flow, 232
- drag coefficient, 232
- in free molecule flow, 803-805
- dynamic stability derivatives, 458-459
- enthalpy on surface, 162
- flow around, hypersonic speed, 463-470
- piston analogy, 631-634
- heat transfer, 198-204
- lift coefficient, 232
- normal force coefficient, supersonic flow, 212-213, 230-231
- linearized flow, 424
- Newtonian flow, 518-521
- pitching moment coefficient, linearized flow, 426-427
- Newtonian flow, 530
- supersonic flow, 232
- pressure coefficient, hypersonic flow, 162, 466-467
- linearized flow, 361
- Newtonian flow, 498-500

- piston analogy, 633
supersonic flow, 182-184
transonic flow, 837-838
- pressure distribution, transonic, 858
- pressure drag coefficient, hypersonic flow, 466-467
linearized flow, 359-361
supersonic flow, 230-231, 238
transonic flow, 838-839, 858-865
- shear stress, 196
- shock wave angle, 179
piston analogy, 633
- similarity law, 180, 184
- skin friction, 194-198, 200-202
- stagnation pressure ratio, 181
- transonic flow, 853-858
- velocity on surface, 162, 178
- Cone-cylinder, center-of-pressure coefficient, 403, 436-438
- normal force slope, 403
- Conical boattail, pressure drag coefficient, 365
- Conical flare, center-of-pressure coefficient, 435
- pressure drag coefficient, 366-367
- Conical flow, angle of attack, 207-236
apple curves, 171, 176
critical cone angle, 171, 177
dissociation and ionization, 186-192
equations, 164-170
- nonequilibrium effects, 193-194
- tables of, 171-175
- variable specific heats, 185-186
- Continuity equation, 72-78
cylindrical coordinates, 73
curvilinear coordinates, 74
normal coordinates, 73
spherical coordinates, 73
- Critical cone angle, 171, 177
- Cylinder, drag coefficient, 404, 422
- Cylindrical afterbody, drag coefficient, free molecule flow, 806
- laminar heat transfer, 724-725
- normal force coefficient, 404, 418, 421-423
- Damping moment, 16-18
- Damping moment coefficient, 16, 453
- Diffusion in boundary layer, 57-62
catalytic recombination, 59-62
diffusional heat transfer, 58
diffusion time, 60
frozen flow, 59-61
- Diffusion equation, 78
- Dissociating diatomic gas, relations for, 41-48
- Dissociation of air, 32, 41
characteristic density, 42
characteristic energy, 43
characteristic pressure, 45
characteristic temperature, 42
characteristic velocity, 45
equation of state, 44, 46, 89
equilibrium enthalpy, 710-711
- Dissociation parameter, non-equilibrium flow, 646-648
- Drag coefficient, see Pressure drag coefficient
- Drag force, definition, 4
- Drag rise at transonic speed, 840-851
- Dynamic stability, 18-19
- Dynamic stability derivatives, 453-459
cone, 458-459
parabolic body, 455-458
- Effective enthalpy, 147, 150, 725, 736
- Effective heat of ablation, definition, 756
fusion, 759, 768-769, 774-776
fusion and vaporization, 758, 769-774
phenolic nylon, 775
teflon, 775-776
vaporization, 756
- Effective temperature, 145
- Elliptical nose, geometry of, 27
laminar heat transfer, 718-719
- Emissivity, effective, 695
of air, 697
- Energy equation, 82-88

- boundary layer, 83-88
 - laminar, 84-87
 - turbulent, 88
- isentropic flow, 83
- Enthalpy-entropy diagram, 34
- Entropy, conservation of, 90
- Entropy layer, 663
- Epicycloid, 251-253
- Equations of motion, 64
 - boundary conditions, 91-95
 - boundary layer, 70-72
 - curvilinear coordinates, 70
 - cylindrical coordinates, 65-67
 - normal coordinates, 69
 - spherical coordinates, 67-68
- Equation of state, 44-46, 88-90
- Fineness ratio, definition, 8, 20
- Flat nose, geometry of, 27
 - laminar heat transfer, 717-718
 - pressure coefficient at shoulder, 578
 - pressure distribution, 573-575
 - pressure drag coefficient, 574-575
 - shock detachment distance, 576-577
 - shock wave curvature, 543, 576-577
 - velocity gradient at stagnation point, 543, 578-580
- Flow separation, 385-387
- Fore drag coefficient, 379-387
- Free molecule flow, 783, 787-807
 - accommodation coefficient, 798
 - adiabatic wall temperature, 800
 - average molecular speed, 789
 - base pressure, 803
 - diffuse reflection, 788
 - drag force, 802
 - effect of angle of attack, 806-807
 - equilibrium wall temperature, 801
 - drag coefficient, cone, 803-805
 - cylindrical afterbody, 806
 - sphere, 804-806
 - friction coefficient, 795-796
 - heat transfer, 798-801
 - Maxwellian distribution function, 789
 - most probable molecular speed, 789
 - pressure coefficient, 793-795
 - specular reflection, 787-788
 - transfer of kinetic energy, 796-797
 - transfer of mass, 788-792
- Friction drag coefficient, 380-385
 - see also* Skin friction coefficient
- Geometry of bodies, 19-29
- Heat transfer, blunt cone, 738-741
 - catalytic surface, 661, 700-710
 - equilibrium temperature, 153-155
 - free molecule flow, 798-801
 - hemisphere cylinder, 728
 - laminar, beveled flat nose, 718-719
 - blunt cone, 720-724
 - cylindrical afterbody, 724-725
 - effect of diffusion, 698-712, 726-727
 - effect of recombination rate, 661, 704-710
 - effect of vorticity, 726
 - ellipsoid, 718-719
 - equilibrium dissociation, 686, 712-725
 - flat nose, 717-718
 - spherical nose, 712-717
 - skin temperature, 204-206
 - slip flow, 816-817, 822-825
 - stagnation point, effect of vorticity, 694-695
 - equilibrium dissociation, 687-693
 - nonequilibrium, 661, 690-691
 - radiation, 661-662, 695-698
 - turbulent, 727-737
 - blunt nose, 730
 - effect of diffusion, 728-730
 - effect of pressure gradient, 736-737
 - with ablation, 760
- Heat transfer coefficient, definition, 156

- Hemisphere cylinder, heat transfer, 728
 pressure distribution, 592-596
 shock wave shape, 594-597
- Hemispherical nose, pressure drag coefficient, transonic, 866-867
- Hodograph of velocity, 113-115
- Hypersonic flow, similarity law, 279, 538-541
 similarity parameter, 116, 464
 small disturbance theory, 470-478
 arbitrary body, 481-491
 cones, 478-480
- Impulse equation, 80
- Inviscid high-entropy layer, definition, 663
 flow in, 661, 663-667, 679-682
 thickness, 663-667
- Isentropic flow, 82-83
 constant specific heats, 95-97
 dissociating and ionizing gas, 100
 variable specific heats, 97-100
- Isentropic flow parameters, 99
- Knudsen number, 783, 785
- Lateral force, definition, 4
- Law of plane sections, 472-474
- Lewis-Semenov number, 85, 700
- Lift force, definition, 4
- Linearized flow, asymmetric pressure coefficient, 407-409
 axial force coefficient, 342
 center-of-pressure coefficient, 430-439
 method of doublets, 407-412
 method of sources, 343-355
 minimum drag body, 376-378
 normal force coefficient, 405, 414-425
 perturbation potential, 336-345, 405-407
 pitching moment coefficient, 425-429
 pressure coefficient, 340-342
 source distribution, 345-346
 unsteady flow, 443-459
- velocity potential, 336
- Local cones, method of, 234, 264-269, 327-329, 491-494
- Mach angle, 254
- Mass transfer, *see Ablation*
- Mean free path, 781-783, 815
- Method of characteristics, at angle of attack, 303-322
 blunt bodies, 612-620
 pointed bodies, 239-296
 characteristic curves, 244
 compatibility conditions, 245, 305-313
 epicycloids, 251-253
 hodograph plane, 247, 271
 irrotational dissociable flow, 292-293
 rotational flow, 270-282, 293-296
- Method of integral relations, 550-554
- Minimum drag body, linearized flow, 376-378
 Newtonian flow, 511-515
- Momentum equation, 79-82
 boundary layer, 80
 integral form, 81
 one-dimensional flow, 80
- Newtonian flow theory, 461, 498-541
 effect of centrifugal force, 535-538
 minimum drag body, 511-515
 modified, 515
 shadow zone, 502, 505-506, 519-521
- Nonequilibrium flow, 48-57
 behind shock wave, 135-139
 blunt nose, 642-650
 characteristic dwell time, 652
 chemical reaction rate, 50-53
 dissociation parameter, 6460-6468
 recombination rate of air, 53
 recombination rate parameter, 658
 relaxation, 49
 relaxation length, 650-651
 relaxation time, 54-56, 651, 658
- Normal force, definition, 4
- Normal force coefficient, 9-12

- arbitrary body, Newtonian flow, 516, 519-520
- blunt cone, 544
- cone, linearized flow, 424
 - Newtonian flow, 518-520
- cylindrical afterbody, linearized flow, 404, 418, 421-423
 - Newtonian flow, 517, 521-524
- effect of boattail, 526-527
- linearized flow, 405-425
- longitudinal distribution, 11
- Newtonian flow, 516-527
- nonlinear variation, 524-526
- parabolic nose, Newtonian flow, 516-517
- slender body theory, 416-417
- transonic flow, 851-852
- unsteady flow, 450-459
- viscous crossflow, 403-404, 420-422
- Normal force slope, cone-cylinder, 403
 - ogive-cylinder, 403
- Nusselt number, definition, 157
- Oblique shock wave, at hypersonic speed, 115-117
 - density ratio, 131
 - dissociable gas, 132-134
 - entropy change, 112
 - equations for, 101-134
 - flow deflection, 108-111, 122-124, 129
 - Mach number behind, 111, 117, 129
 - pressure ratio, 131
 - shock wave angle, 107-111
 - temperature ratio, 130
 - total pressure ratio, 112, 121-122
 - velocity behind, 111
 - with constant specific heats, 106-119
 - with dissociation and ionization, 124-134
 - with variable specific heats, 119-124
- Ogive-cylinders, center-of-pressure coefficient, 403
 - normal force slope, 403
 - pressure distribution, 283
- Ogive nose, center-of-pressure coefficient, linearized flow, 431
 - Newtonian flow, 532
 - geometry of, 20-22
 - pressure drag coefficient,
 - supersonic flow, 238, 264, 269
 - Newtonian flow, 508-509
 - transonic flow, 865-866
 - Parabolic boattail, pressure drag coefficient, 373-374
 - Parabolic body, dynamic stability derivatives, 455-458
 - Parabolic nose, center-of-pressure coefficient, linearized flow, 431
 - Newtonian flow, 532
 - geometry of, 22-24
 - normal force coefficient, 516-517
 - pitching moment coefficient, 528
 - pressure distribution, hypersonic flow, 492-493
 - linearized flow, 349-353, 369
 - pressure drag coefficient,
 - hypersonic flow, 494
 - linearized flow, 369
 - Newtonian flow, 508
 - supersonic flow, 269
 - universal curve, 370
 - Piston analogy, 472-474, 586-588, 597-600
 - Pitching moment, definition, 4
 - Pitching moment coefficient, 12-14
 - arbitrary body, Newtonian flow, 527-530
 - blunt cone, 544
 - cone, linearized flow, 426-427
 - Newtonian flow, 530-531
 - cylindrical afterbody, Newtonian flow, 529
 - linearized flow, 425-429
 - Newtonian flow, 527-531
 - parabolic nose, Newtonian flow, 528
 - slender body theory, 427
 - unsteady flow, 450-452
 - viscous crossflow, 428-429
 - Power law nose, flow around, 634-640
 - geometry of, 24
 - Prandtl number, definition, 85
 - Prandtl-Meyer angle, 254

- Pressure coefficient, cone, hypersonic flow,** 466-467
linearized flow, 361
Newtonian flow, 498-500
piston analogy, 633
supersonic flow, 182-183
transonic flow, 837-838
stagnation point, transonic flow, 866-867
supersonic flow, 567
Pressure distribution, arbitrary body, hypersonic flow, 487-495
linearized flow, 345-359, 372, 407-414
Newtonian flow, 500-504, 640-641
supersonic flow, 263-268, 322-328
beveled flat nose, 580-581
blunt cone, 544, 599-609
universal curve, 544, 606, 623
blunt cylinder, 596
boattail, hypersonic flow, 496
linearized flow, 372
flat nose, 573-575
hemisphere cylinder, 592-596
parabolic body, hypersonic flow, 492-493
linearized flow, 349-353, 369
power law body, 637
sphere cone, 605-608, 611, 619
at angle of attack, 621-624
spherical nose, 566-569
spherical segment nose, 580-582
Pressure drag coefficient, arbitrary body, Newtonian flow, 507
at angle of attack, 329-332
beveled flat nose, 582
blunt cone, 602, 609-611
boattail, 364-366, 373-374, 496
cone, hypersonic flow, 466-468
linearized flow, 359-361
Newtonian flow, 498-500
supersonic flow, 182-184, 238
transonic flow, 838-839, 858-865
conical flare, 366
flat nose, 574-575
ogive nose, method of local cones, 269
Newtonian flow, 508-509
supersonic flow, 238, 264
transonic flow, 865-866
parabolic nose, hypersonic flow, 494
linearized flow, 369
method of local cones, 269
Newtonian flow, 508
supersonic flow, 370
power law body, 637-640
sphere cone, 609-611
spherical nose, 238, 569-570, 866-867
spherical segment nose, 582
transonic flow, 848
Pyrex, physical properties, 768
Rankine-Hugoniot equation, 107
Rarefied gas flow, accommodation coefficient, 779
free molecule flow, 783, 787-807
intermediate regime, 779, 784, 819-820
Knudsen number, 783
mean free path, 781-783, 815
merged layer regime, 819-823
slip coefficient, 809
slip flow regime, 784, 808-825
slip velocity, 809
surface interaction, 779, 787-788
transition regime, 779, 819
Recovery factor, 151
Reynolds analogy, 155-159, 735
Rolling moment, definition, 4
Schmidt number, definition, 85
Shock detachment distance,
beveled flat nose, 583
flat nose, 576-577
low Reynolds number, 821
nonequilibrium flow, 654-656
spherical nose, 560, 570-572
spherical segment nose, 584
Shock expansion theory, 322-327, 494-497
Shock layer radiation, 695-698
Shock polar, 113-115
Shock wave, nonequilibrium flow behind, 134-139
Shock wave angle, cone, 161, 179, 463-465, 633

- Shock wave curvature, beveled
 flat nose, 584-585
 blunt nose, 543
 flat nose, 543, 576-577
 sharp nose, 485-486
 spherical nose, 570-572
 spherical segment nose, 585
- Shock wave shape, blunt cone,
 599-604
 blunt cylinder, 596
 hemisphere cylinder, 594-597
 power law body, 636
- Side force, definition, 4
- Side slip angle, definition, 4
- Similarity law, blunt cone, 603-
 606
 cone, 180
 hypersonic, 464-480
 supersonic, 355-359, 412-414
 transonic, 829-839
- Skin friction and heat transfer,
 relation between, 155-159, 735
- Skin friction coefficient, average value, 141
 cone, 194-198, 200-202
 cylindrical afterbody, 384
 definition, 9
 effect of diffusion, 727-729
 laminar, 2, 141-143, 197-202,
 379-385
 local, 141
 slip flow, 812-816
 turbulent, 2, 141-144, 148-149,
 198-202, 379-385
- Slender body theory, 353-355, 411
 normal force coefficient, 416-
 417
 pitching moment coefficient,
 427
 pressure drag coefficient, 375-
 376
 unsteady flow, 448-449
- Slip flow, 808-825
 skin friction coefficient, 812-
 816
 heat transfer, 816-817, 822, 824-
 825
- Small disturbance theory, hypersonic flow, 470-478
- Specific heat, average for a mixture, 84
 variation with temperature, 30-31
- Sphere, drag coefficient in free molecule flow, 804-806
- Sphere cone, laminar heat transfer, 720-724
 pressure distribution, 605-608,
 611, 619
 at angle of attack, 621-624
 pressure drag coefficient, 609-
 611
- Spherical nose, flow near stagnation point, 554-565
 laminar heat transfer, 712-717
 location of sonic point, 565
 pressure distribution, 566-569
 pressure drag coefficient,
 569-570
 shock detachment distance,
 560, 570-572
 shock wave curvature, 570-572
 velocity gradient at stagnation point, 560-564
- Spherical segment nose, geometry of, 26-27
- Spherically blunted nose, geometry of, 24-27
- Stabilization of bodies, 432-442
 effect of flare, 441-442
 effect of tail surface, 439-441
- Stagnation point, heat transfer, equilibrium dissociation,
 687-693
 nonequilibrium, 661, 690-691
 radiation, 661-662, 695-698
 pressure coefficient, hypersonic flow, 567
 transonic flow, 866-867
 velocity gradient, blunt nose,
 543
 flat nose, 543, 578-580
 spherical nose, 560-564
- Stanton number, definition, 157
- Static margin, 432-435
- Static stability, 15
- Stefan-Boltzmann law, 152-153
- Stream function, 77
- Teflon, physical properties, 774
- Thermodynamic properties of air, 32-40
 atomic and molecular concentrations, 33
 average molecular weight, 36

- enthalpy-entropy diagram, 33-34
speed of sound, 37
thermal conductivity, 39-40
Transition Reynolds number, 381, 399, 670-676, 730-734
Transonic similarity law, 829-839
pressure coefficient, 834-835
similarity parameter, 832, 835
Vaporization coefficient, definition, 758
Velocity potential, cylindrical coordinates, 74
spherical coordinates, 75
Viscosity, glassy materials, 766-768
Viscosity of air, 37-39
Sutherland equation, 38
Viscous crossflow, center-of-pressure coefficient, 439
normal force coefficient, 403-404, 420-423
pitching moment coefficient, 403-404, 428-429
Wind coordinates, definition, 4
Yawing moment, definition, 4

SELECTED RAND BOOKS

- Shanley, F. R. *Weight-Strength Analysis of Aircraft Structures*. New York: McGraw-Hill Book Company, Inc., October 1952.
- Williams, J. D. *The Compleat Strategyst: Being a Primer on the Theory of Games of Strategy*. New York: McGraw-Hill Book Company, Inc., June 1954.
- The RAND Corporation. *A Million Random Digits with 100,000 Normal Deviates*. Glencoe, Illinois: The Free Press, March 1955.
- Bellman, Richard. *Dynamic Programming*. Princeton, New Jersey: Princeton University Press, November 1957.
- Krieger, F. J. *Behind the Sputniks: A Survey of Soviet Space Science*. Washington, D. C.: Public Affairs Press, July 1958.
- Buchheim, Robert W. and the Staff of The RAND Corporation. *Space Handbook: Astronautics and Its Applications*. New York: Random House, Inc., August 1959.
- Brodie, Bernard. *Strategy in the Missile Age*. Princeton, New Jersey, Princeton University Press, September 1959.
- Hitch, Charles J., and Roland McKean. *The Economics of Defense in the Nuclear Age*. Cambridge, Massachusetts: Harvard University Press, September 1960.
- Hirshleifer, Jack, James C. DeHaven, and Jerome W. Milliman. *Water Supply: Economics, Technology, and Policy*. Chicago, Illinois: The University of Chicago, October 1960.
- Dresher, Melvin. *Games of Strategy: Theory and Applications*. Englewood Cliffs, New Jersey: Prentice-Hall, Inc., June 1961.
- Dubyago, A. D. *The Determination of Orbits*. New York: The Macmillan Company, November 1961.
- Gouré, Leon. *The Siege of Leningrad*. Stanford, California: Stanford University Press, June 1962.
- Bellman, Richard E., and Stuart E. Dreyfus. *Applied Dynamic Programming*. Princeton, New Jersey: Princeton University Press, July 1962.
- Ford, L. R., Jr., and D. R. Fulkerson. *Flows in Networks*. Princeton, New Jersey: Princeton University Press, September 1962.
- Sokolovskii, V. D. (ed.). *Soviet Military Strategy*. Englewood Cliffs, New Jersey: Prentice-Hall, Inc., April 1963.

- Bellman, R. E., R. E. Kalaba, and M. C. Prestrud. *Invariant Imbedding and Radiative Transfer in Slabs of Finite Thickness* (Volume 1). New York: American Elsevier Publishing Company, Inc., July 1963.
- Boehm, Barry W. *Rand's Omnibus Calculator of the Kinematics of Earth Trajectories*. Englewood Cliffs, New Jersey: Prentice-Hall, Inc., February 1964.
- Dole, Stephan H. *Habitable Planets for Man*. New York: Blaisdell Publishing Company, March 1964..
- Bellman, R. E., H. H. Kagiwada, R. E. Kalaba, and M. C. Prestrud. *Invariant Imbedding and Time-dependent Transport Processes* (Volume 2). New York: American Elsevier Publishing Company, Inc., April 1964.
- Judd, William R. (ed.). *State of Stress in the Earth's Crust*. New York: American Elsevier Publishing Company, Inc., September 1964.
- Selin, Ivan. *Detection Theory*. Princeton, New Jersey: Princeton University Press, July 1965.
- Bellman, Richard E., and Robert E. Kalaba. *Quasilinearization and Non-linear Boundary-Value Problems* (Volume 3). New York: American Elsevier Publishing Company, Inc., August 1965.
- Meyer, John R., Martin Wohl, and John F. Kain. *The Urban Transportation Problem*. Cambridge, Massachusetts: Harvard University Press, September 1965.
- Novick, David (ed.). *Program Budgeting: Program Analysis and the Federal Budget*. Cambridge, Massachusetts: Harvard University Press, December 1965.
- Horelick, Arnold L., and Nyron Rush. *Strategic Power and Soviet Foreign Policy*. Chicago, Illinois: University of Chicago Press, April 1966.
- Bellman, R. E., R. E. Kalaba, and J. Lockett. *Numerical Inversion of the Laplace Transform* (Volume 4). New York: American Elsevier Publishing Company, Inc., December 1966.
- Gazley, Jr., Hartnett, and Eckert. *Proceedings of the Second All-Soviet Union Conference on Heat and Mass Transfer* (Volumes 1-7). Ann Arbor, Michigan: University Microfilms, February 1968.
- Sheppard, J. J. *Human Color Perception*. New York: American Elsevier Publishing Company, Inc., May 1968.
- Quade, E. S., and W. I. Boucher. *Systems Analysis and Policy Planning Applications in Defense*. New York: American Elsevier Publishing Company, Inc., June 1968.
- Deirmendjian, D. *Electromagnetic Scattering on Spherical Polydispersions*. New York: American Elsevier Publishing Company, Inc., April 1969.